Fluid inclusion, stable and radiogenic isotope, and geochronological investigation of the polymetallic "five-element" vein deposit at the Eldorado Mine, Port Radium, Northwest Territories, Canada

By
Corwin Ronald Maiakôr Trottier

A thesis submitted to Saint Mary's University, Halifax, Nova Scotia in partial fulfillment of the requirements for the Degree of Master of Science in Applied Science

August 13, 2019, Halifax, Nova Scotia

Approved: Dr. Jacob Hanley
Supervisor
Department of Geology
Saint Mary's University

Approved: Dr. Eric Potter
Supervisory Committee
Geological Survey of Canada
Natural Resources Canada

Approved: Dr. James Brenan
Supervisory Committee
Department of Earth Sciences
Dalhousie University

Approved: Dr. Roby Austin
Supervisory Committee
Department of Astronomy and Physics
Saint Mary's University

August 13, 2019

Abstract

Fluid inclusion, stable and radiogenic isotope, and geochronological investigation of the polymetallic "five-element" vein deposit at the Eldorado Mine, Port Radium, Northwest Territories, Canada

By: Corwin Ronald Maiakôr Trottier

Uranium-rich, polymetallic "five-element" (Ni-Co-As-Bi-Ag) veins at the Eldorado Mine were investigated using complementary microanalytical techniques with the goal to improve understanding of the origins of fluids and metals, and timing of vein formation. Fluid inclusion assemblages record overall variability in mineralization P-T conditions from 100–300 °C, and up to 135 MPa. Mineralizing fluids carry the chemical signature of a highly saline brine, derived from evaporated, modified seawater: ~20–35 wt.% NaCl + $CaCl_2$ equivalent bulk salinity, and molar Cl/Br of ~230 during arsenide-stage mineralization and ~125 during sulphide-stage mineralization. The basinal brine was likely introduced from the 1740–1270 Ma Hornby Bay Basin. Arsenide mineralization is constrained at 1442 ± 36 Ma by U-Pb geochronology of coeval hydrothermal xenotime. $^{87}Sr/^{86}Sr$ values of 0.7046–0.7239 for vein carbonates conforms to a similar range of values in host rocks (ca. 1440 Ma), suggesting significant fluid-rock interaction and alteration of wall-rock.

August 13, 2019

Acknowledgments

I offer my thanks to collaborators: Yiwei Yin and Zoltán Zajacz at the University of Toronto LA-ICP-MS lab, Ryan Sharpe and Mostafa Fayek at University of Manitoba SIMS lab, Tom Pestaj and Bill Davis at the Ottawa GSC SHRIMP lab. I am especially thankful for Eric Potter's contributions to this project, by helping collect samples, sharing important documents and research updates, and offering his insight in advisory committee meetings. Thanks also to Roby Austin and James Brenan, for their valuable suggestions, questions, and support as advisory committee members. I am thankful beyond words for Jacob Hanley's supervision. He has shown persistence and faithful enthusiasm in keeping up with all the details of this thesis as it evolved through the years. Neither of us had expected to spend as much time on this project as we have, but I appreciate the valuable time we have had to share ideas and stories. Jake's wisdom never ceases to amaze me, whether it is revealed through a speculation on some distantly related theory or a methodical dismantling of a mental block I had encountered.

I acknowledge the financial support and recognition from the following organizations: Targeted Geoscience Initiative (TGI5; major project funding), Natural Sciences and Engineering Research Council (CGS M), Province of Nova Scotia and Faculty of Graduate Studies and Research at Saint Mary's University (NSGS), Society of Economic Geologists Foundation (GSF), Mineralogical Association of Canada Foundation (MSc scholarship).

I am grateful to many members of the faculty and staff at SMU for their support, advice, and friendship throughout my studies. Georgia Pe-Piper was particularly influential in cultivating my interests in geology and encouraging me to pursue those interests further. I greatly appreciate the help from Randy, Xiang, Fergus, and Mitch for their assistance with sample preparation and training in the lab. I also thank many past and present students, and members of the geology societies at SMU, who helped create a constructive community. Special thanks to Jordan, who helped establish the foundation for the direction of my thesis, and was invaluable in office discussions of both productive and frivolous variety; and Matt, not only for risking life and limb with me during dubious sample prep, but also for being a reliable sounding board during late night petrography reviews, and a companion in the weight room and on the field and throughout the years.

I am indebted to the support of my friends, family, and my wife who graciously put up with my unreliable schedule, especially around major deadlines. At last I thank my mother, who was always enthusiastic about reviewing my work and hearing me through the ups and downs. I appreciate every sacrifice she made to ensure my success.

Table of contents

List of figures

List of tables

List of abbreviations

Abbreviation	Definition
GBMZ	Great Bear Magmatic Zone
WCD	Western Channel Diabase
HBB	Hornby Bay Basin
Mt	million tonnes
Ma	million years ago
Ga	billion years ago
FI	fluid inclusion
FIA	fluid inclusion assemblage
L_{aq}	aqueous liquid phase
V	vapour phase
HH	hydrohalite
H	halite
P	pressure
P_{tr}	trapping pressure for FI
T	temperature
T_e	eutectic
T_m^{ice}	final melting of ice
T_d^{HH}	incongruent melting of HH
T_d^{H}	dissolution of halite
T_v	$V + L_{aq}$ homogenizes to L_{aq}
T_h	total homogenization to L_{aq}
T_{tr}	trapping temperature for FI
X	chemical composition (mole fraction)
wt.%	percent composition by weight
wt.% NaCl eq.	bulk salinity expressed as wt.% equivalent of dissolved NaCl
S_{wt}	bulk salinity (wt.% eq.) as the sum of NaCl and $CaCl_2$
ppm	parts per million
‰	parts per thousand (per mille)
δD	stable isotope ratio $^2H/^1H$ of sample relative to standard
$\delta^{18}O$	stable isotope ratio $^{18}O/^{16}O$ of sample relative to standard
$\delta^{13}C$	stable isotope ratio $^{13}C/^{12}C$ of sample relative to standard
VSMOW	Vienna Standard Mean Ocean Water (H, O isotope standard)
PDB	Pee Dee Belemnite (C, O isotope standard)

REE	rare-earth elements
LREE	light REE (La–Eu)
HREE	heavy REE (Y, Gd–Lu)
SEM	scanning electron microscope
FE	field emission
EDS	energy dispersive X-ray spectroscopy
BSE	backscattered electron
CL	cathodoluminescence
TIMS	thermal ionization mass spectrometry
SIMS	secondary ion mass spectrometry
SHRIMP	sensitive high-resolution ion microprobe
LA-ICP-MS	laser ablation inductively-coupled plasma mass spectrometry
ICP-OES	inductively-coupled plasma optical emission spectrometry

Abbreviation	**Mineral species name**
urn	uraninite
cof	coffinite
nk	nickeline
gdf	gersdorfite
cob	cobaltite
apy	arsenopyrite
ram	rammerlsbergite
saf	safflorite
sk	skutterudite
anna	annabergite
ery	erythrite
BMS	base metal sulphides
cpy	chalcopyrite
bn	bornite
gn	galena
sph	sphalerite
ttr	tetrahedrite
tn	tennantite
py	pyrite
mrc	marcasite

wtc	wittichenite
bis	bismuthinite
qz	quartz
carb	carbonate
cal	calcite
Mn-cal	Mn-rich (manganoan) calcite
dol	dolomite
Fe-dol	Fe-rich (ferroan) dolomite
Mn-dol	Mn-rich (manganoan) dolomite
ank	ankerite
kut	kutnohorite
sdr	siderite
mgs	magnesite
rdc	rhodocrosite
act	actinolite
chl	chlorite
hem	hematite
brt	barite
hul	heulandite
ap	apatite
xn	xenotime

Thesis structure

This thesis comprises three chapters: Chapter 1 is an introduction to the main research topic: polymetallic “five-element” veins. Chapter 2 takes the form of a manuscript intended for submission to *Precambrian Geology*, which describes the concepts, methods, results, and discussions regarding the study of this thesis project. Chapter 3 includes a summary of the conclusions from Chapter 2, a discussion of significant limitations encountered in this study, and recommendations for future work to build upon the information gained from this study.

Chapter 1: Introduction

1.1 Polymetallic veins and associated hydrothermal fluids

Various styles of hydrothermal mineralization are found around the world, and in all tectonic environments. The polymetallic vein style is a subset of hydrothermal mineral occurrences that, itself, include many styles of mineralization (Kissin 1992; Lefebure and Church 1996; Corriveau et al. 2016). As the name suggests, a polymetallic deposit is enriched in multiple metallic commodities, making it a potentially favourable exploration target. Subclassifications of polymetallic vein deposit styles are often named after the dominant metals enriched in the vein mineralogy, although some may be named after type localities. Every polymetallic vein deposit shares the trait of having minerals deposited in veins of variable morphology within a host rock. The mechanism for vein formation is, in part, linked to tectonic activity. Host rocks that experience changes in local or regional stress can develop faults and fractures. These structures provide permeability for hydrothermal fluids. Hydrothermal fluids are heated aqueous solutions that can transport dissolved metals (Pirajno 2009). If metals in these fluids become saturated due to changes in physicochemical conditions, then minerals and native metals may begin to crystallize inside the fractures, forming mineralized veins that may be economically viable to exploit.

As a mineral precipitates from a hydrothermal solution, some of that solution may become trapped on the surface of the growing mineral. Further mineral growth can envelope the solution, resulting in inclusions of trapped fluid (primary inclusions). Fluid inclusions are also commonly formed along healed fractures (secondary), and can be subsequently overgrown by a new generation of the host mineral (pseudo secondary). Fluid

inclusions can be preserved in this way over geologic time, allowing modern analytical tools to measure properties of ancient hydrothermal solutions. Fluid inclusions are ubiquitous and are clearly visible in transparent minerals, though often microscopic. Groups of fluid inclusions that are spatially associated and characteristically similar are called fluid inclusion assemblages (FIA), and represent fluid inclusions that were trapped at the same time and under the same conditions (Bodnar 2003; Goldstein 2003). It is important to characterize the properties of several fluid inclusions in an assemblage to differentiate variability that would indicate post-entrapment modification from real variations in fluid pressure, temperature, or composition that might be relevant to geological processes (Goldstein and Reynolds 1994).

Hydrothermal fluids can be described as having several physical and chemical properties: the physical state of fluid matter, its density (ρ), pressure (P), temperature (T), and chemical composition of the fluid and compounds dissolved therein (X) (Pirajno 2009). The physical state of a fluid may be a liquid, gas, or supercritical fluid; the states common at geologic conditions on Earth (high T, high P). The temperature of hydrothermal fluids ranges from ambient to near magmatic T, and may be related to geothermal gradient or intrusive heat sources. Pressure increases with depth, and is controlled by the depth of surrounding rock (lithostatic pressure) or surrounding fluid (hydrostatic pressure). This collection of properties can be sought to help characterize hydrothermal fluids and hydrothermal systems in ore-forming environments.

The source of hydrothermal fluids may be identified using a combination of previously outlined fluid properties. Common sources of hydrothermal fluids include meteoric water, seawater, formation or connate waters, metamorphic, or magmatic-derived

fluids (Pirajno 2009). Meteoric water comprises fresh rainwater, surface water, and shallow groundwater. Comparatively, seawater is considerably more saline, and can also be distinguished by their more δD and $\delta^{18}O$ enriched stable isotope compositions compared to most meteoric waters. Connate (formation) fluids originate in sedimentary rocks during diagenesis, are typically higher T and more saline than meteoric or seawater, and may contain a greater complexity, and higher concentrations of total dissolved solids. Metamorphic fluids become more prevalent in the deeper crust. These fluids are released during devolatilization reactions involving hydrous minerals at elevated P and T. As such, metamorphic fluids commonly contain volatiles and dissolved metals that reflect bulk regional mineralogy of a range of host rocks within a metamorphic terrane. Magmatic fluids represent the highest temperature hydrothermal fluids. Magmatic fluids may include dissolved sulphur-rich volatiles and metals that were separated from a cooling magma, and/or released during partial melting. Due to the distinct characteristics of each source, hydrothermal fluid properties can be used to relate a mineralized system back to the fluid source. However, hydrothermal polymetallic veins may be produced by a mixture of fluid types, making sourcing more problematic. Despite these difficulties, identifying possible fluid sources can provide valuable insight into the tectonic and regional geological history of an ore deposit.

1.2 "Five-element" veins

Polymetallic cobalt-nickel-arsenic-silver-bismuth (Co-Ni-As-Ag-Bi) veins are commonly referred to as "five-element" veins due to their prevailing chemical signature

(Franklin et al. 1986; Kissin 1992; Markl et al. 2016). “Five-element” vein mineralogy (e.g. Co-Ni sulpharsenide and arsenide minerals, and native Ag-Bi) and ore textures (e.g. open-space filling, dendritic, colloform banding) are remarkably consistent across several deposits and are regarded as characteristic features of this deposit style (Kidd and Haycock 1935; Kissin 1992; Burisch et al. 2016). Although the mineralogy is generally consistent, there are still deposit scale differences. For example, in the Port Radium district of Canada, Robinson and Ohmoto (1973) saw minor variations in the timing and composition of sulphides and Ag minerals between the adjacent Echo Bay and Eldorado mines. Additionally, the Eldorado deposit carries a significant U endowment, whereas the Echo Bay deposit is devoid of U.

The mineralization history and vein paragenetic sequence is tediously complex, and is typically represented by stages of mineralization punctuated with periods of faulting and brecciation (Kidd and Haycock 1935; Kissin 1992; Dolníček et al. 2009; Staude et al. 2012). As with their mineralogy, different “five-element” deposits commonly show slight variations in paragenesis, and in some cases certain mineralization stages are completely absent. Kissin (1992) provided a thorough summary of the typical stages of “five-element” mineralization.

The “five-element” mineralization style has not yet been linked unambiguously to a prerequisite geological setting of formation. Significant occurrences have been found throughout North America, Europe, and Africa, and are likely present throughout the world in a wide range of rock types of diverse ages (Bastin 1939; Kissin 1992; Markl et al. 2016). Mineralizing events in the study area (the Great Bear Magmatic Zone) and other Canadian deposits (e.g. Cobalt, Ontario) are consistently of Proterozoic age (Ruzicka and Thorpe

1995; Gandhi et al. 2018). In contrast, many European deposits were formed during the Paleozoic Era or later (Wagner and Lorenz 2002; Dolníček et al. 2009; Staude et al. 2012; Burisch et al. 2016). The host lithology of these deposits include variably altered metavolcanics and metasediments, commonly associated with nearby granitic intrusions (Kissin 1992). The mineralization itself is structurally controlled within fault zones, often assumed to be related to rifting (Franklin et al. 1986; Ruzicka and Thorpe 1995; Lefebure 1996; Burisch et al. 2016). This thesis explores the origin of "five-element" veins at Port Radium, NWT, Canada using in-situ microanalytical techniques, and aims to revise the genetic model for "five-element" veins on a broader scale.

1.3 References

Bastin ES (1939) The Nickel-Cobalt-Native Silver Ore-type. Econ Geol 34:1-40

Bodnar RJ (2003) Introduction to Fluid Inclusions. In: Samson I, Anderson A, Marshall D (eds) Fluid Inclusions: Analysis and Interpretations. Mineralogical Association of Canada, Short Course no. 32, 1-8

Burisch M, Gerdes A, Walter BF, Neumann U, Fettel M, Markl G (2016) Methane and the origin of five-element veins: Mineralogy, age, fluid inclusion chemistry and ore forming processes in the Odenwald, SW Germany. Ore Geol Rev 81:42-61

Burke JS (2019) The origin of polymetallic Ni-Co-As-Bi-Sb(-Ag-U) veins in the East Arm Basin and southern Slave Province, Northwest Territories. M.Sc. thesis, Saint Mary's University

Corriveau L, Montreuil J, Potter EG (2016) Alteration Facies Linkages Among Iron Oxide Copper-Gold, Iron Oxide-Apatite, and Affiliated Deposits in the Great Bear Magmatic Zone, Northwest Territories, Canada. Econ Geol 111:2045-2072

Dolníček Z, Fojt B, Prochaska W, Kučera J, Sulovský P (2009) Origin of the Zálesí U–Ni–Co–As–Ag/Bi deposit, Bohemian Massif, Czech Republic: fluid inclusion and stable isotope constraints. Miner Deposita 44:81-97

Franklin JM, Kissin SA, Smyk MC, Scott SD (1986) Silver deposits associated with the Proterozoic rocks of the Thunder Bay District, Ontario. Can J Earth Sci 23:1576-1591

Gandhi SS, Potter EG, Fayek M (2018) New constraints on genesis of the polymetallic veins at Port Radium, Great Bear Lake, Northwest Canadian Shield. Ore Geol Rev 96:28-47

Goldstein RH (2003) Petrographic Analysis of Fluid Inclusions. In: Samson I, Anderson A, Marshall D (eds) Fluid Inclusions: Analysis and Interpretations. Mineralogical Association of Canada, Short Course no. 32, 9-53

Goldstein HR, Reynolds TJ (eds) (1994) Systematics of fluid inclusions in diagenetic minerals. SEPM Society for Sedimentary Geology, Short Course no. 31

Kidd DF, Haycock MH (1935) Mineragraphy of the Ores of Great Bear Lake. Bulletin of the Geological Society of America 46:879-960

Kissin SA (1992) Five-element (Ni-Co-As-Ag-Bi) Veins. J Geol Assoc Can 19:113-124

Lefebure DV (1996) Five-element Veins Ag-Ni-Co-As+/-(Bi,U). In: Lefebure DV, Hõy T (eds) Selected British Columbia Mineral Deposit Profiles, Volume 2 - Metallic Deposits. British Columbia Ministry of Employment and Investment, Open File 1996-13, 89-92

Lefebure DV, Church BN (1996) Polymetallic Veins Ag-Pb-Zn+/-Au. In: Lefebure DV, Hõy T (eds) Selected British Columbia Mineral Deposit Profiles, Volume 2 - Metallic

Deposits. British Columbia Ministry of Employment and Investment, Open File 1996-13, 67-70

Markl G, Burisch M, Neumann U (2016) Natural fracking and the genesis of five-element veins. Miner Deposita 51:703-712

Pirajno F (2009) Water and Hydrothermal Fluids on Earth. In: Pirajno F (ed) Hydrothermal Processes and Mineral Systems. Springer, Perth, Australia, 1-65

Robinson BW, Ohmoto H (1973) Mineralogy, Fluid Inclusions, and Stable Isotopes of the Echo Bay U-Ni-Ag-Cu Deposits, Northwest Territories, Canada. Econ Geol 68:635-656

Ruzicka V, Thorpe RI (1995) Arsenide vein silver, uranium. In: Eckstrand OR, Sinclair WD, Thorpe RI (eds) Geology of Canadian Mineral Deposit Types. Geological Survey of Canada, Geology of Canada, no. 8, Natural Resources Canada, 287-306

Staude S, Werner W, Mordhorst T, Wemmer K, Jacob D, Markl G (2012) Multi-stage Ag–Bi–Co–Ni–U and Cu–Bi vein mineralization at Wittichen, Schwarzwald, SW Germany: geological setting, ore mineralogy, and fluid evolution. Miner Deposita 47:251-276

Wagner T, Lorenz J (2002) Mineralogy of complex Co-Ni-Bi vein mineralization, Bieber deposit, Spessart, Germany. Mineral Mag 66:385-407

Chapter 2: Fluid inclusion, stable and radiogenic isotope, and geochronological investigation of the polymetallic "five-element" vein deposit at the Eldorado Mine, Port Radium, Northwest Territories, Canada

Corwin Trottier*[1], Jacob Hanley[1], Eric Potter[2], Bill Davis[2], Mostafa Fayek[3], Zoltán Zajacz[4]

[1]*Department of Geology, Saint Mary's University, Halifax, Nova Scotia, B3H 3C3, Canada*

[2]*Geological Survey of Canada, 601 Booth Street, Ottawa, Ontario, K1A 0E8, Canada*

[3]*Department of Geological Sciences, University of Manitoba, Winnipeg, Manitoba, R3T 2N2, Canada*

[4]*Department of Earth Sciences, University of Toronto, Toronto, Ontario, M5S 3B1, Canada*

*corresponding author email address: corwin.trottier@gmail.com

Abstract

Uranium-rich, polymetallic "five-element" (Ni-Co-As-Bi-Ag) veins at the Eldorado Mine, NWT, Canada were investigated with a range of complementary microanalytical techniques with the goal to improve understanding of the origins of fluids and metals, and timing of vein formation. The existing paragenetic model was revised based on new textural and mineralogical observations, including the co-precipitation of uraninite and Ni-Co-sulpharsenides, and distinct "branches" of the paragenesis that led to Co-dominant vs. Ni-dominant mineral assemblages in different parts of the deposit. Fluid inclusion microthermometric data constrains formation conditions for mineralization from ~ 100 to 300 °C and up to 135 MPa. Significant inter-fluid inclusion assemblage (FIA) variability in T_h records real variations in trapping conditions. Typical intra-FIA ranges in T_v and T_d^H are ~20–40 °C; S_{wt} ranges are typically no more than a few wt.% eq. Mineralizing fluids carry the chemical signature of a highly saline brine, derived from evaporated, modified, seawater; bulk salinity ranges from ~20 to 35 wt.% NaCl + $CaCl_2$ equivalent, with an average molar Cl/Br = 230 in the arsenide stage, and 125 in the sulphide stage. The basinal brine was likely introduced from the 1740–1270 Ma Hornby Bay Basin, unconformably overlying the crystalline Great Bear Magmatic Zone (GBMZ) at the time of mineralization. The age of arsenide mineralization is constrained at 1442 ± 36 Ma by U-Pb geochronology of coeval hydrothermal xenotime. The xenotime geochronometer also lends support to a primary mineralization age for early uraninite ca. 1453 Ma. A wide range in $^{87}Sr/^{86}Sr$ values (0.7046–0.7239 ca. 1440 Ma) for vein carbonates conforms to a similar range of values in host rocks, suggesting significant wall-rock influence on mineralizing fluid composition at low fluid/rock ratios during mineralization.

2.1 Introduction

2.1.1 "Five-element" veins

"Five-element" (Co-Ni-As-Ag-Bi) veins are recognized by their typical ore and accessory mineral assemblages consisting of Fe-Co-Ni sulpharsenide and arsenide minerals, As, Ag, Bi sulphosalts, and native As, Ag, and Bi; and textures including open-space fill, dendrites, colloform banding, and breccias (Kidd and Haycock 1935; Franklin et al. 1986; Kissin 1992; Markl et al. 2016; Burisch et al. 2017). Other metals such as Sb and U may be present in significant quantities with Sb substituting for As in arsenide minerals and solid solution sulphosalts, and U primarily occurring in uraninite and its alteration products (Kidd and Haycock 1935; Badham 1975; Kissin 1992; Ondruš et al. 2003; Zajzon et al. 2005; Dolníček et al. 2009; Staude et al. 2012). These mineral assemblages commonly show a general paragenetic sequence consisting of early, barren quartz with minor oxides or sulphides (stage 1); uraninite and quartz (stage 2); arsenide minerals and native metals (stage 3); sulphides and native metals (stage 4); carbonate and other gangue minerals (stage 5; Kissin 1992). The diversity of valuable metals (e.g. Ag, Bi, and U) presents the propensity for high-grade mineralization, making "five-element" deposits strategic exploration targets.

Deposits of this type are found worldwide, notably in Canada (e.g. Eldorado, NWT; Cobalt-Gowganda, ON; Silver Islet, Thunder Bay, ON; Kidd and Haycock 1935; Franklin et al. 1986; Andrews et al. 1986; Kissin 1992), and Europe (e.g. Jáchymov, Erzgebirge, Czech Republic; Wittichen, Schwarzwald, SW Germany; Kongsberg, Oslo, Norway; Ondruš et al. 2003; Staude et al. 2012; Markl 2016; Kotková et al. 2018). While these deposits may all be classified as "five-element" vein systems, they exhibit some significant

variations in mineralogy and paragenesis from one deposit to another and even within a single deposit (Campbell 1955; Kissin 1992; Gandhi et al. 2018). Additionally, variations in estimated formation temperature, fluid salinity, host rock, and mineralization age preclude a common genetic model (Kissin 1992; Staude et al. 2012). Furthermore, a diversity of host lithologies—including many varieties of igneous, metamorphic, and sedimentary rocks—complicates investigations of fluid and metal sources. The low fluid/rock ratios suggested by commonly narrow, low-intensity alteration haloes can result in fluids that are dominated by local wall-rocks, masking distally derived fluid and metal signatures (Andrews et al. 1986; Pirajno 2009; Mathieu 2018). Clearly, the characteristic "five-element" metal association cannot be derived entirely by local host rocks in every deposit (Kissin 1992).

Numerous genetic models have been proposed to explain the features of different "five-element" deposits. Kissin (1992), and references therein, summarize a variety of proposed models including: (i) magmatic/hydrothermal models, where mineralizing fluids originated from local felsic or mafic intrusions; (ii) metamorphic/hydrothermal models, where local heat sources aid in mobilizing metals from metal-rich source rocks; and (iii) sedimentary models, where metals in various sedimentary source rocks are mobilized by formational brines, which circulate in high-temperature rift settings. Despite a significant effort, historical studies did not have the analytical methodologies suitable to definitively constrain fluid sources, metal sources, and mineralization mechanisms for a general model.

Recently, Markl et al. (2016) and Burisch et al. (2017) revised the model for "five-element" deposits considering the role of methane in producing the typical "five-element" mineralogy and ore textures. This model requires an oxidized, metal-rich fluid, that when

mixed with a reduced fluid containing methane or other hydrocarbons, drives an abrupt decrease in metal solubility. Active fault zones can accelerate this process by releasing previously trapped hydrocarbons and providing permeable structures for fluid mixing (Markl et al. 2016). Recent studies of European "five-element" deposits have also shown promise in applying high-resolution microanalytical techniques to better understand the origin of mineralizing fluids (Dolníček et al. 2009; Staude et al. 2012; Burisch et al. 2017).

This study is the first of its kind to utilize LA-ICP-MS to measure ore metal and other major, minor, and trace element concentrations in fluid inclusions at the Eldorado deposit (Port Radium, NWT, Canada). Fluid chemistry, when combined with other data types from SIMS, fluid inclusion microthermometry, and SHRIMP geochronology, enables the development of a robust genetic interpretation of fluid sources and some key ore formation processes at Eldorado. The ore formation model is further discussed in the context of other polymetallic vein systems in the region.

2.1.2 Regional geology

The Great Bear Magmatic Zone (GBMZ) is a north-south trending suite of plutonic and volcanic rocks that is exposed from the northern extent of Great Slave Lake to the northeastern shores of Great Bear Lake in the NWT, Canada (Figure 2.1; 2.2). This magmatic belt comprises a significant portion of the Bear Province of the Canadian Shield, and is interpreted as an Andean-type continental magmatic arc, formed during a collision between two ancient geologic terranes (Corriveau et al. 2016; Montreuil et al. 2016a; Slack et al. 2016).

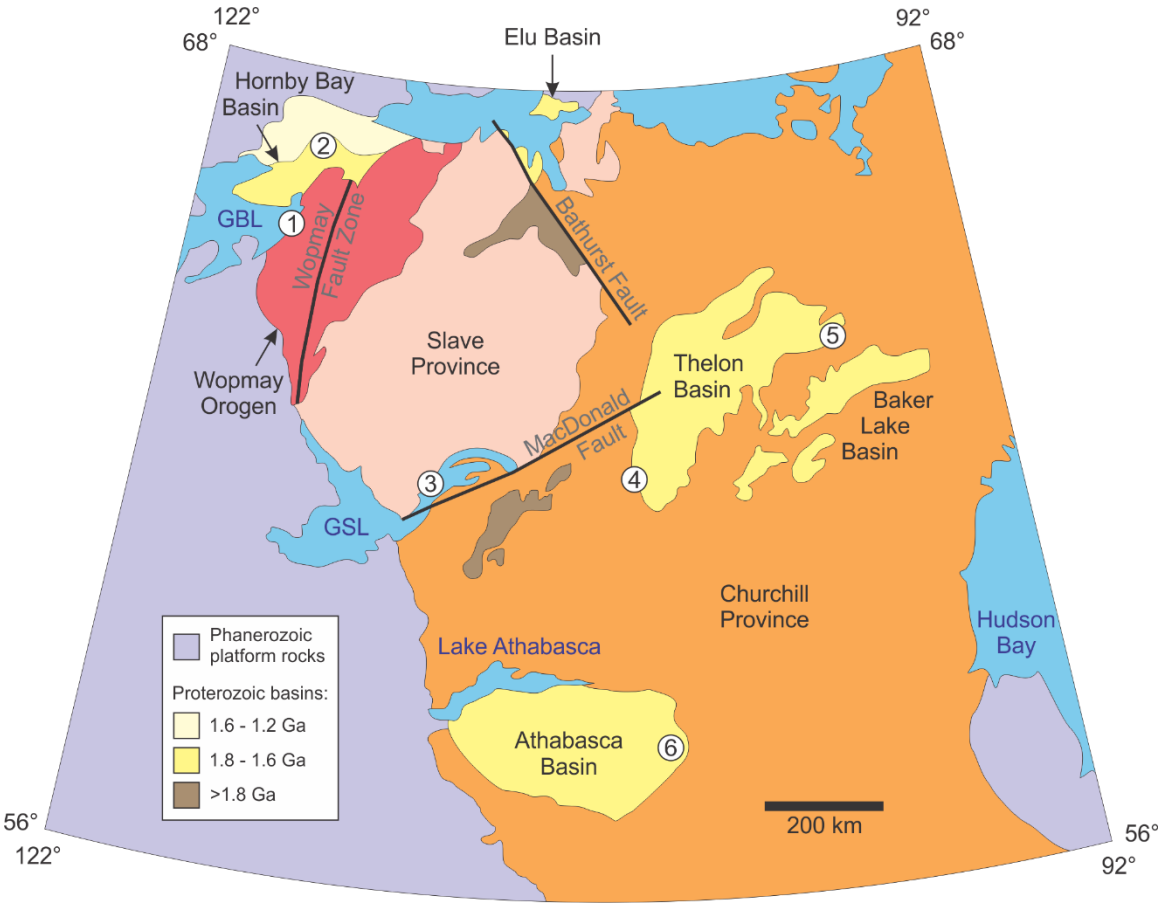

Figure 2.1: Simplified geological map of the northwest Canadian Shield. Numbers correspond to areas of interest with respect to "five-element" or unconformity U mineralization in Proterozoic sedimentary basins. 1: GBMZ U-Ag deposits (Fig. 2.4); 2: Mountain Lake U deposit; 3: Copper Pass and Blanchet Island "five-element" vein occurrences; 4: Boomerang; 5: Kiggavik; 6: Athabasca unconformity U deposits (e.g. Cigar Lake, Rabbit Lake, McArthur River). Modified from Ross (1983).

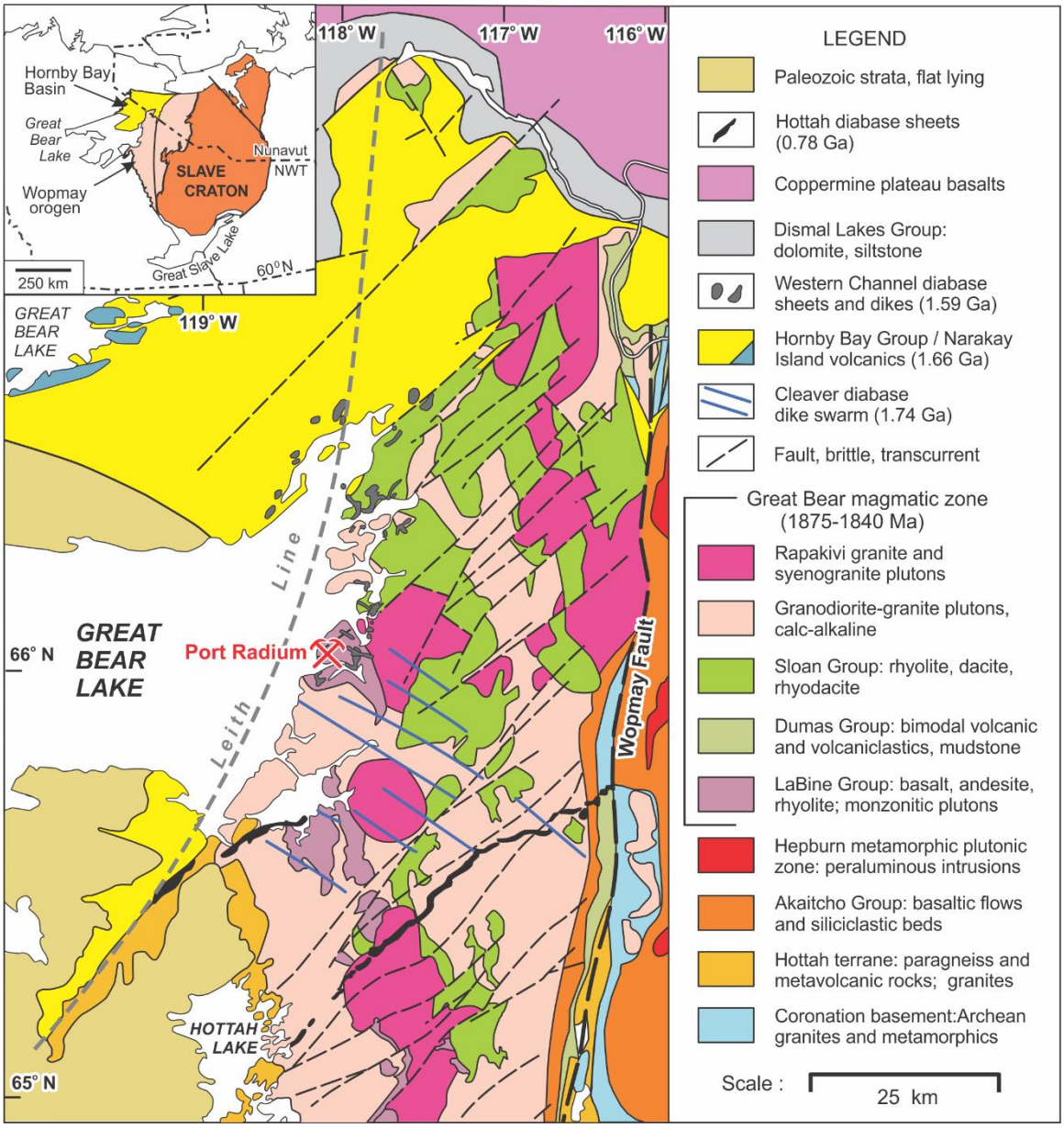

Figure 2.2: Generalized regional geology of the northern Great Bear Magmatic Zone, in the northwestern Canadian Shield, NWT, Canada. Modified from Gandhi et al. (2018).

Around 1.89 Ga the Paleoproterozoic Hottah Terrane (1.89–2.5 Ga, located to the west of the GBMZ) began colliding with the Archean Slave Craton (2.5–4.0 Ga, located to the east of the GBMZ; Bowring et al. 1989; Ootes et al. 2015; Corriveau et al. 2016). The Calderian Orogeny resulted from this collisional event, at 1.89–1.88 Ga (Montreuil et al. 2016a). Further orogenic events in the area formed the extensive Wopmay Orogen, which includes the GBMZ, Coronation Margin, and deformed sections of the Hottah Terrane (Ootes et al. 2015). 1.89–2.0 Ga volcanoclastic and metamorphic rocks of the Hottah Terrane form the basement of the GBMZ. These basement rocks are thought to have formed during episodic arc magmatism in the Hottah Terrane (Slack et al. 2016) before the Calderian Orogeny.

Around 1.88 Ga, thin- to medium-bedded sandstones, siltstones and carbonates of the Treasure Lake Group were deposited over the Hottah Terrane basement (Gandhi and van Breemen 2005; Corriveau et al. 2016). The Treasure Lake Group is considered to be a shallow water platform sedimentary sequence, which experienced tilting and low-grade metamorphism during the end of the Calderian Orogeny (Gandhi and van Breemen 2005; Montreuil et al. 2016a, b). Andesitic volcanism in the GBMZ continental arc began around 1.87 Ga. This volcanism later evolved through many stages of mafic, felsic, and pyroclastic flows, which are collectively referred to as the McTavish Supergroup (Corriveau et al. 2016; Slack et al. 2016). Volcanic rocks and volcaniclastic sediments of the McTavish Supergroup were intruded by syn-volcanic felsic to intermediate batholiths. Syn-volcanic intrusions are characterized by the presence of regional foliation fabric and iron oxide-alkali alteration, which is pervasive in the volcanic sequences (Montreuil et al. 2016b; Slack et al. 2016). Volcanism ceased by 1.86 Ga, and was followed by granitic intrusions

around 1.85 Ga. These later intrusions were not affected by the same regional deformation and alteration as their host rocks (Montreuil et al. 2016a).

The sedimentary Hornby Bay Basin (HBB; aka Coppermine Homocline) unconformably overlies the GBMZ, along with much of the Northern Wopmay Orogen (Figure 2.1; 2.2). The Proterozoic Hornby Bay Group consists of fluvial and shallow marine sandstones, mudstones, and stromatolitic carbonates (Hoffman 1983; Skulski et al. 2018). These units are unconformably overlain by shallow marine siltstones and mudstones, and marine dolostones of the Mesoproterozoic Dismal Lakes Group, and subsequently by continental flood basalts and red beds of the Coppermine River Group (Hahn et al. 2013; Skulski et al. 2018). All units of the HBB were later tilted slightly to the north (Hoffman 1983).

Hoffman (1983) initially estimated the age of the Hornby Bay Basin at 1.5 Ga along with similar intracratonic sedimentary basins in northern Canada (Figure 2.1). The ages of formations and groups within the basin have since been refined to comprise different intervals deposited between 1.74 and 1.27 Ga, based on crosscutting relationships with other units (Bowring and Ross 1985; LeCheminant and Heaman 1989; Irving et al. 2004; Hamilton and Buchan 2010; Hahn et al. 2013). The 1.74 Ga Cleaver Diabase dikes crosscut the underlying GBMZ volcanics but not the Hornby Bay Group, thus constraining its maximum age (Irving et al. 2004). The 1.59 Ga Western Channel Diabase (WCD) sills crosscut the GBMZ volcanics and the lower Hornby Bay Group, which constrains the minimum age for the Hornby Bay Group (Bowring and Ross 1985; Hamilton and Buchan 2010; Gandhi et al. 2018). Basalt and rhyolite flows of the 1.663 Ga Narakay Volcanic

Complex are interbedded with shallow marine sandstones of the upper Hornby Bay Group, which further constrains the age of units within the basin (Bowring and Ross 1985; Ross 1986; Hahn et al. 2013; Skulski et al. 2018). The age of the Dismal Lakes Group is constrained by 1.438 Ga pyrites in black shales from the lower formations (Geospec 2008), and unconformably overlying Coppermine River Group flood basalts, which are coeval with the 1.27 Ga MacKenzie igenous event (LeCheminant and Heaman 1989).

The Hornby Bay Basin has since been mostly eroded away with no observed record of these rocks in the region of Port Radium. A complete sequence stratigraphy for the Hornby Bay Basin is lacking, and the thickness of sedimentary sequences can only be estimated from remaining outliers north of the GBMZ (Skulski et al. 2018). The GBMZ has minimal recent sedimentary cover or dense vegetation, providing excellent exposure of the underlying volcanic and sedimentary sequences (Corriveau et al. 2016).

2.1.3 Local geology (Port Radium District)

The first major study in the area of McTavish Arm was focused on mapping surface geology and describing various field relations for exposed units of the GBMZ (Kidd 1932; Kidd 1933). The country rocks around Port Radium include porphyritic andesitic volcanics with interbedded sediments of the Echo Bay Group and unbedded tuff intercalated by pebble conglomerates and sandstones within the unconformably overlying Cameron Bay Group (Figure 2.3). Granitic plutons with weathered pyrite-bearing thermal aureoles are found to the south and east (Kidd and Haycock 1935; Jory 1964).

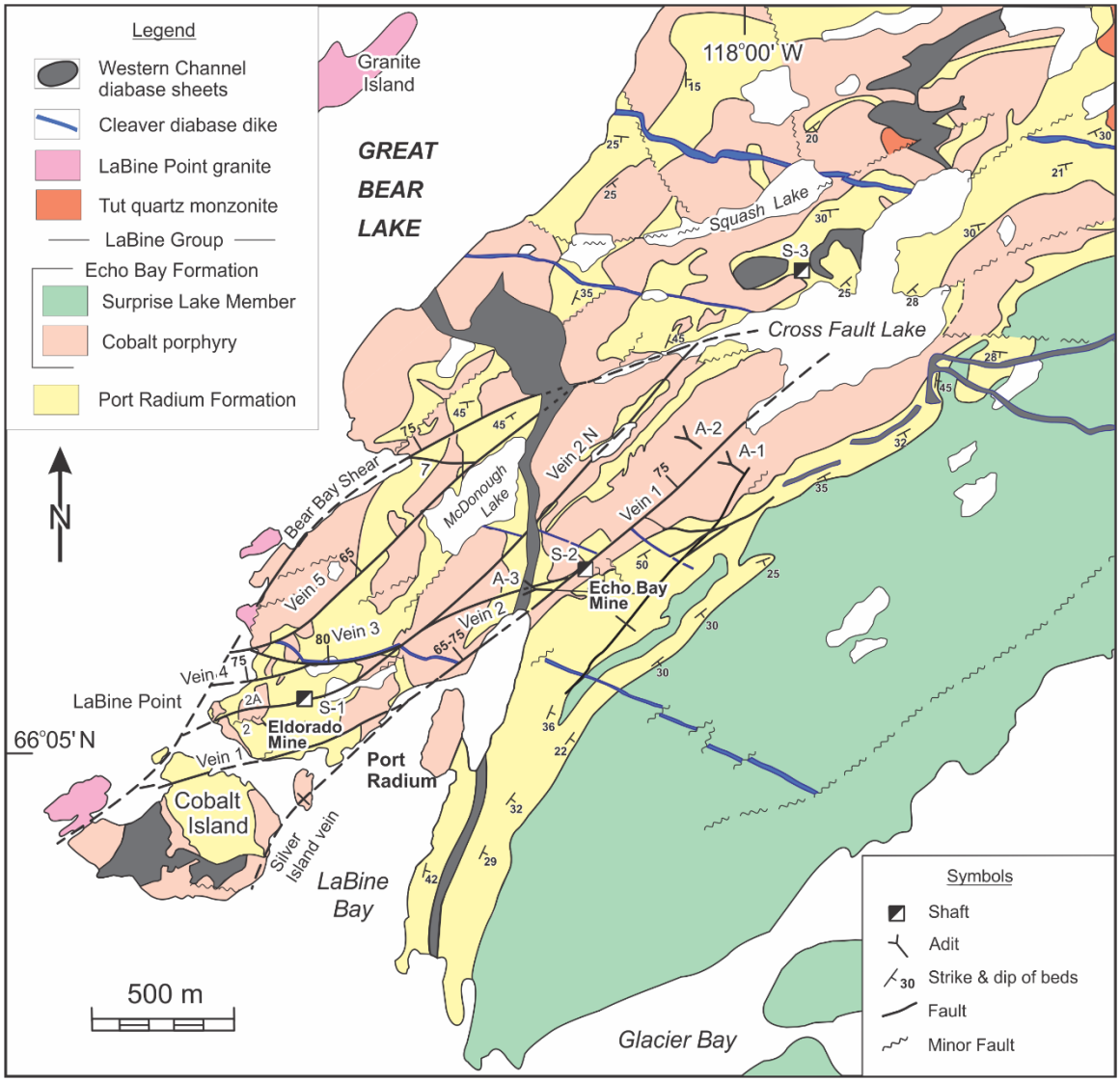

Figure 2.3: Local geology around Port Radium, showing the surface trace of mineralized veins. Modified from Gandhi et al. (2018).

These lithologies were cut by a few E-W trending Cleaver Diabase dikes, WCD sills with various orientations, and many steep, SW-striking, mineralized faults. These major fault systems host the "five-element" ores and are associated with minor conjugate faults throughout the area (Figure 2.3). The trend of these mineralized faults is consistent with larger structural features of the GBMZ. Brittle, northeast-trending dextral transcurrent faults are related to the 1850–1750 Ma McDonald fault system to the south (Hildebrand et al. 1987; Hayward and Corriveau 2014). "Five-element" veins post-date (cross-cut) the local units in the GBMZ, including the Cleaver Diabase dikes.

Local faults were reactivated multiple times, synchronous to the mineralizing events, leading to a complex (telescoping) ore vein system showing overprinting and brecciation textures. Gandhi et al. (2018) also suggested the faults were likely reactivated before and after the two diabase (Cleaver Diabase, WCD) intrusive events. Furthermore, evidence from vein petrography in different major faults suggests that not all faults were synkinematically reactivated. Reactivation of only some of the faults may have prevented migrating fluids from producing the same "five-element" paragenetic sequence in each fault. This also alludes to the separable stages of mineralization in Port Radium, which may be a consequence of periodic fault-activated mineralization (Gandhi et al. 2018).

2.1.4 Eldorado Mine

The Eldorado deposit is one of several "five-element" vein systems discovered along the eastern shore of McTavish Arm in the early 1930s (Kidd 1932; Silke 2009). The

Ag and polymetallic vein discoveries led to production from several mines in the Echo Bay and Camsell River districts (Table 2.1, Figure 2.4). Eldorado was a significant producer of Ag among these mines, and was the only major producer of Co, Ni, and U. Initially, Ra was the primary commodity sought from Port Radium—as the townsite was called—from 1933 until prices dropped in 1940, causing the Eldorado mine to close. Mining at Eldorado resumed, producing U from 1942 until the ore zones were depleted by 1960. Silver was then mined from 1975 until depletion by 1982. A total of 1.24 Mt of ore was produced at Eldorado, including 450 g of Ra, 6079 tonnes of U_3O_8, 379 tonnes of Ag, and 2167 tonnes of Cu. The mine site at Port Radium has since been closed and remediated (Silke 2009).

Table 2.1: Production in the Echo Bay and Camsell River districts. Modified from Silke (2009)

	Production (tonnes)				
Mines	**Ore**	**U_3O_8**	**Ag**	**Cu**	**Ore mineralogy**
Contact Lake	15418	3	19	-	"five-element", urn, py-cpy-bn
Echo Bay	329435	-	668	4087	Ag, BMS (Ag-gn)
El Bonanza	5908	-	1	-	"five-element", urn
Eldorado	1239761	6079	379	2167	"five-element", urn, py-cpy-bn
Norex	48713	-	59	39	"five-element"
Northrim	10886	-	1	-	"five-element", trace U in assay
Smallwood Lake	16514	-	5	-	Ag, BMS (high Pb, Zn)
Terra (Silver Bear)	460513	-	404	2072	"five-element", py-cpy
Other Occurrences					**Ore mineralogy**
Bear Portal	Limited production, none reported				Ag, cpy-bn, trace U
Bonanza	Limited production, none reported				Ag, BMS, Fe-S/O, trace ery
Contact Lake Portal	Limited production, none reported				"five-element", py-cpy
Glacier Bay	Limited production, none reported				Ag, cpy-bn, MnO
Mystery Island	No major development				Ag, Au, U

Mineral abbreviations: urn = uraninite; py = pyrite; cpy = chalcopyrite; bn = bornite; BMS = base metal sulphide; gn = galena; ery = erythrite

Figure 2.4: Echo Bay and Camsell River district mines. From Silke (2009).

Similar deposits in the Cobalt mining camp (Ontario, Canada) also produced historically significant quantities of Ag, and have recently garnered renewed interest from the exploration industry as targets for Ag (for use in solar power production) and Co (for use in batteries). These historic mining camps illustrate the ongoing value of "five-element" vein systems as initially high-grade Ag deposits but now with much greater multi-commodity potential. Presently, Ag production in Canada is mainly limited to low-grade deposits, recoverable as by-products from base metal and Au mining. The potential for a modern, high-grade "five-element" deposit makes them a valuable exploration target for Canada. This is a key motivation for this study, aimed at improving the existing deposit model.

Early research at the Eldorado deposit described its mineralogy, host lithologies and alteration, and attempted to constrain mineralization ages by applying Pb-Pb and U-Pb geochronology to galena and uraninite (Kidd and Haycock 1935; Campbell 1955; Jory 1964). Mining production continued to drive academic interest throughout the mine's operational history, and this interest continued well after production had ceased. Efforts to characterize the timing of mineralization, and origin of mineralizing fluids using fluid inclusion, trace element, and stable and radiogenic isotope techniques became more prominent as analytical technologies were developed and improved (Robinson and Morton 1972; Robinson and Ohmoto 1973; Thorpe 1974; Miller 1982; Changkakoti et al. 1986a, b, c; Changkakoti and Morton 1986; Gandhi et al. 2018). However, a comprehensive model for ore genesis at Eldorado remains elusive, and is complicated by the numerous opposing genetic models (Kissin 1992).

The U content of the ores is an important factor to be considered in developing a genetic model. Several major "five-element" deposits have associated U mineralization (e.g. Echo Bay and Camsell River districts, GBMZ; Zálesí, Bohemian Massif, Czech Republic; Jáchymov, Erzgebirge, Czech Republic; Wittichen, Schwarzwald, SW Germany; Avram Iancu, Bihor Mountains, Romania; Robinson and Ohmoto 1973; Badham 1975; Ondruš et al. 2003; Zajzon et al. 2005; Dolníček et al. 2009; Staude et al. 2012). However, Eldorado is the only known deposit in the Echo Bay and Camsell River mining districts with significant U ore. There are many other similar deposits that lack a U stage (e.g. Cobalt-Gowganda, ON; Silver Islet, Thunder Bay, ON; Bieber, Spessart, Germany; Odenwald, SW Germany; Kongsberg, Oslo, Norway; Bou Azzer, Anti-Atlas, Morocco; Bastin 1939; Franklin et al. 1986; Kissin 1992; Wagner and Lorenz 2002; Ahmed et al. 2009; Markl et al. 2016; Burisch et al. 2017). There is no consensus on the origin of the U endowment at Eldorado (Kissin 1992).

The Eldorado deposit has notable spatial/temporal proximity to other high-grade U deposits and "five-element" occurrences, which may be of relevance in the search for a comprehensive genetic model for regional metallogeny. The Eldorado "five-element" veins are situated in basement rocks that underlie the Hornby Bay Basin, which may be linked to the Athabasca Basin, among other Proterozoic sedimentary basins in Northern Canada (Bowring and Ross 1985; Hahn et al. 2013; Gandhi et al. 2018). This link has driven an ongoing interest in U resource exploration, concerning both the vein and unconformity style occurrences (e.g. Hoffman 1983; Rice and Kyser 2010; Shakotko 2014; Hornby Bay Mineral Exploration 2018). Eldorado is also proximal to many lower grade veins in the GBMZ and may be compared to much smaller "five-element" occurrences in

the East Arm of Great Slave Lake (Burke 2019; Potter et al. 2019). Detailed comparisons between Eldorado and these similar low grade veins in the NWT have not been made in previous literature.

2.2 Methods

2.2.1 Sample collection and preparation

Access to the Eldorado Mine for sampling was not possible as mining operations ceased in the 1980s. A suite of 65 representative samples from the original Eldorado Mine collection of Kidd and Haycock (1935) were obtained from Natural Resources Canada - Geological Survey of Canada (NRCan-GSC) in Ottawa. The sample repository consists of hundreds of host rock and vein samples from various locations in the mine, as well as other reference material including mine drawings and sheets recording the sample locations for most samples. The sampling strategy for this study prioritized obtaining a diversity of samples representative of the different ore stages and dominant mineral associations therein (e.g. uraninite, nickeline, safflorite, base metal sulphides, and native Ag and Bi). Particular attention was given to identifying good fluid inclusion study material containing abundant, well-preserved and paragenetically constrainable host minerals (e.g. quartz and carbonate).

Polished thin and double-polished fluid inclusion thick sections from non-radioactive samples were prepared at Vancouver Petrographics Ltd. Polished thin and thick sections for radioactive samples—containing uraninite—were prepared at the Advanced

Microanalysis Centre of the Saskatchewan Research Council. Double-polished thick sections for radioactive samples were prepared at Saint Mary's University.

2.2.2 Petrography

Mineral phases and textures for paragenetic interpretation were examined with Olympus BX51 and BX41, and Nikon Eclipse 50i polarizing microscopes at Saint Mary's University. Transparent gangue minerals and fluid inclusions in quartz and carbonate were identified and characterized using transmitted light, while opaque minerals were identified using reflected light. Photographs were taken using microscope-mounted high resolution digital cameras.

2.2.3 Scanning electron microscope (SEM) imaging and quantitative analysis

A TESCAN MIRA 3 LMU VPS FE-SEM at Saint Mary's University was used for backscattered electron (BSE) imaging of fine textural details and chemical zoning in samples. An Oxford Instruments X-max 80mm^2 silicon drift detector was used for energy dispersive spectroscopy (EDS) to assist with mineral identification, especially in distinguishing different species of solid solution carbonate and arsenide minerals, and to provide representative compositional analyses of minerals. Routine analytical conditions were a 20 kV accelerating voltage, a 40 μA beam current, and a 17 mm working distance.

The software package INCA (ETAS Embedded Systems Canada Inc.) was used for raw data reduction and X-ray spectral analysis.

2.2.4 Cathodoluminescence

Polished sections containing quartz and carbonate minerals were imaged using a Lumic HC4-LM hot cathode cathodoluminescence (CL) microscope with a Varian turbomolecular vacuum pump, Olympus BXFM focusing unit, and a Kappa DX40C Peltier-cooled camera equipped with a Kappa camera control at Saint Mary's University. Differences in luminescence (intensity and colour) were used to identify growth zones within quartz and to distinguish different species of carbonates. The CL was operated at an acceleration voltage between 11.0 and 12.0 kV, a beam current between 0.22 and 0.35 mA, a filament current of 2.3 A, a deflection of 10 V and a focus of 5.5 V. Exposure times of 2–8 s were used to capture images with optimal CL intensity for each sample.

2.2.5 Bulk C, O, and Sr isotope analyses of vein carbonates

A subset of 15 samples containing clean, texturally constrained carbonate phases were selected for isotope analysis. Approximately 30 mg of carbonate powder was excavated from each sample using a tungsten carbide microdrill bur (Komet Dental; 0.4 mm diameter) mounted on a dremel tool, and weighed into glass vials at Saint Mary's University. Carbon and oxygen isotope ratios were measured for 30–60 μg of carbonate

powder using a Nu Perspective dual-inlet isotope ratio mass spectrometer connected to a NuCarb carbonate preparation system at the McGill University Stable Isotope Laboratory. The powdered carbonates were then reacted individually with H_3PO_4 after heating to 90ºC for one hour. The released CO_2 was collected cryogenically and isotope ratios were measured against an in-house reference gas in dual inlet mode. Samples were calibrated to VPDB using in-house standards and then $\delta^{18}O$ values were converted relative to VSMOW. Uncertainties are ± 0.05‰ (1σ) for both $\delta^{13}C$ and $\delta^{18}O$.

The remaining 30 mg of carbonate powder from each sample was used for Sr isotope analyses. Strontium isotope ratios were measured on a Thermo Scientific Triton™ thermal ionization mass spectrometer (TIMS) at Université de Québec à Montréal/Geotop. Powders were first leached three times in 0.2 M ammonium acetate, and then rinsed three times in type 1 ultrapure water (MQH2O). The carbonate fraction of the samples was then dissolved in 0.5 M acetic acid, which was then separated from the insoluble fraction by centrifugation, dried down, and taken up in 3 N nitric acid. Sr was separated from the matrix following standard Sr chromatography procedures using EICHROM Sr Spec™ resin. Internal mass bias was corrected based on the ratio $^{86}Sr/^{88}Sr = 0.1194$. Major and trace elements, including Rb were also analyzed using ICP-OES at Université de Québec à Montréal/Geotop. Rubidium was used to correct for original Sr isotope ratios.

2.2.6 Secondary ion mass spectrometry (SIMS)

Uraninite and zoned quartz grains were selected for in-situ oxygen stable isotope analysis to resolve compositional information within individual growth zones in single crystals. Individual analysis locations were selected with the guidance of textural information from SEM-BSE and CL images. Oxygen isotopes were measured using the CAMECA 7f SIMS at the University of Manitoba. The SIMS instrument used a ~2 nA primary ion beam of cesium (Cs^+) accelerated at 10 kV to generate and detect secondary ions of $^{18}O^-$ and $^{16}O^-$. The instrument operated at a 300 V sample offset, -9 kV secondary accelerating voltage, and at mass resolving power of 347. Entrance slits were narrowed to 260 μm to obtain flat-topped peaks. A detailed description of operating conditions for oxygen isotope analysis is provided by Fayek et al. (2002). Grains of University of Wisconsin Rose quartz (UWQ-1) with a $\delta^{18}O$ value of 12.33 ± 0.14 ‰ (Kelly et al. 2007) were used as the quartz standard for oxygen isotope analysis. Synthetic uraninite with a $\delta^{18}O$ value of 8.1 ± 0.3 ‰ (Fayek et al. 2002) was used as the uraninite standard. Spot-to-spot reproducibilities for replicate analyses of UWQ-1 and the uraninite standard were 0.8–0.9 ‰, and 0.6–0.8 ‰, respectively. SIMS results from the standards were compared to accepted isotopic compositions in order to calculate correction factors that were applied to the unknowns measured during the same analytical session (e.g. Holliger and Cathelineau 1988) and results are reported as $\delta^{18}O_{VSMOW}$ (‰).

2.2.7 Fluid inclusion petrography and microthermometry

Double-polished thick sections were examined with an optical microscope to identify and characterize fluid inclusions using the fluid inclusion assemblage approach (FIA; Goldstein 2003) in quartz and carbonate. In addition to establishing FIA, fluid inclusions were described by their size, shape, and presence of different included phases at room temperature. The textural context of inclusions, and inclusion host phases, within the mineral assemblage and relevant ore stages was important for categorizing fluid inclusion types. Selected samples were cut into small chips for microthermometric analysis and removed from glass substrate in an acetone bath (24 hours).

Fluid inclusion microthermometry was performed using a Linkam FTIR600 heating-freezing stage mounted on an Olympus BX51 microscope at Saint Mary's University. A microscope-mounted camera was used for capturing images. The heating-freezing apparatus was calibrated using synthetic fluid inclusion standards of pure H_2O (final ice melting at 0 °C and homogenization at the critical point of 374.1 °C), and pure CO_2 (final melting at -56.6 °C). Microthermometric measurements of phase changes included eutectic (first) melting (T_e), final ice melting (T_m^{ice}), hydrohalite incongruent melting (T_m^{HH}; conversion to halite), halite dissolution (T_d^H), liquid-vapour homogenization via vapour bubble disappearance (T_v; bubble point), and total homogenization (T_h). In some inclusions, $T_v = T_h$ whereas in others, halite persisted above T_v and total homogenization occurred by halite dissolution (i.e., $T_d^H = T_h$). Not all phase changes were measurable in each inclusion due to surface ice obscuring the field of view at low temperatures, and the metastable nature of phase transitions involving hydrohalite and halite. Analytical uncertainty for phase transition measurements are ± 0.2 °C and ± 0.5

°C near 0 °C and over 300 °C, respectively, when recorded at heating or cooling rates of 1 °C/min (Kerr et al. 2018; Burke 2019).

Salinity of fluid inclusions was calculated using T_m^{ice} as in Bodnar and Vityk (1994), with additional considerations for the Ca-rich nature of the fluids following Steele-MacInnis et al. (2011). Inputs of T_m^{ice} and T_d^H were used to calculate the bulk salinity (S_{wt}) and mass proportion of major salts (NaCl and $CaCl_2$) in "3-phase" halite-bearing inclusions in a numerical model for the H_2O-NaCl-$CaCl_2$ ternary system, which was developed into a Microsoft Excel-based program (Steele-MacInnis et al. 2011). Isochores were determined using the BULK and ISOC software (Bakker 2003). The software used equations of state for fluids, and volumetric data for quartz and carbonate from Hosieni et al. (1985), Zhang and Frantz (1987), Berman (1988), and Oakes et al. (1990).

2.2.8 Confocal Raman microspectroscopy

A Jobin-Yvon Horiba LabRam HR confocal Raman microscope with an 800 mm spectrograph and Synapse 1024 x 256 pixel CCD detector, at Saint Mary's University, was used to analyze quartz-hosted fluid inclusions. A 600 groves/mm grating with a spectral resolution of 0.5 cm^{-1}, and an 80 μm confocal hole size were used during spectrum collection. A 532 nm (green) Nd-YAG laser (~2.15 mW at sample surface) was used for excitation, directed through a 100x objective. Pure silicon was used as a frequency calibration standard. Spectra were collected over the range 100–2500 cm^{-1} with three accumulations of 30s acquisitions per inclusion. Mineral phases in fluid inclusions were

identified by matching background- and baseline-corrected spectra against reference spectra using the software Crystal Sleuth.

2.2.9 Laser ablation inductively-coupled plasma mass spectrometry (LA-ICP-MS)

The major and trace element composition of fluid inclusions and vein carbonate minerals were determined by LA-ICP-MS at the University of Toronto Magmatic and Ore Forming Processes Research Laboratory. The instrument used was a NWR 193UC ArF Excimer (193 nm) laser ablation system attached to an Agilent 7900 quadrupole mass spectrometer. The typical analytical approach for fluid inclusions, using similar instrumentation, is described by Heinrich et al. (2003). The instrument was tuned to maximum sensitivity while maintaining robust plasma conditions ($U^+/Th^+ = 1.05$) for NIST SRM610 synthetic glass reference standard, and low oxide and doubly charged ion production rates ($ThO^+/Th^+ < 0.3\%$; mass-21/mass-42 < 0.3%). Aerosols from ablation were transported into the mass spectrometer with He carrier gas mixed with Ar neutralizer gas at flow rates of 1.0 and ~0.90 L/min, respectively. Dwell times were 20 ms for ^{59}Co, ^{62}Ni, ^{75}As, ^{107}Ag, ^{232}Th, ^{238}U, and 10 ms for all other isotopes; ^{7}Li, ^{11}B, ^{23}Na, ^{25}Mg, ^{27}Al, ^{29}Si, ^{39}K, ^{44}Ca, ^{55}Mn, ^{56}Fe, ^{65}Cu, ^{66}Zn, ^{85}Rb, ^{88}Sr, ^{95}Mo, ^{121}Sb, ^{133}Cs, ^{137}Ba, ^{139}La, ^{140}Ce, ^{141}Pr, ^{146}Nd, ^{147}Sm, ^{153}Eu, ^{157}Gd, ^{159}Tb, ^{163}Dy, ^{165}Ho, ^{166}Er, ^{169}Tm, ^{172}Yb, ^{175}Lu, ^{182}W, ^{197}Au, ^{208}Pb, ^{209}Bi. The standard SRM610 synthetic glass from NIST was used to externally calibrate analyte sensitivities. Up to 24 unknowns (inclusions or carbonate measurements) were bracketed by two SRM610 analyses at the beginning and end of each analysis block. Fluid inclusions were analyzed with a laser spot size 5–15 μm larger than the diameter of each

inclusion, which were typically 10–25 μm in diameter. Carbonate minerals were ablated using a 60 μm pit size. Table 2.2 summarizes the LA-ICP-MS instrumentation and analytical parameters.

A separate analyte menu was used to investigate the Cl-Br composition of fluid inclusions. This comprised measurement of selected isotopes of ^{7}Li, ^{11}B, ^{23}Na, ^{25}Mg, ^{29}Si, ^{35}Cl, ^{39}K, ^{44}Ca, ^{55}Mn, ^{56}Fe, ^{66}Zn, ^{79}Br, ^{85}Rb, ^{88}Sr, ^{133}Cs, ^{137}Ba, ^{208}Pb, as well as ^{35}Cl and ^{79}Br with dwell times of 10 ms and 20 ms, respectively. Analyte sensitivities were calibrated for Cl and Br determination using a scapolite standard (*Sca17*; Seo et al. 2011; Fusswinkel et al. 2018) containing 438 ± 22 ppm Br and 28900 ± 1960 ppm Cl. The potential interference of $[^{39}K^{40}Ar]^{+}$ and $[^{63}Cu^{16}O]^{+}$ on ^{79}Br, arising from the presence of K and Cu in fluid inclusions, was determined to be insignificant. Oxide production rates were maintained below 0.3% and argide production rates for $[^{39}K^{40}Ar]^{+}$ were determined to be negligible (< 0.01%). An absence of correlation between K and Br in quantified fluid inclusion signals confirmed the negligible effect.

Raw data from the LA-ICP-MS were processed using the SILLS software package (Guillong et al. 2008). Fluid inclusions signals isolated by removing the host signal from the fluid inclusion + host signal (matrix correction). Average salinity values calculated from microthermometry measurements of fluid inclusion assemblages were used as internal standards in order to quantify the elemental concentrations in fluid inclusions. The average $CaCl_2$:NaCl ratio for 3-phase inclusions, determined using the Steele-MacInnis et al. (2011) numerical model, was used as an additional internal standard for inclusions in carbonate, because the high Ca content in the host material masked true Ca values. Trace

elements in calcite and dolomite were quantified using Ca and Mg, respectively, as internal standards, based on stoichiometric compositions.

Table 2.2: LA-ICP-MS operating conditions

LA		
Model		NWR 193 UC
Wavelength		193 nm
Pulse duration (FWHM)		4 ns
Repetition rate		10 Hz
Spot diameter		15-40 µm for fluid inclusions; 60 µm for carbonate
Energy density		ca. 12 J/cm^2
Primary (calibration) standard		NIST SRM610: synthetic basalt glass; Sca17: scapolite
Secondary (quality control) standards		NIST SRM610, Sca17, Br-I-glass (UofT)
ICP-MS		
Model		Agilent 7900
Forward power		1350 W
Shield torch		Used
Sampling depth		6 mm
Gas flow rates	Neutralizer (Ar)	ca. 0.90 L/min
	Transport (He)	1.00 L/min
ThO^+/Th^+		<0.3%
U^+/Th^+ (NIST 610)		ca. 1.05
Data acquisition parameters		
Data acquisition protocol		Time Resolved Analysis
Scanning mode		Peak hopping, 1 point per blank
Dwell time per isotope		10 ms for all masses, except 20 ms for ^{59}Co, ^{62}Ni, ^{75}As, ^{79}Br, ^{107}Ag, ^{232}Th, ^{238}U
Detector mode		Dual (pulse-analogue mode)
Isotopes determined (dwell time ms)		^{7}Li(10), ^{11}B(10), ^{23}Na(10), ^{25}Mg(10), ^{27}Al(10), ^{29}Si(10), ^{35}Cl(10), ^{39}K(10), ^{44}Ca(10), ^{55}Mn(10), ^{56}Fe(10), ^{59}Co(20), ^{62}Ni(20), ^{65}Cu(10), ^{66}Zn(10), ^{75}As(20), ^{79}Br(20),^{85}Rb(10), ^{88}Sr(10), ^{95}Mo(10), ^{107}Ag(20), ^{121}Sb(10), ^{133}Cs(10), ^{137}Ba(10), ^{139}La(10), ^{140}Ce(10), ^{141}Pr(10), ^{146}Nd(10), ^{147}Sm(10), ^{153}Eu(10), ^{157}Gd(10), ^{159}Tb(10), ^{163}Dy(10), ^{165}Ho(10), ^{166}Er(10), ^{169}Tm(10), ^{172}Yb(10), ^{175}Lu(10), ^{182}W(10), ^{197}Au(10), ^{208}Pb(10), ^{209}Bi(10), ^{232}Th(20), ^{238}U(20)
Quadrupole settling time		2 ms
Analysis time		100 s: ~50 s gas blank, ~50 s of ablation
Internal standard:		Combination of NaCl wt% equiv., Ca (ppm) and Na (ppm)

2.2.10 Sensitive high-resolution ion microprobe (SHRIMP) U-Pb geochronology

Reflected light microscopy and SEM-BSE imaging were used to identify numerous 5–10 μm diameter regions of inclusion-free xenotime from two different mineral assemblages. Several 3–4 mm cores of these regions were drilled out of polished sections and assembled in an epoxy mount along with xenotime standards 6410 and 6413 (Stern and Rayner 2003). The epoxy mount was cleaned and Au-coated for analysis.

Yttrium and the isotopes ^{204}Pb, ^{206}Pb, ^{207}Pb, ^{235}U, ^{238}U were measured in-situ using the SHRIMP at the Geological Survey of Canada in Ottawa, Ontario. A primary $^{16}O^-$ ion beam was focused through a 30 μm Köhler aperture at 10 kV and 0.4 nA. The 6–7 μm diameter beam spot was carefully positioned on the sample by cross-referencing reflected light and SEM-BSE images, to ensure that microfractures and uraninite inclusions did not interfere with isotope measurements for xenotime.

A common Pb correction based on measured count rates of ^{204}Pb utilized the Stacey-Kramer (Stacey and Kramer 1975) model lead composition at the measured ^{207}Pb/^{206}Pb age. A two-stage calibration was used to account for relevant matrix effects. The analyses were first calibrated based on correlation of ln^{206}Pb/^{254}UO vs ln$^{270}UO_2$/^{254}UO and an age of 996 Ma for standard 6413 using SQUID 2.5 (Ludwig 2009). An uncertainty of 1% was calculated and applied for the first calibration. A second calibration, to account for the U matrix effect, was determined by linear regression of the percent deviation from accepted ^{206}Pb/^{238}U value against ^{254}UO/$^{194}Y_2O$. This second calibration added an additional 0.6% error. The correction was then applied to all ^{206}Pb/^{238}U ratios and errors

calculated by propagation of the slope and intercept error. Isoplot 4.15 was used for further data reduction (Ludwig 2012).

2.3 Results

2.3.1 Sample characteristics

Mineralization at the Eldorado Mine occurs along several faults, and has been mapped down to depths of 1675 ft. (510 m) in underground mine workings (Figure 2.5). The general characteristics of the mineralized faults have been described at length in previous studies (Kidd and Haycock 1935; Campbell 1955; Jory 1964). In this study, 49 of 65 samples were traced back to original sample locations within the mine, including all levels down to the 1500 ft. level, using archival maps from the GSC, and from Jory (1964). Original sample locations are distributed along many of the veins in underground workings. Sample locations and general petrographic descriptions for each sample are summarized in Table 2.3 in the Appendix.

Figure 2.5 (next page): Sample origins from mineralized veins in Eldorado mine. The surface expression of the Western Channel Diabase (WCD) is projected down to the 250 and 500 levels along its shallow dip to show proximity to nearby sample locations.

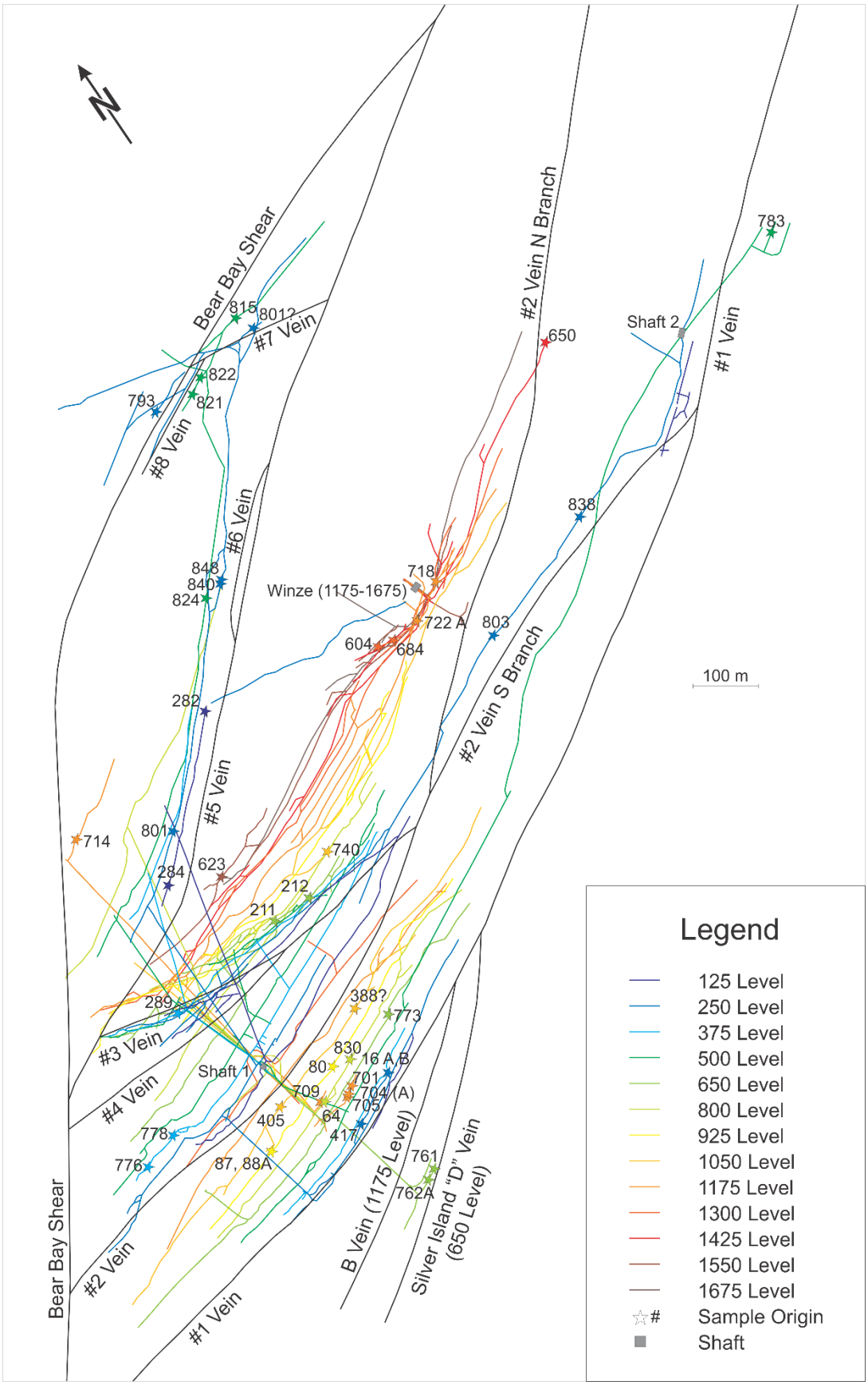
N
Bear Bay Shear
#7 Vein
#8 Vein
#6 Vein
#5 Vein
#3 Vein
#4 Vein
#2 Vein
#1 Vein
#2 Vein N Branch
#2 Vein S Branch
#1 Vein
B Vein (1175 Level)
Silver Island "D" Vein (650 Level)
Bear Bay Shear
Winze (1175-1675)
Shaft 1
Shaft 2
100 m
815
8012
822
793
821
848
840
824
650
718
722 A
604
684
803
838
783
282
714
801
623
284
740
212
211
289
388?
773
830
80
16 A/B
701
709
704 (A)
705
64
405
417
778
776
87, 88A
761
762A
Legend
125 Level
250 Level
375 Level
500 Level
650 Level
800 Level
925 Level
1050 Level
1175 Level
1300 Level
1425 Level
1550 Level
1675 Level
Sample Origin
Shaft

Samples containing uraninite were characterized from various depths along vein #1, including near the WCD intrusion in the north branch. Uraninite was also identified in a few samples from veins #3, #5, #8, and "B", but was not identified in numerous samples from vein #2. Arsenide minerals are present in samples from all of the same veins as those containing uraninite in addition to vein "D" and parts of vein #2, except the north branch. Primary native Ag is consistently associated with arsenide minerals. Samples with secondary Ag and Bi minerals are primarily associated with carbonate minerals, but are also spatially associated with samples that contained primary Ag and arsenide minerals. Sulphide minerals are pervasive in samples from throughout the mine, and occur as the dominant mineralization style in samples from the north branch of vein #2. Likewise, carbonate mineralization is ubiquitous, and not confined to, nor excluded from, any particular vein.

Previous studies showed the apparent localization of some mineralization stages (i.e. metal associations) within specific veins (Campbell 1955; Gandhi et al. 2018). In this study, with the exception of the north branch of vein #2, samples comprising each mineralization stage are spatially distributed throughout the mine, and no spatial localization of mineralization styles in specific veins was observed. However, there are marked differences in the predominance of each mineralization stage between samples, with no apparent correlation between the prevalent stage in a sample and vein number, depth, or mineralogy of nearby samples. This may simply indicate the incomplete representation of the sample suite for the mine as a whole. Four major stages of vein mineralization are recognized within the sample suite:

1: The *uraninite stage* generally texturally predates the classic "five-element" (Co-Ni-As-Ag-Bi) assemblages, but is associated with some early sulpharsenides. Primary uraninite from this stage is preserved as botryoidal and ring-form habits, showing colloform banding in many samples. Uranium alteration minerals (e.g. coffinite) and remobilized secondary uraninite originating from dissolution and re-precipitation in later vein stages were observed. Fractures pervade the primary uraninite and are infilled by minerals from all subsequent mineralization stages.

2: The *arsenide stage* followed the uraninite stage after significant fracturing and dissolution of the earlier uraninite. Nickeline, Co-Ni di- and tri-arsenides, and Fe-Co-Ni sulpharsenides formed sequentially throughout this vein stage, but with significant variation in the Co/Ni ratio between samples. Sulpharsenide and arsenide minerals are also spatially associated with native Ag, Bi, uraninite, apatite, xenotime, and two generations of open-space filling quartz.

3: The *sulphide stage* is physically separated from the arsenide stage by the occurrence of carbonate filling open space around arsenide-stage rims of euhedral quartz. Native Ag and Bi, and Cu sulphides are the most common minerals, often filling open space between grain boundaries of coeval gangue minerals (e.g. quartz, carbonate, chlorite, and carbonate) and fractures within minerals from previous vein stages. Remobilized native Ag and Bi, and Fe-Zn-Pb-Ag-Bi sulphides and sulphosalts are also disseminated throughout gangue minerals.

4: The *late carbonate stage* is characterized by a transition from early Fe-dolomite of the sulphide stage, to later Ca-Mg-Mn-Fe carbonates of various compositions, including

Mn-dolomite, magnesite-siderite, and calcite. Trace quantities of hematite, Fe sulphides, and barite occur in association with late carbonates.

Detailed descriptions from petrographic observations are provided in the following sections.

2.3.1.1 Uraninite stage

Botryoidal and ring-form uraninite is preserved in several vein samples (Figure 2.6a, c, e). SEM-BSE imaging revealed primary concentric zoning in uraninite, which manifests as alternating bands of pure uraninite, and bands of uraninite containing µm-scale dendritic crystal inclusions composed Co-Ni sulpharsenides (Figure 2.6e, f). Most uraninite was thoroughly fractured and partially dissolved, then filled and rimmed by later arsenide minerals, sulphides, and gangue minerals (Figure 2.6a, b, c, d, e). Sulpharsenide inclusions are not spatially associated with the late fractures, which commonly have a radial arrangement, crosscutting uraninite perpendicular to its colloform banding (Figure 2.6c, e, f).

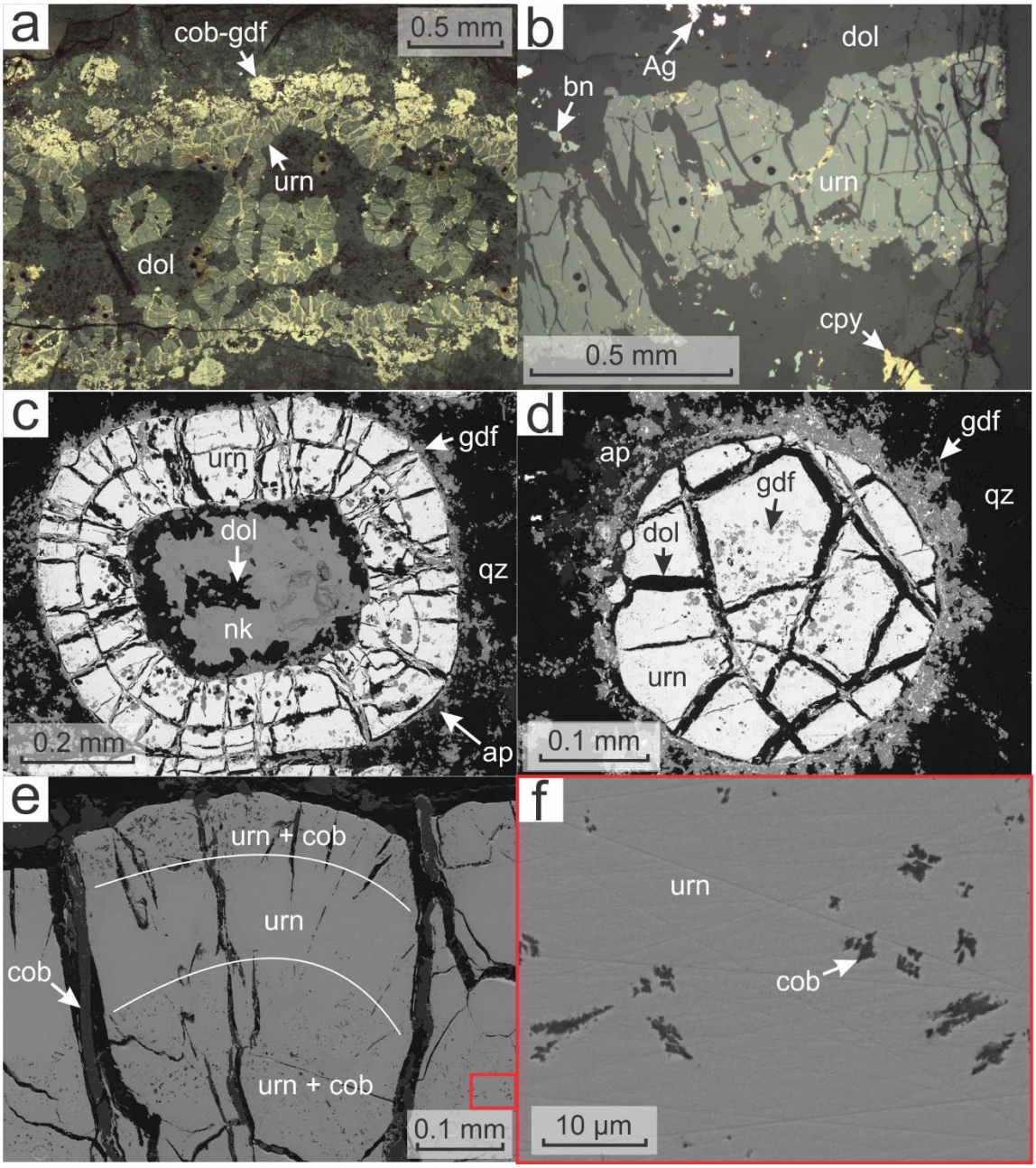

Figure 2.6: Reflected light and SEM-BSE images showing uraninite stage mineralization. Mineral abbreviations: cob-gdf = cobaltite-gersdorffite; urn = uraninite; dol = dolomite; bn = bornite; cpy = chalcopyrite; nk = nickeline; ap = apatite; qz = quartz. **(a)** Reflected light image showing typical fractured botryoidal and ring-form urn with cob-gdf infill and rims. **(b)** Reflected light image of urn with cpy, bn, native Ag, and dol filling fractures. **(c)** BSE image of ring-form urn with gdf and late nk at its core. Open space around urn is filled by qz, ap, and dol. **(d)** BSE image of urn spherule with distinctive gdf inclusions in an inner growth zone. Similar late phases as in (c). **(e)** BSE image showing banded zones of botryoidal urn with and without primary cob inclusions. Late fractures are filled with a different generation of cob. **(f) inset from e)** BSE image of dendritic cob inclusions in sulpharsenide-rich urn zone.

2.3.1.2 Arsenide stage

Many fractures in uraninite are filled by massive Co-Ni sulpharsenides, which also form rims around botryoidal uraninite grains and cores in ring-form uraninite (Figure 2.7a, b, c). These sulpharsenide rims are often themselves rimmed by arsenide minerals and gangue minerals such as quartz, apatite, chlorite, and carbonates. In one sample, small, euhedral cobaltite-gersdorffite grains and grain aggregates occur interstitial to grain boundaries in granular or "sugary" quartz that fills spaces surrounding primary uraninite. This network of Co-Ni sulpharsenide crystals is not always present in the quartz and apatite gangue (Figure 2.7c, d).

Nickeline forms botryoidal rims on the more Ni-rich sulpharsenides, which occur as several banded intervals throughout the massive nickeline domains (Figure 2.7a, b; 2.8a). Safflorite-rammelsbergite and skutterudite consistently enclose other arsenide-stage minerals, either as rims on botryoidal forms, or on isolated arsenide "florets" (Figure 2.7e, f, g). Arsenide florets have botryoidal or dendritic cores, stellate crystal rims, and are mainly comprised of colloform-banded safflorite with elevated, and variable S content (Table 2.4). Some arsenide growth sequences terminate in rims of skutterudite with micrometre- to nanometre-scale rhythmic bands of nickeline (Figure 2.7e). Nickeline in these bands occur as relict domains, and are pervasively replaced by native Bi. Nickeline in other contexts also show significant dissolution features, and are replaced by blocky rammelsbergite, quartz, dolomite, and Bi (Figure 2.7a, b, e, f, g).

Table 2.4: Average chemical composition (wt.%) of major minerals from SEM-EDS analyses.

Arsenides	**S**	**Fe**	**Co**	**Ni**	**As**	**Sb**	**-**	**-**	**-**	**-**	**-**	**-**	**n**
nickeline	0.8	-	0.5	37.3	61.0	0.4							25
gersdorffite	20.4	0.4	9.5	18.4	51.0	0.3							27
- representative analysis	21.9	0.7	10.4	15.8	49.8	1.3							1
- representative analysis	19.1	-	7.6	23.1	50.2	-							1
cobaltite	19.9	0.2	20.2	9.2	50.5	-							13
- representative analysis	21.8	-	21.9	4.8	51.5	-							1
- representative analysis	20.8	-	17.3	12.0	50.0	-							1
S-rich rammelsbergite	11	0.2	11.0	14.4	63.5	-							11
S-rich safflorite	11.4	0.6	16.1	9.1	62.8	-							8
rammelsbergite	1.1	0.3	1.8	21.5	75.4	-							31
safflorite	4.7	2.8	21.1	-	71.5	-							13
skutterudite	0.5	-	9.9	5.2	84.4	-							6
Sulphides	**S**	**Fe**	**Cu**	**Zn**	**As**	**Ag**	**Sb**	**Pb**	**Bi**	**-**	**-**	**-**	
sphalerite	37.5	0.6	-	61.9	-	-	-	-	-				3
tetrahedrite	28.1	2.0	35.2	5.8	3.1	0.8	25.0	-	-				6
tennantite	30.2	2.4	38.6	5.0	15.9	0.3	7.6	-	-				23
annivite	31.6	3.3	39.8	4.7	14.4	-	6.1	-	10.8				4
bismuthinite	19.6	-	-	-	-	-	-	-	80.4				3
aikinite	17.1	-	8.5	-	-	-	-	40.6	33.8				10
miharaite	22.4	5.7	25.8	-	-	-	-	24.9	21.3				3
wittichenite	21	0.3	35.3	-	-	-	-	-	42.7				27
argentite	16.2	-	-	-	-	83.8	-	-	-				2
stromeyerite	17.8	0.2	27.4	-	-	54.6	-	-	-				6
Carbonates*	**Mg**	**Ca**	**Mn**	**Fe**	**-**	**-**	**-**	**-**	**-**	**-**	**-**	**-**	
calcite	0.3	93.8	5.2	0.6									64
ankerite	1.5	55.0	11.2	32.2									7
Fe-rich dolomite	29.9	56.1	4.8	9.3									169
dolomite	36.7	59.9	0.8	2.7									26
dolomite-kutnohorite	21.6	50.8	20.4	7.2									125
kutnohorite	4.0	50.3	40.7	5.0									10
magnesite-siderite	52.9	0.7	9.3	37.1									29
Oxides, phosphates*	**F**	**Si**	**P**	**Ca**	**Y**	**Gd**	**Dy**	**Ho**	**Er**	**Yb**	**Pb**	**U**	
uraninite	-	0.5	-	0.9	-	-	-	-	-	-	15.5	83.0	31
- representative analysis	-	0.6	-	1.0	-	-	-	-	-	-	15.8	82.6	1
- representative analysis	-	0.0	-	1.5	-	-	-	-	-	-	15.1	83.4	1
apatite	13.4	-	30.5	56.1	-	-	-	-	-	-	-	-	7
xenotime 1	-	0.5	25.9	0.5	53.8	4.6	5.3	0.6	3.3	1.6	-	4.0	11
xenotime 2	-	0.7	24.9	0.8	48.7	3.8	6.3	1.1	3.5	4.7	-	4.6	11

*n = number of analyses used for average. *Analyses were normalized after removing C and O.*

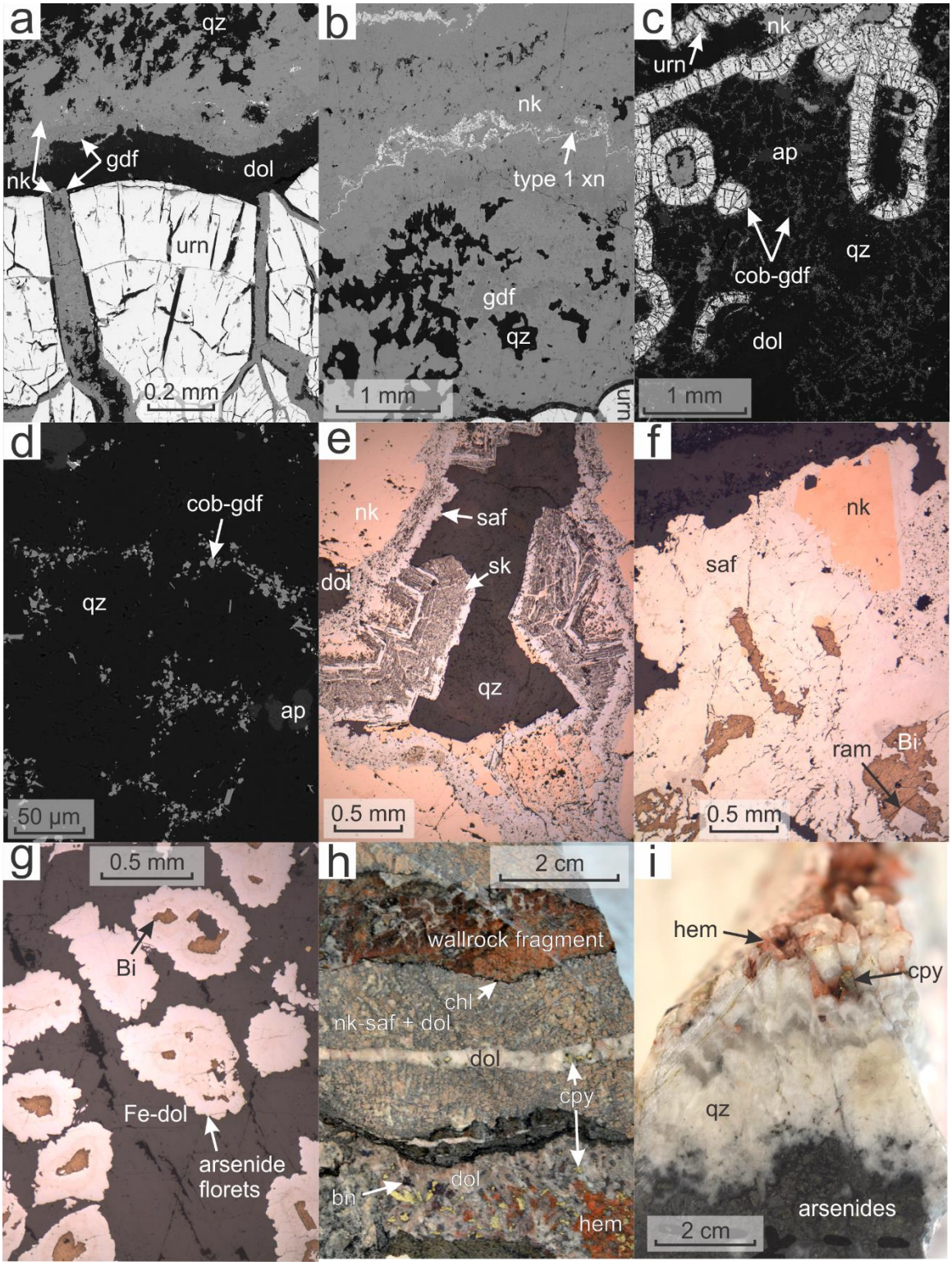
a
qz
nk
gdf
dol
urn
0.2 mm
b
nk
type 1 xn
gdf
qz
1 mm
urn
c
nk
urn
ap
cob-gdf
qz
dol
1 mm
d
cob-gdf
qz
ap
50 µm
e
nk
saf
sk
dol
qz
0.5 mm
f
nk
saf
ram
Bi
0.5 mm
g
0.5 mm
Bi
Fe-dol
arsenide
florets
h
2 cm
wallrock fragment
chl
nk-saf + dol
dol
cpy
dol
bn
hem
i
hem
cpy
qz
arsenides
2 cm

Figure 2.7 (previous page): SEM-BSE, reflected light, and hand sample images showing arsenide stage mineralization. Mineral abbreviations: qz = quartz; nk = nickeline; gdf = gersdorffite; dol = dolomite; urn = uraninite; xn = xenotime; ap = apatite; cob = cobaltite; sk = skutterudite; saf = safflorite; ram = rammelsbergite; chl = chlorite; cpy = chalcopyrite; bn = bornite; hem = hematite. **(a)** BSE image showing botryoidal, fractured urn infilled by gdf (darker grey) and nk (lighter grey) in succession. A similar succession is shown outward from the rims of urn. Late dol cuts through open space formed between urn and gdf, while qz fills dissolution space in nk. **(b)** BSE image showing bands of gdf (darker grey) within massive nk that grew on the surface of botryoidal urn. An assemblage of type 1 xn and urn also formed multiple growth zones within nk. **(c)** BSE image showing uraninite with sulpharsenide and nk fracture-fill and rims, and a network of cob-gdf rims occurring interstitial to grain boundaries in sugary qz that fills spaces surrounding urn. **(d)** BSE image showing textural details of cob-gdf network around qz-ap grain boundaries. **(e)** Reflected light image showing rims of nk overgrown by saf and later sk, which shows oscillatory zoning with more late nk. Open space is filled by late qz. **(f)** Reflected light image of saf-dominated arsenide assemblages with some remnant nk before dissolution and infill by blocky ram and native Bi. **(g)** Reflected light image showing arsenide florets (mostly S-rich saf) with dissolved cores filled by native Bi and Fe-dol, which also fills open space around florets. **(h)** Sample 608 showing cross-cutting relationship between early wall-rock fragment with chloritized rims, arsenide stage (nk-saf-dol) mineralization, and later base metal sulphide stage (cpy-bn-hem-dol) veining. **(i)** Sample 200, showing euhedral, visibly zoned qz growing after massive arsenide minerals. The surface of late arsenide-stage qz crystals are coated with hem and cpy crystals.

Figure 2.8 (next page): SEM-BSE and hand sample images showing xenotime mineralization in the arsenide stage. Mineral abbreviations: nk = nickeline; dol = dolomite; cpy = chalcopyrite; xn = xenotime; urn = uraninite; saf = safflorite; qz = quartz; gdf = gersdorffite; ram = rammelsbergite. **(a)** Sample 704A, showing key minerals from multiple vein stages, highlighted by urn from the uraninite stage; nk, type 1 xn, saf, and qz from the arsenide stage; and dol and cpy from the sulphide stage. **(b)** Sample 850; a vein breccia that includes fragments of wall-rock with chloritized rims, and type 2 xn forming rims on arsenide florets. **(c)** BSE image showing a growth zone of the type 1 xn assemblage occurring as a growth zone in massive nk. **(d) inset from c)** BSE image showing an inclusion-free surface of type 1 xn, with some urn microinclusions. **(e)** BSE image showing arsenide florets comprised of nk cores and ram rims. Florets are rimmed by the type 2 xn assemblage, fractured, and filled by dol. **(f) inset from e)** BSE image showing an inclusion-free surface of type 2 xn accompanied by remobilized urn.

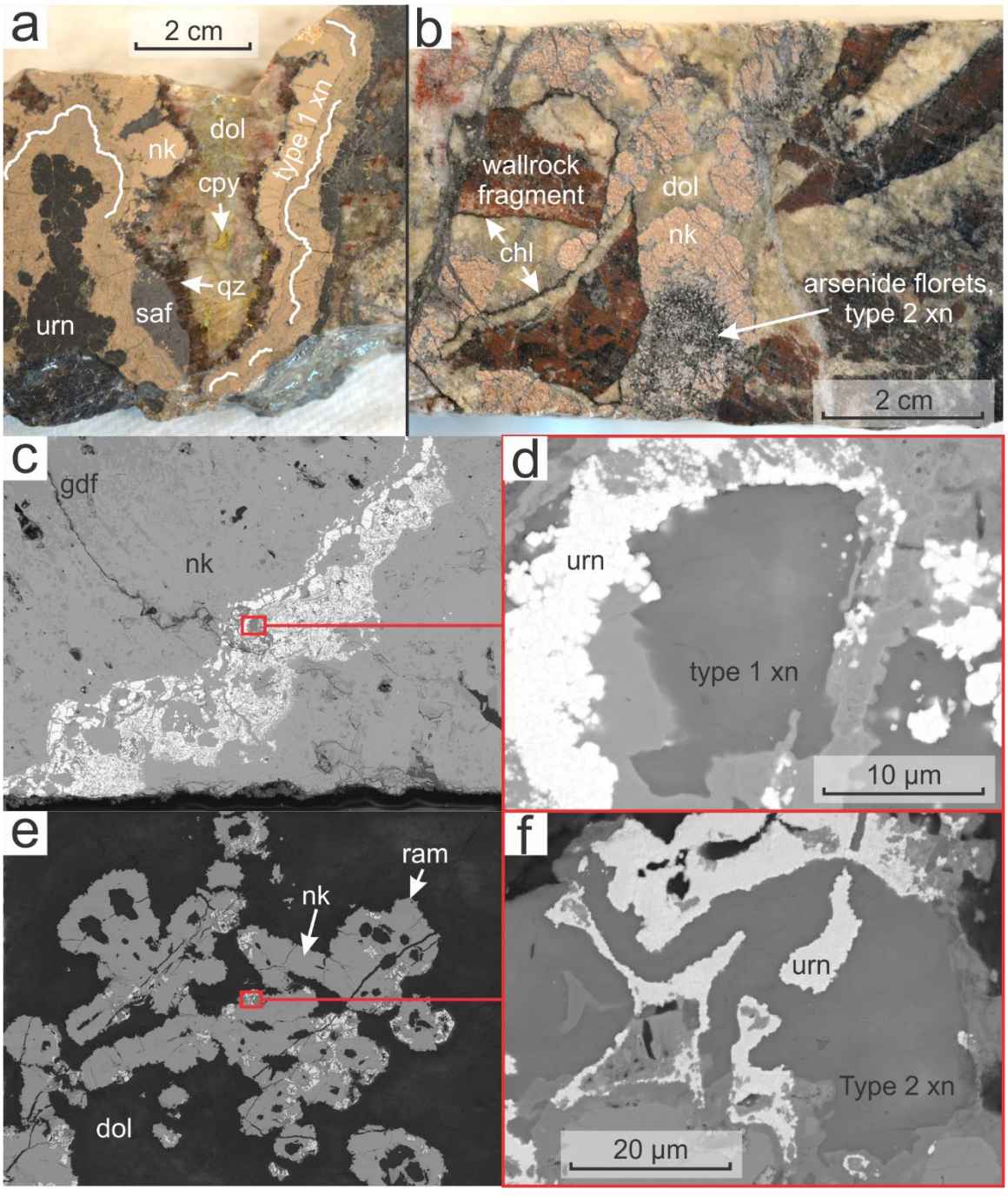
a
2 cm
dol
nk
cpy
type 1 xn
qz
saf
urn
b
wallrock fragment
dol
nk
chl
arsenide florets, type 2 xn
2 cm
c
gdf
nk
d
urn
type 1 xn
10 µm
e
ram
nk
dol
f
urn
Type 2 xn
20 µm

Narrow bands of sugary uraninite, type 1 xenotime crystals (up to 50 μm in diameter), and anhedral apatite crystals occur in two distinct growth zones within a broader domain of massive nickeline (Figure 2.7b; 2.8a, c, d). Textures in the type 1 xenotime assemblage reveal complex intergrowths between nickeline, xenotime, and uraninite. Uraninite often occurs as μm-scale inclusions within xenotime, and also within fractures in xenotime. Xenotime with no uraninite inclusions or fractures rarely exceed 10 μm in diameter on the surface. Type 2 xenotime—with inclusion-free surfaces up to 20 μm in diameter—occurs with sugary uraninite as rims on arsenide florets in one sample (Figure 2.8b, e, f). Type 2 xenotime is coeval with uraninite, and is texturally confined between rammelsbergite and late arsenide-stage dolomite (Figure 2.8e).

Arsenide minerals also occur as rims on native Ag dendrites, isolated from uraninite. Native Ag crystals served as nucleation points for nickeline, safflorite, rammelsbergite, and skutterudite, which sometimes form successive rims on each other (Figure 2.9). Nickeline and Ag in the cores of arsenide florets were partially dissolved in many samples. Evidence for complete dissolution of Ag was recognized as relict dendrites at the cores of arsenide florets (Figure 2.9a, b). Safflorite and native Ag sometimes occur as rhythmic growth bands with each other, and may both have been partially dissolved and replaced by later mineralization (Figure 2.9c, d). Dissolution spaces in Ag-arsenide dendrites are commonly filled with blocky rammelsbergite, quartz, and minerals from the later sulphide stage.

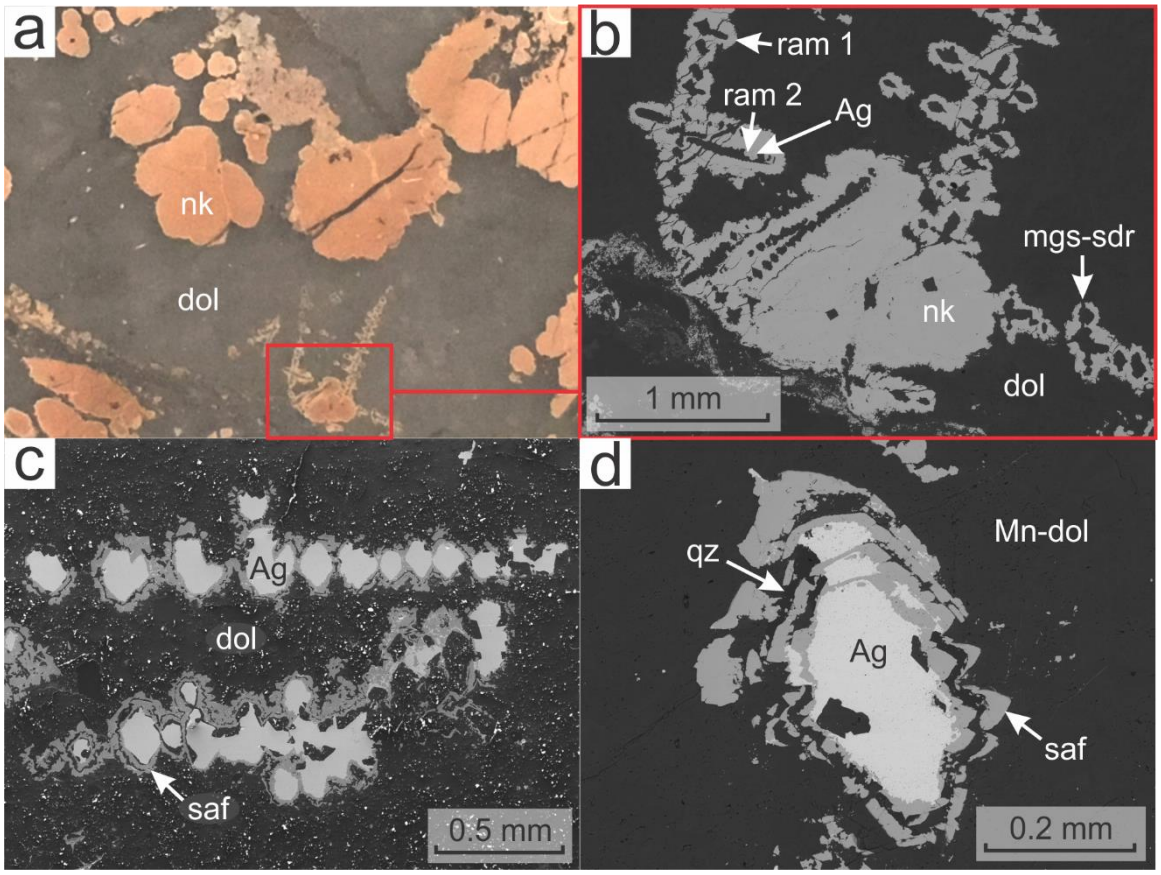

Figure 2.9: Reflected light and SEM-BSE images showing silver dendrite mineralization in the arsenide stage. Mineral abbreviations: nk = nickeline; dol = dolomite; ram = rammelsbergite; mgs-sdr = magnesite-siderite; saf = safflorite; qz = quartz. **(a)** Reflected light image of arsenide florets dominated by nk, with dol infill. **(b) inset from a)** BSE image showing nk and dissolved Ag dendrites with rims of Co-rich ram 1. End-member ram 2 grew into Ag dissolution space. Arsenide minerals and dol are cross cut by fractures which are filled by mgs-sdr. **(c)** BSE image showing dendrites with partially dissolved Ag cores and saf rims. Dissolution space is filled by dol. **(d)** BSE image showing multiple generations of Ag and saf growth, preserved in a partially dissolved dendrite. Dissolution space is filled by qz and Mn-dol.

Some arsenide florets and dendrites showing open-space filling textures are sealed by sparry, dolomite (Figure 2.7h). Assemblages of arsenide minerals with barren dolomite are cross-cut by veins of dolomite and base metal sulphide (BMS) minerals associated with the subsequent sulphide stage (Figure 2.7h). Some late arsenide-stage minerals have rims of comb-textured quartz, which is sometimes recrystallized to sugary grains (Figure 2.7i; 2.8a). The surface of euhedral quartz crystals are often coated with hematite and chalcopyrite crystals associated with the subsequent sulphide stage (Figure 2.7i). Arsenide-stage minerals are moderately fractured, with fractures filled by quartz, chlorite, trace secondary uraninite ± apatite, and carbonates ± disseminated sulphide-stage mineralization.

2.3.1.3 Sulphide stage

The transition into the sulphide stage is characterized by the appearance of the assemblage of chalcopyrite ± hematite ± Fe-dolomite, occurring on the outer rims of arsenide-stage euhedral quartz (Figure 2.10a, b). Euhedral quartz crystals are also found in veins of Fe-dolomite that cross-cut previous mineralization. Arsenide- to sulphide-stage comb quartz is followed paragenetically by abundant Fe-dolomite, hematite, BMS, sulphosalts, and native Ag and Bi. These sulphide stage minerals also fill fractures and dissolution spaces within, and open space adjacent to the rims of, uraninite and arsenide stage minerals (Figure 2.6b; 2.7g, h; 2.8a; 2.10a).

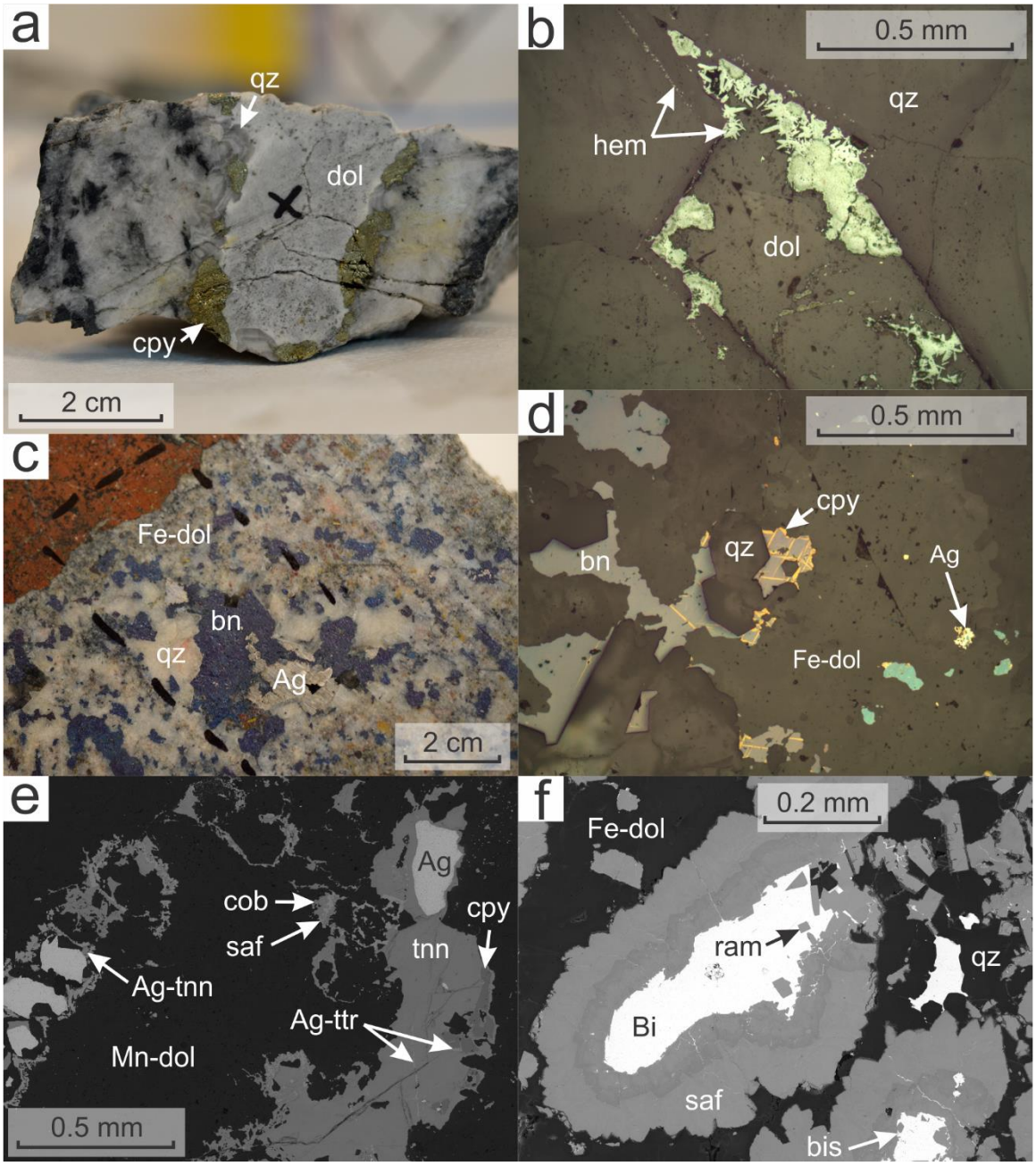
a
qz
dol
cpy
2 cm
b
0.5 mm
qz
hem
dol
c
Fe-dol
bn
qz
Ag
2 cm
d
0.5 mm
cpy
qz
bn
Ag
Fe-dol
e
Ag
cob
saf
cpy
tnn
Ag-tnn
Ag-ttr
Mn-dol
0.5 mm
f
Fe-dol
0.2 mm
ram
qz
Bi
saf
bis

Figure 2.10 (previous page): Hand sample, reflected light, and SEM-BSE images showing sulphide stage mineralization. Mineral abbreviations: qz = quartz; dol = dolomite; cpy = chalcopyrite; hem = hematite; bn = bornite; cob = cobaltite; saf = safflorite; tnn = tennantite; ttr = tetrahedrite; ram = rammelsbergite; bis = bismuthinite. **(a)** Sample 701, showing cpy occurring within growth zones in qz and persisting beyond the end of qz growth, especially as disseminated grains in late dol infill. **(b)** Reflected light image showing hem occurring inside and outside of final euhedral qz growth zones, before dol infill. **(c)** Sample 848, showing native Ag and bn coprecipitated with qz and disseminated in Fe-dol. **(d)** Reflected light image showing even grain boundaries between qz and bn, cpy replacing bn, and all minerals being consumed by late Fe-dol, which also hosts disseminated Ag. **(e)** BSE image showing replacement of Ag, cob, and saf dendrites by Ag-rich ttr-tnn, cpy, and Mn-dol. **(f)** BSE image showing S-rich saf arsenide floret with blocky ram infill and later native Bi infill, which also fills open space around qz and Fe-dol. Minute bis formed along boundaries between Bi and other minerals.

Chalcopyrite, bornite, pyrite, sphalerite, and galena (in order of decreasing abundance) are commonly disseminated in dolomite (Figure 2.10c, d). The sulphide stage is dominated by chalcopyrite, which occurs as open-space filling rims on arsenide-stage minerals and as "boxwork" replacement rims on bornite in some samples (Figure 2.10d). Tennantite-tetrahedrite (sometimes enriched in Ag and Bi) and Ag sulphides, including stromeyerite and argentite, are found in association with Fe-Cu sulphides and native Ag, often filling fractures and replacing, or forming rims around, earlier chalcopyrite and bornite (Figure 2.10e).

Native Bi is commonly seen in association with quartz and dolomite, filling fractures and open space around arsenide florets, and around partially or completely dissolved nickeline in the cores of arsenide florets. Bismuthinite, and wittichenite formed rims around native Bi and Cu sulphides in some samples (Figure 2.10f).

2.3.1.4 Late carbonate stage

The final stage of mineralization formed various carbonates, commonly filling veins, dissolution space, and interstitial space along grain boundaries in sulphide-stage dolomite. Dolomite, magnesite-siderite, and calcite fill a pervasive network of fractures and dissolution channels in early gangue minerals from previous stages (Figure 2.11a, b). Interstitial spaces around sulphide-stage Fe-dolomite crystals are sometimes infilled by botryoidal and acicular/platy marcasite and/or hematite, and by later calcite (Figure 2.11c). Late carbonates are also associated with barite, heulandite, and coffinite (Figure 2.11d). Fluorite, which has been reported as a late stage mineral in previous studies, was not observed in the sample collection.

2.3.1.5 Cathodoluminescence textures

Diverse cathodoluminescence colouration, ranging from various shades of purple-blue to pink, was observed in some euhedral quartz crystals and varied with concentric zoning (Figure 2.12a), whereas other quartz crystals showed little or no CL colour variations from core to rim (Figure 2.12b, c, d). Variations in carbonate composition were also recognized in CL imaging, which helped differentiate various types of carbonates in the later stages of mineralization. Dolomite- and magnesite-series minerals, and calcite, were distinguished mainly by variations in the brightness of CL colours (Figure 2.12e, f, g, h). On the other hand, some dolomites that were visibly zoned in transmitted light did not show significant variations in CL luminescence (Figure 2.12g, h).

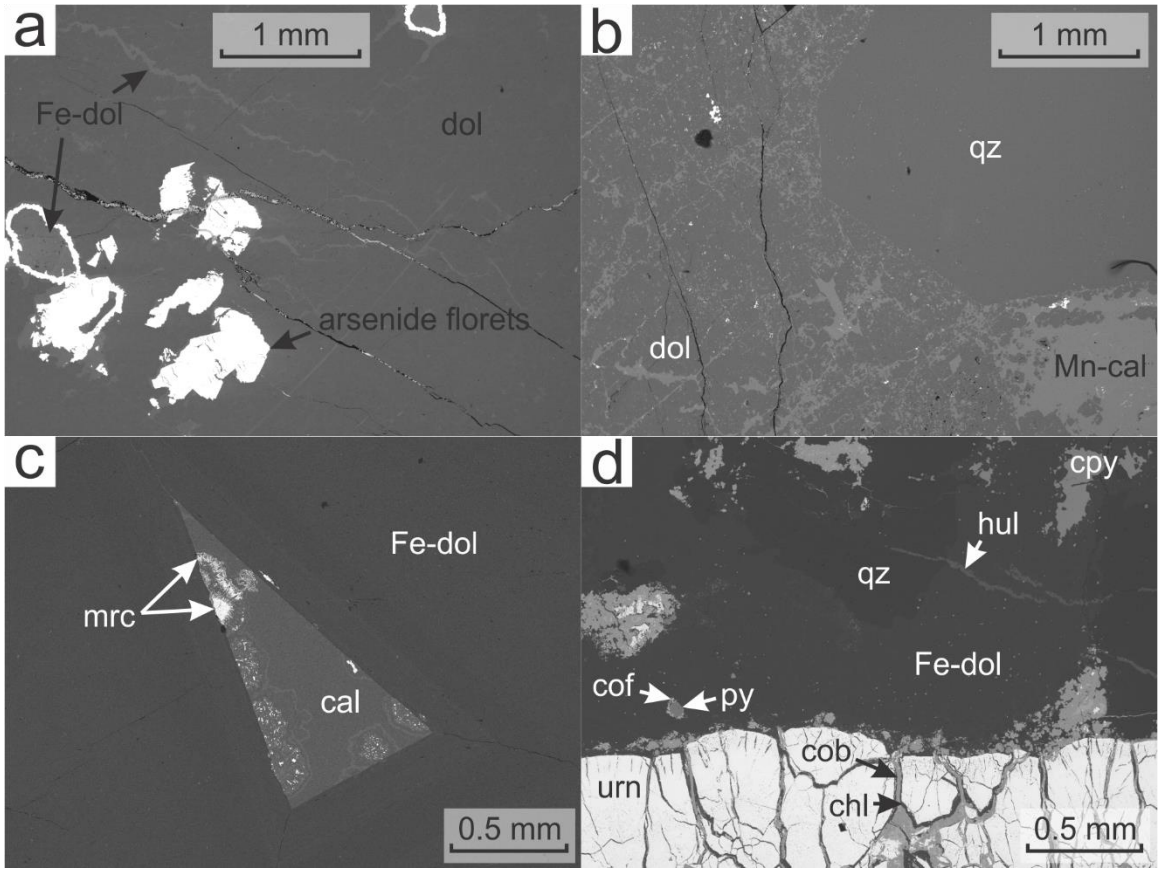

Figure 2.11: SEM-BSE images showing late carbonate stage mineralization. Mineral abbreviations: dol = dolomite; qz = quartz; cal = calcite; mrc = marcasite; cpy = chalcopyrite; hul = heulandite; cof = coffinite; py = pyrite; cob = cobaltite; urn = uraninite; chl = chlorite. **(a)** BSE image showing arsenide florets with dol infill and later veins of Fe-dol. **(b)** BSE image showing dol infill around qz that is also infiltrated by a network of late Mn-cal. **(c)** BSE image showing gradual transition through the sulphide and late carbonate stages, made apparent by mrc growing in cavities in Fe-dol before cal infill. **(d)** BSE image showing the full succession of mineralization, highlighted by urn with cob inclusion-rich rims from the uraninite stage; cob and chl from the arsenide stage; late qz, Fe-dol, py, cpy, and cof from the sulphide stage, and late Ba-rich hul from the late carbonate stage.

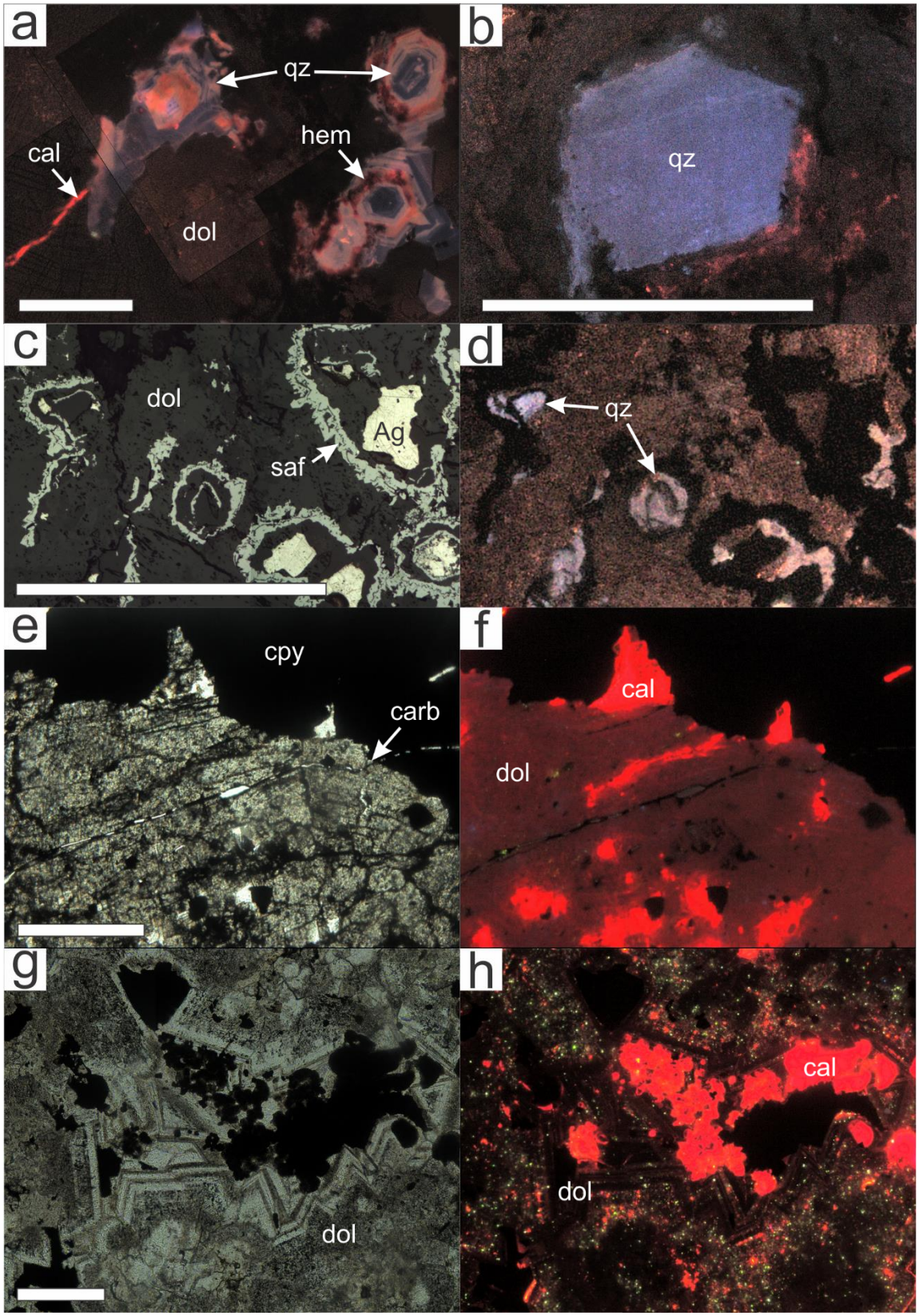
a
qz
hem
cal
dol
b
qz
c
dol
Ag
saf
d
qz
e
cpy
carb
f
cal
dol
g
dol
h
cal
dol

Figure 2.12 (previous page): Colour CL, reflected, and transmitted light photomicrographs of hydrothermal quartz and carbonate. All scale bars are 1 mm across. Mineral abbreviations: qz = quartz; hem = hematite; cal = calcite; dol = dolomite; saf = safflorite; cpy = chalcopyrite; carb = undifferentiated carbonate. **(a)** CL image showing euhedral, concentric zoned qz (orange-blue CL) with hem-rich zones (dark red) in a dol vein. A late cal vein (bright red) cross-cuts the dol. **(b)** CL image showing uniform qz crystal (blue) in chloritized host rock. **(c)** Reflected light image of partially dissolved Ag dendrites with saf rims, qz, and dol infill. **(d)** CL image of (c) showing qz (blue-pink) filling open space after dissolved Ag. **(e)** Transmitted light image of mixed carb and opaque cpy. **(f)** CL image of (e) showing distinct dol (dark red) and cal (bright red) phases. **(g)** Transmitted light image of zoned dol with opaque sulphides and oxides. **(h)** CL image of (g) showing late cal infill (bright red) around opaques.

2.3.2 Ore, accessory, and gangue mineral composition

2.3.2.1 Major element chemistry of ore minerals and carbonates

Average compositions from representative analyses of the most common ore, accessory and carbonate minerals in the Eldorado deposit are summarized in Table 2.4. Uraninite typically has high Pb contents (U/Pb ~ 5.5), reflecting retention of radiogenic Pb since the middle Proterozoic. Coffinite has variable Pb contents (U/Pb ranging from ~5 to negligible Pb). The high Pb content of coffinite confirms it formed by U remobilization or alteration of the original uraninite, closer to the age of the original uraninite mineralization, whereas coffinite with low Pb contents suggests very recent remobilization and negligible radiogenic Pb.

Most arsenide growth successions are strongly chemically zoned, resulting in broad compositional ranges in single samples. Figure 2.13 shows the range of compositional variability in transition metal content in nickeline, diarsenides, and triarsenides. Nickeline is often As-rich compared to ideal compositions, and may contain up to a few wt.% Co and

Sb in zoned crystals. The diarsenides exhibit solid solution between rammelsbergite and (clino)safflorite, with up to 10 wt.% Fe. The diarsenides also contain highly variable S content, up to 17 wt.%, approaching stoichiometric composition for sulpharsenides. Safflorite rarely approaches end-member composition, except at the rims of some arsenide florets. End-member rammelsbergite was only identified as individual blocky grains on the rims of florets, or filling dissolution space in nickeline. Skutterudite often contains up to 10 wt.% Ni.

Sulpharsenide minerals show solid solution compositions between cobaltite and gersdorffite (Table 2.4). End-member compositions are uncommon. Sulpharsenides are poor in Fe, except for some euhedral crystals of end-member arsenopyrite that were identified in rare veins associated with cobaltite. Figure 2.14 shows the range of variability in transition metal composition among the sulpharsenides. Many individual sample sites show a predominance of either Co- or Ni-sulpharsenide and arsenide assemblages throughout the Eldorado deposit.

Carbonate minerals include calcite, dolomite-series, and magnesite-series members. Compositional variations in carbonates are illustrated in Figure 2.15. Calcite is rarely pure and mainly Mn-rich (up to 12 wt.% Mn; Table 2.4). Pure dolomite and kutnohorite are rare, while samples showing distinct compositional fields of Fe- and Mn-dolomite are common (Figure 2.15). Magnesite-siderite solid solution was also identified.

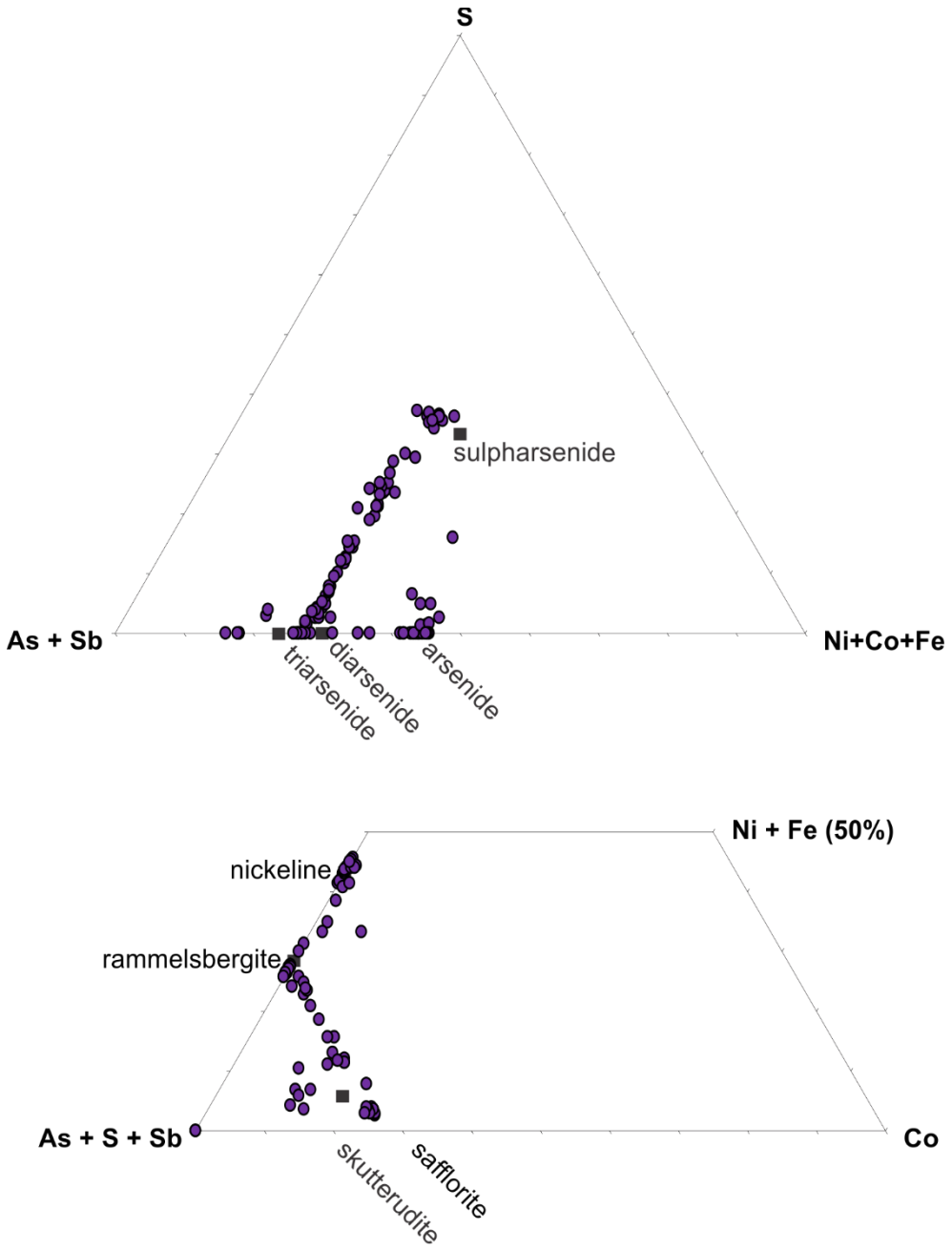

Figure 2.13: Ternary diagrams showing relative abundances (atomic %) of major elements in arsenide minerals from all analysed samples. Top: composition of all sulpharsenide and arsenide minerals. Bottom: composition of nickeline, diarsenides and triarsenides. Stoichiometric compositions of major mineral phases are shown for comparison.

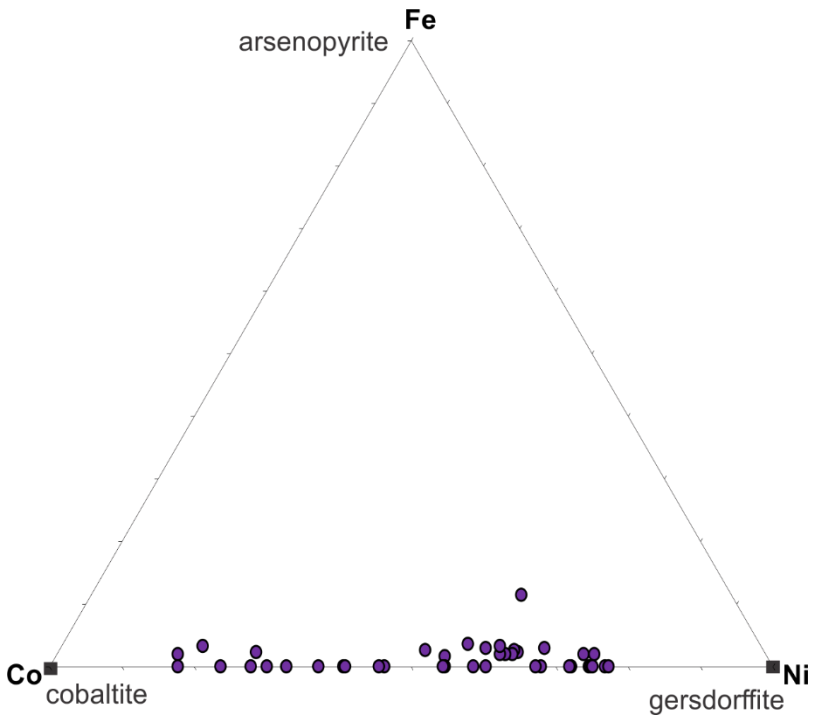

Figure 2.14: Ternary diagram showing relative abundance (atomic %) of major transition metals in sulpharsenides from all analysed samples. Stoichiometric compositions of major mineral phases are shown for comparison.

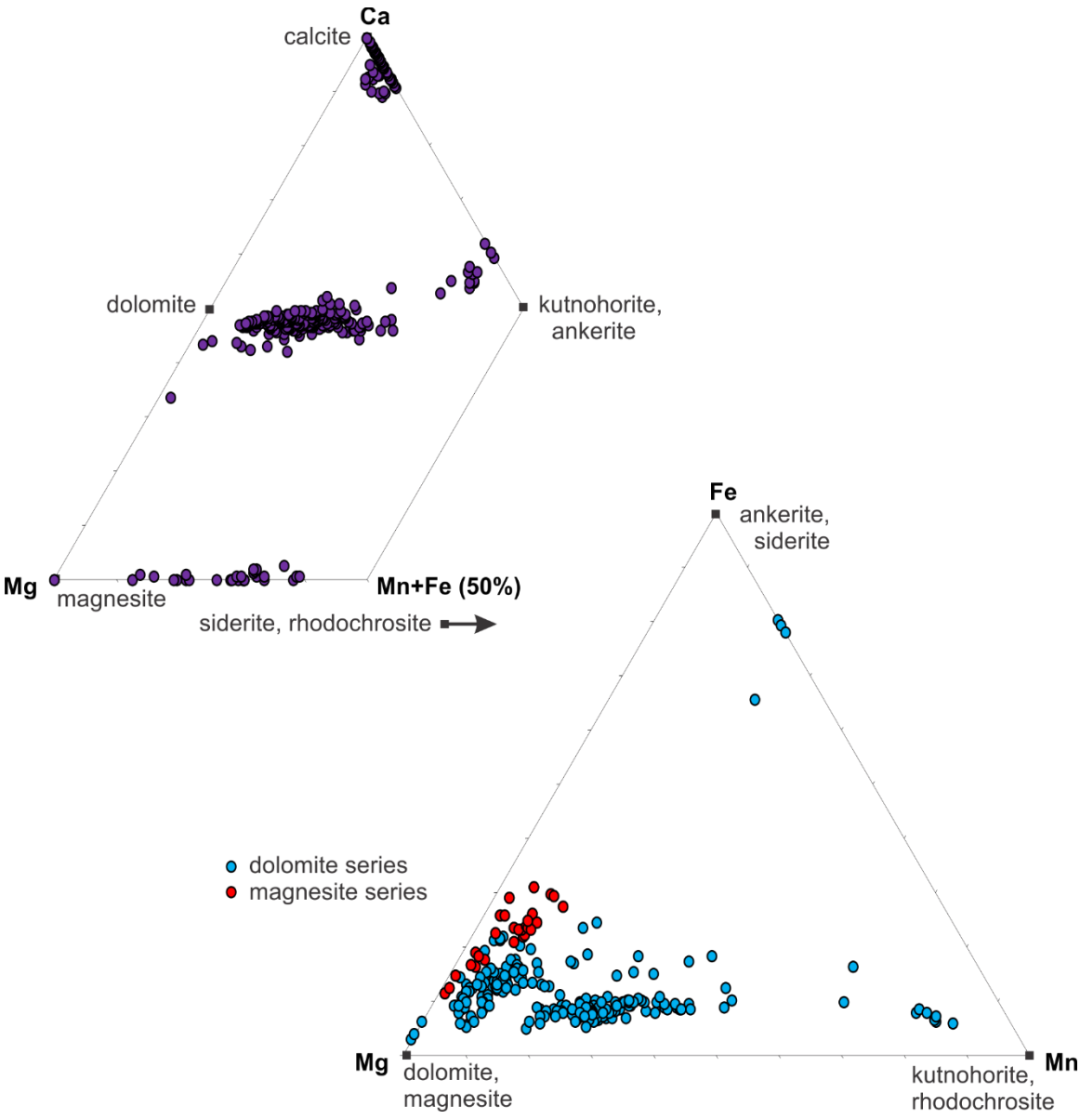

Figure 2.15: Ternary diagrams showing relative abundance (atomic %) of major cations in carbonates from all analysed samples. Top: composition of all carbonates. Bottom: composition of end-member cations in solid solution dolomite- and magnesite-series minerals. Stoichiometric compositions of major mineral phases are shown for comparison.

2.3.2.2 Carbonate REE signatures

LA-ICP-MS analyses of REE in carbonates (Mn-calcite, Fe-dolomite, and Mn-dolomite) are summarized in Table 2.5. Chondrite-normalized abundance patterns show two general trends (Figure 2.16). REE patterns for dolomites are flat or gently downward bell-shaped, show LREE < HREE, and most have a distinct negative Eu anomaly. One Mn-dolomite sample shows a slight positive Eu anomaly, and the flattest REE pattern overall. Calcites have a distinct negative slope (LREE > HREE) and a less pronounced negative Eu anomaly compared to dolomites.

Table 2.5: REE composition (ppm) of carbonates from LA-ICP-MS analysis.

Sample	Mineral	Spot ID	La	Ce	Pr	Nd	Sm	Eu	Gd	Tb	Dy	Ho	Er	Tm	Yb	Lu
701	Mn-cal	08a10	69.8	166	19.6	66.1	8.36	1.10	6.17	0.966	5.29	0.961	2.88	0.503	3.07	0.521
701	Mn-dol	08a11	0.827	3.51	0.585	3.01	2.45	0.688	4.09	0.663	3.01	0.529	1.31	0.227	1.65	0.233
701	Mn-dol	08a14	8.54	43.3	6.84	35.7	14.0	6.21	18.4	2.45	12.0	1.92	4.81	0.774	6.10	0.988
714	Mn-dol	08a17	0.318	1.46	0.248	1.04	0.705	0.295	0.960	0.160	0.843	0.176	0.518	0.0874	0.451	0.0861
714	Mn-dol	08a18	0.830	3.50	0.585	3.02	2.43	0.688	4.11	0.668	3.03	0.529	1.32	0.227	1.64	0.234
714	Mn-dol	08a23	6.48	28.9	4.22	20.3	8.40	4.30	10.9	1.29	5.45	0.900	2.23	0.324	2.51	0.368
714	Mn-dol	08a24.1	8.69	38.9	6.05	29.4	12.5	6.57	16.5	1.97	8.70	1.32	3.67	0.578	3.88	0.622
714	Mn-dol	08a24.2	8.53	38.8	6.14	30.4	12.2	6.51	16.9	1.97	8.89	1.28	3.56	0.572	3.98	0.598
714	Mn-dol	08a25	4.96	23.0	3.83	19.3	9.74	4.42	12.5	1.64	7.32	1.04	2.91	0.416	3.34	0.555
714	Mn-dol	08a28	5.07	26.8	4.63	22.9	9.96	5.14	14.0	1.80	8.30	1.29	3.55	0.501	3.69	0.546
822	Mn-dol	08a81	2.54	14.1	3.04	18.5	14.4	1.46	28.7	5.33	27.1	3.68	6.81	0.809	3.70	0.490
822	Fe-dol	08a86	0.0295	0.190	0.0485	0.233	0.277	0.0159	0.272	0.0828	0.360	0.0524	0.152	0.0272	0.162	0.0276
822	Fe-dol	08a87	0.0477	0.251	0.0522	0.315	0.139	0.0334	0.180	0.0259	0.154	0.0232	0.0931	0.0138	0.0570	0.0091
822	Fe-dol	08a88	0.0174	0.123	0.0176	0.136	0.0313	0.0138	0.0905	0.0167	0.0528	0.0071	0.0212	0.0053	0.0292	0.0039
718	Mn-cal	10a24	66.4	93.4	8.39	26.0	3.29	0.571	3.37	0.400	1.92	0.380	0.905	0.118	0.590	0.0992
718	Mn-cal	10a26	7.62	9.50	1.05	3.30	0.443	0.123	1.08	0.0962	0.764	0.213	0.585	0.0894	0.559	0.100
718	Mn-cal	10a27	15.8	19.3	2.08	7.04	1.05	0.326	1.77	0.264	2.06	0.518	1.66	0.200	0.835	0.204
SFB240	Mn-dol	10a45	0.0608	0.682	0.302	2.96	2.94	0.290	3.89	0.661	3.25	0.547	1.65	0.207	1.42	0.226
SFB240	Mn-dol	10a46	0.101	1.59	0.667	6.11	6.61	1.04	9.65	1.68	9.54	1.71	4.75	0.686	4.59	0.692
SFB240	Mn-dol	10a48	0.0766	0.998	0.411	4.12	4.80	0.788	7.59	1.37	7.91	1.49	4.39	0.702	5.37	0.896
SFB240	Mn-dol	10a49	0.0772	1.36	0.641	5.47	6.08	0.909	9.37	1.60	8.99	1.73	4.36	0.607	4.74	0.737
SFB240	Mn-dol	10a50	0.167	1.68	0.585	5.85	5.99	0.867	8.33	1.38	7.30	1.42	3.65	0.568	3.65	0.529
SFB240	Mn-dol	10a51.1	0.0773	1.36	0.643	5.50	6.09	0.910	9.41	1.61	9.04	1.74	4.38	0.609	4.76	0.740
718	Mn-cal	12a28	16.9	19.7	2.32	8.52	1.07	0.261	1.86	0.246	1.74	0.405	1.20	0.147	0.899	0.146
848	Fe-dol	12a32	0.304	2.03	0.481	2.30	1.20	0.0730	1.62	0.330	2.07	0.363	1.14	0.191	1.24	0.199
848	Mn-dol	12a36	0.602	1.83	0.255	1.18	0.528	0.0780	0.914	0.126	0.797	0.163	0.402	0.0743	0.582	0.107
848	Fe-dol	12a37	0.416	3.61	0.780	4.47	2.87	0.118	3.22	0.708	5.02	0.952	2.62	0.355	2.68	0.440
848	Mn-dol	12a38	0.203	0.891	0.173	0.864	0.397	0.0661	0.654	0.114	0.640	0.106	0.323	0.0619	0.530	0.0972
848	Fe-dol	12a39	0.128	0.525	0.0989	0.488	0.261	0.0399	0.399	0.0643	0.363	0.0630	0.169	0.0381	0.368	0.0608
848	Mn-dol	12a40	0.203	0.892	0.173	0.865	0.398	0.0659	0.657	0.114	0.641	0.106	0.323	0.0617	0.530	0.0971
848	Fe-dol	12a41	0.101	0.841	0.212	1.00	0.610	0.0366	0.859	0.247	1.36	0.294	0.794	0.126	1.01	0.149
848	Fe-dol	12a42	0.0989	0.776	0.204	0.932	0.424	0.0215	0.587	0.174	1.02	0.229	0.645	0.128	0.776	0.108
714	Mn-dol	12a48	8.21	78.8	20.1	123	72.2	10.4	83.1	11.3	53.9	8.65	20.8	2.83	18.4	2.68
211	Fe-dol	12a57	13.3	48.6	7.10	30.6	11.6	1.69	16.6	2.55	12.7	2.05	4.25	0.547	3.28	0.402
211	Fe-dol	12a58	14.4	52.7	8.03	33.9	12.4	1.74	18.1	2.61	13.6	2.09	4.47	0.539	3.16	0.399
211	Fe-dol	12a59	15.5	54.8	7.96	34.9	12.4	2.01	18.9	2.80	13.5	2.21	4.70	0.531	3.17	0.408
211	Fe-dol	12a60	17.8	62.3	8.89	39.1	14.1	2.12	20.9	3.02	14.9	2.44	5.41	0.623	3.39	0.448
211	Fe-dol	12a61.1	16.1	57.1	8.69	35.5	13.3	1.97	19.0	2.81	13.9	2.24	4.90	0.571	3.14	0.421

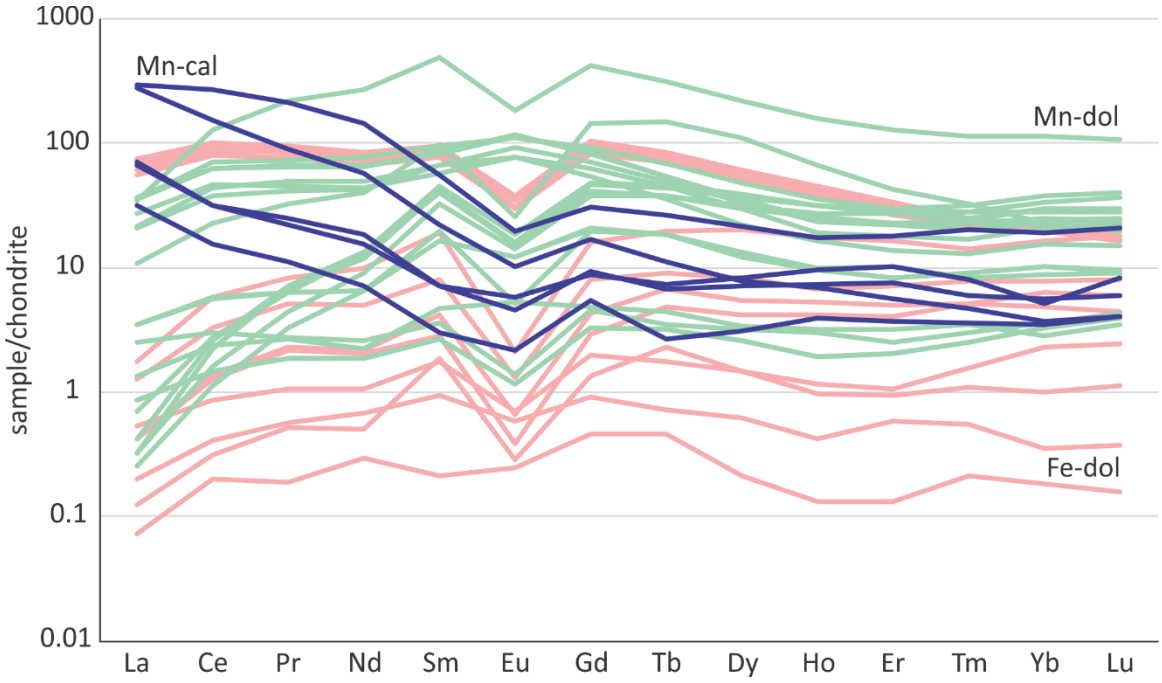

Figure 2.16: Chondrite-normalized spider plot showing REE trends for different stages of carbonate mineralization. Chondrite data from McDonough and Sun (1995).

2.3.2.3 Stable and radiogenic isotope compositions of gangue minerals and uraninite

2.3.2.3.1 Bulk C, O, Sr isotope analysis of vein carbonates

Bulk chemical analysis of carbonates provided isotopes of Rb and Sr, $^{87}Sr/^{86}Sr$ and $^{87}Sr/^{86}Sr_o$ and stable isotopes of C and O (Table 2.6 in the Appendix). Additionally, selected major and trace element chemistry (wt.% Mg, Ca, Mn, and Fe; ppm Na, Al, K, Ba, Rb, and Sr; Table 2.6) of carbonates was obtained to confirm compositional purity, identify type of carbonate with respect to vein stage, and correct for any radiogenic ingrowth. Rubidium content was negligible, but $^{87}Sr/^{86}Sr$ ratios were corrected anyway, yielding $^{87}Sr/^{86}Sr_o$ values (calculated at ca. 1440 Ma) in the range of 0.70459–0.72361, with individual analysis errors of < 1%. Carbonates did not show significant distinction between vein stages: 0.71077–0.71496, 0.70459–0.72183, and 0.71008–0.72361 for the late arsenide, sulphide, and late carbonate stages, respectively (Table 2.6).

Dolomite from the late arsenide and sulphide stages, and magnesite-series carbonates from the late carbonate stage have relatively consistent C isotope composition, are slightly ^{13}C-depleted ($\delta^{13}C_{VPDB}$ ranging from -3.4 to -1.4 ‰ ± 0.47; 1σ), and showed no significant distinction by mineralization stage. Values of $\delta^{18}O_{VSMOW}$ are similarly consistent, showing strong enrichment in ^{18}O, ranging from 13.2 to 22.4 ‰, but with the majority of analyses between 13.2 and 16.1‰ ± 2.6 (1σ). A single calcite analysis from the late carbonate stage has $\delta^{13}C_{VPDB}$ = -6.7 ‰ and $\delta^{18}O_{VSMOW}$ = 10.9 ‰.

2.3.2.3.2 SIMS O isotope analysis of quartz and uraninite

Stable isotope data for O in quartz and uraninite are tabulated in Table 2.7 in the Appendix. Hydrothermal quartz showing various textures, and in various mineral associations, was analyzed with core-rim spatial control provided by CL imaging of zoning. Two textural variants were analyzed in early quartz associated with the early arsenide stage with no significant differences seen. Quartz with sulpharsenide (network) rims gave values of $\delta^{18}O_{VSMOW}$ = 17.3 ± 1.5 ‰ (1σ; n = 9). Quartz without the sulpharsenide rims gave values of $\delta^{18}O_{VSMOW}$ = 17.2 ± 0.7 ‰ (n = 9). A different generation of quartz in the arsenide stage, replacing dendritic Ag has $\delta^{18}O_{VSMOW}$ = 18.2–19.2 ‰ (n = 3). Unfortunately there is no clear evidence for timing of this quartz relative to other quartz generations, but it is considered to be mid-late arsenide stage. All quartz from the late arsenide and sulphide stage veins gave a range of similar values of $\delta^{18}O_{VSMOW}$ = 12.1–18.2 ‰. Different key textures of the analyzed quartz include (i) euhedral quartz associated with native Bi, $\delta^{18}O_{VSMOW}$ = 15.2 ± 1.6 ‰ (n = 17); (ii) quartz in barren carbonate veins, $\delta^{18}O_{VSMOW}$ = 15.4 ± 1.3 ‰ (n = 10); (iii) quartz associated with chalcopyrite and other sulphide stage minerals, $\delta^{18}O_{VSMOW}$ = 15.3 ± 1.1 ‰ (n = 34); and (iv) euhedral, zoned quartz associated with late carbonate infill, $\delta^{18}O_{VSMOW}$ = 14.9 ± 1.7 ‰ (n = 9). There appears to be no significant differences in $\delta^{18}O_{VSMOW}$ across all textural variants with the exception of the minor decrease by a few ‰ from the early quartz to the later generations. Core and rim analyses of zoned quartz crystals in the late arsenide and sulphide stages were generally consistent within error (14.7 ± 1.3 ‰ for core analyses, vs. 15.5 ± 1.3 ‰ for rim analyses; 1σ).

Botryoidal uraninite with rhythmic bands of sulpharsenide inclusions show relatively consistent $\delta^{18}O_{VSMOW}$ values across all analyzed grains (-37.5 to -30.0 ‰; n = 28). No differences were noted between inner bands and outer bands in uraninite, nor between the sulpharsenide inclusion-rich zone and the inclusion-free uraninite zones (average $\delta^{18}O_{VSMOW}$ = -31.5 and -32.3 ‰, respectively; n = 7 and 5, respectively).

2.3.3 Fluid inclusion systematics

2.3.3.1 Fluid inclusion petrography and classification

Four types of fluid inclusions were documented petrographically. Their type-designation is based on the fluid inclusion host mineral and timing of entrapment relative to different mineralized vein stages. The fluid inclusion assemblage (FIA) method was used for classification (Goldstein 2003). Generally, the scope of phases observed in inclusions comprised: aqueous liquid (L_{aq}), vapour (V), halite (H), hydrohalite (HH; at low T only), ice (at low T only), and other solids (chlorite and hematite). Fluid inclusions described here are hosted by quartz and carbonate minerals from the late arsenide and sulphide mineralization stages. Fluid inclusions too small to characterize sufficiently, commonly of secondary origin, or visibly showing signs of post-entrapment modification (i.e. necking down, leakage) were not characterized beyond basic petrographic observations.

Type 1 fluid inclusions occur in late arsenide-stage quartz, and are primary or have an ambiguous, unclassified origin. Primary inclusions occur in inclusion-rich growth zones in the cores of euhedral crystals (Figure 2.17a, b). They occur as isolated inclusions or as

part of a FIA containing other type 1 inclusions. They are distinguished from FIA that contain abundant similar two-phase inclusions occurring within healed fractures indicating secondary origin. Type 1 inclusions are rounded to irregular in shape, 5–25 μm in diameter, and usually contain two phases (L_{aq} + ~5 vol. % V) at room temperature (Figure 2.17b). They may also contain chlorite crystals, which were identified by their platy habit, colour in plane-polarized light, birefringence in cross-polarized light (Figure 2.17c, d), and characteristic Raman spectra (strong peaks around ~550 and 680 cm^{-1}). Chlorite shows highly variable vol. % proportions between inclusions, and is not present in every inclusion indicating that it is an accidentally-trapped (saturated) phase.

Type 2 fluid inclusions also occur within late arsenide-stage quartz and are of unclassified origin. They occur in massive, unzoned quartz (Figure 2.17e). They may be negative-crystal shaped, rounded, or oblong, and up to 30 μm in length. They usually contain three phases (L_{aq} + ~1–3 vol. % V + ~5–10 vol. % H) at room temperature (Figure 2.17e, f, g) and may also contain accidentally-trapped chlorite crystals (Figure 2.17f, g). Evidence of post-entrapment modification is common in Type 2 inclusions (necking down, variable phase ratios).

Type 3 fluid inclusions occur in sulphide stage dolomite and are also primary in origin. Their FIAs are confined within, or along, distinct growth surfaces that alternate between being inclusion-rich, and inclusion-poor (Figure 2.17k, l, m). They are either isolated or occurring as FIA containing other type 3 inclusions. Type 3 inclusions occur as blocky or irregular shapes up to 50 μm in length (Figure 2.17n, o, p, q, r). They typically contain three phases (L_{aq} + 1–3 vol. % V + 3–5 vol. % H) at room temperature and often

also contain accidentally trapped hematite (showing variable phase proportion, and not always present), identified by their red-orange colour and platy habit (Figure 2.17p, q, r). Evidence of post-entrapment modification (notably, leakage of L_{aq}) is common. Secondary inclusions are also abundant in dolomite and may contain 2 or 3 phases (Figure 2.17s).

Type 4 fluid inclusions occur in sulphide stage dolomite and are of secondary or unclassified origin. They occur as isolated inclusions or as part of FIA, along trails of other secondary inclusions. Type 4 inclusions are typically rounded, 5–20 μm in diameter, and contain two phases (L_{aq} + ~5 vol. % V) at room temperature (Figure 2.17n, s).

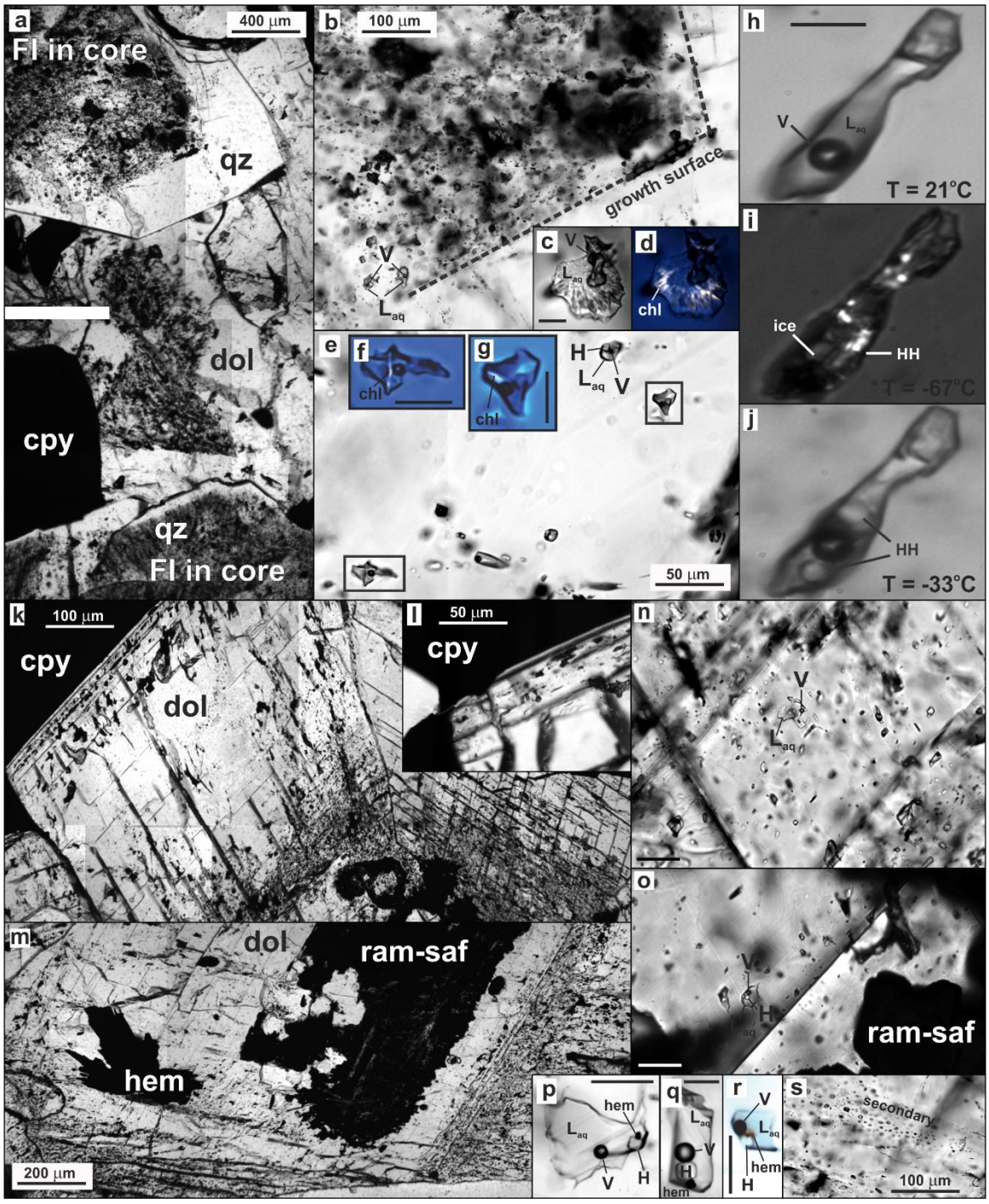
a
400 µm
FI in core
qz
dol
cpy
qz
FI in core
b
100 µm
growth surface
V
L aq
c
V
L aq
d
chl
e
f
chl
g
chl
H
L aq
V
50 µm
h
V
L aq
T = 21°C
i
ice
HH
T = -67°C
j
HH
T = -33°C
k
100 µm
cpy
dol
l
50 µm
cpy
n
V
L aq
o
V
H
aq
ram-saf
m
dol
ram-saf
hem
200 µm
p
hem
L aq
V
H
q
L aq
V
H
hem
r
V
L aq
hem
H
s
secondary
100 µm

Figure 2.17 (previous page): Petrographic characteristics of fluid inclusions in quartz and carbonate hosts. All images taken in transmitted, plane-polarized light with the exception of (d), (f), (g), and (i) taken in cross-polarized light. All images taken at 21 °C except (i) and (j). Scale bar = 20 μm unless otherwise indicated. Phase abbreviations: qz = quartz; dol = dolomite; cpy = chalcopyrite; chl = chlorite; hem = hematite; ram-saf = rammelsbergite-safflorite; L_{aq} = aqueous liquid; V = vapour; H = halite; HH = hydrohalite. **(a)** Euhedral qz crystals (syn-post late arsenide stage) showing a primary inclusion-rich growth zone in the core of the crystals, and inclusion-free rims. Infilling dol from the sulphide stage shows inclusion-rich region in the center of the infill. **(b)** Enlarged view of the zoned qz crystal in (a) showing the growth zone surface between inclusion-rich and inclusion poor zones, and 2-phase, primary (L_{aq}+V) inclusions within the inner growth zone. **(c-d)** 2-phase (L_{aq}+V) inclusion in plane-(c) and cross-polarized (d) light showing the presence of accidentally trapped chl (birefringent phase). **(e)** Primary, 3-phase (L_{aq}+V+H) inclusions in qz from the late arsenide stage. **(f-g)** Enlarged views of fluid inclusions in (e) showing accidentally trapped chl crystals (birefringent in cross-polarized light). **(h-j)** Primary inclusion in qz shown at 21 °C (L_{aq}+V), at -67 °C showing H_2O ice and birefringent HH crystals (cross-polarized light), and at -33 °C showing HH (after heating beyond ice melting). H was a metastable phase, not originally present in (h), but formed at the expense of HH upon reheating above 0 °C. **(k)** Euhedral dol crystal showing variations in primary inclusion abundance from core (inclusion-rich) to main intermediate zone (inclusion-poor) to rim (inclusion-rich). Sulphide-stage cpy infilling post-dates dol. **(l)** Enlarged area of dol crystal rim showing 2 phase (L_{aq}+V) inclusions. **(m)** Rhombic crystal of dol with a relict core of ram-saf from the late arsenide stage and a syngenetic hem crystal aggregate from the sulphide stage. Primary inclusion density varies through growth zones (inclusion-poor inner zone; inclusion-rich outer zone). **(n)** Primary, 2-phase (L_{aq}+V) inclusions in dol from the sulphide stage. **(o)** Primary, 3-phase (L_{aq}+V+H) inclusions in dol from the sulphide stage. Relict ram-saf floret from the late arsenide stage has been overgrown/replaced by the dol. **(p-r)** 3-phase (L_{aq}+V+H) inclusions in dol that also contain accidentally-trapped hem. **(s)** Secondary trails of 2-phase (L_{aq}+V) inclusions in dol.

2.3.3.2 Fluid inclusion microthermometry

Microthermometric measurements are summarized in Table 2.8 in the Appendix. Two phase changes were measured in type 1 fluid inclusions; T_m^{ice} ranged from -26 to -21 °C, and $T_h = T_v$ ranged widely from 149 to 356.6 °C. Some outliers were removed from the range in T_v due to evidence of post-entrapment modification. Most individual FIA have narrower ranges in T_v (1σ on the order of ±5-20°C; Table 2.9). Significant variability

between assemblages is also observed (e.g. FIA A7 vs. A10; Table 2.9). Some type 1 fluid inclusions decrepitated immediately after homogenization.

Table 2.9: Average microthermometry measurements and salinity determinations within FIA.

			Phase change temperatures (°C)				Salinity (wt.%) *						
Sample	**FIA**	**FI Type**	**T_v**	**error (1σ)**	**T_d^H**	**error (1σ)**	**NaCl**	**error (1σ)**	**$CaCl_2$**	**error (1σ)**	**S_{wt}**	**error (1σ)**	**n**
709	A7	Type 1	328.1	21.9			12.2	0.3	10.4	0.3	22.6	0.6	7
709	A10	Type 1	165.0	4.4			13.2	0.01	11.3	0.01	24.5	0.03	3
718	A14	Type 1	166.5	103.9			12.9	0.4	11.0	0.3	23.9	0.7	4
714	A19	Type 2	151.0	20.4	100.0	-	13.0	-	18.5	-	31.6	-	4
709	A20	Type 2	135.5	9.8									5
709	A21	Type 2	97.0	10.5	173.5	20.5	15.5	-	19.1	-	34.6	-	2
709	A22	Type 2	168.0	101.8									2
709	A23	Type 2	215.6	16.9	154.9	6.6	15.0	-	19.2	-	34.2	-	6
709	A25	Type 2	216.6	43.0	320.0	-	31.0	-	13.9	-	44.9	-	5
709	A26	Type 2	189.6	13.5	207.6	3.7	20.7	-	15.1	-	35.8	-	2
709	A27	Type 2	262.5	81.6	146.3	9.5	15.5	-	18.4	-	33.9	-	2
709	A28	Type 2	133.0	13.6	204.7	10.4							4
718	A32	Type 2	140.4	0.2	159.2	4.1							5
718	A33	Type 2	106.8	12.1	151.0	9.7	14.4	0.4	20.9	0.6	35.4	0.7	6
718	A34	Type 2	133.8	6.6	155.2	2.0	14.1	0.2	21.6	0.3	35.7	0.17	4
718	A35	Type 2	229.7	35.9	158.5	14.8	14.4	1.1	21.4	0.4	35.8	0.7	2
SFB240	A36	Type 3	135.9	32.7	152.5	3.5	16.6	0.9	16.5	1.3	33.0	0.4	7
SFB240	A37	Type 3	205.7	4.0	215.0	-							9
SFB240	A38	Type 3	198.0	10.6	220.2	-	21.6	-	14.8	-	36.4	-	3
709	A40	Type 3	91.6	36.6									2
SFB240	A41	Type 3	137.2	0.3	132.7	0.1	12.8	-	21.7	-	34.5	-	3
SFB240	A42	Type 3	201.3	4.1	219.5	1.2	21.2	-	15.5	-	36.7	-	3
SFB240	A43	Type 4	135.9	2.2									4
SFB240	A44	Type 4	123.8	1.4									2
SFB240	A45	Type 4	198.4	5.9									2
SFB240	A46	Type 4	102.9	15.9									5
SFB240	B1	Type 3	183.7	0.3	214.0	2.8	21.0	0.1	15.1	0.6	36.1	0.5	2
SFB240	B2	Type 3	188.0	7.6	217.7	4.7	21.4	0.1	14.8	0.4	36.2	0.6	4
709	B4	Type 2	117.0	12.6	175.9	7.4	18.6	0.4	15.1	0.01	33.7	0.4	2
709	B5	Type 2	290.7	8.9	170.8	18.3	17.7	0.7	16.2	0.5	33.9	1.3	2
709	B6	Type 2	187.5	10.0	220.0	-							2
709	B9	Type 2	112.9	1.1	150.0	28.3	14.1	2.0	21.1	0.9	35.1	1.2	2
718	B10	Type 1	160.3	11.4			12.4	0.2	10.6	0.1	23.0	0.3	3
718	B11	Type 1	216.7	28.8			10.7	0.1	9.1	0.1	19.8	0.1	5
718	B12	Type 2	128.1	17.0	190.0	52.3	19.3	3.6	15.7	0.6	35.0	3.0	2

n = number of fluid inclusions in assemblage. Average values may be calculated from a smaller sample within the FIA.
**The proportion of NaCl to $CaCl_2$ salts in fluid inclusion types 1 and 4 are assumed to be 54% NaCl and 46% $CaCl_2$ based on corresponding average Na and Ca content in Type 1 inclusions, measured by LA-ICP-MS.*

Type 2 and 3 fluid inclusions sometimes contained halite, which did not always reprecipitate on cooling to room T after dissolution during microthermometry measurements (Figure 2.17h). This is an indication that the fluids are near the threshold of halite saturation (Becker et al. 2008). Type 2 and 3 inclusions were cooled below -140 °C

in order to ensure the reappearance of halite after successive heating and freezing cycles. Upon heating, T_e was often estimated in the range of -70 to -50 °C. This phase change T marked the appearance of ice and HH in the inclusions (Figure 2.17i). Type 2 and 3 inclusions had T_m^{ice} = -37.6 ± 4.4 °C (1σ; n = 29) and -34.4 ± 4.2 °C (n = 13), respectively. The lower freezing point depression indicates a much higher S_{wt} than that for type 1 inclusions, which is consistent with the observation of solid halite in these inclusion types. Hydrohalite persisted in type 2 and 3 inclusions after observing final ice melting (Figure 2.17j). Values of T_d^{HH} were often in the range of 0 to 20 °C. Measurements of T_v were generally consistent between type 2 and 3 inclusions, with average values of T_v = 151.2 ± 45.9 °C (n = 68) and 157.1 ± 43.2 °C (n = 35), respectively. T_d^H values were also consistent in type 2 and 3 inclusions (average T_d^H = 180.6 ± 48.2 °C; n = 46 and 180.8 ± 39.3 °C; n = 16, respectively). Dissolution of halite was often the last observed phase transition. In instances where $T_h = T_v$, there was often an oversized vapour bubble, or other evidence of post-entrapment modification. Some type 2 and 3 fluid inclusions decrepitated immediately after homogenization. Two measurements of decrepitation at 222.2 and 231.4 °C were recorded in type 2 fluid inclusions that homogenized around 215 °C. Several decrepitation events were observed at ~133 °C in FIA of type 3 fluid inclusions.

Four assemblages and two individual type 4 fluid inclusions gave average T_v = 133.1 ± 45.9 °C. A single analysis of a type 4 fluid inclusion provided T_m^{ice} = -23.4 °C, but other inclusions did not appear to freeze, or were obscured by surface ice. Average measurements and calculated salinities for FIA are summarized in Table 2.9.

2.3.3.3 Fluid chemistry

The concentrations of various major and trace elements including the halogens (Cl, Br), major and minor cations, and ore/accessory metals associated with "five-element" mineralization, were analyzed in fluid inclusion types 1–3 using LA-ICP-MS. Figure 2.18 shows representative transient signals obtained during routine ablations. The halogens, major and minor cations, and some metals (Cu, Ag; Figure 2.18b, h) show coincident rises and falls in signal intensity, consistent with their occurrence in the inclusions. On the other hand, many metals (Co, Ni, As, Bi, U) show enrichment in polymetallic inclusions that are accidentally trapped in quartz (Figure 2.18d) or at surface (i.e. surface contamination; Figure 2.18b, f, h). Polymetallic inclusions and surface contamination are unrelated to the actual fluid metal concentrations. Signals for metals consistent with fluid species (i.e. coincident with major and trace cation signals) were not seen in any signals, other than for Cu and Ag. Concentrations of elements in fluid inclusions (ppm), and detection limits (for concentrations < detection limits) are summarized in Table 2.10 in the Appendix.

With respect to the halogens, the average Cl concentration in type 1 fluid inclusions is 160000 ± 22400 ppm (1σ). The higher salinity type 2 and 3 inclusions have average Cl concentrations of 270000 ± 59500 and 277000 ± 29800 ppm, respectively. Molar Cl/Br ratios in type 1 and 2 fluid inclusions are variable but similar in range (average: 221 ± 146 and 244 ± 126, respectively). Type 3 inclusions have a lower, and much narrower range, in molar Cl/Br (average: 125 ± 16).

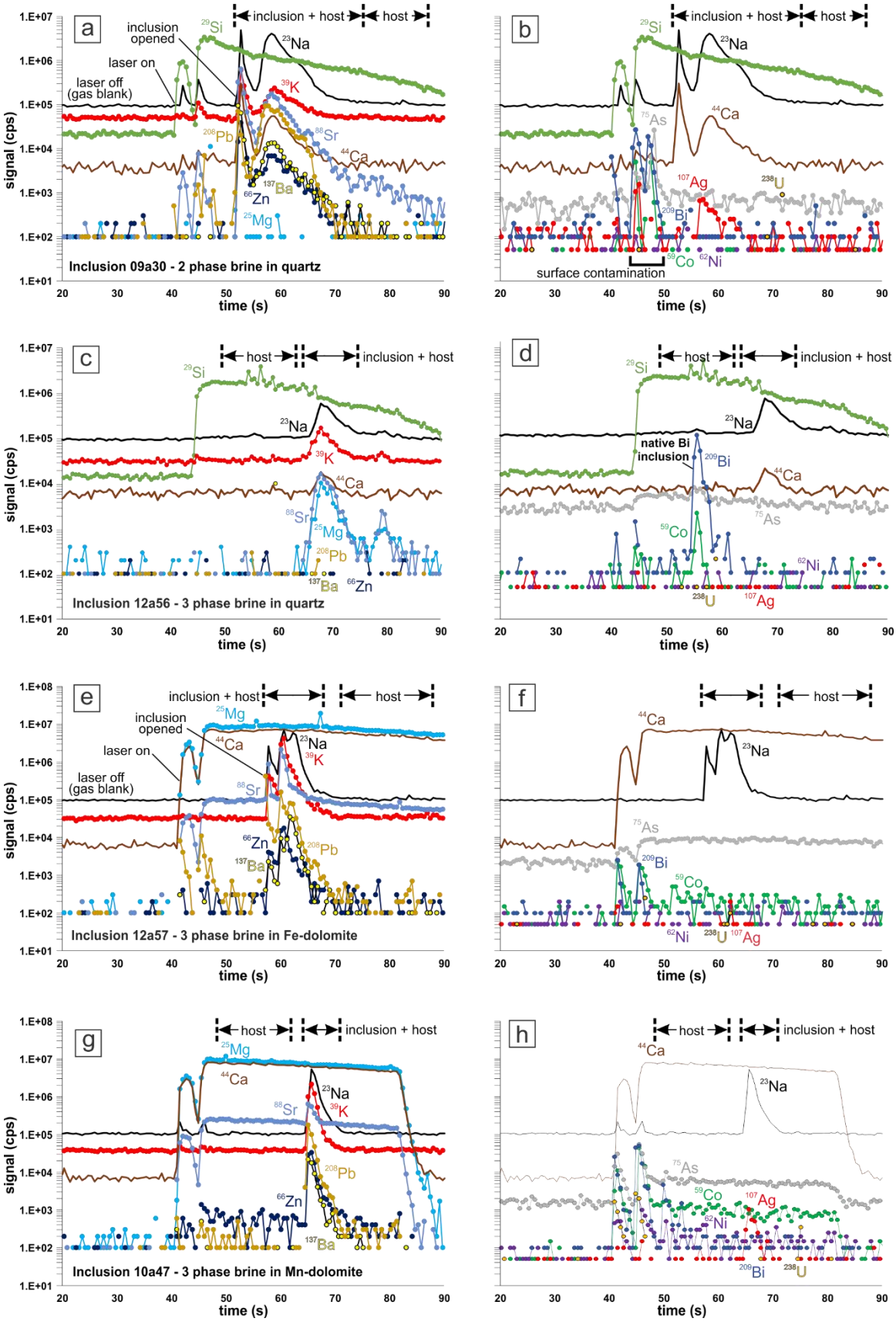
a
inclusion opened
laser on
laser off (gas blank)
inclusion + host
host
29Si
23Na
39K
208Pb
88Sr
44Ca
137Ba
66Zn
25Mg
Inclusion 09a30 - 2 phase brine in quartz
b
75As
107Ag
238U
209Bi
59Co
62Ni
surface contamination
c
host
inclusion + host
Inclusion 12a56 - 3 phase brine in quartz
d
native Bi inclusion
e
Inclusion 12a57 - 3 phase brine in Fe-dolomite
f
g
Inclusion 10a47 - 3 phase brine in Mn-dolomite
h
signal (cps)
time (s)

Figure 2.18 (previous page): LA-ICP-MS transient signals (counts per second vs. time) for ablations of quartz-and carbonate-hosted inclusions. All ablation profiles include a background interval (laser off) of ~40 s before the laser is turned on. The inclusion is reached after ~10–25 s. Duplicate profiles show different isotopes for each inclusion; Ca–Na±Si in both frames, a selection of the most abundant minor and trace cations (Mg, K, Zn, Sr, Ba, Pb) in the first frame, and selected ore metals (Co, Ni, As, Ag, Bi, U) in the second frame. Selected intervals for inclusion+host and host signal integration are also shown. **(a-b)** Transient signal for a 2-phase (L_{aq}+V) brine inclusion in quartz, with an increase in beam diameter after ~4 s of ablation. Note the surface contamination during initial ablation and beam expansion over a ~10 s period, and time-resolved, uncontaminated inclusion+host signal beginning at ~52s. With the exception of Ag showing a clear signal coincident with other cations, ore metals were not detected in the inclusion. **(c-d)** Transient signal for a 3-phase (L_{aq}+V+H) brine inclusion in quartz using a single ablation pit diameter. Note the ablation of a native Bi inclusion at ~56s, and the inclusion+host signal at ~65s with no detectable ore metals. **(e-f)** Transient signal for a 3-phase (L_{aq}+V+H) brine inclusion in Fe-dolomite, showing surface contamination by metals during initial ablation and beam diameter expansion over a ~10 s period, and time-resolved, uncontaminated inclusion+host signal beginning at ~58s. Trace U and Ag (near the limit of detection) are seen in the inclusion+host signal interval. **(g-h)** Transient signal for a 3-phase (L_{aq}+V+H) brine inclusion in Mn-dolomite, showing surface contamination by metals with initial ablation and beam diameter expansion over a ~15 s period, and time-resolved, uncontaminated inclusion+host signal beginning at ~65s. A clear Ag signal is resolved in the inclusion+host signal interval, coincident to the increase in Na count rates.

Major, minor, and trace cations routinely detected and quantified in all three fluid inclusion types are Na, Ca, K, Mg, Zn, Sr, Pb, Ba, Rb, and Cs, in decreasing order of abundance by mass (Table 2.10). Figure 2.19 shows variation in these element concentrations within, and across, FIA for fluid inclusion types 1–3. Concentrations of Mg, Ca, Mn, and Fe in the inclusions could not be quantified for carbonate-hosted inclusions due to unresolvable host phase interferences. The Ca content of type 3 inclusions, based on estimated $CaCl_2$ from T_m^{ice} and T_d^H measurements (Steele-MacInnis et al. 2011), was instead fixed as an internal standard. This model was also used to estimate the Na/Ca mass ratios in type 2 and type 3 fluid inclusions (Figure 2.20). Based on microthermometric data, type 2 fluid inclusions had higher average Ca (by mass) and lower Na/Ca ratios than type

3 inclusions. However, results from LA-ICP-MS analyses show that fluid inclusions of all types have Na/Ca > 1 (by mass, on average) but with significant variability (Na/Ca = 1.9 ± 1.6, 1.8 ± 1.2, and 1.5 ± 0.2; 1σ, for types 1, 2, and 3, respectively).

Figure 2.19 (next page): Major and minor cation concentrations (ppm) in fluid inclusions determined by LA-ICP-MS. Symbols indicate values for each inclusion in the indicated FIA. Analyses that were below detection limits are not represented. Ca and Mg could not be quantified in carbonate-hosted inclusions due to host interference. Ca content used as internal standards for type 3 fluid inclusions are provided for reference.

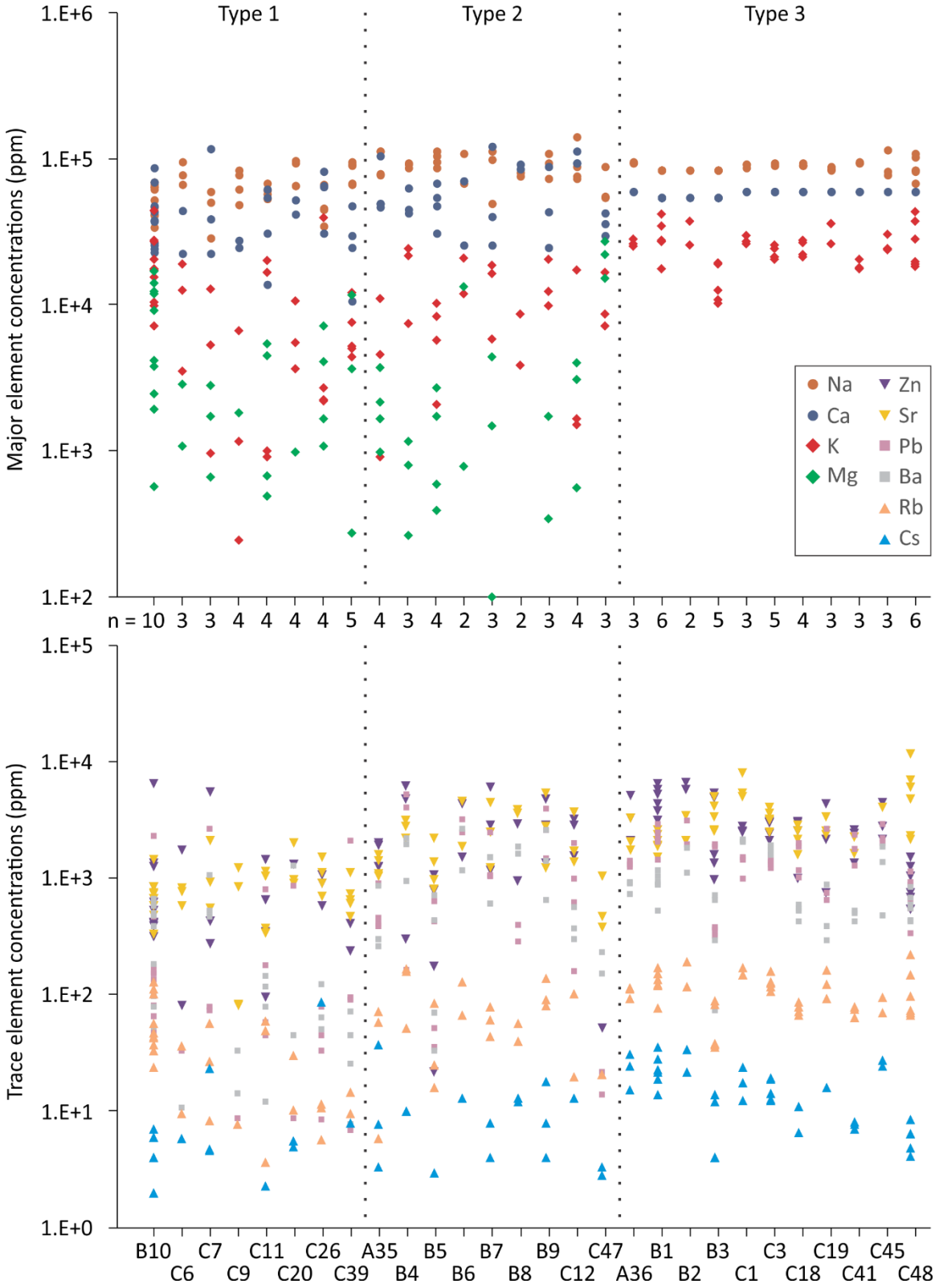
Type 1
Type 2
Type 3
Major element concentrations (ppm)
1.E+6
1.E+5
1.E+4
1.E+3
1.E+2
Na
Ca
K
Mg
Zn
Sr
Pb
Ba
Rb
Cs
n = 10 3 3 4 4 4 4 5 4 3 4 2 3 2 3 4 3 3 6 2 5 3 5 4 3 3 3 6
Trace element concentrations (ppm)
1.E+5
1.E+4
1.E+3
1.E+2
1.E+1
1.E+0
B10 C6 C7 C9 C11 C20 C26 C39 A35 B4 B5 B6 B7 B8 B9 C12 C47 A36 B1 B2 B3 C1 C3 C18 C19 C41 C45 C48

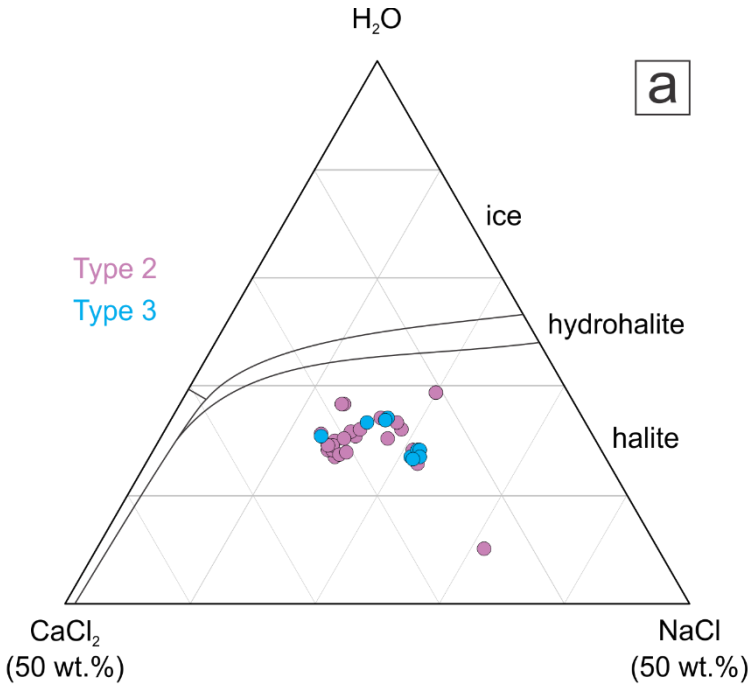
H2O
a
ice
Type 2
Type 3
hydrohalite
halite
CaCl2
(50 wt.%)
NaCl
(50 wt.%)

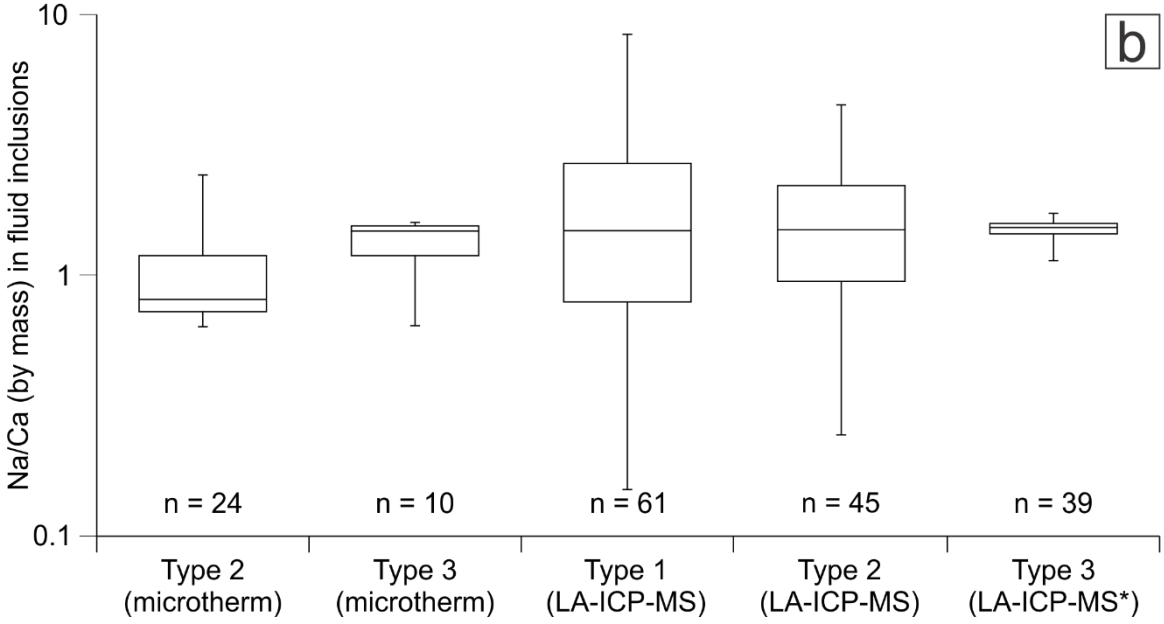
b
Na/Ca (by mass) in fluid inclusions
10
1
0.1
n = 24
n = 10
n = 61
n = 45
n = 39
Type 2
(microtherm)
Type 3
(microtherm)
Type 1
(LA-ICP-MS)
Type 2
(LA-ICP-MS)
Type 3
(LA-ICP-MS*)

Figure 2.20 (previous page): Mass ratio of dominant cations (Na/Ca) in fluid inclusions determined by microthermometry and LA-ICP-MS. **(a)** Quartz-hosted type 2 and carbonate-hosted type 3 inclusions were modeled in the H_2O-NaCl-$CaCl_2$ ternary system (Steele-MacInnis et al. 2011) using microthermometric measurements of T_m^{ice} and T_d^H. Both fluid inclusion types have NaCl ≈ $CaCl_2$. **(b)** Box and whiskers plot showing Na/Ca ratio determined from microthermometry for type 2 and 3 fluid inclusions, as shown in (a), and all fluid inclusion types analyzed with LA-ICP-MS. * Type 3 inclusions in carbonate required fixed input Ca values, due to interference from Ca in the host. Thus variability in Na/Ca for type 3 inclusions is only due to variability in measured Na values.

Metals associated with "five-element" mineralization were rarely detected in fluids (Table 2.10). Signals that included Co, Ni, As, Sb, Bi, and U were the result of surface contamination or accidentally trapped mineral grains (Figure 2.18). Figure 2.21 shows the few analyses in which these metals could be quantified in the inclusions, along with average detection limits for those metals (n = 25–33 for signals that fell below detection limits for different metals in fluid inclusions; with no surface contamination). Rare outliers are likely erroneous because they are well above the maximum concentration inferred from detection limits, while most data from the same assemblage are below detection limits. Detection limits are maximum values for true metal concentrations in the fluid inclusions. However, some FIAs of type 3 fluid inclusions had consistently detectable and quantifiable Cu and Ag concentrations in the ranges of 21–93 and 5–25 ppm, respectively. Some of these values fall below average detection limits (52.6 ppm for Cu, 10.2 ppm for Ag), which means they likely represent real values in fluids (Figures 2.19, 2.21).

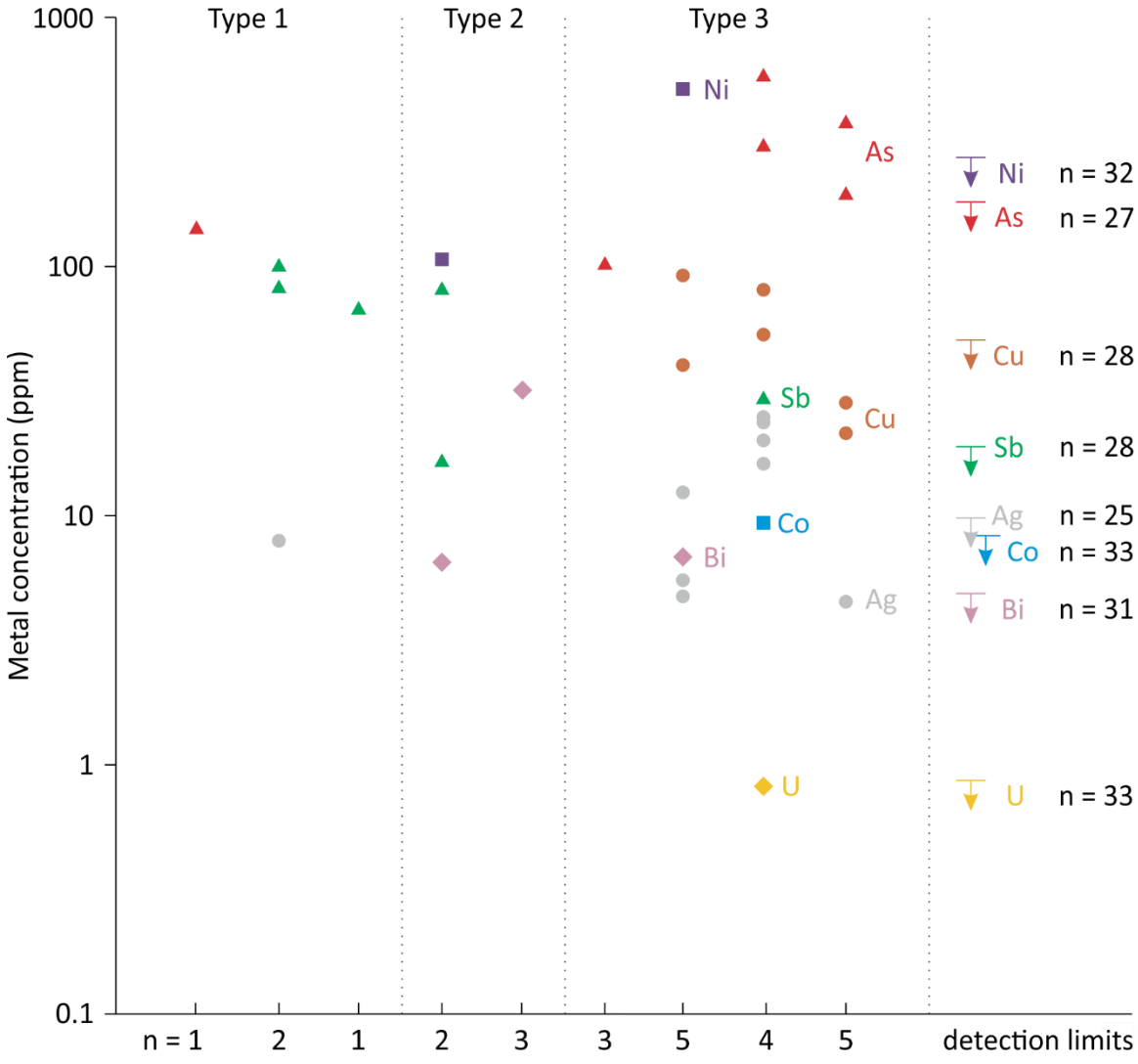

Figure 2.21: Metal concentrations (ppm) in fluid inclusions detected by LA-ICP-MS. Detection limits for each element indicate maximum values for metal concentrations. Individual analyses that fall above detection limits may represent accidentally ablated minerals or surface contamination, rather than real fluid concentrations. Some Cu and Ag values consistently analyzed in FIAs were below the average detection limits, indicating real measured values.

2.3.4 Geochronology

A total of 39 in-situ U-Pb analyses were collected from type 1 and type 2 xenotime, including four replicates. Count rates for Y and ^{204}Pb were determined for the reference standards, which helped guide the cut-off selection for sample rejection. In some signals, the most likely cause for reduced Y and elevated ^{204}Pb counts were due to the presence of uraninite, which bordered most xenotime grains, and occurred as nm-scale inclusions in xenotime. Beam spot locations were reconciled with the location of inclusion-free xenotime from petrographic imaging, and some analyses were rejected on the basis of inaccuracy in this comparison. Analyses that yielded < 9000 counts/s Y or > 1 counts/s ^{204}Pb were rejected to minimize contamination from bordering uraninite grains. In total, 16 analyses (including two replicates) were rejected from the data set. The remaining 23 analyses are recorded in Table 2.11.

Measurements were used to determine weighted average ^{207}Pb/^{206}Pb ages of 1415 ± 24 Ma and 1453 ± 35 Ma for type 1 and type 2 xenotime, respectively (1σ errors). ^{206}Pb/^{238}U ages were less consistent, ranging as low as 932 Ma, most likely due to more recent remobilization of Pb. The U-Pb data were used to generate concordia plots, which showed that both types of xenotime plot along similar discordant lines, with upper intercepts of 1428 ± 8 Ma and 1463 ± 23 Ma for type 1 and type 2 xenotime, respectively (1σ errors; Figure 2.22). An upper intercept of 1449 ± 18 Ma is determined for all xenotime plotted together. Most analyses provided concordant ages, but as previously mentioned, a few analyses plotted further down the discordant line. The opportunity to use ^{208}Pb/^{232}Th

geochronology was hindered by extremely low Th content in both type 1 and 2 xenotime (13.1 ± 1.7 ppm and 0.9 ± 0.6 ppm, respectively; 1σ errors).

Table 2.11: Geochronological data from SHRIMP analysis of xenotime.

Sample	Spot ID	U (ppm)	$^{206}Pb^*$ (ppm)	$^{207}Pb^*/^{235}U$	% error	$^{206}Pb^*/^{238}U$	% error	error coefficient
W	12366-8.1	11157	1842	2.0568	4.71	0.1702	4.68	0.9936
704	12369-2.1	13516	2154	1.9053	5.74	0.1555	5.71	0.9959
704	12369-2.2	6630	1452	3.1386	1.45	0.2534	1.38	0.9524
704	12369-2.3	6172	1201	2.8151	5.22	0.2280	5.21	0.9980
704	12369-2.4	8490	1861	2.9992	2.32	0.2413	2.31	0.9941
704	12369-2.5	5752	1178	3.0413	1.44	0.2426	1.21	0.8405
850	12370-1.2	5593	996	2.6370	2.19	0.2119	2.15	0.9827
850	12370-1.4	4257	894	3.3277	1.30	0.2595	1.16	0.8900
850	12370-1.7	5484	1042	2.8399	10.97	0.2270	10.91	0.9948
850	12370-1.8	8824	1558	2.3963	4.02	0.1927	4.01	0.9968
850	12370-1.11	3224	667	3.2474	1.48	0.2636	1.18	0.7977
850	12370-1.12	5222	1122	3.2831	3.43	0.2583	3.36	0.9788
850	12370-1.12.2	5718	1212	3.1890	3.40	0.2513	3.29	0.9678
850	12370-1.13	3881	802	3.2220	1.74	0.2582	1.69	0.9728
850	12370-2.1	4290	852	3.0397	7.12	0.2452	7.05	0.9899
850	12370-2.2	3907	584	2.3174	2.23	0.1864	1.93	0.8638
850	12370-3.1	3948	821	3.3123	4.50	0.2593	4.47	0.9942
850	12370-3.2	3563	758	3.4265	1.67	0.2682	1.61	0.9634
850	12370-3.3	5454	1170	3.2826	4.07	0.2563	4.03	0.9880
850	12370-3.3.2	5506	998	2.7347	3.96	0.2162	3.95	0.9958
850	12370-3.4	5595	1028	2.7715	19.34	0.2187	19.34	0.9997
850	12370-3.6	3545	699	3.0442	2.14	0.2487	1.17	0.5474
850	12370-3.7	5414	1199	3.4661	1.20	0.2648	1.15	0.9609

Sample	Spot ID	$^{207}Pb^*/^{206}Pb^*$	% error	$^{206}Pb^*/^{238}U$ age (Ma)	absolute error (Ma)	$^{207}Pb^*/^{206}Pb^*$ age (Ma)	absolute error (Ma)	% Discordance
W	12366-8.1	0.0877	0.53	1013	44	1375	10	28.45
704	12369-2.1	0.0889	0.52	932	49	1402	10	35.99
704	12369-2.2	0.0898	0.44	1456	18	1422	8	-2.67
704	12369-2.3	0.0895	0.33	1324	62	1416	6	7.17
704	12369-2.4	0.0901	0.25	1394	29	1428	5	2.71
704	12369-2.5	0.0909	0.78	1400	15	1445	15	3.40
850	12370-1.2	0.0903	0.41	1239	24	1431	8	14.75
850	12370-1.4	0.0930	0.59	1487	15	1488	11	0.06
850	12370-1.7	0.0907	1.11	1319	129	1441	21	9.40
850	12370-1.8	0.0902	0.32	1136	42	1430	6	22.38
850	12370-1.11	0.0894	0.89	1508	16	1412	17	-7.63
850	12370-1.12	0.0922	0.70	1481	44	1471	13	-0.76
850	12370-1.12.2	0.0920	0.86	1445	43	1468	16	1.73
850	12370-1.13	0.0905	0.40	1481	22	1436	8	-3.48
850	12370-2.1	0.0899	1.01	1414	89	1423	19	0.76
850	12370-2.2	0.0902	1.12	1102	19	1429	21	24.91
850	12370-3.1	0.0926	0.49	1486	59	1480	9	-0.45
850	12370-3.2	0.0927	0.45	1532	22	1481	8	-3.86
850	12370-3.3	0.0929	0.63	1471	53	1486	12	1.12
850	12370-3.3.2	0.0917	0.36	1262	45	1462	7	15.05
850	12370-3.4	0.0919	0.44	1275	220	1465	8	14.31
850	12370-3.6	0.0888	1.79	1432	15	1399	34	-2.58
850	12370-3.7	0.0949	0.33	1514	15	1527	6	0.89

*Samples W and 704 include type 1 xenotime. Sample 850 includes type 2 xenotime. Replicate analyses (12370-001.12.2 & 12370-003.3.2) are shown for comparison. *Values are corrected for 204Pb content. Assumed isotope ratios for common Pb correction: $^{206}Pb/^{204}Pb = 17.334$, $^{207}Pb/^{206}Pb = 0.895$, $^{208}Pb/^{206}Pb = 2.1384$.*

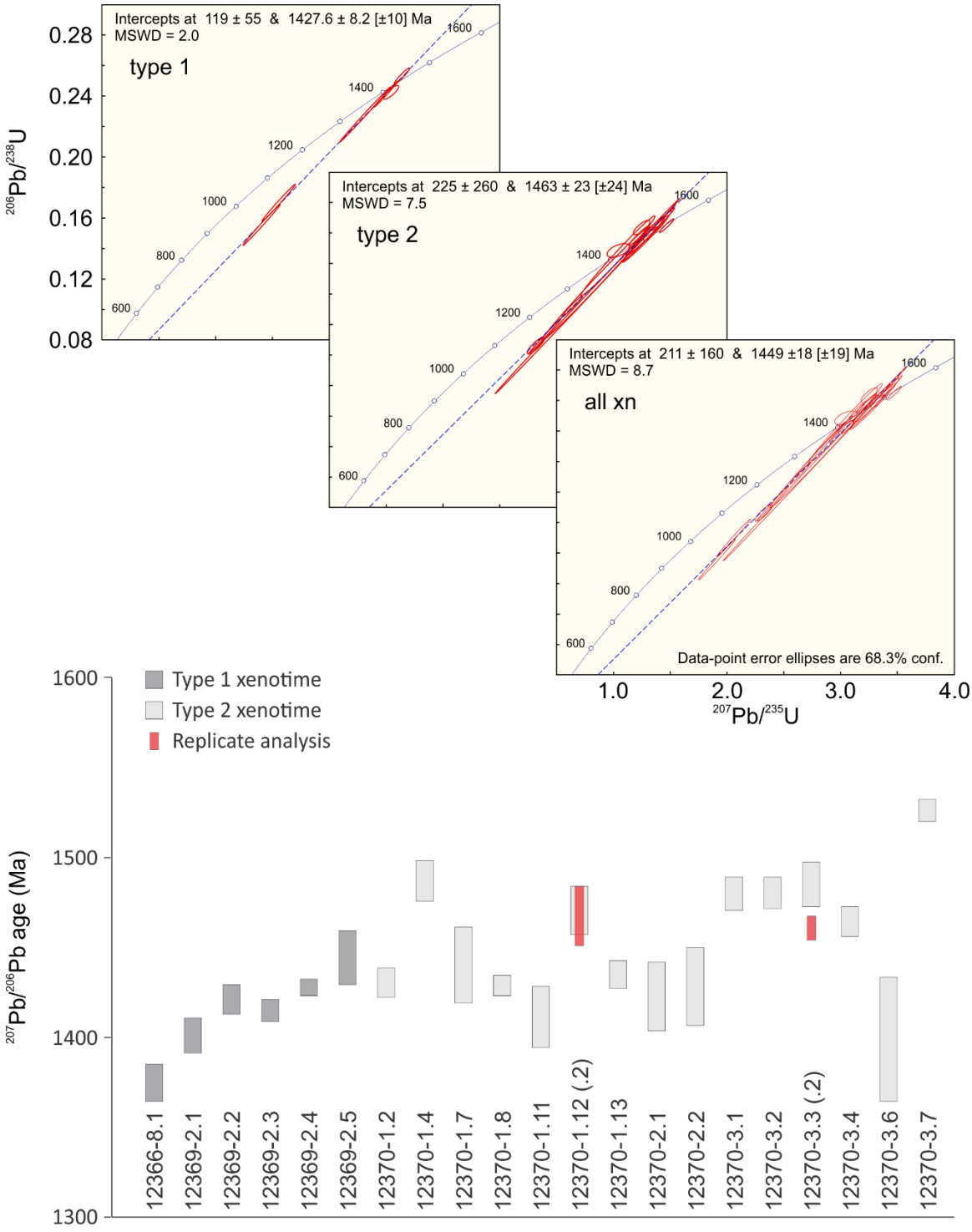

Figure 2.22: U-Pb and Pb-Pb geochronology of type 1 and 2 xenotime. Concordia plots show similar discordant lines for both types of xenotime, with upper intercepts ca. 1449 Ma. $^{207}Pb/^{206}Pb$ ages with absolute errors show more accurate ages for individual analyses.

2.4 Discussion

2.4.1 Mineral paragenesis

A revised paragenetic interpretation of mineralization stages at Eldorado was determined based on new observations from vein petrography in this study, building on detailed descriptions from previous research (e.g. Kidd and Haycock 1935; Jory 1964; Gandhi et al. 2018). A summary of the sequence of mineralization through the four main stages is presented in Figure 2.23.

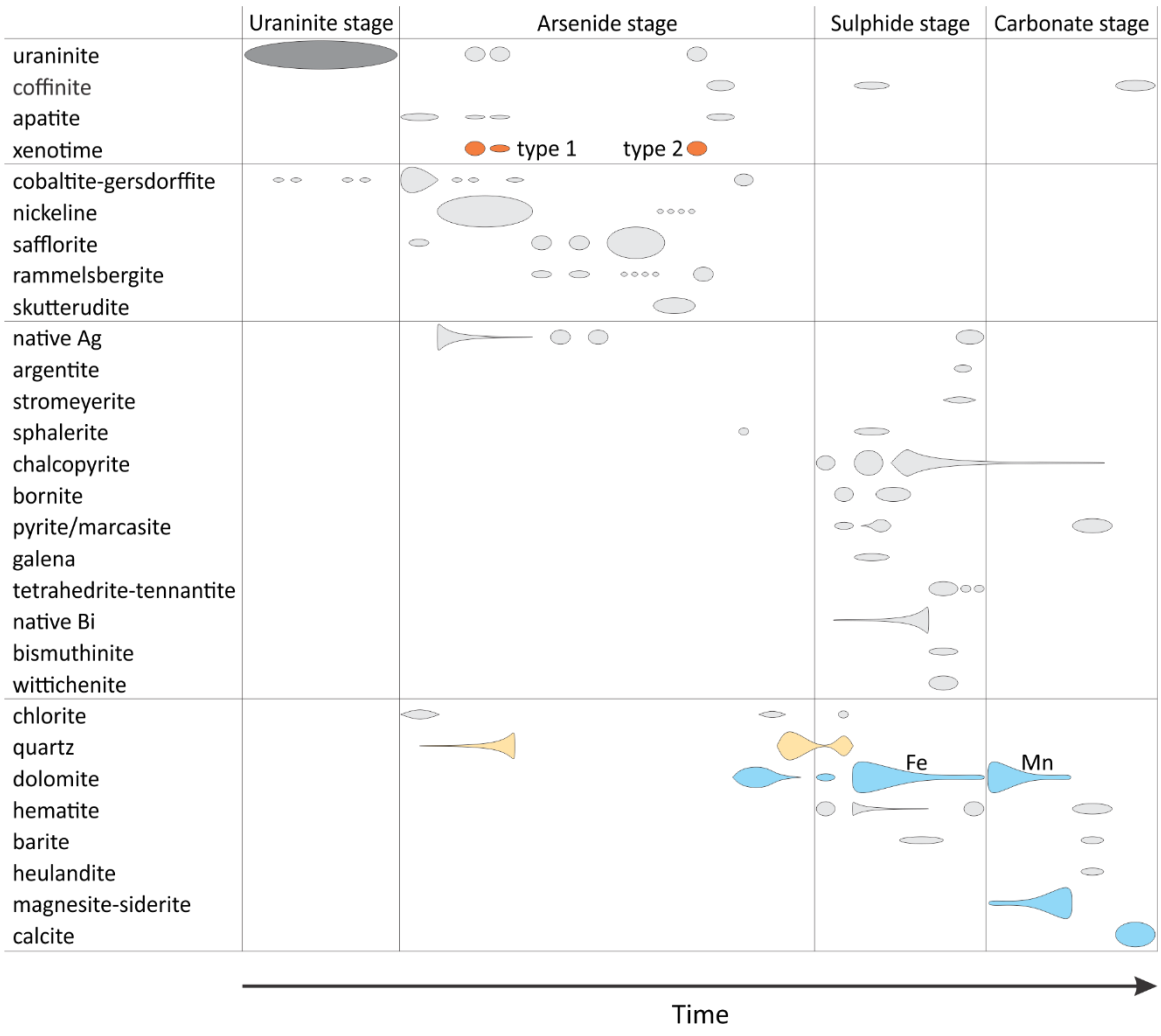

Figure 2.23: Paragenetic sequence of mineralization. The breadth of fields in the vertical direction indicates the prevalence (modal abundance) and certainty of temporal position relative to other minerals in vein assemblages. Select minerals are highlighted to emphasize the relevant timing for phases analyzed with microanalytical techniques; uraninite for SIMS O isotope analysis (dark gray); xenotime types 1 and 2 for SHRIMP U-Pb geochronology (orange); quartz for fluid inclusion microthermometry and SIMS O isotope analysis (beige); Fe-Mn dolomite for fluid inclusion microthermometry, and all carbonates for bulk O, C, and Sr isotope analysis and REE characterization (cyan).

The paragenesis is summarized in the following four main stages of mineralization:

1: The *uraninite stage* is comprised mostly of uraninite, the earliest mineral in the "five-element" paragenesis (Figure 2.23). Its botryoidal growth habit is consistent throughout the uraninite stage, and is not interrupted by any other mineral phase. Almost all minerals spatially-associated with uraninite were precipitated in fractures and dissolution spaces in uraninite during later mineralization stages. However, there is evidence that Co-Ni sulpharsenides periodically co-precipitated with uraninite within specific growth zones (Figure 2.6c, d, e, f). Specifically, these (1–10 μm) dendritic sulpharsenide inclusions are interpreted to have nucleated and crystallized on uraninite growth surfaces, becoming included in uraninite growth zones. The sulpharsenide inclusions vary significantly in relative proportions of Co and Ni across different samples, but are consistent within samples (Table 2.4). Thus, variations in local conditions seem to have dictated whether inclusions in uraninite are more compositionally akin to cobaltite or gersdorffite end-members. Similar to the observations of gersdorffite in the Wenzel deposit (Staude et al. 2007), the Fe-Co-Ni composition of these sulpharsenides do not seem to demonstrate conditions of equilibrium. Rather, periodic disequilibrium conditions with variable metal availability in the fluid may have been responsible for the observed dendritic textures and variable chemical compositions.

Eventually, the fluids in this stage became depleted in U, or conditions became unfavourable for uraninite deposition. In some samples, conditions eventually became favourae for significant uraninite dissolution and reprecipitation. Fractures perpendicular to, and concentric with, growth banding in uraninite indicate the end of the uraninite stage. These fractures are filled by minerals from later vein stages.

2: The *arsenide stage* comprises early Co-Ni sulpharsenides and gangue minerals (chlorite, quartz, and apatite), followed by a succession of arsenide minerals ± dendritic native Ag, and various accessory minerals (uraninite, xenotime, sphalerite, quartz, dolomite) (Figure 2.23). Some samples showed chloritized rims on brecciated wall-rock fragments, with open-space filling arsenide and carbonate minerals in between wall-rock fragments (Figure 2.7h; 2.8b). Cross-cutting textures indicate chlorite pre-dates arsenide mineralization, at least as a hydrothermal alteration mineral. The timing of chloritization relative to the uraninite stage, however, is unclear. Early sulpharsenides and nickeline formed rims around pre-existing uraninite grains and filled fractures therein. Sulpharsenide and nickeline rims are coeval with a network of small polycrystalline sulpharsenide grains that form around, and interstitial to grain boundaries of, open-space filling quartz and apatite (Figure 2.7c, d). This early quartz is a unique occurrence in the sample set; it was the only quartz that appears to pre-date the majority of arsenide-stage mineralization. Unfortunately, there were no suitable targets for fluid inclusion microanalysis in early quartz. Dolomite occurring between uraninite and the outer margins of sulpharsenides and nickeline represents late fracture-fill, likely incurred after a fracturing event between the arsenide and sulphide stages (Figure 2.7a).

Different arsenide-stage mineral assemblages form distinct compositional or evolutionary "branches" of the overall paragenetic sequence, similar to the paragenesis of "five-element" veins in the Jáchymov ore district (Ondruš et al. 2003). For example, Ondruš et al. (2003) described two sequences, based on the presence of the two main native elements: Ag and Bi. Several different branches were identified at Eldorado, based on

variations in mineral chemistry, ore textures, or mineral assemblages. These branches are presented throughout the following discussion.

Two branches of the arsenide stage are apparent from differences in the chemical composition of its mineral phases. In the case where cobaltite inclusions had crystallized in uraninite growth zones instead of gersdorffite, the sulpharsenide rims truncating uraninite continued to preferentially accumulate Co rather than Ni, and vice-versa. This resulted in areas of the veins dominated by one element or the other. The Co-dominated successions commonly have cobaltite rims and fracture-fill in uraninite with coeval safflorite, while Ni-dominated successions precipitated gersdorffite followed by nickeline as both rims and fracture-fill in uraninite. The distinct differences in paragenetic pathways between Co- or Ni-dominated parts of the deposit suggests similar availability of Co and Ni in the fluid as in the uraninite stage. There may have been locally variably conditions in the early arsenide stage, which led to zones of selective metal preference in sulpharsenide and arsenide deposition.

Nickeline is a major mineral in the ensuing succession of arsenide-stage mineralization. Massive, botryoidal nickeline encases uraninite and Ag dendrites, and fills the cores of other arsenide aggregates (Figure 2.7e, f; 2.9a, b). The periodic bands and disseminated single crystals of gersdorffite found throughout massive nickeline shows that gersdorffite mineralization occurred over an extended timeline, and may be interpreted as the fluctuating but waning availability of S in solution (Burisch et al. 2016; Markl et al. 2016; Scharrer et al. 2019). Nickeline also coprecipitated with the type 1 xenotime assemblage in at least two separate growth zones (Figure 2.7b, 2.8a, c, d). The inclusion and intergrowth textures of nickeline, uraninite, apatite, and xenotime in this assemblage

indicates that these minerals are coeval, and temporally constrained *within* the period of massive nickeline growth.

Native Ag dendrites are not spatially or temporally constrained with respect to uraninite, so they are interpreted to have grown independently, perhaps representing another distinct branch of paragenesis in the arsenide stage. Remnant Ag in relict dendrites overgrown by nickeline constrains the beginning of Ag growth to sometime in the early arsenide stage (Figure 2.9a, b). Native Ag growth continued throughout the arsenide stage since dendrites appear to have grown periodically with diarsenides and triarsenides (Figure 2.9c, d). The reactions required for coprecipitation of arsenide minerals and native Ag are described in detail by Markl et al. (2016). At Eldorado, native Ag precipitation was followed by safflorite or skutterudite when Co was the dominant available metal, or by nickeline and rammelsbergite when Ni was the dominant locally available metal. The conditions favouring Ag and safflorite precipitation oscillated locally before stabilizing in the arsenide stability field. Native As was not identified at Eldorado, but there is clear evidence of Ag dissolution before conditions changed to favour carbonate precipitation. Markl et al. (2016) and Scharrer et al. (2019) suggested that fluid chemistry must change quickly to produce dendritic and other open-space filling textures in "five-element" systems, and to explain the variable mineralization sequence consistent with that in veins at Eldorado.

A succession of diarsenides, consistently followed by triarsenides, grew in arsenide florets and on the rims of massive, botryoidal nickeline (Figure 2.7e, f, g). Safflorite is the dominant late arsenide mineral, and is frequently zoned, showing highly variable S and Ni contents (Figure 2.13; Table 2.4). End-member safflorite formed on the rims of arsenide

florets before, or synchronous to, blocky aggregates of inter-banded skutterudite and nickeline (Figure 2.7e). Dissolution of arsenide minerals—especially nickeline—was pervasive in all contexts. Dissolved nickeline was replaced partly by blocky rammelsbergite (Figure 2.7f; 2.10f), but was mostly replaced by quartz, dolomite, and native Bi, which indicates a significant dissolution and replacement process through the end of the arsenide stage and into the sulphide stage.

Another example of the different branches of the paragenesis occurs in the type 2 xenotime assemblage, which was only observed on the rims of nickeline florets, in association with late rammelsbergite. This assemblage has similar textural features and identical arsenide associations as the dissolved Ag dendrites enclosed in nickeline and rammelsbergite (Figure 2.8e; 2.9a, b). It is possible that the nickeline and rammelsbergite shown in Figure 2.8e once enclosed native Ag as well, but it is clear from Figure 2.9b that type 2 xenotime is not present in all assemblages, an indicator of separate branches of the paragenesis. The intergrowth textures between type 2 xenotime, nickeline, rammelsbergite, and uraninite are evidence that they are also coeval, which constrains type 2 xenotime to the period of rammelsbergite growth in the late arsenide stage. The similar intergrown textures and mineralogy of type 1 and 2 xenotime might indicate a more fundamental connection between them (i.e. akin to the occurrence of two spatially separable growth zones in nickeline, both with type 1 xenotime). There is no other textural evidence to suggest this connection, but it is worth consideration with regard to geochronological data, which is discussed in section 2.4.4.

Open space around arsenide dendrites and florets was commonly sealed with barren dolomite, and then cross-cut by BMS-bearing dolomite of the sulphide stage (Figure 2.7h).

The barren dolomite is considered to be one of the last phases in the arsenide stage. Two distinct stages of quartz formed at the end of the arsenide stage: (i) an inner zone of sugary quartz is observed in some samples around skutterudite, and (ii) large, euhedral quartz crystals grew into open space (vugs) with comb texture preserved in many samples (Figure 2.7i; 2.8a; 2.10a). Quartz also commonly grew in dissolution space throughout earlier Ag and nickeline mineralization (Figure 2.7a, b; 2.9d; 2.12c, d).

Type 1 and 2 primary fluid inclusions constrain the conditions of mineralizing fluids within the late arsenide stage of the paragenesis. Hematite, chalcopyrite, and dolomite coat outer growth surfaces of euhedral quartz crystals (Figure 2.7i; 2.10a, b). This observation illustrates the end of the arsenide stage and the beginning of the sulphide stage. The end of the arsenide stage is also identified by numerous fractures that cut through previous mineralization. These fractures are primary filled by dolomite, with minor quartz and various other sulphide stage minerals associated with dolomite (Figure 2.7h; 2.8a; 2.10a, c, d).

3: The *sulphide stage* is comprised of a complex assemblage of Fe-Cu-Zn-Ag-Pb-Bi sulphides and sulphosalts, native metals, and other accessory and gangue minerals disseminated through dolomite and filling open spaces (Figure 2.23). Euhedral quartz from the arsenide stage continued to grow for a relatively short period after the initial formation of hematite, chalcopyrite, and dolomite (Figure 2.10a, b). Hematite and chalcopyrite persisted after the end of quartz growth, in association with dolomite, which pervades fractures and open space around previous mineralization. Dolomite is also commonly

identified as a replacement mineral in dissolution space. Primary type 3 fluid inclusions constrain the conditions of mineralizing fluids within this stage of the paragenesis.

In one branch of the sulphide stage paragenesis, quartz, dolomite, and native Bi are the dominant replacement minerals (Figure 2.7e, f, g; 2.10f). Dolomite fills open space around quartz, sometimes with coeval Bi. Native Bi always appears as the latest phase in this assemblage, except for trace bismuthinite-aikinite occurring on Bi rims. Many other observed branches of the sulphide stage paragenesis do not include Bi, except as a component in wittichenite, annivite, and miharaite, which all occur with other Cu sulphides and sulphosalts (Table 4).

Chalcopyrite is the dominant early sulphide mineral and occurs throughout the sulphide stage. Bornite is also present as an early sulphide that grew in association with sulphide-stage quartz (Figure 2.10c, d). Both bornite and chalcopyrite form rims on one another in different samples of vein material and persist through most of the sulphide stage. Dolomite commonly shows partial replacement of these sulphides, quartz, and various botryoidal and dendritic aggregates from earlier mineralization stages. Minor sulphides include pyrite, galena and sphalerite, and are disseminated throughout dolomite in veins, open space infill, and in wall-rock fragments. Chalcopyrite and bornite are commonly partially replaced by wittichenite, miharaite, tennantite-tetrahedrite, stromeyerite and argentite, especially in the presence of dissolved Ag dendrites, which suggests remobilized Ag did not travel far (Figure 2.10e). Native Ag is also disseminated throughout dolomite and commonly occurs in texturally ambiguous relationships to other Ag-sulphides, suggesting coeval deposition.

4: The *late carbonate stage* is defined by a succession of carbonate minerals of various composition, replacing, and forming veins cross-cutting previous mineralization, sometimes accompanied by other gangue minerals and associated with alteration of uraninite to coffinite (Figure 2.23). This mineralization stage post-dates the sulphide stage as indicated by veins of Mn-rich dolomite, magnesite-siderite, and Mn-rich calcite cross-cutting sulphide stage mineralization (Figure 2.9b; 2.11a, b). The transition from Fe-rich to Mn-rich dolomite is an inferred indicator of the transition to the late carbonate stage because the late carbonate stage is associated with later Mn-rich calcite (Table 2.4). Open space around dolomite was sometimes filled by botryoidal to acicular radiating marcasite and hematite, and commonly filled by later Mn-rich calcite. Late hematite is also found in close textural association with barite and Ba-rich heulandite, which are thought to be coeval. Calcite is observed as the final infill stage in many samples, and is texturally coeval with coffinite.

2.4.2 Fluid temperature and pressure constraints

Microthermometry results show significant ranges in phase change temperatures for each fluid inclusion type, (Table 2.8; Figure 2.24). Total ranges in phase change temperature and S_{wt} (either from T_m^{ice} or T_d^H) are summarized below:

Type 1: T_v = 149.0–356.6 °C, S_{wt} = 19.7–24.6 wt.%

Type 2: T_d^H = 100.0–320.0 °C, T_v = 89.6–320.2 °C, S_{wt} = 31.6–37.1 wt.% (one outlier at 44.9 wt.%)

Type 3: T_d^H = 132.6–221.0 °C, T_v = 65.7–215.7 °C, S_{wt} = 32.8–36.7 wt.%

Type 4: T_v = 80.0–202.5 °C, S_{wt} = 23.4 wt.% (n = 1)

Individual FIA, generally show much narrower ranges in these parameters. With respect to T_d^H (and corresponding salinity), there is no evidence that halite was a saturated phase that could be accidentally trapped during primary fluid entrapment. Variability in T_d^H at constant T_v could arise in fluid inclusions that experienced necking down after cooling below the halite liquidus; necked fluid inclusions would show a highly variable H volume within single FIA (Becker et al. 2008). However, only a few FIA showed this (e.g., FIA B12; Figure 2.24). Considerable variation in T_v at constant T_d^H is also apparent (Figure 2.25a), and may be the result of post-entrapment stretching or leakage (Becker et al. 2008). The effects of post-entrapment modification on fluid inclusion types 1–3 can be seen in the rare, anomalously wide intra-assemblage ranges in microthermometric data (e.g. FIA A14, A22, A27; Figure 2.24). However, variations in temperature are rarely so broad in individual FIAs, and salinity variations are even less extreme (Table 2.9; Figure 2.24). Typical intra-assemblage ranges in T_v or T_d^H are ~20–40 °C, whereas intra-assemblage S_{wt} ranges are typically no more than a few wt.% eq.

Figure 2.24 (next page): Comparison of phase change temperatures and salinity for FIAs. Bulk salinity (wt.% NaCl + $CaCl_2$ eq.) and T_v are shown for assemblages of fluid inclusion types 1–4, while T_d^H and dominant salt concentrations (wt.% NaCl and wt.% $CaCl_2$) are only shown for assemblages of fluid inclusions 3 and 4. Salt proportions were determined according to Steele-MacInnis et al. (2011). Some FIA had fewer measurements for a particular property in individual fluid inclusions than the total number of analyzed fluid inclusions (n); e.g. FIA A19 only produced one measurement of T_d^H out of four analyzed inclusions.

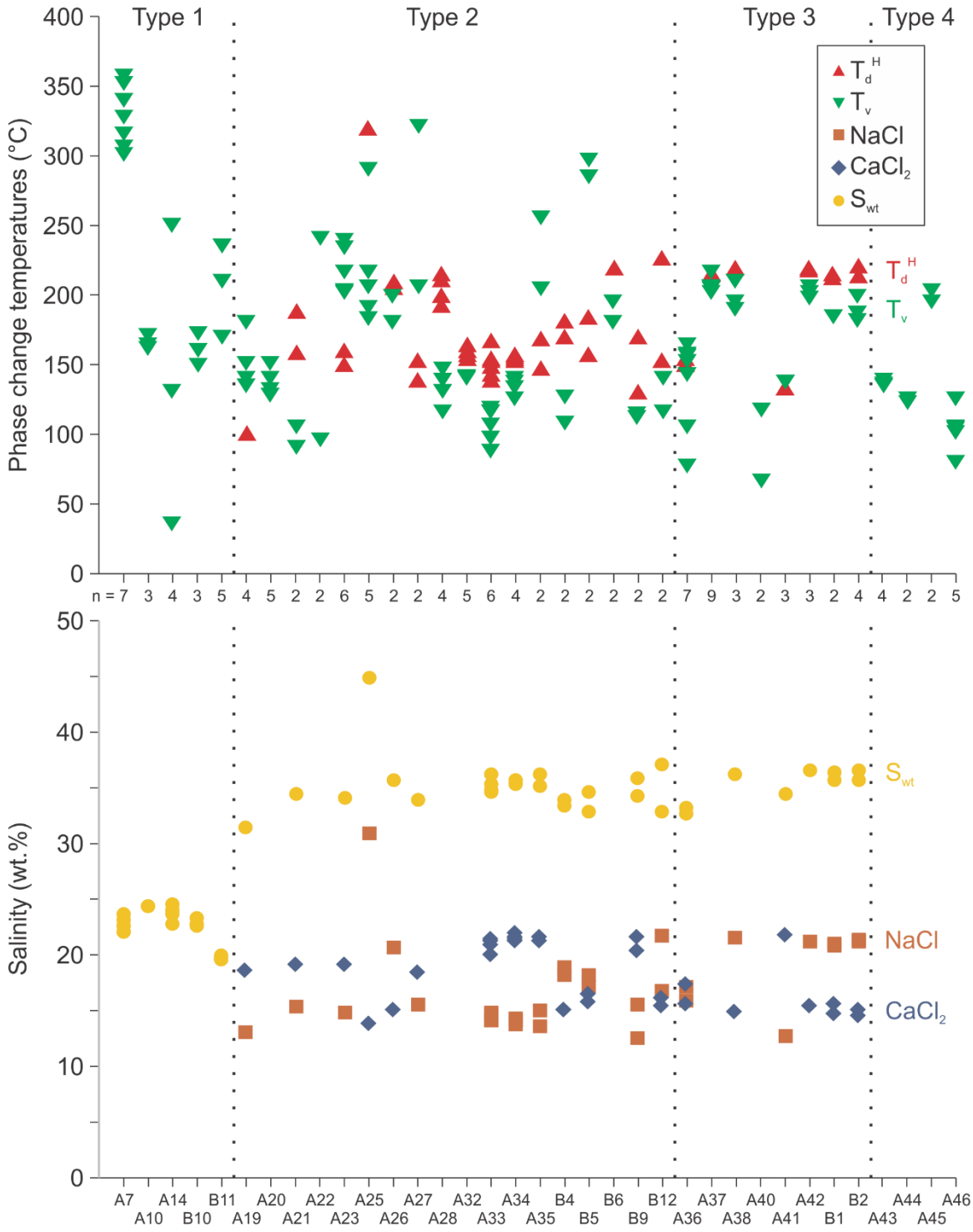
Type 1
Type 2
Type 3
Type 4
Phase change temperatures (°C)
400
350
300
250
200
150
100
50
0
T_d^H
T_v
NaCl
$CaCl_2$
S_{wt}
n = 7 3 4 3 5 4 5 2 2 6 5 2 2 4 5 6 4 2 2 2 2 2 2 7 9 3 2 3 3 2 4 4 2 2 5
Salinity (wt.%)
50
40
30
20
10
0
A7 A10 A14 B10 B11 A19 A20 A21 A22 A23 A25 A26 A27 A28 A32 A33 A34 A35 B4 B5 B6 B9 B12 A36 A37 A38 A40 A41 A42 B1 B2 A43 A44 A45 A46

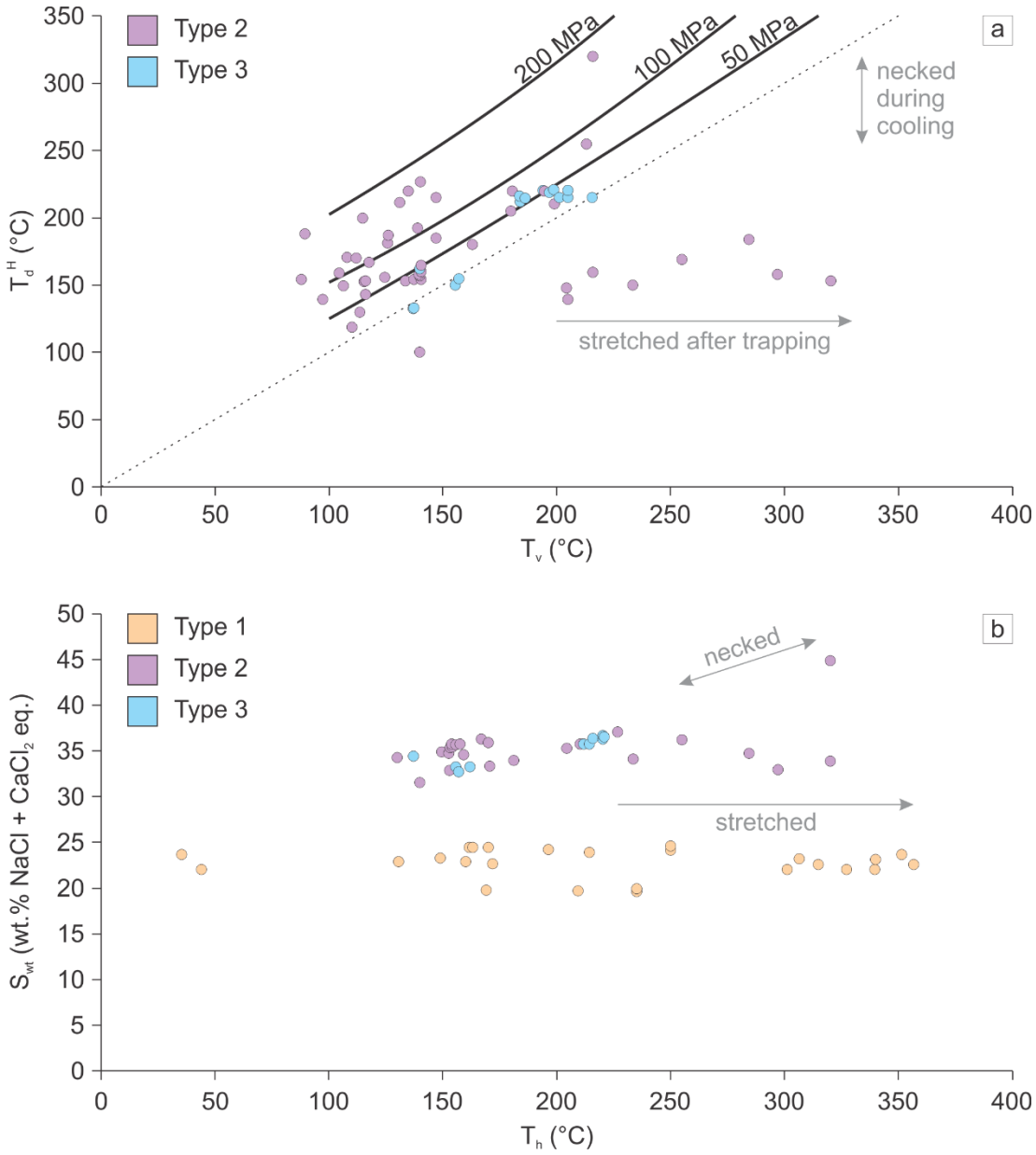

Figure 2.25: **Comparison of phase change temperatures and salinity for fluid inclusion types 1–3. a)** Scatter plot of T_d^H and T_v for fluid inclusion types 2 and 3 showing trends for post-entrapment modification of stretched or necked inclusions, and minimum P_{tr} estimation for inclusions that homogenize by halite dissolution (Lecumberri-Sanchez et al. 2012; Steele-MacInnis et al. 2012). Most inclusions of both types have $T_d^H > T_v$ (plot above the dashed line); most inclusions cluster along the 50 MPa curve; significant variation (0–200 MPa) might be influenced by variable halite content in necked inclusions. Evidence of post-entrapment stretching is most noticeable in type 2 fluid inclusions that plot below the dashed line. **b)** Scatterplot of S_{wt} and T_h for fluid inclusion types 1–3 showing possible trends for post-entrapment modification of stretched or necked inclusions. Salinity ranges are consistent for types 2 and 3, and distinct from type 1. The positive correlation between S_{wt} and T_h for types 2 and 3 may arise in necked inclusions due to $S_{wt} \propto T_d^H$, where $T_h = T_d^H$ in most type 2 and 3 fluid inclusions.

Individual FIA with tight intra-assemblage T_v and T_d^H values show significant inter-assemblage variation (Figure 2.24). This real variation, not due to post-entrapment modifications, shows fluctuations in the T_h (minimum T_{tr}; from T_v or T_d^H) of 150–350 °C for type 1 inclusions and 75–300 °C type 2 inclusions. Narrower ranges in inter-FIA T_h values are observed for types 3 and 4 inclusions (100–225 °C and 75–200 °C, respectively). This amount of inter-FIA variability is striking for FIAs within the same host grains of quartz or dolomite, from one healed fracture to another, or one growth zone to another.

If the inter-assemblage variability in T_h represents real variability during entrapment, and is not a product of post-entrapment modification, then there must have been a correspondingly wide variability in trapping pressure (P_{tr}) and/or temperature (T_{tr}) during mineralization. Using the models of Becker et al. (2008), Lecumberri-Sanchez et al. (2012) and Steele-MacInnis et al. (2012), the value of T_d^H (when = T_h) provides a minimum constraint on P_{tr} for type 2 and 3 fluid inclusions. Figure 2.25a shows the distribution of microthermometry data and empirically-based isobars for minimum P_{tr} estimation. Variability in the minimum P_{tr} may reflect post-entrapment modification if the array of data for an FIA or inclusion type crosses the isobars, whereas the best estimates of P_{tr} (with no post-entrapment influence) made by this graphical method (and numerical model; Steele-MacInnis et al. 2012) are for those FIA or inclusion type that cluster on or lie along an isobar. Fluid inclusions that plot at higher pressures in Figure 2.25a belong to FIAs that show significant variability in T_d^H, making them unreliable for estimations of minimum P_{tr} by this method. The most reliable estimate for minimum P_{tr} in type 2 fluid inclusions is 175 MPa (from FIA A28). This is a realistic estimate of minimum P (~ 6.5 km lithostatic); the overburden thickness for the entire Hornby Bay Basin that would have been overlying

the deposit at the time of mineralization is estimated to be < 10 km, and may have been closer to 5 km (Bowring and Ross 1984; Gandhi et al. 2018; Skulski et al. 2018). It is not known how much higher the true P_{tr} and T_{tr} were relative to these minimum estimates and the additional thickness of crystalline basement below the basin rocks is not known. Isochore fields for types 1–3 fluid inclusions are plotted with estimated trapping conditions in Figure 2.26. Trapping conditions for type 1 fluid inclusions could not be constrained using isochore fields as no secondary constraint on T_{tr} or P_{tr} is available, aside from the P approximations above.

The inter-assemblage variability in trapping conditions may be related to some combination of three processes: (i) mixing of two fluids of different T during mineralization; (ii) large fluctuations in T with time, owing to a heat source other than the regional geothermal gradient; and (iii) fluctuations in P related to alternations between ~lithostatic and ~hydrostatic conditions (i.e., during fault movement if mineralization was synkinematic). With respect to a mixing hypothesis, the distinct gap in S_{wt} between type 1 and types 2 and 3 inclusions is not bridged in such a way that suggests simple mixing of fluids with different salinities, and no correlation between S_{wt} and T_h is apparent for any inclusion type (Figure 2.25b). Mixing of two fluids with substantially different T but ~identical S_{wt} is possible, however, and is discussed below.

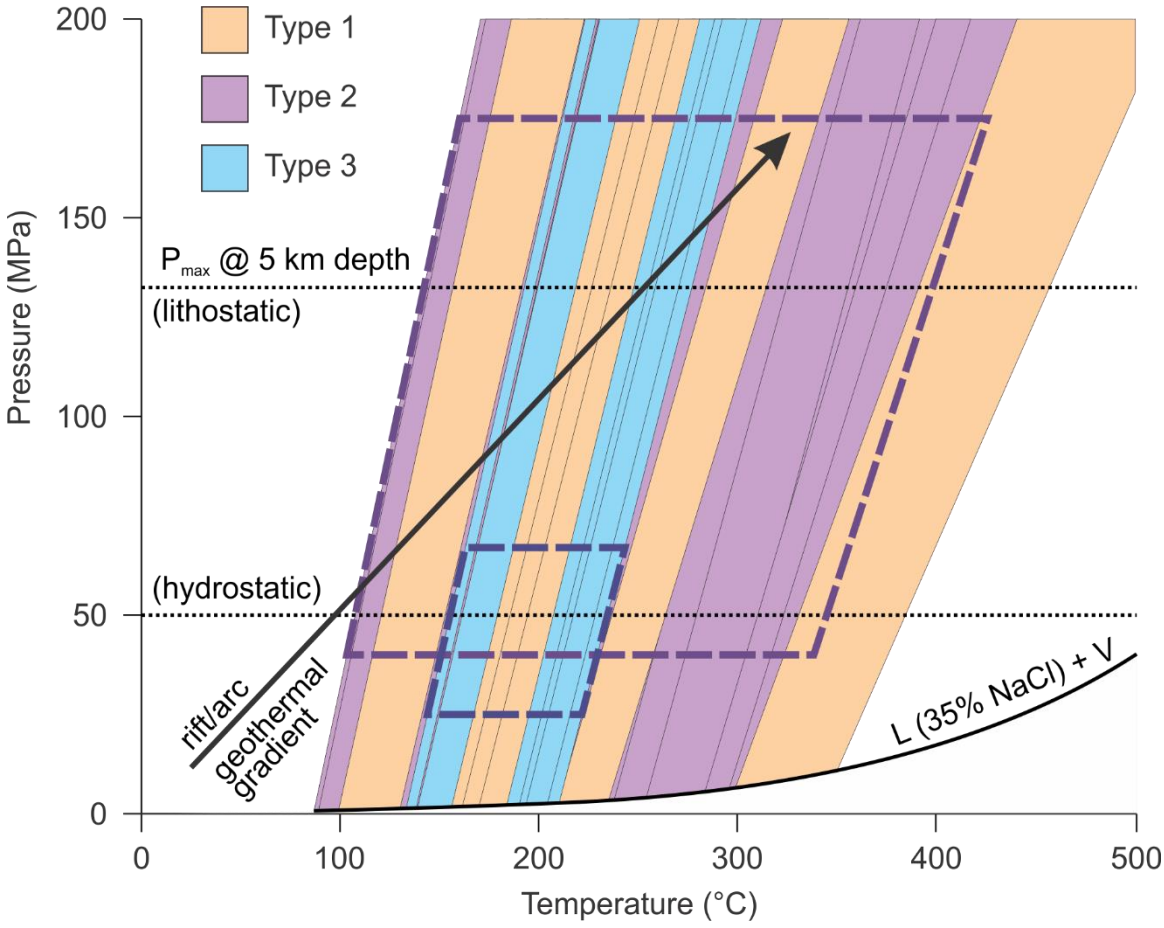

Figure 2.26: Isochore fields for type 1 and 2 fluid inclusions in late arsenide stage quartz, and type 3 fluid inclusions in sulphide stage dolomite. Isochore fields were generated from microthermometric measurements of T_m^{ice} and T_v. The liquid-vapour curve shown is for a 35 wt.% NaCl eq. fluid (Bodnar 1994; Bodnar 2003). Further suggested constraints for entrapment conditions include an estimated 5 km burial depth (Gandhi et al. 2018) beneath the overlying Hornby Bay Basin ca. 1440 Ma. The dashed outlines represents the field of entrapment conditions constrained from the model of Steele-MacInnis et al. (2012) for fluid inclusion types 2 and 3. The high geothermal gradient of an arc or rift setting (50 °C/km; Robinson and Morton 1972) is also shown for reference.

With respect to anomalous heat sources, it unlikely some local heat source contributed to fluids periodically unless there was a substantial time gap between FIA entrapment showing large inter-assemblage variability in T_h; all known igneous intrusions in the region are >100 Ma older or younger than mineralization. Lacking an external heat source, T was likely not significantly higher than minimum T_{tr} since regional lithologies were only metamorphosed to zeolite–lower greenschist facies (Robinson and Morton 1972; Robinson and Ohmoto 1973).

The third process, pressure fluctuation, is the most likely explanation for inter-assemblage variability in trapping conditions. Significant pressure fluctuations may have occurred during repeated movements/reactivation of mineralized faults. Local faults have inferred displacements on the order of 4–16 km (Hayward and Corriveau 2014). Small scale evidence of repeated fault movement is apparent from brecciation textures in the ore and gangue veins at Eldorado. The estimated thickness of the Hornby Bay Basin suggests that depths of formation could be 5 km or more at the time of mineralization (Bowring and Ross 1984; Gandhi et al. 2018). Large pressure changes may reflect fluctuations in confining load (between hydrostatic and lithostatic conditions) during movement of basement- and basin-hosted faults. Open-space filling textures show that ~hydrostatic fluid conditions existed at times during mineralization. Periodically open fault structures might have also assisted with sourcing fluids that could contribute to temperature fluctuations. As an example, colder fluids from the overlying Hornby Bay Basin migrating down faults into the basement hydrothermal system would possibly mix with already T-equilibrated fluids that had been derived from the same basin source, leading to some of the variation see for inclusion types in Figure 2.25b.

Trapping fields for fluid inclusion types 2 and 3 are significantly different (Figure 2.26). Since these fluid inclusions represent fluids from late arsenide stage quartz and sulphide stage carbonate, respectively, these differences in ranges of trapping conditions may indicate real physical changes during the evolution of "five-element" mineralization. For example, at 5 km depth, type 2 fluid inclusions from the arsenide stage may have been trapped throughout a wide range of pressures during fluctuations from lithostatic to hydrostatic conditions. Then, during the sulphide stage, type 3 fluid inclusions may have formed exclusively in open-space filling carbonates at ~hydrostatic conditions. Rapid variations in both P and T are likely throughout mineralization; these conditions are conducive to the various disequilibrium textures identified throughout the paragenesis (e.g. concentric growth zones, dissolution and reprecipitation, dendritic and open-space filling crystals). There was no evidence of boiling identified in this study, which is consistent with hypersaline brines up to 350 °C at moderate depths with P_{tr} > 20 MPa (Bodnar 1994; Bodnar 2003).

Stable O isotope data provides additional insight into the fluid P-T history of the Eldorado veins. Oxygen isotope data in quartz showed a slight decrease from $\delta^{18}O^{qz}_{VSMOW}$ = 17.2 ± 1.1 ‰ in early quartz associated with sulpharsenides to $\delta^{18}O^{qz}_{VSMOW}$ = 15.4 ± 1.3 ‰ in quartz associated with the late-arsenide-, sulphide- and late carbonate-stages. Values showed little variation in the later mineralization stages. A decrease in $\delta^{18}O^{qz}_{VSMOW}$ indicates the fluid T was increasing through this part of mineralization (a decrease of 1.8 ‰ in quartz could be accommodated by an increase of up to 100 °C at constant $\delta^{18}O^{fluid}_{VSMOW}$), or there was an incursion of an isotopically lighter fluid. The range in T_h of 75–300 °C for type 2 fluid inclusions in late arsenide- and sulphide-stage quartz gives a

wide range of $\delta^{18}O^{fluid}_{VSMOW}$ = -9.9–8.4 ‰ during those stages of mineralization. If T was actually varying so widely, it would be unlikely to produce such consistent values of $\delta^{18}O^{qz}_{VSMOW}$ as seen in quartz from the late arsenide and subsequent mineralization stages. Carbonate O isotope values were also consistent through the late arsenide to late carbonate stage ($\delta^{18}O_{VSMOW}$ = 16.0 ± 2.9 ‰). The range in T_h of 100–225 °C for type 3 fluid inclusions in sulphide- and late carbonate-stage carbonate gives a range of $\delta^{18}O^{fluid}_{VSMOW}$ = -2.5–8.4 ‰.

Constant $\delta^{18}O$ values across many variants of quartz is consistent with (i) limited variation in T and (ii) no mixing with another aqueous fluid phase. These data are not influenced by P, which has already been identified as a likely variable property during mineralization. Considerable variations in P could accommodate most of the variability in T_h data in fluid inclusions. However, very high T_h (300+ °C) must also be related to fluctuations to higher T, because the maximum P is limited to the extent of overburden from both basement rocks and the Hornby Bay Basin up to, and including part of, the Dismal Lakes Group. This succession of overburden could not have been much more that 5 km thick.

2.4.3 Fluid pH and fO_2 constraints

Eldorado fluid inclusions have a significant salt component from $CaCl_2$; Na/Ca ratios ~2 (Figure 2.20a, b). $CaCl_2$ is also considered a major component in “five-element” fluids in the Cobalt district, accounting for up to 50% of dissolved salts (Kerrich et al. 1986). Kerrich et al. (1986) recorded a broad range of salinities and temperatures from fluid

inclusions in both quartz and carbonate in the Cobalt district. The most striking feature of these fluids is their extremely high salinites, averaging around 34 wt.% NaCl equivalent. Marshall and Watkinson (2000) suggested that Ag was likely transported in Cl complexes in a Cl-rich and S-poor brine. Fluid reduction may have enhanced mineralization via interaction with S-Co-Ni-As minerals in the underlying Archean basement rocks (Marshall and Watkinson 2000). The same mechanisms of transport and deposition may also be relevant at Eldorado. Further constraints on chemical conditions such as pH and fO_2 are discussed in the ensuing paragraphs in order to explain the evolution of fluids required to produce the full paragenetic sequence of mineralization, observed at Eldorado.

Numerous styles of mineralization aside from the Eldorado "five-element" veins are found near Port Radium including pyrite dominated assemblages, magnetite-actinolite-apatite veins, and giant quartz veins with associated hematite (Jory 1964; Robinson and Ohmoto 1973; Mumin et al. 2007; Gandhi et al. 2018). The giant quartz veins are most spatially and temporally constrained with respect to "five-element" mineralization; they occur within the same fault structures and predate the uraninite stage mineralization (Jory 1964). The presence of hematite in these fault structures prior to ore mineralization provides a potential constraint on fO_2, at least if fO_2 was internally buffered. Mumin et al. (2007) discussed the association of quartz-hematite veins and propylitic alteration in the distal regions of an IOCG setting. The IOCG mineralization is synmagmatic, making them much older than the Eldorado "five-element" mineralization ca. 1440 Ma (Mumin et al. 2007; Montreuil et al. 2016b; Gandhi et al. 2018). However, Eldorado veins also show a similar propylitic alteration assemblage (Jory 1964), so the temporal connection between the early hematite and uraninite stage mineralization is not fully defined.

Clay minerals were identified in an early alteration assemblage at Eldorado, often around uraninite veins, but there is no specific correlation with uraninite-stage mineralization (Campbell 1955). Jory (1964) claimed that early alteration assemblages may be confused with earlier retrograde metamorphic assemblages and that some of the previously identified clay minerals were actually white micas, which constituted an incomplete phyllic alteration assemblage. Either way, the early assemblage of alteration minerals seems to indicate the presence of weakly acidic fluids (Jory 1964; Smith et al. 2017). White micas and sparse clay minerals are ubiquitously overprinted by alteration assemblages of chlorite and carbonate; which resemble a propylitic assemblage (Campbell 1955; Jory 1964; Bastravok et al. 2010). Chloritization is mostly associated with late arsenide-stage mineralization, while carbonatization is associated with the sulphide- and carbonate-stage mineralization. When buffered by alkaline rocks, these alteration assemblages often results in neutral pH fluids; around 6 or higher (Pirajno 2009; Bastravok et al. 2010; Smith et al. 2017). This model of ore fluids being neutralized by wall-rocks assumes an initially acidic fluid, and is most effective at low fluid/rock ratios. The overall extent of wall-rock alteration varies from a few centimetres to several metres in brecciated zones (Campbell 1955).

Mineralization of the “five-element” suite began with coprecipitation of uraninite and trace sulpharsenides, which demonstrates decreasing solubility of these metals and fluctuating stability of sulpharsenides. This is also important evidence that U was transported in the same solution as many of the important “five-element” components, namely S, Co, Ni, and As. Temperature of mineralization is believed to have been relatively stable throughout the mineralization history, and although pressure is not well-constrained,

it is not a significant factor in determining U solubility (Romberger 1984). Markl et al. (2016) described the conditions required to precipitate arsenide minerals from an oxidizing fluid, and entertained the possibility of fluctuating conditions or locally variable pH to explain the disequilibrium textures associated with "five-element" ore minerals. In general, a reduction in fO_2 or an increase in pH is necessary for arsenide precipitation. Conditions for sulpharsenide precipitation are not well constrained, but considering the activity of S to be the only discriminating factor, the same relative change in these parameters should apply to sulpharsenide precipitation. Staude et al. (2007) suggested multiple pulses of fluid injection as a possible mechanism for the cyclical stability of arsenide minerals inferred from this type of zonation in "five-element" veins.

Uranium is generally soluble as U^{6+} and insoluble in the reduced oxidation state U^{4+} at low T (Romberger 1984; Cumberland et al. 2016; Timofeev et al. 2018). Thus, reduction of an oxidizing fluid is an effective way to precipitate U out of solution (Timofeev 2018). Uraninite and coffinite are common products of insoluble U^{4+}, found throughout the Eldorado deposit and many other reduced U environments (Bastravok et al. 2010). Soluble U can occur in numerous hydroxide, sulphate, carbonate, phosphate, chloride, and fluoride complexes. The stability of these complexes are controlled by the activity of their constituents and the local fluid conditions (Romberger 1984; Bastravok et al. 2010). At 200 °C, fluoride and phosphate complexes are dominant in slightly acidic to neutral conditions (Romberger 1984). Chloride and hydroxide complexes are generally dominant in extremely acidic and basic conditions, respectively (Bastravok et al. 2010).

The activity of various complexing components is critical, and especially relevant to the uraninite stage at Eldorado, which is associated with hydrothermal apatite (Campbell

1955), and the arsenide stage, which has assemblages of uraninite in association with xenotime and apatite. Precipitation of these phosphate minerals would directly reduce the activity of the phosphate anion in solution, which could change the stability of associated U complexes in neutral pH fluid. The extremely high salinity and analyzed Cl content of 28 ± 3 wt.% in type 2 and 3 fluid inclusions suggests that chloride complexes may have also been important for U transport at Eldorado. Bastravok et al. (2010) showed that highly saline fluids tend to form U-Cl complexes at reducing or very acidic conditions, at least around 100 °C. Timofeev (2018) confirmed the positive correlation between Cl activity and U solubility for reducing fluids at low pH, for temperatures up to 350 °C. As such, a neutralizing reaction is another effective method of precipitating U out of an acidic solution.

Richard et al. (2012) discussed the conditions and mechanisms relevant to U precipitation in the Athabasca Basin, many characteristics of which are analogous the present model at Eldorado. Fluids that percolated down through the basin were highly saline (up to 35 wt.% NaCl equivalent), and thought to be derived from evaporated seawater. Fluid inclusion analysis revealed formation temperatures up to 200 °C and U contents up to 2×10^{-3} mol/L, which is orders of magnitude greater than most crustal fluids (Richard 2012). The conditions for solubility of such vast quantities of U in a Cl-rich brine would require a low pH; ~2.5–4.5. Near-surface oxidation of sulphides was proposed as a mechanism for the desired acidification of seawater (Richard 2012). If uraninite precipitation at Eldorado occurred due to neutralization of a similarly acidic fluid, then the solubility of U would easily be reduced to concentrations observed in arsenide-stage fluids (concentrations below detection limits of 0.2 ppm; ~10^{-6} mol/L).

Considering early fluid conditions to be slightly acidic and conducive to hematite stability, the most effective change in conditions to precipitate uraninite and arsenide minerals would be to neutralize the potentially acidic fluid and/or reduce fO_2. After the uraninite stage, arsenide minerals dominate the mineralization succession. Markl et al. (2016) demonstrated how changes in pH and fO_2 could produce different assemblages of arsenide minerals with native Ag at 200 °C and 50 MPa. With similar conditions at Eldorado, the pH must be at least neutral (6 or higher) to begin precipitating Ag dendrites before arsenide minerals. A drop in fO_2 would allow Ag to precipitate before being enclosed by safflorite, rammelsbergie, or skutterudite. The observed dissolution of Ag, and relatively retained stability of arsenide minerals, would then require a significant reduction in pH. However, there is just as much evidence of arsenide dissolution, such that a simple reoxidation of the fluid could explain the remobilization of both Ag and arsenide minerals near the end of the arsenide stage. Type 2 fluid inclusions in quartz constrain the temperature and pressure at this point in the paragenesis. Also, the concurrent precipitation of chlorite, both in the veins and as a wall-rock alteration product is a clear indicator of fluid-rock interaction and pH neutralization taking place in the system.

The sulphide stage is characterized by pervasive veins of dolomite, hematite, and various sulphides with associated host-rock alteration. Type 3 fluid inclusions in carbonate from this stage were found to homogenize around 200 °C. Carbonate precipitation is dramatically favoured by an increase in pH to more alkaline conditions (Staude et al. 2007; Markl et al. 2016). Sulphide-stage carbonates also replace pre-existing Ag and arsenide dendrites, which requires an increase in oxygen fugacity, and would be consistent with the precipitation of hematite. The coprecipitation of carbonates, hematite, and chalcopyrite,

along with the cyclical relationship between chalcopyrite and bornite mineralization can be used to further restrict the known constraints on fluid conditions for the sulphide stage. At fluid conditions of around 200 °C, these minerals may all precipitate around log fO_2 = -36 and pH = 6 (Thiersch 1997). At the end of the sulphide stage, native Ag reprecipitates with Ag-rich sulphides and sulphosalts. This would also benefit from a change to alkaline conditions (Markl et al. 2016). At the same time, quartz solubility is increasingly pH-dependant above neutral conditions; it becomes very soluble when pH increases to around 8 or beyond at 200 °C (Staude et al. 2007). Thus, the intermittent dissolution of quartz is consistent with precipitation of carbonates and Ag during the sulphide stage. Also, increased activity of dissolved silica in solution causes coffinite to precipitate preferentially over uraninite, especially at high salinities (Bastravok et al. 2010). This is again consistent with the observations of uraninite remobilization and alteration to coffinite in late carbonate veins.

The latest stages of mineralization include calcite, barite, and zeolites such as heulandite. As with previous carbonate mineralization, calcite precipitation is strongly encouraged by an increase in pH. This could arise due to a further increase beyond that at which dolomite precipitation began, or a change in the relative reduction in the activity of Mg in solution. Concentrations of the relevant cations were not quantifiable by LA-ICP-MS in Type 3 fluid inclusions due to the overwhelming signal from Mg and Ca in the host dolomite. There were no fluid inclusion analyses in calcite for comparison anyway, but it would have been beneficial to see if there was a difference in Mg content between fluids in these two carbonates.

As some of the last minerals associated with the "five-element" paragenesis, barite and heulandite may help constrain final conditions before mineralization stopped. Precipitation of barite requires dissolved S as sulphate, which must have been oxidized since the previous mineralization stage was dominated by sulphides. Heulandite simply helps constrain final fluid conditions within the low pressure, and low temperature realm of epithermal settings; generally below 300 °C and 200 MPa. Despite the uncertainty of exact P, T, pH, and fO_2 conditions, the relative stability fields of minerals and aqueous phases will be generally consistent (Romberger 1984). Thus, relative changes in pH and fO_2 can still be defined semi-quantitatively.

2.4.4 Revised geochronology of the Eldorado deposit

2.4.4.1 Xenotime ages and U-Pb systematics

While paragenesis is an important tool for determining the qualitative chronology of mineralizing events, the geochronological data for xenotime unambiguously constrains the absolute age of related mineralization stages. Petrographic observations show that type 1 xenotime is coeval with early nickeline in the arsenide stage, while type 2 xenotime and late nickeline both formed (separately) on the outer rims of arsenide floret assemblages. These textural observations suggest that type 1 xenotime is older than type 2 xenotime. However, U-Pb SHRIMP data indicates a slightly younger age for type 1 xenotime; U-Pb concordia plots of type 1 and type 2 xenotime show upper intercepts of 1428 ± 8 Ma and 1463 ± 23 Ma, respectively (Table 2.11; Figure 2.22). This dissonance complicates the interpretation of these ages.

As it turns out, U-Pb age determinations may not be appropriate for xenotime. An important consideration for SHRIMP analysis of xenotime is its sensitivity to matrix effects, which are inconsistencies in the composition of an unknown sample to reference materials, mostly related to U content (Fletcher et al. 2000, 2004; Cross and Williams 2018). The dominant matrix effects can be partially accounted for by using the multi-standard calibration method, but there may still be some U-based correlations in the data due to poor matrix matching (Cross and Williams 2018). Variations in U content may produce large discrepancies in $^{206}Pb/^{238}U$ values, but they do not affect $^{207}Pb/^{206}Pb$ values (Cross and Williams 2018). While $^{207}Pb/^{206}Pb$ ages are reliable for older samples that have had time to accumulate sufficient radiogenic Pb, the imprecision of this method may be noticeable in samples ca. 1 Ga or younger. The O^- ion beam used in this study to produce a stronger signal is particularly susceptible to matrix effects when compared with an O_2^- beam (Cross and Williams 2018). Considering all factors, the $^{207}Pb/^{206}Pb$ method for single analyses may provide the most reliable age for the >1.4 Ga xenotime at Eldorado. Average $^{207}Pb/^{206}Pb$ ages for type 1 and 2 xenotime are 1415 ± 24 Ma and 1453 ± 35 Ma, respectively (1σ errors), and 1442 ± 36 Ma for all xenotime (Table 2.11; Figure 2.22).

It is possible that both types of xenotime crystallized around the same time, because there is significant age overlap between the two types. Variations in $^{207}Pb/^{206}Pb$ between individual analyses may result from contamination by adjacent grains of uraninite or nickeline, or microscopic inclusions of these minerals in the analysis volume. The type 1 and type 2 xenotime-bearing assemblages both comprise nickeline + uraninite ± apatite ± gersdorffite ± rammelsbergite. The similarity of the xenotime-bearing assemblages bracketing the entire arsenide stage indicates consistent availability of these mineral

components within the overall arsenide succession. Since the arsenide stage is considered to be a continuous succession of mineralization, likely formed under rapidly fluctuating fluid conditions (Burisch et al. 2016; Markl et al. 2016), there may have been a relatively short timespan between both types of xenotime mineralization, making them more or less contemporaneous.

Another possibility is that the older individual ages for some type 2 xenotime represents an older crystallization age (i.e. 1527 Ma or older; Table 2.11). In this case, if both types of xenotime crystallized earlier, the younger ages may reflect Pb loss during recrystallization at a later time. However, an older crystallization age is not easily explained because it would require one or more U-Pb isotope resetting events within the age range bracketed by the determined ages, and a complete resetting for type 1 xenotime, since there is no evidence of an earlier crystallization event preserved in the U-Pb data (Figure 2.22). Whereas previous studies have interpreted similar U-Pb ages in uraninite as a ca. 1453 Ma resetting event (Thorpe 1971; Ruzicka and Thorpe 1995; Mumin et al. 2007; Gandhi et al. 2018), it is well known that uraninite behaves poorly as a closed system, especially at elevated temperatures. Lead diffusion and dissolution-precipitation reactions commonly reset the U-Pb chronometer (Fayek and Kyser 1997). Uraninite altered to secondary minerals (e.g. coffinite) can still allow determination of primary mineralization age (Chipley et al. 2007; Sharpe and Fayek 2011). However, no pre-resetting age has been observed for uraninite at Eldorado (Jory 1964; Miller 1982; Gandhi et al. 2018).

Xenotime has favourable geochemistry for radiometric dating because of its typically high U content, low common Pb content, and lower susceptibility to Pb diffusion than uraninite (Sharpe and Fayek 2011; Cross and Williams 2018; Vasconcelos et al. 2018).

Closure temperatures for Pb diffusion in xenotime can be up to 750 °C at typical crustal cooling rates (Dahl 1997; Cherniak 2006). Lead diffusion rates in 10 μm scale xenotime grains are negligible at temperatures below 600 °C through any geological time scale (Cherniak 2006). However, Pb loss might be more significant through post-crystallization fluid interaction. Xenotime may experience complete resetting due to dissolution-precipitation reactions in high deformation shear zones at temperatures as low as 400 °C (Teufel and Heinrich 1997; Cherniak 2006).

Rasmussen et al. (2011) demonstrated the suitability of xenotime for U-Pb geochronology at different metamorphic conditions using SHRIMP. 1.7–1.65 Ga xenotime from Mount Barren Group metasedimentary rocks—in the Albany-Fraser Orogen in southwestern Australia—were subjected to variable metamorphic conditions and deformation before peak metamorphism ca. 1.2 Ga. U-Pb ages were retained at lower greenschist facies, but were completely reset at amphibolite facies (Vallini et al. 2002; Dawson et al. 2002; Rasmussen et al. 2011). This suggests that xenotime U-Pb systematics should not be completely reset, and may not even demonstrate significant Pb diffusion up to ~400 °C, but would likely be completely reset above ~650 °C. Rasmussen et al. (2007) confirmed robust preservation of many xenotime crystallization events in an active hydrothermal environment at temperatures up to 400 °C.

Of critical importance to the interpretation of xenotime ages in this study, regional T around Port Radium is not considered to have surpassed 200 °C, based on lower zeolite facies metamorphism (Robinson and Morton 1972; Robinson and Ohmoto 1973). Hornblende hornfels and albite-epidote hornfels facies contact metamorphism is locally present (Robinson and Morton 1972), but the known local intrusions (e.g. Mystery Island

Intrusive Suite) are too old to have influenced the ore system (Mumin et al. 2007). The most relevant former heat source in the immediate vicinity of the Eldorado deposit is the Western Channel Diabase (WCD). A high T (>600 °C) thermal aureole would have developed within the ore zone. However, the 1590 Ma WCD is too old to have caused the resetting of uraninite or xenotime, and there are no known intrusions of a younger age around Port Radium (Hamilton and Buchan 2010).

Hydrothermal fluids at Eldorado were generally trapped at low temperature: $T_h = T_d^H = 180.6 \pm 48.2$ and 180.8 ± 39.3 °C (1σ) for type 2 and 3 fluid inclusions, respectively, though T_h ranged up to 350 °C in some samples. While these are minimum entrapment temperatures for late arsenide and sulphide stages of mineralization, a large pressure correction is unlikely since the known overburden from basement and overlying sedimentary basin are not expected to have exceeded 5 km before the deposition of the ca. 1267 Coppermine River Group basalts (LeCheminant and Heaman 1989; Gandhi et al. 2018). Trapping conditions for the late arsenide stage are considered to have fluctuated significantly, with maximum P_{tr} and T_{tr} up to ~175 MPa and ~350 °C. It was also noted during microthermometry that many fluid inclusions with T_h ~200 °C were decrepitated upon heating to temperatures up to ~230 °C. These low temperature fluid inclusions, even at a ~175 MPa confining pressure, could not have survived had they been subjected to a significantly elevated heat source after formation (Prezbindowski and Larese 1987). Lacking an elevated heat source, the U-Pb systematics of uraninite and xenotime were likely not reset.

2.4.4.2 Reconciliation with existing age data

The age of "five-element" mineralization at Eldorado has been a provocative discussion topic since its discovery. Kidd and Haycock (1935) estimated an approximate age for uraninite and established a detailed paragenesis, which confirmed that uraninite was an early mineralization phase within the "five-element" vein assemblage. Jory (1964) produced the first concordant U-Pb age for uraninite (1445 ± 20 Ma), and also described cross-cutting relationships between the ore veins and the local mafic dikes and sills, which broadly constrained the age range for mineralization. The early Cleaver dikes were cross-cut by "five-element" mineralization, including the uraninite stage (Jory 1964). A U-Pb age of ~1740 Ma for the Cleaver dike swarm (Irving et al. 2004) constrains the maximum age of "five-element" mineralization. This relative timing relationship has not been challenged by any other geochronological study to date.

The age of the younger WCD has a more controversial implication for the age of ore mineralization. Kidd and Haycock (1935) noted that the WCD cut the early giant quartz veins, which follow the major fault structures, but did not show evidence of being displaced by later reactivation of these faults. Jory (1964) noted that the WCD was not offset near quartz-carbonate veinlets, but that some mineralized fractures were reactivated after the emplacement of the WCD. The only evidence that might suggest a cross-cutting relationship between the WCD and "five-element" mineralization is where vein 1 was reported to have pinched out against the WCD, with only a few quartz-carbonate veinlets cross-cutting the WCD (Jory 1964). In this case, the WCD crosses the path of the vein structure, but not the ore mineralogy. Jory (1964) interpreted this to indicate that while the final gangue mineralization stage postdates the WCD, the ore stages predate the WCD.

Multiple determinations of the age of "five-element" mineralization followed after this cross-cutting relationship was proposed. Uraninite ages of 1424 ± 29 Ma (Miller 1982) and 1453 ± 18 Ma (Gandhi et al. 2018) support those of Jory (1964), while conflicting ages for the paragenetically late galena and other sulphides returned older ages ca. 1755–1600 Ma (Jory 1964; Thorpe 1971; Thorpe 1974; Miller 1982; Changkakoti et al. 1986a; Ruzicka and Thorpe 1995). Thorpe (1971) argued that 1625 Ma model Pb ages accurately constrained the mineralization age for the BMS, and thus the ca. 1445 Ma uraninite age (Jory 1964) may represent an isotopic resetting event. However, the model Pb ages require several assumptions about the inheritance of Pb throughout the Earth's history, and variable Pb isotopic composition make it difficult to account for the abundance of common Pb (Robinson and Ohmoto 1973). Upon further investigation into the model Pb age dilemma, Thorpe (1974) rejected the older model Pb ages for mineralization, explaining them using a mixing model involving Pb from older volcanic host rocks and the WCD (Thorpe 1974; Miller 1982; Changkakoti et al. 1986a). Later, Bowring and Ross (1985) produced a zircon U-Pb age of 1663 ± 8 Ma for the Narakay Volcanics within the Hornby Bay Group. Ruzicka and Thorpe (1995) argued that this volcanism was a potential heat source for early mineralization at Eldorado, in accordance with the 1625 Ma model Pb ages. Young uraninite ages ca. 1500 Ma (Miller 1982; Changkakoti 1986a) and 1445 Ma were again considered to represent resetting events (Ruzicka and Thorpe 1995; Mumin et al. 2007).

More recently, Hamilton and Buchan (2010) reported two concordant U-Pb ages of 1592 ± 3 and 1590 ± 4 Ma for baddelyite in the WCD. The revised mineralization bracket, constrained between the early Cleaver and late WCD intrusives (1740–1590 Ma), and Jory's (1964) misinterpreted cross-cutting relations, was consistent with previously

reported model Pb ages for sulphide mineralization (1625 Ma, Thorpe 1971; 1755–1600 Ma, Gandhi et al. 2018). Gandhi et al. (2018) seemed to confirm the suspected resetting age reported in earlier studies by determining a maximum concordant U-Pb age of 1453 ± 18 Ma for uraninite using SIMS. This was supported by similar uraninite ages, within the GBMZ and more widely in the Thelon and Athabasca basins, which might indicate a large-scale isotopic resetting event (Gandhi et al. 2018).

The prevailing arguments for a resetting event ca. 1453 Ma are the older Pb-Pb ages from galena and other sulphides and the ambiguous cross-cutting relationship between "five-element" veins and the WCD. The Pb-Pb ages are susceptible to errors owing to the assumptions of the origins of Pb, while the cross-cutting relationships were not based on strong evidence (Kidd and Haycock 1935; Jory 1964). The WCD is only known to have cross-cut giant quartz veins and related veinlets of quartz and hematite, which are regionally pervasive in pre-"five-element" mineralization (Campbell 1955; Jory 1964; Robinson and Ohmoto 1973). These quartz veins do share the same reactivated fault structures as later "five-element" mineralization, but this is not evidence to suggest that the WCD cross-cut the later mineralization as well. The xenotime ages presented in this study are more robust and reliable than previous Pb-Pb age determinations, due to very low common lead. Furthermore, there is no evidence of a prior mineralization age from which the xenotime has been thermally reset ca. 1440 Ma. This establishes a mineralization age of 1442 ± 36 Ma for xenotime in the contextually continuous arsenide stage, and provides support for a primary mineralization age of 1453 ± 18 Ma for the uraninite stage (Gandhi et al. 2018).

2.4.5 Fluid source

Fluid inclusion microthermometry and LA-ICP-MS data show that primary fluids from the late arsenide and sulphide stages were highly saline Ca-Na-Cl brines, with very high concentrations of Br, Mg, K, Pb, Zn, Sr, and Ba. Type 1 inclusions have distinctly lower salinities than types 2 and 3, which might appear indicative of two different fluids. However fluid inclusion types 1 and 2, both trapped in late arsenide stage quartz, have the same ranges in Na/Ca and Cl/Br, and the association of various major and trace cations are the same in relative proportions (Figure 2.27). The lower concentrations of major and trace cations in type 1 fluid inclusions relative to type 2 likely reflects the influence of lower salinity on chloride-complexed cation concentrations.

Figure 2.27 (next page): Halogen compositions and molar ratios in fluid inclusion types 1–3, determined by LA-ICP-MS. Raw data were acquired using LA-ICP-MS and processed using SILLS. **a)** Molar Cl/Br vs. molar Na/Br diagram compared to modern seawater composition with expected trajectories for evaporation and halite dissolution (Carpenter 1978; Richard et al. 2011). Most data for all fluid inclusion types cluster along the evaporation curve, beyond the end of halite precipitation, indicating significant evaporation beyond saturation of halite, and possibly other evaporite salts. A range of compositions for evaporated seawater associated with unconformity U in the Athabasca Basin is shown for comparison (Richard et al. 2011). **b)** Molar Cl/Br vs. Cl (ppm) diagram with the position of evaporite salts along a modern seawater evaporation trend for comparison (Fontes and Matray 1993). SW = seawater, precipitated salts: G = gypsum, H = halite (H^0 = onset of precipitation, H^3 = end of precipitation), E = epsomite, S = sylvite, C = carnallite, B = bischofite, T = tachyhydrite. The salinity of two-phase inclusions are consistent with those from the Athabasca Basin (Richard et al. 2011). Three-phase inclusions show salinity beyond the natural trend of evaporated seawater, and significant spread to higher Cl/Br values outside the bounds of halite precipitation curve.

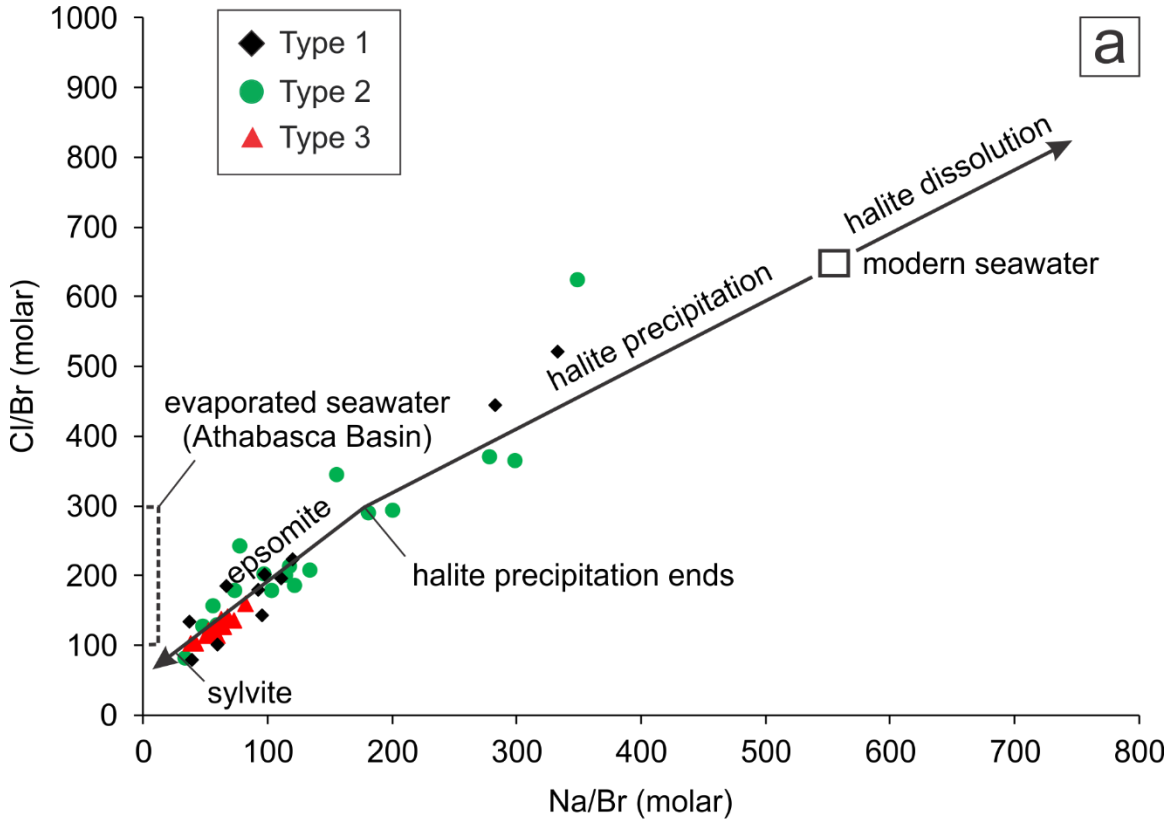
a
Type 1
Type 2
Type 3
halite dissolution
modern seawater
halite precipitation
evaporated seawater
(Athabasca Basin)
epsomite
halite precipitation ends
sylvite
Cl/Br (molar)
Na/Br (molar)
0
100
200
300
400
500
600
700
800
900
1000

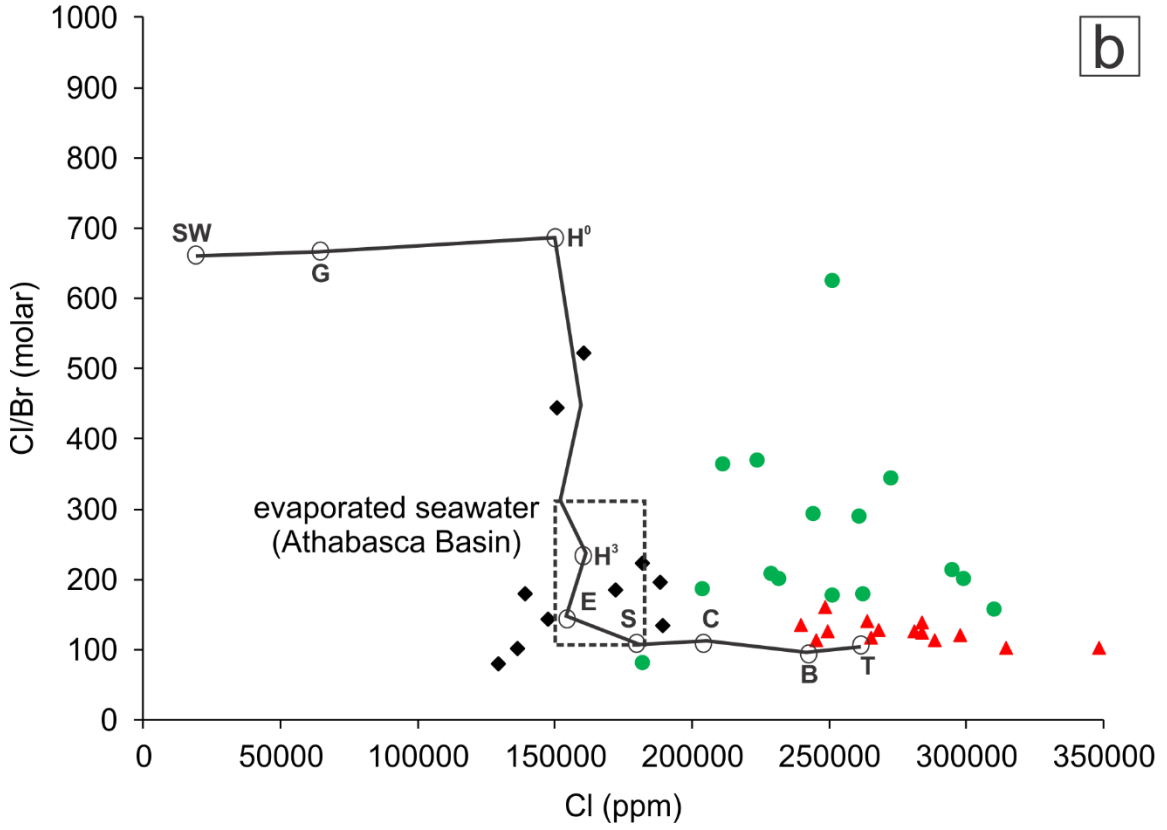
b
SW
G
H⁰
H³
E
S
C
B
T
evaporated seawater
(Athabasca Basin)
Cl/Br (molar)
Cl (ppm)
0
50000
100000
150000
200000
250000
300000
350000

Figure 2.27a shows the full range in fluid inclusion halogen data, plotted on a molar Cl/Br vs. Na/Br diagram, showing relative Br enrichment through precipitation of halite and other salts during evaporation of seawater composition (Richard et al. 2011; Fusswinkel et al. 2018). Seawater Cl/Br values may have changed since the Archean, but are generally considered to have been similar to present-day values (Cl/Br ~650 molar ratio) since the Paleoproterozoic (Foriel et al. 2004; Kendrick et al. 2007; Richard et al. 2011, Fusswinkel et al. 2018). Fluid compositions for all fluid inclusion types lie tightly along the evaporation trajectory, with 90% of the analyzed inclusions having molar Cl/Br < 250, suggesting derivation after more than 90% evaporation of seawater (epsomite–sylvite saturated). Type 3 fluid inclusions show particularly tight clustering with molar Cl/Br < 200, while types 1 and 2 show much more scatter along the evaporation trajectory.

High salinity fluids are broadly associated with igneous, metamorphic, and sedimentary source environments (Becker et al. 2008; Yardley and Bodnar 2014; Lecumberri-Sanchez and Bodnar 2018). They are prevalent in porphyry Cu and other magmatic-hydrothermal ore systems, among many other ore systems (e.g. IOCG, MVT, orogenic Au, massive sulphide, manto-type, and unconformity U; Becker et al. 2008). Chloride is a critical ligand for metal complexation in basin-hosted ore systems (e.g. MVT, manto-type, unconformity U; Richard et al. 2011). In this study, fluids with high Cl concentrations also have very low molar Cl/Br and Na/Br ratios. The combination of very high salinity, and low Cl/Br and Na/Br ratios are uniquely characteristic of evaporitic basinal brines, formed through progressive evaporation of seawater (Richard et al. 2011; Walter et al. 2016). Fluid-rock interactions alone are not capable of producing brines with such extreme compositions (Walter et al. 2016).

Figure 2.27b shows data plotted on a Cl/Br (molar) vs. Cl (ppm) diagram (Richard et al. 2011), and shows significant enrichment in Cl and Br beyond what is expected through evaporation alone. Thus, some modification of the residual seawater brines must have occurred after evaporation. The scatter in Cl/Br values in type 2 fluid inclusions also appears to indicate modification subsequent to Br enrichment from evaporation. This could be evidence of mixing between residual evaporitic brines and halite dissolution brines within the basin prior to mineralization (Chi and Savard 1997). Chlorite precipitation could be another possible mechanism for late depletion in Br and increase in salinity, as this mineral can incorporate Br and H_2O into its structure (Kendrick 2019). Chlorite is pervasive in wall-rocks as a hydrothermal alteration product formed in association with mineralization, occurs regularly in veins associated with quartz, and is sometimes accidentally trapped as a saturated phase in fluid inclusion types 1 and 2. During late arsenide stage mineralization, Br and H_2O may be incorporated into chlorite, effectively increasing Cl/Br in type 2 fluid inclusions, and boosting the salinity of residual brines, resembling type 3 fluid inclusions from the sulpharsenide stage.

With respect to a likely source for an evaporitic brine, the Hornby Bay Basin unconformably overlies regional lithologies in the northern parts of the GBMZ, and is considered to have been a much broader basin than the currently preserved margins. The Hornby Bay Basin had been accumulating sediments since at least 1.74 Ga (Irving et al. 2004), and at the time of vein formation (1442 ± 36 Ma from xenotime in the arsenide stage), formations of the Dismal Lakes Group were still being deposited in the basin (1438 ± 8 Ma for pyrite in Leroux and Fort Confidence formation black shales; Geospec 2008). Evaporites occur in several formations within the upper Dismal Lakes Group, as evidenced

by halite casts in the Dease Lake Formation, which immediately overlies the Fort Confidence Formation. This was a likely source environment for residual evaporitic brines that migrated down through the basin into the basement. This process is analogous to that which was proposed for unconformity U deposits in the Athabasca Basin by Richard et al. (2011).

There are no compositional distinctions between fluid inclusion types 1 and 2 for any comparison in Figure 2.28. Despite the difference in S_{wt}, the major and trace cation proportions are consistent, which suggests a similar source for both fluid types, and that type 2 fluid is a modified type 1 fluid (i.e. H_2O removed by chloritization). Type 3 fluid inclusions are also quite consistent in composition with types 1 and 2, containing similarly low Zn + Pb, very high Ca and Mg, and high variability in Ba. However, type 3 fluid inclusions have lower Na relative to Types 1 and 2 (Figure 2.28b). Note that relative concentration of Ca in type 3 fluid inclusions in Figure 2.28d should be ignored because a common Ca concentration was set as an internal standard for LA-ICP-MS data reduction and reflects an average value. Figure 2.28a shows a difference in type 3 fluid composition in Fe-dolomite host (sulphide stage) vs. Mn-dolomite host (late carbonate stage). Specifically, the higher Ba content in Type 3 fluid inclusions from the late carbonate stage may be related to the presence of barite and Ba-heulandite in the late carbonate stage (Figure 2.28a, c, d). There was no evidence of accidentally trapped Ba-bearing minerals so this may show a real increase in Ba during the late carbonate stage. Enrichment in Ba in the fluid over time could have occurred through wall-rock interaction (i.e. Ba from K-feldspar), or through relative enrichment as other major cations were used up in the precipitation of other minerals (e.g. Ca-Mg carbonate and chlorite).

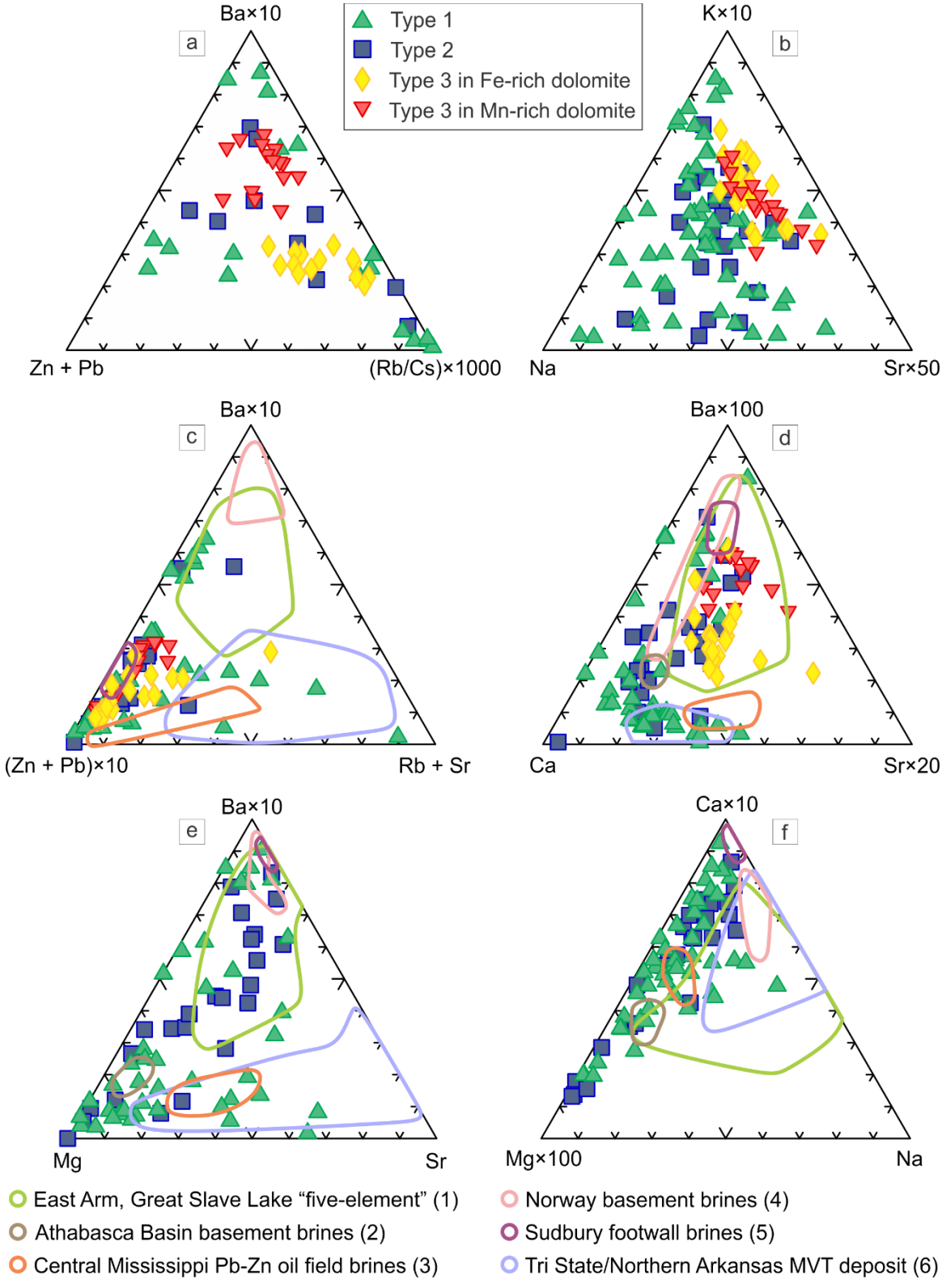
Type 1
Type 2
Type 3 in Fe-rich dolomite
Type 3 in Mn-rich dolomite
a
Ba×10
Zn + Pb
(Rb/Cs)×1000
b
K×10
Na
Sr×50
c
Ba×10
(Zn + Pb)×10
Rb + Sr
d
Ba×100
Ca
Sr×20
e
Ba×10
Mg
Sr
f
Ca×10
Mg×100
Na
East Arm, Great Slave Lake “five-element” (1)
Athabasca Basin basement brines (2)
Central Mississippi Pb-Zn oil field brines (3)
Norway basement brines (4)
Sudbury footwall brines (5)
Tri State/Northern Arkansas MVT deposit (6)

Figure 2.28 (previous page): Ternary diagrams showing variations in chemical composition of major and trace cations in fluid inclusion types 1–3, determined by LA-ICP-MS. Compositional fields for fluids from various basin and basement environments are provided for reference: (1) Fluid inclusions in pre-mineralization quartz from a polymetallic "five-element" occurrence at Copper Pass, NWT (Burke 2019); (2) basement brines associated with unconformity U in the Athabasca Basin (Richard et al. 2010); (3) oil field brines from a Pb-Zn deposit in Central Mississippi (Carpenter et al. 1974); (4) crystalline basement brines in southern Norway (Munz et al. 1995); (5) basement brines from the North Range footwall of the Sudbury Igneous Complex (Frape and Fritz 1982; Hanley et al. 2005); (6) basin brine from MVT deposits in The Tri-State and Northern Arkansas districts of the Ozark plateau (Stoffell et al. 2008). **a)** compositional ternary diagram for Ba×10, Zn+Pb, (Rb/Cs)×1000. Type 3 fluid inclusions in compositionally distinct dolomites show significant variability in Ba and Rb/Cs. **b)** compositional ternary diagram for K×10, Na, Sr×10. Fluid inclusion types 1 and 2 have higher Na content relative to K and Sr than type 3 fluid inclusions. **c)** compositional ternary diagram for Ba×10, (Zn+Pb)×10, Rb+Sr. Eldorado fluids are more akin to oil field brines with high Zn + Pb, rather than typical MVT or crystalline basement brines. **d)** compositional ternary diagram for Ba×100, Ca, Sr×1000. Fluid inclusion types 1 and 2 show very high Ca, consistent with other sedimentary basin-related fluids. **e)** compositional ternary diagram for Ba×10, Mg, Sr. Fluid inclusion types 2 and 3 show wide ranges in Mg and Ba relative composition, spanning compositional fields for both sedimentary basin and classic basement brines. **f)** compositional ternary diagram for Ca×10, Mg×100, Na. Very high Ca and Mg brines at Eldorado are most consistent with oil field brines and Athabasca basin brines.

Compositional fields for different global examples of sedimentary and basement (shield) brines are plotted for comparison with Eldorado fluids, shown to have been derived from modified, evaporated seawater (Figure 2.28c, d, e, f). There is a tight cluster of analyses with relatively high Zn+Pb in Figure 2.28c, consistent with the Zn- and Pb-enriched Sudbury footwall brines (Frape and Fritz 1982; Hanley et al. 2005) and Central Mississippi oil field brines (Carpenter et al. 1974). Other than the anomalously high Zn+Pb (in Sudbury footwall brines), Eldorado fluids are largely dissimilar to crystalline basement brines, which tend to be very rich in Ba, including those from Sudbury and southern Norway (Munz et al. 1995), though there is some overlap in compositional fields (Figure 2.28c, d, e, f). Eldorado fluids are also dissimilar to typical MVT fluids (Stoffell et al.

2008), which have relatively higher Na and Sr concentrations. Eldorado fluids are *most* consistent with unconformity-related brines from the Athabasca Basin (Richard et al. 2010) and Central Mississippi oil field brines due to their relatively high Ca and Mg content (fluid inclusion types 1 and 2; Figure 2.28d, e, f). Some Eldorado fluid compositions spread between Ca- and Mg-rich (typical of sedimentary source environments) and Ba-rich (typical of crystalline basement source environments) fields (Figure 2.28d, e). A similar spread in composition was observed in "five-element" brines from the East Arm, Great Slave Lake (Burke 2019; Figure 2.28d, e). Burke (2019) interpreted this compositional distribution as a possible mixing trend between Ca- and Mg-rich brines from an overlying basin and Ba-rich brines from the basement. Relative Ba enrichment could also have occurred through wall-rock interaction as previously discussed.

Intracratonic basinal fluids sourced from the evaporation of seawater would have original Sr isotope ratios ($^{87}Sr/^{86}Sr_o$) that reflect seawater composition. No mass fractionation of Sr isotopes occurs during precipitation of carbonates, and radiogenic ingrowth from decaying ^{87}Rb was neglibible. Thus, the reported range in values of $^{87}Sr/^{86}Sr_o$ = 0.7046–0.7239 for vein carbonates in this study represent the composition of ca. 1440 Ma mineralizing fluids. Changkakoti et al. (1986b) reported a similar range in values for vein carbonates in "five-element" style deposits in the Echo Bay and Camsell River districts ($^{87}Sr/^{86}Sr_o$ = 0.7090–0.7192 ca. 1440 Ma), but only analyzed two samples from Eldorado dolomite ($^{87}Sr/^{86}Sr_o$ = 0.7090, 0.7114). Values from this study are highly variable relative to 1440 Ma seawater (Figure 2.29), which likely ranged between 0.705 and 0.706 (Veizer 1989; Mirota and Veizer 1994; Hall and Veizer 1996). These variations

in vein carbonate $^{87}Sr/^{86}Sr_o$ indicates that significant compositional modification occurred from fluid source to the time and place of carbonate deposition.

In order to introduce evaporated seawater brines (bitterns) into the basement rocks at Port Radium, the original brine must have migrated down through structures in the overlying sedimentary units (related to the Hornby Bay Basin). Strontium isotope modification of a brine occurs if more radiogenic Sr is added to the brine via destruction of non-marine carbonates or Sr-bearing minerals like plagioglase. There are no available Sr isotope data of the Hornby Bay Basin for comparison, but sedimentary rocks in the stratigraphically-correlated Athabasca Basin are analogous (Bleeker and LeCheminant 2012; Hahn et al. 2013). Athabasca Basin sedimentary units ca. 1440 Ma had $^{87}Sr/^{86}Sr$ = 0.7046–0.7086, which is within the range, and slightly heavier than, ca. 1440 Ma seawater (Figure 2.29). Assuming similar values for the Hornby Bay Basin, brines could not attain sufficient radiogenic Sr during modification to account for the high variability observed in Eldorado carbonates.

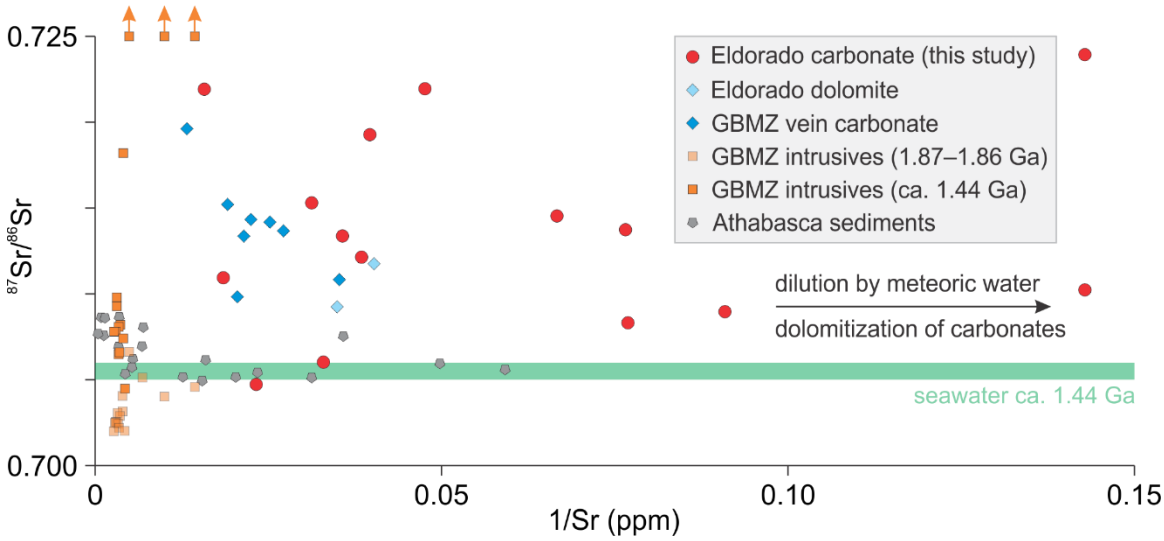

Figure 2.29: Strontium isotope systematics in Eldorado vein carbonates. Radiogenic Sr isotope ratios in carbonate from this study are plotted relative to values for vein carbonates in the Echo Bay and Camsell River districts (Changkakoti et al. 1986b), Mesoproterozoic seawater (green bar; Veizer 1989; Mirota and Veizer 1994; Hall and Veizer 1996), igneous intrusive host rocks in the GBMZ (Ootes et al. 2017), and basin sediments from the Athabasca Basin (Armstrong and Ramaekers 1985)—as a proxy for overlying sediments of the Hornby Bay Basin. The intrusive and sedimentary rocks are included to show the range in strontium isotope ratios that may have modified seawater-derived brines through fluid-rock interaction.

Basement rocks at Eldorado include various igneous intrusive and volcanic rocks, for which Sr isotope data are available. Some felsic intrusive rocks in the area with high Rb content (e.g. porphyry) accumulated significant radiogenic Sr since their crystallization ca. 1860 Ma (Ootes et al. 2017). Other local rocks (i.e. Port Radium Fm. clastic and volcaniclastic rocks, mafic dikes) were likely less Rb-rich, and did not accumulate as much radiogenic Sr since their formation (Robinson and Morton 1972; Wanless and Loveridge 1978). The igneous rocks characterized by Ootes et al. (2017) have a wide range of Sr isotope values ca. 1440 ($^{87}Sr/^{86}Sr_o$ = 0.7044–0.7693), which encompasses the full range of Sr isotope values in Eldorado vein carbonates (Figure 2.29). Thus, the wide range in Sr isotope values in basin brines can be accommodated by significant modification via destruction of minerals in the basement rocks with high radiogenic Sr concentrations.

Fayek and Kyser (1997) noted distinct ranges in Sr isotope ratios for different U mineralization styles association with the Athabasca Basin. For example unconformity- and basement-hosted U minerals have contrasting $^{87}Sr/^{86}Sr_o$ of 0.707–0.710 and 0.713–0.715, respectively. Their interpretation of these Sr isotope systematics recognized the distinct geochemistry of the two dominant lithologies in the area (Athabasca Basin sandstones and basement gneiss). Strontium isotope systematics in basinal sedimentary units are similar to those of Proterozoic seawater and basement-hosted U mineralization (Armstrong and Ramaekers 1985; Veizer 1989; Fayek and Kyser 1997). Underlying basement rocks had relatively high $^{87}Sr/^{86}Sr_o$ values (>> 0.72) reflecting (in part) illitization of feldspars (Fayek and Kyser 1997, Fahrig and Loveridge 1981). The low $^{87}Sr/^{86}Sr_o$ values of basement-hosted U mineralization was suggested to reflect a hydrothermal system dominated by basinal fluid, presumably during a predominance of basinal fluid relative to

basement fluid, or a reduction in basement fluid circulation through those particular basement rocks where incursion of basinal fluid was occurring. The $^{87}Sr/^{86}Sr_o$ values in sandstone-hosted U mineralization were higher than those of the basement-hosted U minerals, which suggests significant mixing between the two fluid types. There is no evidence of any significant mixing identified in this study, based on relatively consistent fluid salinities, O isotope systematics, and fluid major and trace element chemistry during vein development. However, the mechanism for Sr isotope modification is still relevant to the evaporitic basinal fluid and host rocks. Instead of fluid mixing, Sr isotope modification of the Eldorado fluids likely occurred through fluid-rock interaction (i.e. the introduction of more or less radiogenic Sr through the hydrothermal destruction of feldspars). As such, the variable Sr isotope signatures of the different host rocks observed in the Eldorado vein carbonates are indicative of low fluid/rock ratios during mineralization.

2.4.6 Metal source

Nearly all fluid inclusions had concentrations of "five-element" and associated metals (Co-Ni-As-Ag-Bi + Cu-Sb-U) below detection limits, with real values only rarely quantified for Cu and Ag in the sulphide mineralization stage (Figure 2.21). The fluids in the late arsenide and sulphide stages are late relative to most of the ore mineralization, but there is still significant precipitation of As sulphosalts and native Ag and Bi during the sulphide stage. The lack of these elements in primary fluid inclusions either indicates an efficient process of metal precipitation, or that these fluids were not carrying the metals to begin with. There is no evidence of another fluid to have sourced the metals and mixed

with the evaporitic basin brines, so this latter scenario is unlikely. It is more likely that metals were efficiently precipitated from solution during conditions of rapid P, T fluctuation, leading to dendritic minerals and dissolution-reprecipitation textures.

If evaporitic brines were carrying the metals, they must have either sourced them locally from the basement rocks or from within the sedimentary basin. Both environments have been proposed as a source for U in the Athabasca U deposits (Alexandre and Kyser 2006; Richard 2010). Morton and Changkakoti (1986) suggested that the "five-element" suite of metals found at Eldorado and surrounding deposits could be sourced from black shale protoliths that had been metamorphosed in the basement. Organic compounds in black shales can readily form complexes with Co, Ni, As, Ag, and U that can then be transported from the source to the ore deposit (Morton and Changkakoti 1986). However, a few problems are encountered with reconciling basement sources for metals: (i) metamorphism in the GBMZ occurred prior to vein formation, so metals may have already been mobilized out of local metal-rich lithologies; (ii) basement rock lithologies vary globally, yet the metal association and paragenesis of "five-element" deposits are frequently very similar; (iii) there is no magmatic or metamorphic component in the fluids, as evidenced by a distinct evaporitic brine signature, so a sedimentary metal source is supported by association.

Black shales in the basin overlying the Eldorado deposit provide a likely source for metals, akin to "five-element" style metals reported in other Proterozoic basins, particularly in black shales (e.g. Hulbert 1996; Alexandre and Kyser 2006; Pasava et al. 2008; Johnson et al. 2017; Joyce et al. 2017). Mineralization at Eldorado ca. 1440 Ma is coeval with pyrite mineralization in black shales in the Dease Lake Formation of the Dismal Lakes Group,

which confirms the possibility of suitable source rocks in the basin sequence overlying Eldorado (Geospec 2008; Skulski et al. 2018). Metals, along with brines and any associated hydrocarbons could have migrated down through the basins along faults into the basement (Schubert et al. 2007; Chi et al. 2014; Feely et al. 2017). Large fault structures are pervasive in the basement and show a long history of reactivation, which makes them suitable conduits for fluid migration.

2.4.6 Conclusions

Petrography and paragenesis of Eldorado mineralization described in this study is similar to that outlined in previous studies (e.g. Kidd and Haycock 1935; Campbell 1955; Jory 1964; Gandhi et al. 2018), with a few major additions and clarifications. (i) Co-precipitation of primary uraninite with µm- scale inclusions of dendritic sulpharsenides confirms that the uraninite stage is not an unrelated stage in the paragenesis, and that Co, Ni, As, and U were all transported together in the same fluid during the first stages of mineralization. (ii) Rhythmic mineralization such as uraninite with sulpharsenides, native Ag with safflorite, and nickeline with xenotime-uraninite show that conditions were not stable during mineralization and fluctuated periodically throughout the mineralization history. (iii) The xenotime-uraninite assemblage is constrained within the arsenide stage and provides an age of mineralization of 1442 ± 36 Ma. This age supplants the understanding that veins formed before the emplacement of the WCD ca. 1590 Ma, and the hypothesis that the earlier mafic intrusions and volcanics could have served as heat or metal sources for mineralization.

The younger age of mineralization is consistent with the development of the Dismal Lakes Group of the Hornby Bay Basin, in which there are 1438 Ma black shales in the Fort Confidence Formation and evidence of evaporite sequences in overlying formations. The Dismal Lakes Group evaporite environment is a likely source for Br-enriched seawater (Cl/Br mostly in the range 100–250) identified in hypersaline (bulk salinity up to 37 wt.% NaCl + $CaCl_2$ eq.) fluid inclusions. Black shales in the Hornby Bay Basin provide a potential source of "five-element" metals, from which descending residual evaporitic brines could have passed through. Residual brines underwent significant modification during interaction at low fluid/rock ratios with basement (GBMZ) rocks. Felsic plutonic rocks in the basement among other lithologies with high $^{87}Sr/^{86}Sr$ values effectively modified $^{87}Sr/^{86}Sr$ values in the residual brine away from seawater composition toward values in the range of 0.7046–0.7239.

Mineralization in the arsenide and sulphide stages occurred during periods of extreme fluctuations in T, P (T_h = 75–350 °C, P_h = 40–175 MPa during the late arsenide stage and T_h = 75–225 °C, P_h = 25–67 MPa during the sulphide stage). These ranges for minimum trapping conditions from microthermometric analysis are reconciled with consistent values of $\delta^{18}O_{VSMOW}$ = 15.4 ± 1.3‰ (1σ) throughout quartz precipitation, which is inconsistent with extreme fluctuations in T given a single source fluid. Fluctuations in P due to fractures periodically opening and sealing can accommodate much of the variations in microthermometric data. The depth of burial beneath the Hornby Bay Basin, which is not considered to be much more than 5 km thick up to, and including, the Dismal Lakes Group, constrains the maximum pressure at lithostatic conditions around 135 MPa.

2.5 References

Ahmed A, Arai S, Ikenne M (2009) Mineralogy and Paragenesis of the Co-Ni Arsenide Ores of Bou Azzer, Anti-Atlas, Morocco. Econ Geol 104:249-266

Alexandre P, Kyser TK (2006) Geochemistry of uraniferous bitumen in the Southwestern Athabasca Basin, Saskatchewan, Canada. Econ Geol 101:1605-1612

Andrews AJ, Owsiacki L, Kerrich R, Strong DF (1986) The silver deposits at Cobalt and Gowganda, Ontario. I: Geology, petrography, and whole-rock geochemistry. Can J Earth Sci 23:1480-1506

Annen C (2017) Factors Affecting the Thickness of Thermal Aureoles. Front Earth Sci 5:82

Armstrong RL, Ramaekers P (1985) Sr isotopic study of Helikian sediment and diabase dikes in the Athabasca Basin, northern Saskatchewan. Can J Earth Sci 22:399-407

Badham JPN (1975) Mineralogy, paragenesis and origin of the Ag-Ni, Co arsenide mineralisation, Camsell River, N. W. T. Canada. Miner Deposita 10:153-175

Bakker RJ (2003) Package FLUIDS 1. Computer programs for analysis of fluid inclusion data and for modelling bulk fluid properties. Chem Geol 194:3-23

Bastin ES (1939) The Nickel-Cobalt-Native Silver Ore-type. Econ Geol 34:1-40

Bastrakov EN, Jaireth S, Mernagh TP (2010) Solubility of uranium in hydrothermal fluids at 25° to 300°C: Implications for the formation of uranium deposits. Geoscience Australia Record 2010/29.

Becker SP, Fall A, Bodnar RJ (2008) Synthetic Fluid Inclusions. XVII. PVTX Properties of High Salinity H2O-NaCl Solutions (>30 wt % NaCl): Application to Fluid Inclusions that Homogenize by Halite Disappearance from Porphyry Copper and Other Hydrothermal Ore Deposits. Econ Geol 103:539-554

Berman RG (1988) Internally-Consistent Thermodynamic Data for Minerals in the System Na2O-K2O-CaO-MgO-FeO-Fe2O3-Al2O3-SiO2-TiO2-H2O-CO2. J Petrol 29:445-522

Bleeker W, LeCheminant A (2012) The Proterozoic Dessert Lake red bed basin, target for uranium exploration—an update. GEM Poster. Geological Survey of Canada,

Bodnar RJ, Vityk MO (1994) Interpretation of microthermometric data of H2O-NaCl fluid inclusions. In: De Vivo B, Frezzotti ML (eds) Fluid Inclusions in Minerals: Methods and Applications. Virginia Tech, Blacksburg, Virginia, 117-130

Bodnar RJ (1994) Synthetic fluid inclusions: XII. The system H2O-NaCI. Experimental determination of the halite liquidus and isochores for a 40 wt% NaCl solution. Geochim Cosmochim Acta 58:1053-1063

Bodnar RJ (2003) Introduction to aqueous fluid systems. In: Samson I, Anderson A, Marshall D (eds) Fluid Inclusions: Analysis and Interpretations. Mineralogical Association of Canada, Short Course no. 32, 81-99

Bowring SA, Williams IS, Compston W (1989) 3.96 Ga gneisses from the Slave province, Northwest Territories, Canada. Geology 17:971-975

Bowring SA, Ross GM (1985) Geochronology of the Narakay Volcanic Complex: implications for the age of the Coppermine Homocline and Mackenzie igneous events. Can J Earth Sci 22:774-781

Burisch M, Gerdes A, Walter BF, Neumann U, Fettel M, Markl G (2016) Methane and the origin of five-element veins: Mineralogy, age, fluid inclusion chemistry and ore forming processes in the Odenwald, SW Germany. Ore Geol Rev 81:42-61

Burke JS (2019) The origin of polymetallic Ni-Co-As-Bi-Sb(-Ag-U) veins in the East Arm Basin and southern Slave Province, Northwest Territories. M.Sc. thesis, Saint Mary's University

Campbell DD (1955) Geology of the pitchblende deposits of Port Radium, Great Bear Lake, N.W.T. Ph.D. thesis, California Institute of Technology

Carpenter AB, Trout ML, Pickett EE (1974) Preliminary Report on the Origin and Chemical Evolution of Lead-and Zinc-Rich Oil Field Brines in Central Mississippi. Econ Geol 69:1191-1206

Carpenter AB (1978) Origin and chemical evolution of brines in sedimentary basins. Oklahoma Geological Survey Circular 79:60-77

Changkakoti A, Morton RD (1986) Electron microprobe analyses of native silver and associated arsenides from the Great Bear Lake silver deposits, Northwest Territories, Canada. Can J Earth Sci 23:1470-1479

Changkakoti A, Ghosh DK, Krstic D, Gray J, Morton RD (1986a) Pb and Sr isotope compositions of hydrothermal minerals from the Great Bear Lake silver deposits, N.W.T., Canada. Econ Geol 81:739-743

Changkakoti A, Morton RD, Gray J, Yonge CJ (1986b) Oxygen, hydrogen, and carbon isotopic studies of the Great Bear Lake silver deposits, Northwest Territories. Can J Earth Sci 23:1463-1469

Changkakoti A, Morton RD, Gray J (1986c) Hydrothermal environments during the genesis of silver deposits in the Northwest Territories of Canada: Evidence from fluid inclusions. Miner Deposita 21:63-69

Cherniak DJ (2006) Pb and rare earth element diffusion in xenotime. Lithos 88:1-14

Chi G, Savard MM (1997) Sources of basinal and Mississippi Valley-type mineralizing brines: mixing of evaporated seawater and halite-dissolution brine. Chem Geol 143:121-125

Chi G, Li Z, Bethune K (2014) Numerical modeling of hydrocarbon generation in the Douglas Formation of the Athabasca basin (Canada) and implications for unconformity-related uranium mineralization. J Geochem Explor 114:37-48

Chipley D, Polito PA, Kyser TK (2007) Measurement of U-Pb ages of uraninite and davidite by laser ablation-HR-ICP-MS. Am Mineral 92:1925-1935

Corriveau L, Montreuil J, Potter EG (2016) Alteration Facies Linkages Among Iron Oxide Copper-Gold, Iron Oxide-Apatite, and Affiliated Deposits in the Great Bear Magmatic Zone, Northwest Territories, Canada. Econ Geol 111:2045-2072

Cross AJ, Williams IS (2018) SHRIMP U–Pb–Th xenotime (YPO4) geochronology: A novel approach for the correction of SIMS matrix effects. Chem Geol 484:81-108

Cumberland SA, Douglas G, Grice K, Moreau JW (2016) Uranium mobility in organic matter-rich sediments: A review of geological and geochemical processes. Earth Sci Rev 159:160-185

Dahl PS (1997) A crystal-chemical basis for Pb retention and fission-track annealing systematics in U-bearing minerals, with implications for geochronology. Earth Planet Sci Lett 150:277-290

Dawson GC, Krapež B, Fletcher IR, McNaughton NJ, Rasmussen B (2002) Did late Palaeoproterozoic assembly of proto-Australia involve collision between the Pilbara, Yilgarn and Gawler Cratons? Geochronological evidence from the Mount Barren Group in the Albany–Fraser Orogen of Western Australia. Precambrian Res 118:195-220

Dolníček Z, Fojt B, Prochaska W, Kučera J, Sulovský P (2009) Origin of the Zálesí U–Ni–Co–As–Ag/Bi deposit, Bohemian Massif, Czech Republic: fluid inclusion and stable isotope constraints. Miner Deposita 44:81-97

Fahrig WF, Loveridge WD (1981) Rb-Sr isochron age of weathered pre-Athabaska Formation basement gneiss, northern Saskatchewan. Current Research Part C. Geological Survey of Canada, Paper 81-1C, 127-129

Fayek M, Horita J, Ripley EM (2011) The oxygen isotopic composition of uranium minerals: A review. Ore Geol Rev 41:1-21

Fayek M, Kyser KK (1997) Characterization of multiple fluid events and rare-earth-element mobility associated with formation of unconformity-type uranium deposits in the Athabasca Basin, Saskatchewan. Can Mineral 35:627-658

Fayek M, Harrison TM, Ewing RC, Grove M, Coath CD (2002) O and Pb isotopic analyses of uranium minerals by ion microprobe and U–Pb ages from the Cigar Lake deposit. Chem Geol 185:205-225

Feely M, Costanzo A, Lindner F, George J, Parnell J, Bowden S, Baba M, Owens P (2017) Quartz-amethyst hosted hydrocarbon-bearing fluid inclusions from the Green Ridge Breccia in the Snoqualmie Granite, North Cascades, WA, USA. Minerals 7: 1-16

Fletcher IR, Rasmussen B, McNaughton NJ (2000) SHRIMP U–Pb geochronology of authigenic xenotime and its potential for dating sedimentary basins. Aust J Earth Sci 47:845-859

Fletcher IR, McNaughton NJ, Aleinikoff JA, Rasmussen B, Kamo SL (2004) Improved calibration procedures and new standards for U–Pb and Th–Pb dating of Phanerozoic xenotime by ion microprobe. Chem Geol 209:295-314

Fontes JC, Matray JM (1993) Geochemistry and origin of formation brines from the Paris Basin, France: 1. Brines associated with Triassic salts. Chem Geol 109:149-175

Foriel J, Philippot P, Rey P, Somogyi A, Banks D, Ménez B (2004) Biological control of Cl/Br and low sulfate concentration in a 3.5-Gyr-old seawater from North Pole, Western Australia. Earth Planet Sci Lett 228:451-463

Franklin JM, Kissin SA, Smyk MC, Scott SD (1986) Silver deposits associated with the Proterozoic rocks of the Thunder Bay District, Ontario. Can J Earth Sci 23:1576-1591

Frape SK, Fritz P (1982) The chemistry and isotopic composition of saline groundwaters from the Sudbury Basin, Ontario. Can J Earth Sci 19:645-661

Fusswinkel T, Giehl C, Beermann O et al. (2018) Combined LA-ICP-MS microanalysis of iodine, bromine and chlorine in fluid inclusions. J Anal At Spectrom 33:768-783

Gandhi SS, van Breemen O (2005) SHRIMP U–Pb geochronology of detrital zircons from the Treasure Lake Group — new evidence for Paleoproterozoic collisional tectonics in the southern Hottah terrane, northwestern Canadian Shield. Can J Earth Sci 42:833-845

Gandhi SS, Mortensen JK, Prasad N, van Breemen O (2001) Magmatic evolution of the southern Great Bear continental arc, northwestern Canadian Shield: geochronological constraints. Can J Earth Sci 38:767-785

Gandhi SS, Potter EG, Fayek M (2018) New constraints on genesis of the polymetallic veins at Port Radium, Great Bear Lake, Northwest Canadian Shield. Ore Geol Rev 96:28-47

Geospec Consultants Limited (2008) Re-Os isotopic analyses and age dating of pyrite. Report on Geological studies and diamond drilling, Coppermine River project, Coppermine River area, Nunavut and NWT

Goldstein RH (2003) Petrographic Analysis of Fluid Inclusions. In: Samson I, Anderson A, Marshall D (eds) Fluid Inclusions: Analysis and Interpretations. Mineralogical Association of Canada, Short Course no. 32, 9-53

Guillong M, Meier DL, Allan MM, Heinrich CA, Yardley BWD (2008) SILLS: A MATLAB-based program for the reduction of laser ablation ICP-MS data of homogeneous materials and inclusions. In: Sylvester P (ed) Laser Ablation ICP-MS in the Earth Sciences: Current Practices and Outstanding Issues. Mineralogical Association of Canada Short Course Series, vol. 40, Vancouver, B.C., 328-333

Hahn K, Rainbird R, Cousens B (2013) Sequence stratigraphy, provenance, C and O isotopic composition, and correlation of the late Paleoproterozoic–early Mesoproterozoic

upper Hornby Bay and lower Dismal Lakes groups, NWT and Nunavut. Precambrian Res 232:209-225

Hamilton MA, Buchan KL (2010) U–Pb geochronology of the Western Channel Diabase, northwestern Laurentia: Implications for a large 1.59 Ga magmatic province, Laurentia's APWP and paleocontinental reconstructions of Laurentia, Baltica and Gawler craton of southern Australia. Precambrian Res 183:463-473

Hanley JJ, Mungall JE, Pettke T, Spooner ETC, Bray CJ (2005) Ore metal redistribution by hydrocarbon–brine and hydrocarbon–halide melt phases, North Range footwall of the Sudbury Igneous Complex, Ontario, Canada. Miner Deposita 40:237-256

Hayward N, Corriveau L (2014) Fault reconstructions using aeromagnetic data in the Great Bear magmatic zone, Northwest Territories, Canada. Can J Earth Sci 51:927-942

Heinrich CA, Pettke T, Halter WE et al. (2003) Quantitative multi-element analysis of minerals, fluid and melt inclusions by laser-ablation inductively-coupled-plasma mass-spectrometry. Geochim Cosmochim Acta 67:3473-3497

Hildebrand RS, Hoffman PF, Bowring SA (1987) Tectono-magmatic evolution of the 1.9-Ga great bear magmatic zone, Wopmay orogen, northwestern Canada. J Volcanol Geotherm Res 32:99-118

Hoffman SJ (1983) Geochemical exploration for unconformity-type uranium deposits in permafrost terrain, Hornby bay basin, Northwest Territories, Canada. J Geochem Explor 19:11-32

Holliger P, Cathelineau M (1988) In situ U-Pb age determination by secondary ion mass spectrometry. Chem Geol 70:173

Hornby Bay Mineral Exploration (2018) Coppermine River Properties, Hornby Bay Basin. http://www.hornbybay.com/coppermine-property.php. Accessed 2 April 2019

Hosieni KR, Howald RA, Scanlon MW (1985) Thermodynamics of the lambda transition and the equation of state of quartz. Am Mineral 70:782-793

Hulbert L (1996) Sedimentary nickel sulfides. Geology of Canadian Mineral Deposit Types. Geological Survey of Canada, Geology of Canada 8:152-158

Irving E, Baker J, Hamilton M, Wynne PJ (2004) Early Proterozoic geomagnetic field in western Laurentia: implications for paleolatitudes, local rotations and stratigraphy. Precambrian Res 129:251-270

Johnson S, Large R, Coveney R, Kelley K, Slack J, Steadman J, Gregory D, Sack P, Meffre S (2017) Secular distribution of highly metalliferous black shales corresponds with peaks in past atmosphere oxygenation. Miner Deposita 52:791-798

Jory LT (1964) Mineralogical and isotopic relations in the Port Radium pitchblende deposit, Great Bear Lake, Canada. Ph.D. thesis, California Institute of Technology

Joyce N, Layton-Matthews D, Kyser K, Ansdell K, Quirt D, Kotzer T (2017) Alteration mineralogy and pathfinder element inventory in the footprint of the McArthur River unconformity-related uranium deposit, Canada. Geological Association of Canada Abstracts, Kingston, Ontario

Kelly JL, Fu B, Kita NT, Valley JW (2007) Optically continuous silcrete quartz cements of the St. Peter Sandstone: High precision oxygen isotope analysis by ion microprobe. Geochim Cosmochim Acta 71:3812-3832

Kendrick MA, Mark G, Phillips D (2007) Mid-crustal fluid mixing in a Proterozoic Fe oxide–Cu–Au deposit, Ernest Henry, Australia: Evidence from Ar, Kr, Xe, Cl, Br, and I. Earth Planet Sci Lett 256:328-343

Kendrick MA (2019) Halogens in altered ocean crust from the East Pacific Rise (ODP/IODP Hole 1256D). Geochim Cosmochim Acta (in press)

Kerr MJ, Hanley JJ, Kontak DJ et al. (2018) Evidence of upgrading of gold tenor in an orogenic quartz-carbonate vein system by late magmatic-hydrothermal fluids at the Madrid Deposit, Hope Bay Greenstone Belt, Nunavut, Canada. Geochim Cosmochim Acta 241:180-218

Kerrich R, Strong DF, Andrews AJ, Owsiacki L (1986) The silver deposits at Cobalt and Gowganda, Ontario. III: Hydrothermal regimes and source reservoirs—evidence from H, O, C, and Sr isotopes and fluid inclusions. Can J Earth Sci 23:1519-1550

Kidd DF (1933) Great Bear Lake, McTavish Arm, Between Richardson Island and Hornby Bay, District of Mackenzie, NWT, Geological Survey of Canada, "A" Series Map no. 296A

Kidd DF (1932) Great Bear Lake area, Northwest Territories. Summary Report 1932 Part C; Geological Survey of Canada 1-36

Kidd DF, Haycock MH (1935) Mineragraphy of the Ores of Great Bear Lake. Bulletin of the Geological Society of America 46:879-960

Kissin SA (1992) Five-element (Ni-Co-As-Ag-Bi) Veins. J Geol Assoc Can 19:113-124

Kositcin N, McNaughton NJ, Griffin BJ, Fletcher IR, Groves DI, Rasmussen B (2003) Textural and geochemical discrimination between xenotime of different origin in the Archaean Witwatersrand Basin, South Africa. Geochim Cosmochim Acta 67:709-731

Kotková J, Kullerud K, Šrein V, Drábek M, Škoda R (2018) The Kongsberg silver deposits, Norway: Ag-Hg-Sb mineralization and constraints for the formation of the deposits. Miner Deposita 53:531-545

LeCheminant AN, Heaman LM (1989) Mackenzie igneous events, Canada: Middle Proterozoic hotspot magmatism associated with ocean opening. Earth Planet Sci Lett 96:38-48

Lecumberri-Sanchez P, Steele-MacInnis M, Bodnar RJ (2012) A numerical model to estimate trapping conditions of fluid inclusions that homogenize by halite disappearance. Geochim Cosmochim Acta 92:14-22

Lecumberri-Sanchez P, Bodnar RJ (2018) Halogen Geochemistry of Ore Deposits: Contributions Towards Understanding Sources and Processes. In: Aranovich L, Harlov D (eds) The Role of Halogens in Terrestrial and Extraterrestrial Geochemical Processes: Surface, Crust, and Mantle. Springer Geochemistry, 261-305

Ludwig KR (2009) SQUID 2.5. A User's Manual. Berkeley Geochronology Center, Berkeley, California

Ludwig KR (2012) A User's Manual for Isoplot 4.15: A Geochronological Toolkit for Microsoft Excel. Berkely Geochronology Center, Berkeley, California

Markl G, Burisch M, Neumann U (2016) Natural fracking and the genesis of five-element veins. Miner Deposita 51:703-712

Marshall DD, Watkinson DH (2000) The Cobalt Mining District: Silver Sources, Transport and Deposition. Explor Min Geol 9:81-90

Mathieu L (2018) Quantifying Hydrothermal Alteration: A Review of Methods. Geosciences 8:1-27

McDonough WF, Sun S (1995) The composition of the Earth. Chem Geol 120:223-253

Miller RG (1982) The geochronology of uranium deposits in the Greath Bear batholith, Northwest Territories. Can J Earth Sci 19:1428-1448

Montreuil J, Corriveau L, Davis WJ (2016a) Tectonomagmatic Evolution of the Southern Great Bear Magmatic Zone (Northwest Territories, Canada): Implications for the Genesis of Iron Oxide-Alkali–Altered Hydrothermal Systems. Econ Geol 111:2111-2138

Montreuil J, Corriveau L, Potter EG, De Toni AF (2016b) On the Relationship Between Alteration Facies and Metal Endowment of Iron Oxide-Alkali-Altered Systems, Southern Great Bear Magmatic Zone (Canada). Econ Geol 111:2139-2168

Mumin AH, Corriveau L, Somarin AK, Ootes L (2007) Iron Oxide Copper-Gold-type Polymetallic Mineralization in the Contact Lake Belt, Great Bear Magmatic Zone, Northwest Territories, Canada. Explor Min Geol 16:187-208

Munz IA, Yardley BWD, Banks DA, Wayne D (1995) Deep penetration of sedimentary fluids in basement rocks from southern Norway: Evidence from hydrocarbon and brine inclusions in quartz veins. Geochim Cosmochim Acta 59:239-254

Oakes CS, Bodnar RJ, Simonson JM (1990) The system NaCl-CaCl2-H2O: I. The ice liquidus at 1 atm total pressure. Geochim Cosmochim Acta 54:603-610

Ondruš P, Veselovský F, Drábek M et al. (2003) Ore-forming processes and mineral parageneses of the Jáchymov ore district. J Czech Geol Soc 48:157-192

Ootes L, Davis WJ, Jackson VA, van Breemen O (2015) Chronostratigraphy of the Hottah terrane and Great Bear magmatic zone of Wopmay Orogen, Canada, and exploration of a terrane translation model. Can J Earth Sci 52:1062-1092

Ootes L, Snyder D, Davis WJ et al. (2017) A Paleoproterozoic Andean-type iron oxide copper-gold environment, the Great Bear magmatic zone, Northwest Canada. Ore Geol Rev 81:123-139

Pasava J, Kribek B, Vymazalova A, Sykorova I, Zak K, Orberger B (2008) Multiple sources of metals of mineralization in Lower Cambrian black shales of south China: evidence from geochemical and petrographic study. Resour Geol 58:25-42

Pirajno F (2009) Hydrothermal Processes and Wall Rock Alteration. In: Pirajno F (ed) Hydrothermal Processes and Mineral Systems. Springer, Perth, Australia, 73-164

Potter E, Corriveau L, Kjarsgaard B (2019) Paleoproterozoic Iron Oxide Apatite (IOA) and Iron Oxide-Copper-Gold (IOCG) mineralization in the East Arm Basin, Northwest Territories, Canada. Can J Earth Sci (in press)

Rasmussen B, Fletcher IR, Muhling JR (2011) Response of xenotime to prograde metamorphism. Contrib Mineral Petrol 162:1259-1277

Rasmussen B, Fletcher IR, Muhling JR, Thorne WS, Broadbent GC (2007) Prolonged history of episodic fluid flow in giant hematite ore bodies: Evidence from in situ U–Pb geochronology of hydrothermal xenotime. Earth Planet Sci Lett 258:249-259

Rice S, Kyser K (2010) Fluid History and Uranium Mineralization in the Hornby Bay Basin, Nunavut, Canada. GeoCanada 2010 – Working with the Earth 1-4

Richard A, Pettke T, Cathelineau M et al. (2010) Brine–rock interaction in the Athabasca basement (McArthur River U deposit, Canada): consequences for fluid chemistry and uranium uptake. Terra Nova 22:303-308

Richard A, Rozsypal C, Mercadier J et al. (2012) Giant uranium deposits formed from exceptionally uranium-rich acidic brines. Nature Geoscience. 5:142–146. Nat Geosci 5:142-146

Richard A, Banks DA, Mercadier J, Boiron M, Cuney M, Cathelineau M (2011) An evaporated seawater origin for the ore-forming brines in unconformity-related uranium deposits (Athabasca Basin, Canada): Cl/Br and δ37Cl analysis of fluid inclusions. Geochim Cosmochim Acta 75:2792-2810

Robinson BW, Morton RD (1972) The geology and geochronology of the Echo Bay area, Northwest Territories, Canada. Can J Earth Sci 9:158-171

Robinson BW, Ohmoto H (1973) Mineralogy, Fluid Inclusions, and Stable Isotopes of the Echo Bay U-Ni-Ag-Cu Deposits, Northwest Territories, Canada. Econ Geol 68:635-656

Romberger SB (1984) Transport and deposition of uranium in hydrothermal systems at temperatures up to 300°C: geological implications . In: De Vivo B, Ippolito F, Capaldi G, Simpson PR (eds) Uranium geochemistry, mineralogy, geology, exploration and resources. Institution of Mining and Metallurgy, London, 12-17

Ross GM (1983) Geology and depositional history of the Hornby Bay Group, Northwest Territories, Canada. Ph.D. thesis, Carleton University

Ross GM (1986) Eruptive style and construction of shallow marine mafic tuff cones in the Narakay Volcanic Complex (Proterozoic, Hornby Bay Group, Northwest Territories, Canada). J Volcanol Geotherm Res 27:265-297

Ruzicka V, Thorpe RI (1995) Arsenide vein silver, uranium. In: Eckstrand OR, Sinclair WD, Thorpe RI (eds) Geology of Canadian Mineral Deposit Types. Geological Survey of Canada, Geology of Canada, no. 8, Natural Resources Canada, 287-306

Scharrer M, Kreissl S, Markl G (2019) The mineralogical variability of hydrothermal native element-arsenide (five-element) associations and the role of physicochemical and kinetic factors concerning sulfur. Ore Geol Rev (in press)

Schubert F, Diamond L, Toth T (2007) Fluid-inclusion evidence of petroleum migration through a buried metamorphic dome in the Pannonian Basin, Hungary. Chem Geol 244: 357-381

Seo JH, Guillong M, Aerts M, Zajacz Z, Zajacz Z (2011) Microanalysis of S, Cl, and Br in fluid inclusions by LA–ICP-MS. Chem Geol 284:35-44

Shakotko PH (2014) Paleoregolith and unconformity-type uranium mineralization at Beaverlodge Lake, Great Bear Magmatic Zone, Northwest Territories. M.Sc. thesis, University of Saskatchewan

Sharpe R, Fayek M (2011) The world's oldest observed primary uraninite. Can Mineral 49:1199-1210

Silke R (2009) The Operational History of Mines in the Northwest Territories, Canada. 1-511

Slack JF, Corriveau L, Hitzman MW (2016) A Special Issue Devoted to Proterozoic Iron Oxide-Apatite (±REE) and Iron Oxide Copper-Gold and Affiliated Deposits of Southeast Missouri, USA, and the Great Bear Magmatic Zone, Northwest Territories, Canada: Preface. Econ Geol 111:1803-1814

Smith DJ, Naden J, Jenkin GRT, Keith M (2017) Hydrothermal alteration and fluid pH in alkaline-hosted epithermal systems. Ore Geol Rev 89:772-779

Stacey JS, Kramers JD (1975) Approximation of terrestrial lead isotope evolution by a two-stage model. Earth Planet Sci Lett 26:207-221

Staude S, Wagner T, Markl G (2007) Mineralogy, mineral compositions and fluid evolution at the Wenzel hydrothermal deposit, Southern Germany: implications for the formation of Kongsberg-type silver dposits. Can Mineral 45:1147-1176

Staude S, Werner W, Mordhorst T, Wemmer K, Jacob D, Markl G (2012) Multi-stage Ag–Bi–Co–Ni–U and Cu–Bi vein mineralization at Wittichen, Schwarzwald, SW Germany: geological setting, ore mineralogy, and fluid evolution. Miner Deposita 47:251-276

Steele-MacInnis M, Bodnar RJ, Naden J (2011) Numerical model to determine the composition of H2O–NaCl–CaCl2 fluid inclusions based on microthermometric and microanalytical data. Geochim Cosmochim Acta 75:21-40

Steele-MacInnis M, Lecumberri-Sanchez P, Bodnar RJ (2012) HokieFlincs_H2O-NaCl: A Microsoft Excel spreadsheet for interpreting microthermometric data from fluid inclusions based on the PVTX properties of H2O–NaCl. Comput Geosci 49:334-337

Stern RA, Rayner N (2003) Ages of several xenotime megacrysts by ID-TIMS: potential reference materials for ion probe U–Pb geochronology; Radiogenic Age and Isotopic Studies. Report 16. Geological Survey of Canada, Current Research 2003-F1,

Števko M, Uher P, Ondrejka M, Ozdín D, Bačík P (2014) Quartz–apatite–REE phosphates–uraninite vein mineralization near Čučma (eastern Slovakia): a product of early Alpine hydrothermal activity in the Gemeric Superunit, Western Carpathians. J Geosci 59:209-222

Stoffell B, Appold MS, Wilkinson JJ, McClean NA, Jeffries TE (2008) Geochemistry and Evolution of Mississippi Valley-Type Mineralizing Brines from the Tri-State and Northern Arkansas Districts Determined by LA-ICP-MS Microanalysis of Fluid Inclusions. Econ Geol 103:1411-1435

Teufel S, Heinrich W (1997) Partial resetting of the U-Pb isotope system in monazite through hydrothermal experiments: An SEM and U-Pb isotope study. Chem Geol 137:273-281

Thiersch P,C., Williams-Jones A, Clark J (1997) Epithermal mineralization and ore controls of the Shasta Au-Ag deposit, Toodoggone District, British Columbia, Canada. Miner Deposita 32:44-57

Thorpe R (1974) Lead isotope evidence on the genesis of the silver-arsenide vein deposits of the Cobalt and Great Bear Lake areas, Canada. Econ Geol 69:777-791

Thorpe RI (1971) Lead isotopic evidence on age of mineralization, Great Bear Lake, District of Mackenzie. In: Blackadar RG (ed) Report of activities: Canada Geol. Survey Paper 71-1, pt. B. 72-75

Timofeev A (2018) The solubility, speciation, and transport of the high field strength elements (HFSE) niobium, tantalum, and uranium. Ph.D. Thesis, McGill University

Timofeev A, Migdisov AA, Williams-Jones AE, Roback R, Nelson AT, Xu H (2018) Uranium transport in acidic brines under reducing conditions. Nat Commun 9:1469

Vallini D, Rasmussen B, Krapež B, Fletcher IR, McNaughton NJ (2002) Obtaining diagenetic ages from metamorphosed sedimentary rocks: U-Pb dating of unusually coarse xenotime cement in phosphatic sandstone. Geol 30:1083-1086

Vasconcelos AD, Gonçalves GO, Lana C et al. (2018) Characterization of Xenotime From Datas (Brazil) as a Potential Reference Material for In Situ U-Pb Geochronology. Geochem Geophys 19:2262-2282

Veizer J (1989) Strontium isotopes in seawater through time. Ann Rev Earth Planet Sci 17:141-167

Wagner T, Lorenz J (2002) Mineralogy of complex Co-Ni-Bi vein mineralization, Bieber deposit, Spessart, Germany. Mineral Mag 66:385-407

Walter BF, Burisch M, Markl G (2016) Long-term chemical evolution and modification of continental basement brines – a field study from the Schwarzwald, SW Germany. Geofluids 16:604-623

Wanless RK, Stevens RD, Lachance GR, Delabio RN (1970) Age determinations and geological studies. K-Ar isotopic ages. Report 9. Geological Survey of Canada, Paper 69-2A,

Wanless RK, Loveridge WD (1978) Rubidium-strontium isotopic age studies. Report 2 (Canadian Shield). Geological Survey of Canada, Paper 77-14,

Yardley BWD, Bodnar RJ (2014) Fluids in the Continental Crust. Geochem Perspect 3:1-127

Zajzon N, Szentpeteri K, Szakáll S, Kristály F (2015) The origin of the Avram Iancu U–Ni–Co–Bi–As mineralization, Băiţa (Bihor)metallogenic district, Bihor Mts., Romania. Int J Earth Sci 104:1865-1887

Zhang Y, Frantz JD (1987) Determination of the homogenization temperatures and densities of supercritical fluids in the system NaCl-KCl-CaCl2-H2O using synthetic fluid inclusions. Chem Geol 64:335-350

Chapter 3: Key conclusions and future work

3.1 Key takeaways

This thesis expanded on the working knowledge of mineralization at Eldorado by focusing on key problems in the literature that had not been resolved, often by using analytical techniques that were not available or mainstream during the historic academic interest in the deposit. Detailed ore petrography revealed several rhythmic zoning textures that had been missed, or only hinted at in previous studies without much attention to detail. Fluid inclusion microthermometry and chemical analysis provides new constraints on the composition of ore fluids before and/or during sulphide-stage mineralization, but after the bulk of arsenide-stage mineralization. Fluid composition, along with isotope geochemistry of selected minerals, provides indicators for the source of fluids, and mechanisms that can be used as a model for "five-element" mineralization beneath overlying evaporitic basins.

The most significant conclusions that I would like to stress are as follows:

1: Sulpharsenide inclusions in uraninite were crucial in determining the temporal overlap of relevant metals in circulating fluids. Specifically, the gap between the uraninite and arsenide stage was bridged by observations of sulpharsenides in both assemblages, despite evidence of fracture and dissolution, which might suggest the passage of time and significant changes in equilibrium conditions in mineralizing fluids.

2: Fluid inclusion microthermometry from previous literature (e.g. Changkakoti et al. 1986) had not captured the true nature of primary fluid inclusions in the Eldorado deposit. The very high salinity in fluid inclusion types 2 and 3 had not been properly documented,

and claims of boiling assemblages were not confirmed. Boiling is not a viable trigger for either mineralization or the elevation of salinity in fluid inclusions. Rather, hypersaline brines must have been sourced from elsewhere.

3: LA-ICP-MS analysis of fluid inclusions provide a signature for sedimentary basinal brines that concentrated elements like Ca, Mg, and Br through evaporation of seawater. The origin of fluids from an evaporitic basin is supported by the age of mineralization constrained to a period when evaporates were known to have been developing in the thick succession of the Hornby Basin that likely extended several kilometres above Port Radium ca. 1440 Ma.

4: Radiogenic strontium isotope analysis provides evidence for low fluid/rock ratios, from which it is proposed that wall-rock buffering was an important mechanism for ore deposition. Markl et al. (2016) proposed that rapid reduction of ore fluids by hydrocarbons could explain the pervasive disequilibrium textures and oscillatory zoning observed in some “five-element” veins. Fluid conditions at Eldorado are expected to require an early reductant other than hydrocarbons, which were not observed. Wall-rock buffering could be an adequate buffer for both fO_2 and pH at low fluid/rock ratios, and wall-rock alteration assemblages support the requisite changes. Staude et al. (2007) suggested that multiple pulses of fluid injection from the same source could be a mechanism for the periodic zoning of arsenide and other minerals, which would aptly explain how mineralization proceeded at Eldorado.

3.2 Limitations

A great deal of emphasis was placed on interpreting a paragenetic sequence in order to describe the relative timing of various fluid conditions through microanalysis. The paragenetic sequence presented in this thesis summarizes the most important timing relationships assembled from petrography. However, repetitious zoning, pervasive dissolution textures, and apparent absences of some minerals from one sample to the next, show that a simple timeline is an oversimplification. In many cases there was ambiguity in perceived timing relationships between two or more minerals, which was generalized as an overlap in mineral stability. Perhaps some of the ambiguity could be resolved with a broader representation of samples, but due to the nature of the study area, that was not possible.

Neither the subset of 65 samples used for this study, nor the full sample collection at the GSC, had been exhaustive in representative vein material. Also, many samples had not been well-documented in terms of original location and context within the mine. The limited context was helpfully supplemented by a thorough literature review, but I did desire more source material to further constrain the extent of sulpharsenide zoning within the uraninite stage and xenotime mineralization in the arsenide stage. These were new discoveries that greatly influenced the direction of this project, and it would have been beneficial to see these features in the mine itself.

Both the aforementioned sulpharsenide zoning and xenotime mineralization were identified in uraninite-bearing samples. These samples were difficult to manage during transport, storage, and especially sample preparation. An in-house method for cutting and

polishing fluid inclusion sections from radioactive samples had to be developed, which took more time than expected and discouraged repeat sampling. The arduous preparation process for uraninite-bearing samples turned out to be extremely beneficial and worth the time investment, but in the case of xenotime samples, I just scraped by with enough material for U-Pb analysis. Had there not been enough inclusion-free, 5–10 μm diameter surfaces of xenotime, the geochronological investigation would have been compromised.

In all of the hand samples and cut sections, I was unable to identify any viable fluid inclusion material that corresponded to the uraninite and early arsenide mineralization stages. The clear interpretation from my sample set is that quartz and carbonate did not coprecipitate with uraninite or early arsenide minerals, with the exception of early quartz with network rims of sulpharsenide grains. Most of these gangue minerals fill late fractures and dissolution space. Furthermore, the one "giant quartz vein" sample from my collection that might represent the early stage of mineralization (e.g. Campbell 1955; Jory 1964; Gandhi et al. 2018) did not have any contextual connection with uraninite. It is unclear whether the timing of gangue minerals had been misinterpreted in previous literature or if my sample subset had missed this feature. Either way, the results are limited without a direct constraint on fluid properties during the earliest, and most economically productive, stages of mineralization

The most dramatic limitation encountered in this study was the quality of fluid inclusions themselves. Most inclusions were too small to be viable for microthermometry, and were often marred by recurring problems with metastable phase transitions. After microthermometric analysis had been completed on many assemblages of inclusions, it was

a challenge to ensure reliable data collection from LA-ICP-MS. Fortunately, there were no unexpected issues with laser ablation, but many of the smaller inclusions with good microthermometric data could not be quantified within the detection limits of the mass spectrometer.

3.3 Suggestions for future work

The source of metals for the Eldorado deposit is not well constrained. Eldorado lacks the evidence of significant influence from hydrocarbons, and so is not explained by prevailing theories on the role of hydrocarbons as a metal source, transport agent, and reductant in basin–basement vein deposits (Richard et al. 2010; Burisch et al. 2016; Burke 2019). If a microanalytical study focused on characterizing the metals in brines from the earliest vein stages, it might me possible to better constrain metal signatures.

The wall-rock alteration is not very well described in relation to chemical reactions during ore mineralization. This study did not characterize wall-rocks, but it did determine that mineralizing fluids had undergone significant modification from wall-rock interaction. Ore-stage alteration analysis may provide new information about the evolution of the Eldorado deposit, from a perspective that has not been considered with modern microanalytical techniques.

Lastly, the U endowment throughout the Athabasca and Hornby Bay Basins remain an intriguing topic, both academically, and for mineral exploration. The age of mineralization at Eldorado does not appear to be a coincidence, and is likely linked to many

other U systems in the Canadian Proterozoic basins. My suggestion for future work on this topic is to re-examine the similarities and differences between deposits on local and regional scales, and attempt to solve the question of where Co-Ni-As-Ag-Bi-U vein deposits fit in to the model for other U deposits.

3.4 References

Burisch M, Gerdes A, Walter BF, Neumann U, Fettel M, Markl G (2016) Methane and the origin of five-element veins: Mineralogy, age, fluid inclusion chemistry and ore forming processes in the Odenwald, SW Germany. Ore Geol Rev 81:42-61

Burke JS (2019) The origin of polymetallic Ni-Co-As-Bi-Sb(-Ag-U) veins in the East Arm Basin and southern Slave Province, Northwest Territories. M.Sc. thesis, Saint Mary's University

Campbell DD (1955) Geology of the pitchblende deposits of Port Radium, Great Bear Lake, N.W.T. Ph.D. thesis, California Institute of Technology

Changkakoti A, Morton RD, Gray J (1986) Hydrothermal environments during the genesis of silver deposits in the Northwest Territories of Canada: Evidence from fluid inclusions. Miner Deposita 21:63-69

Gandhi SS, Potter EG, Fayek M (2018) New constraints on genesis of the polymetallic veins at Port Radium, Great Bear Lake, Northwest Canadian Shield. Ore Geol Rev 96:28-47

Jory LT (1964) Mineralogical and isotopic relations in the Port Radium pitchblende deposit, Great Bear Lake, Canada. Ph.D. thesis, California Institute of Technology

Markl G, Burisch M, Neumann U (2016) Natural fracking and the genesis of five-element veins. Miner Deposita 51:703-712

Richard A, Pettke T, Cathelineau M et al. (2010) Brine–rock interaction in the Athabasca basement (McArthur River U deposit, Canada): consequences for fluid chemistry and uranium uptake. Terra Nova 22:303-308

Staude S, Wagner T, Markl G (2007) Mineralogy, mineral compositions and fluid evolution at the Wenzel hydrothermal deposit, Southern Germany: implications for the formation of Kongsberg-type silver dposits. Can Mineral 45:1147-1176

Appendix

Table 2.3: Origin and description of vein samples from the Eldorado mine

Sample #	Vein *	Mine Level *	Mineralogical Description
16 A	#1	250	Massive rdc, qz-carb vein
64	#1	800	Lacking distinct urn textures. Pervasive arsenides and cpy veins
80	#1	925	Chloritized host, cross-cut by successive qz and carb veins. Late disseminated BMS
87	#1	925	Botryoidal urn, qz-hem-carb host with disseminated and vein BMS
88 A	#1	925	Breccia with urn, hem, qz, and some Bi + Ni-Co arsenides
200	-	-	Co-arsenides with ery weathering and qz-carb veins, open-space filling euhedral zoned qz with cpy and dusty hem staining on surface of crystals
201	-	-	Co-arsenides, BMS in qz-carb vein
211	#3	650	nk-saf-Bi florets with white qz-carb infill
212	#3	650	cpy vein
282	#5	125	Massive carb vein
284	#5	125	Weathered breccia with fractured botryoidal urn, concentric saf rims on dissolved dendritic Ag
289	#3	375	Rims of cob-saf around urn, breccia with chloritized host, massive carb, and qz-carb veins with disseminated BMS
388	#1	1050	urn in qz-hem-carb host breccia. BMS in carb veins
405	#1	1050	carb vein and host breccia
415	-	-	Disseminated BMS throughout chloritized, hematized, and brecciated host. Early euhedral vein qz replaced by vein carb
417	#1	250	qz-carb vein breccia
601	-	-	urn and disseminated BMS in qz-carb vein
604	#2 N	1300	Open-space smokey qz vein with late cpy on the surface
608	-	-	nk-saf-Ag (Ag partially dissolved) dendrites, urn with cob veins and nk-saf rim, brecciated hem-chl-act host, late disseminated bn-cpy-sph, and Ag in qz-carb infill
609	-	-	Fractured urn stringers in wall rock, being cross-cut by small qz-hem-cpy-carb veins. Disseminated bn, cpy, ttr, Ag in qz-carb infill
623	#3	1500	Co-arsenides, carb vein
650	#2 N	1400	qz-hem-chl veins with late BMS
684	#2 N	1300	Comb qz vein, disseminated BMS
701	"B" (1175 level only)	1175	Euhedral zoned qz with cpy in outer growth zone, and disseminated cpy-hem in carb infill
704	"B" (1175 level only)	1175	Concentric saf rims on Ag dendrites, minor urn, nk veins, disseminated BMS in qz-carb veins and hem-carb host. Late botryoidal hem-mrc in cavities
704 A	"B" (1175 level only)	1175	Botryoidal urn with associated sulpharsenides, early qz. Massive botryoidal nk with gdf, xn, urn growth zones, saf rims, qz-carb-Bi infill
705	"B" (1175 level only)	1175	Ni-arsenide with anna weathering in carb vein
709	"B" (1175 level only)	1175	nk-saf florets, massive Co-arsenides and ery weathering. Clear euhedral qz crystals with pink carb infill. Late cal-cpy-hem
714	#5	1175	Carb vein material and nk-saf florets with Bi cores, surrounded by chl-act-qz-carb alteration zone
718	#2 N	1175	Euhedral qz growing on dark chloritized host. Cpy-hem-carb filling open space around qz
722 A	#2 N	1175	BMS in hem, qz, carb vein
740	#2	1050	hem, qz vein
761	"D" (650 level only)	650	BMS in carb vein breccia
762 A	"D" (650 level only)	650	Ag vein
773	#1	925	Ni-Co arsenide vein with late BMS
776	#2	375	Arsenide breccia within blocky tan carb vein
778	#2	375	Massive Co-arsenides and BMS in carb vein
783 (2)	#1 N extension	500	Urn and BMS in qz-hem-carb vein breccia

Table 2.3 (continued): Origin and description of vein samples from the Eldorado mine

Sample #	Vein *	Mine Level *	Mineralogical Description
793	#8 / Bear Bay Shear jct.	250	massive nk with saf rims, and Bi-saf in qz-hem-carb breccia
793 (5)	#8 / Bear Bay Shear jct.	250	nk-saf-Bi-ram paragenesis, hematized sugary qz rim, second stage of euhedral clear qz, blocky clear carb with late Bi and hem
801	#5	250	Minor urn vein. Aggregates of nk-saf with qz-carb-Bi infill. Disseminated cpy, py, hem
803	#2 S	250	nk-saf florets (weathered to anna) cut by qz-carb veins. Disseminated BMS in carb
815	#5	500	nk-saf florets with qz-carb veins
815 (2)	#5	500	nk-saf florets with qz-carb veins
821	#8	500	Co-arsenide and carb vein
822	#8	500	nk-saf florets with qz-carb veins
824	#5	500	Ni-Co arsenide and carb breccia
830	#1	800	Urn-qz-carb vein in hematized host
838	#2 S	250	carb vein
840	#5	250	Disseminated BMS in carb vein
841 (27)	Bear Bay Shear	250	Zoned, botryoidal urn with cpy-ttr-cob infill, zoned gdf. carb infill and breccia
841 (60)	Bear Bay Shear	250	Arsenides, urn, hematized qz in carb breccia
845	Bear Bay Shear	250	Ag vein
848	#5	250	qz-chl-act-carb-hem altered host cut by qz and massive carb veins. Disseminated Ag-bn-cpy-ttr
848 (B)	#5	250	qz-chl-act-carb-hem altered host cut by qz and massive carb veins. Disseminated Ag-bn-cpy-ttr
849	-	-	Wall-rock breccia
850	-	-	Urn with cob haloes. Carbonatized and hematized host. Arsenide breccias, nk-Ag dendrites with carb veins and infill
Giant qz vein	-	-	Massive comb qz
SFB240	Sample from box B240	-	nk-saf-Bi-ram paragenesis, hematized sugary qz rim, second stage of euhedral clear qz, blocky clear carb with late Bi and hem
W	Sample from tray T1323	-	Botryoidal urn with associated sulpharsenides, early qz. Massive botryoidal nk with gdf, xn, urn growth zones, saf rims. Bi-bn-cpy disseminated in qz-carb infill

* Original mine locations were retrieved from drawings by Campbell (1955) and Jory (1964), and other documents in the GSC archive. Some samples could not be traced back to their exact location.

Table 2.6: Carbonate major element, stable isotope, and radiogenic isotope chemistry.

Sample	Mineral	Vein stage	Description
201	dol	sulphide	Grey, in vug in qz, pre- to syn-cpy
211	dol	sulphide	White, post-qz, pre-Bi
608	Fe-dol	late arsenide	Pink, interweaving, post-Ag-arsenide dendrite
701	dol	sulphide	White, massive, post-qz, syn- to post-cpy
718	cal	late carbonate	White, in vug in dol, syn- to post-cpy, hem
762 A	sdr-rdc	late carbonate	Pink, post-Ag
776	dol	late arsenide	Buff, blocky, post-arsenide
793 (5)	Fe-dol	sulphide	Grey, post-qz, syn-hem, pre-Bi
801	dol	sulphide	Pink, post-qz, pre- to syn-cpy
803	sdr-mgs	late carbonate	White, massive, post-dol
815	dol	late arsenide	White, sparry, barren, immediately post-arsenide
840	Fe-dol	sulphide	Grey, pre- to syn-bn, cpy
848	dol	sulphide	Grey, syn-bn, cpy, Ag
850	sdr-mgs	late carbonate	Pink, interweaving, post-dol, Ag-arsenide dendrite
SFB240	Fe-dol	sulphide	Grey, post-qz, syn-hem, pre-Bi

Sample	Mg (wt.%)	Ca (wt.%)	Mn (wt.%)	Fe (wt.%)	Na (ppm)	Al (ppm)	K (ppm)	Ba (ppm)	Rb (ppm)	Sr (ppm)
201	8.43	16.3	0.976	2.23	93.7	2.77	40.1	1.44	0.0782	27.8
211	7.99	14.7	0.321	1.79	58.0	6.27	30.7	4.74	0.0418	30.5
608	9.49	9.48	0.794	3.49	47.7	21.3	38.7	46.0	0.107	25.8
701	8.80	16.7	1.93	1.51	67.1	2.45	29.5	1.71	0.0260	11.4
718	0.0505	30.1	0.923	0.347	19.9	2.88	20.8	1.07	0.00765	20.6
762 A	1.35	3.77	15.5	11.7	79.1	10.1	16.2	2.07	0.0187	7.31
776	7.94	15.3	1.37	2.63	126	3.88	41.9	3.64	0.127	31.7
793 (5)	7.32	14.0	0.950	3.15	30.5	3.65	23.5	85.5	0.0208	24.6
801	10.3	16.9	0.0731	0.625	54.1	9.84	26.5	1.66	0.0239	42.8
803	7.79	3.05	0.834	4.68	65.8	12.1	29.0	58.9	0.0488	13.1
815	9.12	15.9	0.609	2.19	114	3.70	37.7	1.85	0.0770	52.5
840	7.35	14.9	2.74	3.27	72.9	2.85	24.6	3.43	0.0334	14.8
848	9.24	16.9	1.40	2.68	62.3	2.11	23.7	1.00	0.0202	13.1
850	11.3	1.14	2.99	9.68	88.7	23.0	36.4	18.0	0.0388	6.86
SFB240	7.38	13.6	1.09	2.71	41.0	3.38	20.9	1.72	0.0187	62.3

Sample	$\delta^{13}C_{VPDB}$ (‰)	$\delta^{18}O_{VSMOW}$ (‰)	$^{87}Rb/^{86}Sr$	$^{87}Rb/^{86}Sr_o$	$^{87}Sr/^{86}Sr$	Absolute error	$^{87}Sr/^{86}Sr_o$
201	-2.6	15.6	0.00794	0.00811	0.71327	0.00056	0.71311
211	-3.2	15.2	0.00387	0.00394	0.70594	0.00001	0.70586
608	-2.6	14.4	0.0117	0.0120	0.71213	0.00017	0.71189
701	-3.4 (-3.3)	22.4 (22.5)	0.00642	0.00655	0.70916	0.00002	0.70903
718	-6.7 (6.5)	10.9 (11.2)	0.00105	0.00107	0.72216	0.00002	0.72213
762 A	-2.5	18.5	0.00721	0.00736	0.71022	0.00001	0.71008
776	-2.8	13.2	0.0113	0.0116	0.71519	0.00003	0.71496
793 (5)	-1.4	18.2	0.00239	0.00244	0.71919	0.00011	0.71914
801	-2.2	14.3	0.00158	0.00161	0.70462	0.00008	0.70459
803	-2.7 (2.8)	20.2 (20.3)	0.0105	0.0107	0.71366	0.00002	0.71344
815	-2.8	14.7	0.00414	0.00422	0.71086	0.00004	0.71077
840	-2.5	16.1	0.00637	0.00650	0.71443	0.00079	0.71431
848	-2.3	16.0	0.00436	0.00445	0.70830	0.00009	0.70821
850	-2.3	15.6	0.0160	0.0163	0.72393	0.00106	0.72361
SFB240	-2.6	14.0	0.000845	0.000863	0.72185	0.00415	0.72183

Stable isotope replicate analyses are displayed in parentheses. Isotope ratios involving intial ^{86}Sr were calculated using $\lambda = 1.42 \times 10^{-11}$ y^{-1}, with an assumed age of 1440 Ma. Age-dependent error for calculations of initial isotope ratios are negligible due to extremely low Rb content. Thus, the often negligible difference between $^{87}Sr/^{86}Sr$ and $^{87}Sr/^{86}Sr_o$.

Table 2.7: In situ oxygen isotope data for arsenide- and sulphide-stage quartz, and primary uraninite

Sample	Vein Stage (qz)	Spot ID	$\delta^{18}O_{V\text{-}SMOW}$(‰)	Description	Zoning
608	late arsenide	b 01	13.8	Euhedral in barren carbonate vein, cross-cutting chloritized wallrock	core-rim
	"	b 02	13.5	"	rim
	"	b 03	15.5	"	core-rim
	sulphide	c 04	17.9	Euhedral in chloritized wallrock on margins of sulphide-stage carbonate vein	rim
	"	c 05	13.8	"	core
841	late arsenide	d 06	15.4	Massive, euhedral with growth zones. Late infill by chl → blocky dol → cal + cof	clear rim
	"	d 07	16.3	"	clear rim
	"	d 08	15.2	"	clear rim
	"	d 09	14.1	"	rim of incl.-rich core
	"	d 10	16.5	"	clear rim
	"	d 11	14.7	"	clear rim
	"	d 12	18.2	"	clear rim
	"	d 13	15.0	"	rim of incl.-rich core
609	sulphide	e 14	15.5	Euhedral with CL zoning, in dol-hem-cpy-brt veins cross-cutting urn → dol + cpy	inclusion-rich core
	"	e 15	13.5	"	rim of incl.-rich core
	"	e 16	15.3	"	clear rim
	"	e 17	15.5	"	clear rim
	"	e 18	16.6	"	inclusion-rich core
	"	e 19	16.1	"	rim of incl.-rich core
	"	e 20	13.7	"	clear rim
	late arsenide	i 01	15.6	Euhedral with CL zoning. Late infill by Fe-dol → cpy	clear rim
	"	i 02	14.8	"	core
704	arsenide	l 03	18.7	Replacing Ag-saf dendrite. Late infill by Mn-dol	-
	"	l 04	18.2	"	-
	"	l 05	19.2	"	-
SFB240	late arsenide	o 07	17.8	Euhedral, post-saf. Late infill by Bi	rim
	"	o 08	15.5	"	core
	"	o 09	17.6	"	rim
	"	o 10	14.5	"	core
	"	o 11	16.4	"	core
	late arsenide	p 12	15.8	Euhedral, growing from sugary, hematized quartz. Late infill by (Fe) dol → Bi	core
	"	p 13	16.0	"	rim
	late arsenide	p 14	17.0	Sugary, hematized. Growing from saf rims on S-saf florets	interior
	"	p 15	17.7	"	interior

Table 2.7 (continued): In situ oxygen isotope data for arsenide- and sulphide-stage quartz, and primary uraninite

Sample	Vein Stage (qz)	Spot ID	$\delta^{18}O_{V\text{-}SMOW}$(‰)	Description	Zoning
714	late arsenide	q 20	12.9 (12.6)	Euhedral, post-apy, cob, saf. Late infill by dol → Bi	core
	"	q 21	15.9	"	rim
	late arsenide	q 17	14.9	Euhedral in massive qz vein cross-cutting arsenides	core
	"	q 18	14.8	"	core
	"	q 19	14.2	"	rim
211	late arsenide	r 01	16.7 (15.7)	Euhedral, post-nk, S-saf florets. Late infill by dol → Bi → cal	rim
	"	r 02	12.6	"	core
	"	r 03	13.3	"	core
	"	r 04	14.6	"	core-rim
	"	r 05	15.1	"	core-rim
	"	r 06	15.8	"	rim
822	late arsenide	s 21	16.7	Euhedral in barren carbonate vein, cross-cutting chloritized wallrock	grain 1 rim
	"	s 22	17.5	"	grain 2 core-rim
	"	s 23	16.5	"	grain 2 core-rim
	"	s 24	15.8	"	grain 3 rim
	"	s 25	14.1	"	grain 3 core
	"	s 26	15.0	"	grain 3 core
	"	s 27	15.3	"	grain 3 rim
709	late arsenide	t 07	15.0	Massive, euhedral with growth zones. Late infill by pink dol → Fe-dol → Mn-cal	core
	"	t 08	17.9	"	messy
	"	t 09	12.1	"	core
	"	t 10	16.9	"	core
	"	t 11	14.2	"	rim
	"	t 12	14.5	"	rim
701	late arsenide	u 13	14.2	Euhedral with CL zoning. Syn-cpy with late infill by dol → cpy → cal	pale CL rim
	"	u 14	12.9	"	dark CL core
	"	u 15	14.8	"	pale CL core
	"	u 16	13.2	"	dark CL core
	"	u 17	14.9	"	dark CL core
	"	u 18	15.5	"	pale CL inner core
	"	u 19	15.4	"	pale CL inner core
	"	u 20	16.9	"	dark CL inner core
	"	u 21	16.4	"	pale CL inner core
	"	u 22	14.2	"	dark CL inner core

Table 2.7 (continued): In situ oxygen isotope data for arsenide- and sulphide-stage quartz, and primary uraninite

Sample	Vein Stage (qz)	Spot ID	$\delta^{18}O_{V\text{-}SMOW}$(‰)	Description	Zoning
718	late arsenide	v 23	14.6	Massive, euhedral with CL zoning. Late infill by cpy + cal	CL light rim
	"	v 24	15.8	"	CL light rim
	"	v 25	15.9	"	CL light rim
	"	v 26	16.0	"	CL light rim
	"	v 27	16.4	"	CL light rim
	"	v 28	15.0	"	CL dark core
	"	v 29	16.0	"	CL dark core
W	early arsenide	w 03	16.2	near botryoidal urn wall; interior zone with cob-gdf crystals along qz rims	-
	"	w 04	17.4	"	-
	"	w 05	20.3	"	-
	"	w 19	18.6	open-space filling just outside of ring-form urn grains	-
	"	w 22	17.5	"	-
	"	w 24	17.2	"	-
	"	w 30	16.0	"	-
	"	w 67	16.8	between botryoidal urn walls; interior zone with cob-gdf crystals along qz rims	-
	"	w 64	15.3	"	-
	"	w 01	18.3	near botryoidal urn wall; might have some cob-gdf crystals along qz rims	-
	"	w 14	16.7	near botryoidal urn wall; exterior zone with barren qz rims	-
	"	w 15	17.6	"	-
	"	w 41	17.4	inside ring-form urn, associated with nk+gdf	-
	"	w 45	17.2	"	-
	"	w 44	17.6	"	-
	"	w 39	17.6	"	-
	"	w 60	16.1	between botryoidal urn walls; exterior zone with barren qz rims	-
	"	w 54	16.5	"	-

Table 2.7 (continued): In situ oxygen isotope data for arsenide- and sulphide-stage quartz, and primary uraninite

Sample	Vein Stage (urn)	Spot ID	$\delta^{18}O_{V\text{-}SMOW}$(‰)	Description	Zoning
608	uraninite	x 1	-30.0	Sulpharsenide and chlorite fracture infill	-
	"	x 2	-27.8	"	-
	"	x 3	-30.9	"	-
609	"	y 1	-31.1	Chalcopyrite, dolomite, tetrahedrite fracture infill	-
	"	y 2	-33.9	"	-
	"	y 3	-34.6	"	-
	"	y 4	-35.4	"	-
	"	y 5	-32.3	"	-
	"	y 6	-31.5	"	-
	"	y 7	-35.6	"	-
	"	y 11	-37.3	"	-
	"	y 12	-37.5	"	-
	"	y 13	-35.4	"	-
	"	y 14	-33.7	Sulpharsenide and chlorite fracture infill	-
	"	y 15	-34.5	"	-
	"	y 16	-31.2	"	-
289	"	z 1	-32.4	Sulpharsenide inclusion zone	core (transect 1)
	"	z 2	-32.6	Inclusion-free zone	transect 1
	"	z 3	-27.7	Sulpharsenide inclusion zone. Inclusion caught in beam	transect 1
	"	z 4	-30.9	Sulpharsenide inclusion zone	transect 1
	"	z 5	-32.2	Inclusion-free zone	transect 1
	"	z 6	-33.7	Sulpharsenide inclusion zone	rim (transect 1)
	"	z 7	-31.2	Inclusion-free zone	core (transect 2)
	"	z 8	-30.4	Sulpharsenide inclusion zone	transect 2
	"	z 9	-35.4	Inclusion-free zone	transect 2
	"	z 10	-30.4	Sulpharsenide inclusion zone	transect 2
	"	z 11	-30.3	Inclusion-free zone	transect 2
	"	z 12	-31.0	Sulpharsenide inclusion zone	rim (transect 2)

Table 2.8: Fluid inclusion microthermometry measurements and salinity determinations.

						Phase change temperatures (°C)				Salinity (wt. %) *		
Sample	**FIA**	**FI Type**	**Phases (21 °C)**	**Host**	**Vein Stage**	**T_m^{ice}**	**T_v**	**T_d^H**	**T_h**	**S_{wt}**	**wt% NaCl**	**wt% $CaCl_2$**
709	A5	Type 1	L, V	qz	late arsenide	-24.5	214.3		214.3	23.9	12.9	11.0
709	Single	Type 1	L, V	qz	late arsenide	-23.0	340.0		340.0	23.2	12.5	10.7
709	A7	Type 1	L, V	qz	late arsenide	-21.0	327.1		327.1	22.1	11.9	10.2
709	A7	Type 1	L, V	qz	late arsenide	-22.0	314.7		314.7	22.6	12.2	10.4
709	A7	Type 1	L, V	qz	late arsenide	-22.0	356.6		356.6	22.6	12.2	10.4
709	A7	Type 1	L, V	qz	late arsenide	-23.1	306.3		306.3	23.2	12.5	10.7
709	A7	Type 1	L, V	qz	late arsenide	-21.0	301.1		301.1	22.1	11.9	10.2
709	A7	Type 1	L, V	qz	late arsenide	-21.0	339.6		339.6	22.1	11.9	10.2
709	A7	Type 1	L, V	qz	late arsenide	-24.0	351.5		351.5	23.7	12.8	10.9
709	A10	Type 1	L, V	qz	late arsenide	-25.7	170.0		170.0	24.5	13.2	11.3
709	A10	Type 1	L, V	qz	late arsenide	-25.6	161.6		161.6	24.5	13.2	11.2
709	A10	Type 1	L, V	qz	late arsenide	-25.6	163.3		163.3	24.5	13.2	11.2
718	Single	Type 1	L, V	qz	late arsenide	-21.0	44.0		44.0	22.1	11.9	10.2
718	A14	Type 1	L, V	qz	late arsenide	-22.5	130.6		130.6	22.9	12.4	10.5
718	A14	Type 1	L, V	qz	late arsenide	-24.0	35.5		35.5	23.7	12.8	10.9
718	A14	Type 1	L, V	qz	late arsenide	-25.0	250.0		250.0	24.2	13.1	11.1
718	A14	Type 1	L, V	qz	late arsenide	-26.0	250.0		250.0	24.6	13.3	11.3
714	A19	Type 2	L, V, H	qz	late arsenide	-33.0	140.0	100.0	140.0	31.6	13.0	18.5
714	A19	Type 2	L, V, H	qz	late arsenide		150.0		150.0			
714	A19	Type 2	L, V, H	qz	late arsenide		180.0		180.0			
714	A19	Type 2	L, V, H	qz	late arsenide		134.0		134.0			
709	A20	Type 2	L, V, H	qz	late arsenide	-31.0	128.0		128.0			
709	A20	Type 2	L, V, H	qz	late arsenide		127.5		127.5			
709	A20	Type 2	L, V, H	qz	late arsenide		131.6		131.6			
709	A20	Type 2	L, V, H	qz	late arsenide		140.1		140.1			
709	A20	Type 2	L, V, H	qz	late arsenide		150.5		150.5			
709	Single	Type 2	L, V, H	qz	late arsenide	-38.5						
709	A21	Type 2	L, V, H	qz	late arsenide	-36.3	104.4	159.0	159.0	34.6	15.5	19.1
709	A21	Type 2	L, V, H	qz	late arsenide		89.6	188.0	188.0			
709	A22	Type 2	L, V, H	qz	late arsenide	-31.4	240.0		240.0			
709	A22	Type 2	L, V, H	qz	late arsenide	-31.4	96.0		96.0			
709	A23	Type 2	L, V, H	qz	late arsenide		238.7		238.7			
709	A23	Type 2	L, V, H	qz	late arsenide		216.0	159.5	216.0			
709	A23	Type 2	L, V, H	qz	late arsenide	-36.0	233.5	150.2	233.5	34.2	15.0	19.2
709	A23	Type 2	L, V, H	qz	late arsenide		202.1		202.1			
709	A23	Type 2	L, V, H	qz	late arsenide		200.9		200.9			
709	A23	Type 2	L, V, H	qz	late arsenide		202.5		202.5			
709	A25	Type 2	L, V, H	qz	late arsenide	-42.0	215.8	320.0	320.0	44.9	31.0	13.9
709	A25	Type 2	L, V, H	qz	late arsenide		190.2		190.2			
709	A25	Type 2	L, V, H	qz	late arsenide		204.9		204.9			
709	A25	Type 2	L, V, H	qz	late arsenide		290.0		290.0			
709	A25	Type 2	L, V, H	qz	late arsenide		182.1		182.1			
709	A26	Type 2	L, V, H	qz	late arsenide	-32.0	199.1	210.2	210.2	35.8	20.7	15.1
709	A26	Type 2	L, V, H	qz	late arsenide		180.0	205.0	205.0			
709	A27	Type 2	L, V, H	qz	late arsenide	-34.7	320.2	153.0	320.2	33.9	15.5	18.4
709	A27	Type 2	L, V, H	qz	late arsenide		204.8	139.6	204.8			
709	A28	Type 2	L, V, H	qz	late arsenide		131.0	211.5	211.5			
709	A28	Type 2	L, V, H	qz	late arsenide		115.0	200.0	200.0			
709	A28	Type 2	L, V, H	qz	late arsenide		147.0	215.0	215.0			
709	A28	Type 2	L, V, H	qz	late arsenide		138.9	192.4	192.4			
709	Single	Type 2	L, V, H	qz	late arsenide		110.2		110.2			
709	Single	Type 2	L, V, H	qz	late arsenide		165.7		165.7			

Table 2.8 (continued): Fluid inclusion microthermometry measurements and salinity determinations.

						Phase change temperatures (°C)				Salinity (wt. %) *		
Sample	**FIA**	**FI Type**	**Phases (21 °C)**	**Host**	**Vein Stage**	**T_m^{ice}**	**T_v**	**T_d^H**	**T_h**	**S_{wt}**	**wt% NaCl**	**wt% $CaCl_2$**
709	A30	Type 2	L, V, H	qz	late arsenide	-33.9			0.0			
709	A30	Type 2	L, V, H	qz	late arsenide	-35.9			0.0			
709	Single	Type 2	L, V, H	qz	late arsenide	-34.0			0.0			
709	Single	Type 2	L, V, H	qz	late arsenide		163.0	180.0	180.0			
709	Single	Type 2	L, V, H	qz	late arsenide		220.0		220.0			
709	Single	Type 2	L, V, H	qz	late arsenide			300.0	300.0			
709	Single	Type 2	L, V, H	qz	late arsenide		134.9	220.0	220.0			
718	Single	Type 2	L, V, H	qz	late arsenide		110.0	119.0	119.0			
718	A32	Type 2	L, V, H	qz	late arsenide		140.0	157.0	157.0			
718	A32	Type 2	L, V, H	qz	late arsenide		140.5	165.0	165.0			
718	A32	Type 2	L, V, H	qz	late arsenide		140.5	154.0	154.0			
718	A32	Type 2	L, V, H	qz	late arsenide		140.5	160.0	160.0			
718	A32	Type 2	L, V, H	qz	late arsenide		140.5	160.0	160.0			
718	A33	Type 2	L, V, H	qz	late arsenide	-41.2	87.8	154.2	154.2	35.4	14.2	21.3
718	A33	Type 2	L, V, H	qz	late arsenide	-39.6	106.5	149.5	149.5	34.9	14.1	20.8
718	A33	Type 2	L, V, H	qz	late arsenide	-38.1	115.6	152.7	152.7	34.8	14.6	20.1
718	A33	Type 2	L, V, H	qz	late arsenide		116.0	143.0	143.0			
718	A33	Type 2	L, V, H	qz	late arsenide		97.4	139.4	139.4			
718	A33	Type 2	L, V, H	qz	late arsenide	-43.4	117.7	167.0	167.0	36.4	14.8	21.5
718	Single	Type 2	L, V, H	qz	late arsenide		147.0	185.0	185.0			
718	A34	Type 2	L, V, H	qz	late arsenide	-42.2	124.6	155.7	155.7	35.7	14.1	21.5
718	A34	Type 2	L, V, H	qz	late arsenide	-43.3	137.4	154.0	154.0	35.8	13.9	21.9
718	A34	Type 2	L, V, H	qz	late arsenide	-42.2	139.6	157.7	157.7	35.8	14.3	21.5
718	A34	Type 2	L, V, H	qz	late arsenide	-41.3	133.6	153.2	153.2	35.4	14.1	21.3
718	Single	Type 2	L, V, H	qz	late arsenide		90.5		90.5			
718	Single	Type 2	L, V, H	qz	late arsenide		212.9	254.7	254.7			
718	A35	Type 2	L, V, H	qz	late arsenide	-41.9	204.3	148.0	204.3	35.3	13.6	21.7
718	A35	Type 2	L, V, H	qz	late arsenide	-42.5	255.0	169.0	255.0	36.3	15.1	21.2
709	Single	Type 2	L, V, H	qz	late arsenide		116.9		116.9			
SFB240	A36	Type 3	L, V, H	carb	sulphide	-32.9	155.6	150.0	155.6	33.3	15.9	17.4
SFB240	A36	Type 3	L, V, H	carb	sulphide	-30.6	157.0	154.9	157.0	32.8	17.2	15.5
SFB240	A36	Type 3	L, V, H	carb	sulphide		76.4		76.4			
SFB240	A36	Type 3	L, V, H	carb	sulphide		104.6		104.6			
SFB240	A36	Type 3	L, V, H	carb	sulphide		143.0		143.0			
SFB240	A36	Type 3	L, V, H	carb	sulphide		151.3		151.3			
SFB240	A36	Type 3	L, V, H	carb	sulphide		163.7		163.7			
SFB240	A37	Type 3	L, V, H	carb	sulphide		201.1	215.0	215.0			
SFB240	A37	Type 3	L, V, H	carb	sulphide		205.0	215.0	215.0			
SFB240	A37	Type 3	L, V, H	carb	sulphide		215.7	215.0	215.7			
SFB240	A37	Type 3	L, V, H	carb	sulphide		204.4		204.4			
SFB240	A37	Type 3	L, V, H	carb	sulphide		205.0		205.0			
SFB240	A37	Type 3	L, V, H	carb	sulphide		205.0		205.0			
SFB240	A37	Type 3	L, V, H	carb	sulphide		205.0		205.0			
SFB240	A37	Type 3	L, V, H	carb	sulphide		205.0		205.0			
SFB240	A37	Type 3	L, V, H	carb	sulphide		205.0		205.0			
SFB240	A38	Type 3	L, V, H	carb	sulphide		189.9		189.9			
SFB240	A38	Type 3	L, V, H	carb	sulphide	-32.0	194.0	220.2	220.2	36.4	21.6	14.8
SFB240	A38	Type 3	L, V, H	carb	sulphide		210.0		210.0			
709	Single	Type 3	L, V, H	carb	sulphide	-40.4	138.5		138.5			
709	A40	Type 3	L, V, H	carb	sulphide		65.7		65.7			
709	A40	Type 3	L, V, H	carb	sulphide		117.4		117.4			

Table 2.8 (continued): Fluid inclusion microthermometry measurements and salinity determinations.

						Phase change temperatures (°C)				Salinity (wt. %) *		
Sample	**FIA**	**FI Type**	**Phases (21 °C)**	**Host**	**Vein Stage**	**T_m^{ice}**	**T_v**	**T_d^H**	**T_h**	**S_{wt}**	**wt% NaCl**	**wt% $CaCl_2$**
SFB240	A41	Type 3	L, V, H	carb	sulphide		137.4	132.8	137.4			
SFB240	A41	Type 3	L, V, H	carb	sulphide			132.7	132.7			
SFB240	A41	Type 3	L, V, H	carb	sulphide	-40.6	137.0	132.6	137.0	34.5	12.8	21.7
SFB240	Single	Type 3	L, V, H	carb	sulphide	-31.3	140.0	162.0	162.0	33.3	17.3	15.9
SFB240	A42	Type 3	L, V, H	carb	sulphide		202.0		202.0			
SFB240	A42	Type 3	L, V, H	carb	sulphide		196.9	218.6	218.6			
SFB240	A42	Type 3	L, V, H	carb	sulphide	-33.1	204.9	220.3	220.3	36.7	21.2	15.5
SFB240	Single	Type 4	L, V	carb	sulphide	-23.4				23.4	12.6	10.8
SFB240	A43	Type 4	L, V	carb	sulphide		136.3		136.3			
SFB240	A43	Type 4	L, V	carb	sulphide		134.1		134.1			
SFB240	A43	Type 4	L, V	carb	sulphide		134.4		134.4			
SFB240	A43	Type 4	L, V	carb	sulphide		138.9		138.9			
SFB240	A44	Type 4	L, V	carb	sulphide		122.8		122.8			
SFB240	A44	Type 4	L, V	carb	sulphide		124.8		124.8			
SFB240	Single	Type 4	L, V	carb	sulphide		160.4		160.4			
SFB240	A45	Type 4	L, V	carb	sulphide		194.2		194.2			
SFB240	A45	Type 4	L, V	carb	sulphide		202.5		202.5			
SFB240	A46	Type 4	L, V	carb	sulphide		105.4		105.4			
SFB240	A46	Type 4	L, V	carb	sulphide		80.0		80.0			
SFB240	A46	Type 4	L, V	carb	sulphide		100.3		100.3			
SFB240	A46	Type 4	L, V	carb	sulphide		104.1		104.1			
SFB240	A46	Type 4	L, V	carb	sulphide		124.5		124.5			
SFB240	B1	Type 3	L, V, H	carb	sulphide	-33.0	183.5	216.0	216.0	36.4	20.9	15.5
SFB240	B1	Type 3	L, V, H	carb	sulphide	-31.5	183.9	212.0	212.0	35.8	21.0	14.7
SFB240	Single	Type 3	L, V, H	carb	sulphide		195.0					
SFB240	B2	Type 3	L, V, H	carb	sulphide	-32.6	198.8	221.0	221.0	36.6	21.4	15.1
SFB240	B2	Type 3	L, V, H	carb	sulphide	-31.3	186.3	214.3	214.3	35.8	21.3	14.5
SFB240	B2	Type 3	L, V, H	carb	sulphide	-31.9	180.8		180.8			
SFB240	B2	Type 3	L, V, H	carb	sulphide	-33.0	186.0		186.0			
709	B4	Type 2	L, V, H	qz	late arsenide	30.8	125.9	181.1	181.1	34.0	18.9	15.1
709	B4	Type 2	L, V, H	qz	late arsenide	30.5	108.1	170.7	170.7	33.4	18.3	15.1
709	B5	Type 2	L, V, H	qz	late arsenide	-33.0	284.4	183.7	284.4	34.8	18.2	16.6
709	B5	Type 2	L, V, H	qz	late arsenide	-31.0	297.0	157.8	297.0	33.0	17.2	15.8
709	Single	Type 2	L, V, H	qz	late arsenide		236.0		236.0			
709	B6	Type 2	L, V, H	qz	late arsenide		180.4	220.0	220.0			
709	B6	Type 2	L, V, H	qz	late arsenide		194.5	220.0	220.0			
709	B9	Type 2	L, V, H	qz	late arsenide	-40.3	113.7	130.0	130.0	34.3	12.6	21.7
709	Single	Type 2	L, V, H	qz	late arsenide			144.0	144.0			
709	B9	Type 2	L, V, H	qz	late arsenide	-40.4	112.1	170.0	170.0	36.0	15.5	20.4
718	B10	Type 1	L, V	qz	late arsenide	-22.5	160.1		160.1	22.9	12.4	10.5
718	B10	Type 1	L, V	qz	late arsenide	-23.3	149.0		149.0	23.3	12.6	10.7
718	B10	Type 1	L, V	qz	late arsenide	-22.1	171.8		171.8	22.7	12.3	10.4
718	B11	Type 1	L, V	qz	late arsenide	-17.3	169.1		169.1	19.8	10.7	9.1
718	B11	Type 1	L, V	qz	late arsenide	-17.6	235.0		235.0	20.0	10.8	9.2
718	B11	Type 1	L, V	qz	late arsenide	-17.1	235.0		235.0	19.7	10.6	9.0
718	B11	Type 1	L, V	qz	late arsenide	-17.1	235.0		235.0	19.7	10.6	9.0
718	B11	Type 1	L, V	qz	late arsenide	-17.2	209.4		209.4	19.7	10.7	9.1
718	Single	Type 1	L, V	qz	late arsenide	-25.2	196.5		196.5	24.3	13.1	11.2
718	Single	Type 2	L, V, H	qz	late arsenide		126.2	187.0	187.0			
718	B12	Type 2	L, V, H	qz	late arsenide	-31.3	116.1	153.0	153.0	32.9	16.8	16.2
718	B12	Type 2	L, V, H	qz	late arsenide	-33.3	140.1	226.9	226.9	37.1	21.8	15.3

** The ratio of NaCl to $CaCl_2$ salts in fluid inclusion types 1 and 4 are set at 54% NaCl, and 46% $CaCl_2$, based on corresponding average ratios for Na and Ca content in type 1 inclusions, measured by LA-ICP-MS.*

Table 2.10: Chemical composition (ppm) of fluid inclusions from LA-ICP-MS analysis.

Sample	FIA	Fl Type	Host	Spot ID	Li	B	Na	Mg	Al	Si	Cl	K	Ca	Mn	Fe
714	C1	Type 3	Mn-dol	08a23	152	<302	86700	-	257	<13200	-	29800	58900	-	-
714	C1	Type 3	Mn-dol	08a24.1	109	<537	91800	-	<171	<24800	-	26000	58900	-	-
714	C1	Type 3	Mn-dol	08a24.2	172	<407	91400	-	<127	<18300	-	27000	58900	-	-
714	C2	Type 3	Mn-dol	08a25	<131	<688	86200	-	<220	<33300	-	30400	58900	-	-
714	C3	Type 3	Mn-dol	08a26.1	149	307	92100	-	4960	<5630	-	20200	58900	-	-
714	C3	Type 3	Mn-dol	08a26.2	118	<380	92200	-	5430	<16000	-	21200	58900	-	-
714	C3	Type 3	Mn-dol	08a27.1	194	<572	91900	-	<165	<25100	-	20900	58900	-	-
714	C3	Type 3	Mn-dol	08a27.2	153	275	89600	-	<58.8	9280	-	25700	58900	-	-
714	C3	Type 3	Mn-dol	08a28	138	268	90300	-	<76.9	<11700	-	24000	58900	-	-
714	C5	Type 3	qz	08a34	2170	692	93100	592	61100	-	-	13300	57700	7280	3860
714	Single	Type 3	qz	08a37	<90.7	<580	65400	21200	<150	-	-	6140	87100	8410	8560
718	Single	Type 1	qz	08a38	<19.3	<118	55000	9130	10800	-	-	5410	59500	932	269
718	C6	Type 1	qz	08a39	1310	<1250	95600	<711	32300	-	-	3460	<16100	<219	<1350
718	C6	Type 1	qz	08a40	<87.0	<534	66100	2830	13600	-	-	12600	43900	<89.2	5080
718	C6	Type 1	qz	08a41	133	<266	76600	1060	49700	-	-	19000	22400	192	1380
718	Single	Type 1	qz	08a42	684	169	42100	19500	91200	-	-	33200	49500	1150	22800
718	Single	Type 1	qz	08a44	<1.87	193	53200	1900	12100	-	-	8370	67400	4740	1710
718	C7	Type 1	qz	08a45	32.1	112	49700	2790	27300	-	-	12800	22500	783	1250
718	C7	Type 1	qz	08a46	1510	<50.1	59600	1720	10300	-	-	5290	38800	3110	1810
718	Single	Type 1	qz	08a47	<6.73	141	50900	2050	<11.0	-	-	702	74600	6980	1960
718	C7	Type 1	qz	08a48	825	109	28800	663	<12.6	-	-	951	116000	693	<46.7
718	Single	Type 1	qz	08a50	1230	227	65800	497	31200	-	-	824	51100	5000	318
718	C8	Type 1	qz	08a54	<300	<1690	79600	2440	<465	-	-	2050	26400	319	<1680
718	C9	Type 1	qz	08a55	1490	681	47800	<170	46500	-	-	243	<3750	<47.3	<288
718	C9	Type 1	qz	08a56	<350	<1970	61200	<1270	36900	-	-	<1430	<25200	<324	<1910
718	C9	Type 1	qz	08a57	379	481	77800	1790	52200	-	-	6630	27600	78.9	<176
718	C10	Type 1	qz	08a58	314	<19.9	58600	1270	<5.68	-	-	2930	64800	22.5	<20.8
718	C10	Type 1	qz	08a59	<89.3	<500	85400	<302	<148	-	-	2970	19100	130	<528
718	C8	Type 1	qz	08a60	<7.12	124	68100	1440	3680	-	-	10000	43300	157	75.9
718	C9	Type 1	qz	08a61	<108	<622	83100	<352	<173	-	-	1160	24500	<105	<622
718	C11	Type 1	qz	08a62	<22.9	<121	56600	5320	10500	-	-	16600	53900	618	618
718	C12	Type 2	qz	08a63.1	9150	<4990	140000	<2910	126000	-	-	<3620	<64300	<819	<4900
718	C12	Type 2	qz	08a63.2	<93.3	<529	73500	3070	<147	-	-	1490	113000	3640	<536
718	C12	Type 2	qz	08a64	<126	<713	87900	557	<193	-	-	1650	92500	<114	<694
718	C11	Type 1	qz	08a65	<21.6	139	60400	487	29000	-	-	899	13700	476	<124
718	C11	Type 1	qz	08a67	381	265	67600	4450	<69.4	-	-	19900	30500	1280	2160
718	C12	Type 2	qz	08a68	432	277	76300	4000	3650	-	-	17300	93500	1510	347
718	C11	Type 1	qz	08a69	299	148	52500	664	7990	-	-	988	61700	1090	166
718	C13	Type 1	qz	08a73	622	<638	69600	421	11200	-	-	21600	14100	<96.5	2290
718	C13	Type 1	qz	08a75	1040	<218	65200	859	19900	-	-	9600	12600	167	<218
718	C13	Type 1	qz	08a76	2860	<892	92500	1100	3340	-	-	3040	<12000	<154	<929
718	C15	Type 1	qz	08a79	135	<499	68800	2490	1520	-	-	7500	36200	2540	1240
718	C15	Type 1	qz	08a80	185	<377	58500	8430	2740	-	-	6910	47200	169	1090
822	C16	Type 3	Mn-dol	08a81	<202	<1250	101000	-	318	<62700	-	22200	58900	-	-
822	C17	Type 3	Fe-dol	08a85	192	414	85600	-	1390	11300	-	38000	58900	-	-
822	C18	Type 3	Fe-dol	08b01	<230	<1330	92800	-	<307	<63200	-	21900	58900	-	-
822	C18	Type 3	Fe-dol	08b02	<126	760	89400	-	<172	<35600	-	27700	58900	-	-
822	C18	Type 3	Fe-dol	08b03	259	1360	89100	-	<84.3	<17600	-	26300	58900	-	-
822	C18	Type 3	Fe-dol	08b04	262	984	89900	-	104	<12900	-	21300	58900	-	-
822	C19	Type 3	Fe-dol	08b05	304	1600	85000	-	991	<46100	-	35600	58900	-	-
822	C19	Type 3	Fe-dol	08b06	215	1550	88300	-	1830	42900	-	25900	58900	-	-
822	C19	Type 3	Fe-dol	08b07	240	1520	82600	-	<181	<38600	-	35900	58900	-	-
709	C20	Type 1	qz	09a30	207	206	65100	<29.9	4030	-	-	3640	41200	5540	1740
709	C20	Type 1	qz	09a31	700	<162	65600	970	11500	-	-	5490	52100	169	7280
709	C20	Type 1	qz	09a33	<125	<895	97200	<360	5050	-	-	<710	<7380	<157	<1600
709	C20	Type 1	qz	09a34	<1020	<7700	92800	<2580	<1380	-	-	10600	<61500	<1330	<13300
709	C21	Type 1	qz	09a38	294	551	29300	1200	42500	-	-	18400	17700	4980	5210
709	C21	Type 1	qz	09a39	<249	<1620	12000	4620	<316	-	-	9670	79400	2120	9430
714	C22	Type 2	qz	10a04	<193	<925	85800	2550	1500	-	-	7460	58200	320	<1770
714	C23	Type 1	qz	10a05	<14.0	152	33700	5550	<20.0	-	-	5740	74500	441	192
714	C23	Type 1	qz	10a06	<126	<692	72400	904	805	-	-	3130	12900	<141	<1170
714	C22	Type 2	qz	10a07	<81.5	<439	79200	4060	4360	-	-	8430	59400	369	<772
714	C23	Type 1	qz	10a08	<17.0	142	29300	7120	2360	-	-	5640	80200	591	1520
718	C26	Type 1	qz	10a15	<177	<998	66600	1640	40500	-	-	38900	30500	<209	<1840
718	C26	Type 1	qz	10a16	<30.4	349	45300	7170	<42.8	-	-	2700	63400	468	998
718	C26	Type 1	qz	10a18	306	169	44500	4040	12300	-	-	2230	65000	619	<204
718	C26	Type 1	qz	10a19	<39.1	<233	34500	1070	<52.9	-	-	2200	81500	652	524

Table 2.10: Chemical composition (ppm) of fluid inclusions from LA-ICP-MS analysis.

Sample	FIA	Fl Type	Host	Spot ID	Li	B	Na	Mg	Al	Si	Cl	K	Ca	Mn	Fe
714	C1	Type 3	Mn-dol	08a23	152	<302	86700	-	257	<13200	-	29800	58900	-	-
714	C1	Type 3	Mn-dol	08a24.1	109	<537	91800	-	<171	<24800	-	26000	58900	-	-
714	C1	Type 3	Mn-dol	08a24.2	172	<407	91400	-	<127	<18300	-	27000	58900	-	-
714	C2	Type 3	Mn-dol	08a25	<131	<688	86200	-	<220	<33300	-	30400	58900	-	-
714	C3	Type 3	Mn-dol	08a26.1	149	307	92100	-	4960	<5630	-	20200	58900	-	-
714	C3	Type 3	Mn-dol	08a26.2	118	<380	92200	-	5430	<16000	-	21200	58900	-	-
714	C3	Type 3	Mn-dol	08a27.1	194	<572	91900	-	<165	<25100	-	20900	58900	-	-
714	C3	Type 3	Mn-dol	08a27.2	153	275	89600	-	<58.8	9280	-	25700	58900	-	-
714	C3	Type 3	Mn-dol	08a28	138	268	90300	-	<76.9	<11700	-	24000	58900	-	-
714	C5	Type 3	qz	08a34	2170	692	93100	592	61100	-	-	13300	57700	7280	3860
714	Single	Type 3	qz	08a37	<90.7	<580	65400	21200	<150	-	-	6140	87100	8410	8560
718	Single	Type 1	qz	08a38	<19.3	<118	55000	9130	10800	-	-	5410	59500	932	269
718	C6	Type 1	qz	08a39	1310	<1250	95600	<711	32300	-	-	3460	<16100	<219	<1350
718	C6	Type 1	qz	08a40	<87.0	<534	66100	2830	13600	-	-	12600	43900	<89.2	5080
718	C6	Type 1	qz	08a41	133	<266	76600	1060	49700	-	-	19000	22400	192	1380
718	Single	Type 1	qz	08a42	684	169	42100	19500	91200	-	-	33200	49500	1150	22800
718	Single	Type 1	qz	08a44	<1.87	193	53200	1900	12100	-	-	8370	67400	4740	1710
718	C7	Type 1	qz	08a45	32.1	112	49700	2790	27300	-	-	12800	22500	783	1250
718	C7	Type 1	qz	08a46	1510	<50.1	59600	1720	10300	-	-	5290	38800	3110	1810
718	Single	Type 1	qz	08a47	<6.73	141	50900	2050	<11.0	-	-	702	74600	6980	1960
718	C7	Type 1	qz	08a48	825	109	28800	663	<12.6	-	-	951	116000	693	<46.7
718	Single	Type 1	qz	08a50	1230	227	65800	497	31200	-	-	824	51100	5000	318
718	C8	Type 1	qz	08a54	<300	<1690	79600	2440	<465	-	-	2050	26400	319	<1680
718	C9	Type 1	qz	08a55	1490	681	47800	<170	46500	-	-	243	<3750	<47.3	<288
718	C9	Type 1	qz	08a56	<350	<1970	61200	<1270	36900	-	-	<1430	<25200	<324	<1910
718	C9	Type 1	qz	08a57	379	481	77800	1790	52200	-	-	6630	27600	78.9	<176
718	C10	Type 1	qz	08a58	314	<19.9	58600	1270	<5.68	-	-	2930	64800	22.5	<20.8
718	C10	Type 1	qz	08a59	<89.3	<500	85400	<302	<148	-	-	2970	19100	130	<528
718	C8	Type 1	qz	08a60	<7.12	124	68100	1440	3680	-	-	10000	43300	157	75.9
718	C9	Type 1	qz	08a61	<108	<622	83100	<352	<173	-	-	1160	24500	<105	<622
718	C11	Type 1	qz	08a62	<22.9	<121	56600	5320	10500	-	-	16600	53900	618	618
718	C12	Type 2	qz	08a63.1	9150	<4990	140000	<2910	126000	-	-	<3620	<64300	<819	<4900
718	C12	Type 2	qz	08a63.2	<93.3	<529	73500	3070	<147	-	-	1490	113000	3640	<536
718	C12	Type 2	qz	08a64	<126	<713	87900	557	<193	-	-	1650	92500	<114	<694
718	C11	Type 1	qz	08a65	<21.6	139	60400	487	29000	-	-	899	13700	476	<124
718	C11	Type 1	qz	08a67	381	265	67600	4450	<69.4	-	-	19900	30500	1280	2160
718	C12	Type 2	qz	08a68	432	277	76300	4000	3650	-	-	17300	93500	1510	347
718	C11	Type 1	qz	08a69	299	148	52500	664	7990	-	-	988	61700	1090	166
718	C13	Type 1	qz	08a73	622	<638	69600	421	11200	-	-	21600	14100	<96.5	2290
718	C13	Type 1	qz	08a75	1040	<218	65200	859	19900	-	-	9600	12600	167	<218
718	C13	Type 1	qz	08a76	2860	<892	92500	1100	3340	-	-	3040	<12000	<154	<929
718	C15	Type 1	qz	08a79	135	<499	68800	2490	1520	-	-	7500	36200	2540	1240
718	C15	Type 1	qz	08a80	185	<377	58500	8430	2740	-	-	6910	47200	169	1090
822	C16	Type 3	Mn-dol	08a81	<202	<1250	101000	-	318	<62700	-	22200	58900	-	-
822	C17	Type 3	Fe-dol	08a85	192	414	85600	-	1390	11300	-	38000	58900	-	-
822	C18	Type 3	Fe-dol	08b01	<230	<1330	92800	-	<307	<63200	-	21900	58900	-	-
822	C18	Type 3	Fe-dol	08b02	<126	760	89400	-	<172	<35600	-	27700	58900	-	-
822	C18	Type 3	Fe-dol	08b03	259	1360	89100	-	<84.3	<17600	-	26300	58900	-	-
822	C18	Type 3	Fe-dol	08b04	262	984	89900	-	104	<12900	-	21300	58900	-	-
822	C19	Type 3	Fe-dol	08b05	304	1600	85000	-	991	<46100	-	35600	58900	-	-
822	C19	Type 3	Fe-dol	08b06	215	1550	88300	-	1830	42900	-	25900	58900	-	-
822	C19	Type 3	Fe-dol	08b07	240	1520	82600	-	<181	<38600	-	35900	58900	-	-
709	C20	Type 1	qz	09a30	207	206	65100	<29.9	4030	-	-	3640	41200	5540	1740
709	C20	Type 1	qz	09a31	700	<162	65600	970	11500	-	-	5490	52100	169	7280
709	C20	Type 1	qz	09a33	<125	<895	97200	<360	5050	-	-	<710	<7380	<157	<1600
709	C20	Type 1	qz	09a34	<1020	<7700	92800	<2580	<1380	-	-	10600	<61500	<1330	<13300
709	C21	Type 1	qz	09a38	294	551	29300	1200	42500	-	-	18400	17700	4980	5210
709	C21	Type 1	qz	09a39	<249	<1620	12000	4620	<316	-	-	9670	79400	2120	9430
714	C22	Type 2	qz	10a04	<193	<925	85800	2550	1500	-	-	7460	58200	320	<1770
714	C23	Type 1	qz	10a05	<14.0	152	33700	5550	<20.0	-	-	5740	74500	441	192
714	C23	Type 1	qz	10a06	<126	<692	72400	904	805	-	-	3130	12900	<141	<1170
714	C22	Type 2	qz	10a07	<81.5	<439	79200	4060	4360	-	-	8430	59400	369	<772
714	C23	Type 1	qz	10a08	<17.0	142	29300	7120	2360	-	-	5640	80200	591	1520
718	C26	Type 1	qz	10a15	<177	<998	66600	1640	40500	-	-	38900	30500	<209	<1840
718	C26	Type 1	qz	10a16	<30.4	349	45300	7170	<42.8	-	-	2700	63400	468	998
718	C26	Type 1	qz	10a18	306	169	44500	4040	12300	-	-	2230	65000	619	<204
718	C26	Type 1	qz	10a19	<39.1	<233	34500	1070	<52.9	-	-	2200	81500	652	524

Table 2.10 (continued): Chemical composition (ppm) of fluid inclusions from LA-ICP-MS analysis.

Sample	FIA	FI Type	Host	Spot ID	Co	Ni	Cu	Zn	As	Br	Rb	Sr	Mo	Ag	Sb
714	C1	Type 3	Mn-dol	08a23	<7.04	<214	<51.8	2810	<71.2	-	170	8120	<12.6	<7.23	<19.6
714	C1	Type 3	Mn-dol	08a24.1	<11.4	<389	<76.1	2500	<129	-	149	5020	<23.0	<10.9	<31.7
714	C1	Type 3	Mn-dol	08a24.2	<8.91	<300	<59.7	2580	103	-	151	5430	<20.1	<8.71	<24.9
714	C2	Type 3	Mn-dol	08a25	<16.6	<537	<114	3180	<166	-	148	10700	<10.7	<11.4	<40.1
714	C3	Type 3	Mn-dol	08a26.1	<2.97	<92.7	<20.4	2450	<29.0	-	119	3260	<5.85	5.47	<6.50
714	C3	Type 3	Mn-dol	08a26.2	<8.63	<272	<58.7	2100	<83.0	-	109	2470	<17.9	<6.14	<18.8
714	C3	Type 3	Mn-dol	08a27.1	<11.7	518	92.6	3060	<123	-	131	3150	<27.1	12.4	<28.6
714	C3	Type 3	Mn-dol	08a27.2	<4.08	<153	40.0	3010	<43.7	-	160	3660	<9.16	<3.76	<9.93
714	C3	Type 3	Mn-dol	08a28	<5.16	<162	<35.3	2980	<57.2	-	125	4070	<1.91	4.73	<15.2
714	C5	Type 3	qz	08a34	<10.8	<427	<75.9	2930	<140	-	37.6	2620	<21.3	10.5	<29.5
714	Single	Type 3	qz	08a37	83.7	934	458	1240	<128	-	43.5	1250	<21.2	<9.90	<26.8
718	Single	Type 1	qz	08a38	13.1	1380	<12.6	156	170	-	4.20	760	<4.58	<2.23	7.75
718	C6	Type 1	qz	08a39	<27.1	<799	<166	<248	<292	-	<37.7	773	<21.4	<18.5	<61.3
718	C6	Type 1	qz	08a40	41.4	<343	<59.1	1770	316	-	36.5	579	<16.8	<8.38	34.5
718	C6	Type 1	qz	08a41	307	954	170	80.6	7280	-	9.63	827	<11.1	11.6	113
718	Single	Type 1	qz	08a42	2000	4150	1500	942	7210	-	139	344	<5.07	76.5	158
718	Single	Type 1	qz	08a44	1.65	<7.72	55.3	951	3.81	-	49.0	1410	<0.133	<0.154	99.4
718	C7	Type 1	qz	08a45	28.3	<5.43	7.71	277	62.2	-	57.2	550	<0.0950	0.528	8.46
718	C7	Type 1	qz	08a46	33.7	270	32.8	428	210	-	26.9	924	3.35	3.86	6.80
718	Single	Type 1	qz	08a47	4.40	<27.6	<4.84	1220	242	-	28.7	1830	<1.14	2.52	33.1
718	C7	Type 1	qz	08a48	7.75	<30.1	9.74	5590	123	-	8.25	2110	<1.91	<0.560	7.24
718	Single	Type 1	qz	08a50	134	367	79.3	1250	546	-	13.0	1760	<3.80	2.13	21.4
718	C8	Type 1	qz	08a54	<34.7	<1230	<226	<323	<441	-	<46.4	1460	<66.5	<36.2	<127
718	C9	Type 1	qz	08a55	<6.31	<201	<39.7	<48.3	<76.3	-	<7.98	84.0	<13.0	<5.43	<15.9
718	C9	Type 1	qz	08a56	<43.6	<1360	<255	<365	<517	-	<56.6	80.7	<74.2	<37.0	<108
718	C9	Type 1	qz	08a57	<4.02	<135	49.7	<31.2	56.2	-	7.73	1240	<4.16	<2.95	<9.23
718	C10	Type 1	qz	08a58	3.49	<12.6	3.57	11.6	<5.15	-	10.5	2390	<0.693	<0.286	<1.10
718	C10	Type 1	qz	08a59	<10.2	<358	<61.4	<89.3	145	-	<14.1	640	<14.9	<9.66	<23.9
718	C8	Type 1	qz	08a60	<0.946	30.5	8.21	22.7	<9.84	-	29.1	1590	<1.21	<0.690	<1.85
718	C9	Type 1	qz	08a61	<13.0	<424	<94.7	<93.5	<166	-	<19.7	848	<31.1	<10.3	<27.7
718	C11	Type 1	qz	08a62	<2.77	<84.5	30.0	345	<32.1	-	50.1	1050	<6.42	<2.25	20.7
718	C12	Type 2	qz	08a63.1	<125	<3280	<677	<1000	<1270	-	<131	1720	<276	<73.0	<246
718	C12	Type 2	qz	08a63.2	<13.0	<337	<69.5	3220	<136	-	19.6	1700	<26.7	<6.86	<25.4
718	C12	Type 2	qz	08a64	<15.7	<538	<104	1560	<178	-	<22.1	1390	<30.8	<11.3	<35.6
718	C11	Type 1	qz	08a65	16.8	<86.5	<14.0	95.1	95.7	-	<3.42	373	<3.76	<1.94	21.6
718	C11	Type 1	qz	08a67	161	1670	113	660	892	-	60.1	343	<11.1	<3.91	60.9
718	C12	Type 2	qz	08a68	<3.53	271	66.4	2860	<44.6	-	101	3690	<7.23	<2.48	<6.81
718	C11	Type 1	qz	08a69	31.0	85.3	56.0	1460	151	-	3.70	1150	<0.119	1.26	4.76
718	C13	Type 1	qz	08a73	<14.3	<473	817	<112	196	-	<17.6	596	<29.4	<13.3	<35.0
718	C13	Type 1	qz	08a75	<5.48	<151	96.6	66.7	<60.6	-	10.5	511	<9.71	<4.10	21.8
718	C13	Type 1	qz	08a76	<21.3	<703	<110	<161	<257	-	<26.6	388	<48.1	<15.9	67.8
718	C15	Type 1	qz	08a79	<10.0	<346	<64.3	1270	<126	-	62.6	1600	<14.5	<7.35	<23.1
718	C15	Type 1	qz	08a80	<8.31	<260	<51.7	97.8	<95.8	-	19.8	905	<6.24	<5.56	<16.2
822	C16	Type 3	Mn-dol	08a81	588	1510	<106	4950	9450	-	115	2200	50.3	34.2	<71.2
822	C17	Type 3	Fe-dol	08a85	2700	9110	79.2	2000	26100	-	138	2950	2.72	759	31.3
822	C18	Type 3	Fe-dol	08b01	256	2430	<122	2990	2240	-	87.5	2570	<48.1	34.0	<98.9
822	C18	Type 3	Fe-dol	08b02	37.9	<445	<66.0	2530	<327	-	79.6	2150	<24.7	<15.8	<53.4
822	C18	Type 3	Fe-dol	08b03	<5.30	<209	<35.4	1010	<161	-	66.6	1600	<14.2	<5.63	<24.8
822	C18	Type 3	Fe-dol	08b04	30.0	<150	<23.7	3110	<122	-	72.8	2850	11.1	896	<16.3
822	C19	Type 3	Fe-dol	08b05	661	919	<72.0	753	11600	-	124	2550	<35.5	48.8	<51.8
822	C19	Type 3	Fe-dol	08b06	<4.85	827	54.8	2150	1220	-	94.4	2390	<2.82	20.2	<16.9
822	C19	Type 3	Fe-dol	08b07	<14.1	563	79.8	4360	1780	-	163	3390	21.0	<20.9	<48.3
709	C20	Type 1	qz	09a30	<1.02	<46.0	<7.45	1320	<27.9	-	30.4	2010	<1.23	7.91	83.3
709	C20	Type 1	qz	09a31	4.37	<105	<12.8	<36.3	<63.8	-	10.3	912	<5.60	<5.68	61.8
709	C20	Type 1	qz	09a33	<14.0	<573	<69.7	<195	<407	-	<25.0	<13.0	<37.3	<30.8	101
709	C20	Type 1	qz	09a34	<134	<4740	<689	<1690	<3470	-	<209	971	<309	<280	<492
709	C21	Type 1	qz	09a38	<2.05	<80.9	<12.0	2470	<77.0	-	95.4	4310	<4.67	<4.33	<8.15
709	C21	Type 1	qz	09a39	643	1350	371	782	5030	-	<45.7	189	<40.8	80.8	<92.0
714	C22	Type 2	qz	10a04	<21.7	<760	<131	<226	<670	-	<33.7	1230	<48.3	<53.2	<72.1
714	C23	Type 1	qz	10a05	415	914	717	295	309	-	123	1380	<3.34	13.9	<5.14
714	C23	Type 1	qz	10a06	<14.2	<524	<104	<158	<450	-	<23.6	141	<16.8	<21.1	<49.7
714	C22	Type 2	qz	10a07	<9.37	<303	<54.0	<110	<305	-	27.7	1220	<17.5	<13.1	<27.0
714	C23	Type 1	qz	10a08	6.46	<74.3	547	111	<64.7	-	6.16	1360	3.62	<2.73	<5.78
718	C26	Type 1	qz	10a15	614	3040	163	905	2990	-	<31.2	707	<26.9	<27.0	<63.8
718	C26	Type 1	qz	10a16	237	572	1630	1070	3460	-	10.8	901	<7.16	2210	24.1
718	C26	Type 1	qz	10a18	28.3	113	132	585	250	-	5.70	1130	2.30	<3.22	12.3
718	C26	Type 1	qz	10a19	<3.73	211	<18.3	<51.3	<189	-	11.5	1540	<11.8	<6.78	<11.6

Table 2.10 (continued): Chemical composition (ppm) of fluid inclusions from LA-ICP-MS analysis.

Sample	FIA	FI Type	Host	Spot ID	Cs	Ba	La	Ce	Pr	Nd	Sm	Eu	Gd	Tb	Dy
714	C1	Type 3	Mn-dol	08a23	12.5	2080	79.0	<0.717	10.2	161	25.3	4.70	<6.90	3.91	7.06
714	C1	Type 3	Mn-dol	08a24.1	24.1	2110	<3.35	150	48.8	431	282	48.2	<14.9	45.3	65.3
714	C1	Type 3	Mn-dol	08a24.2	17.8	2140	<2.85	109	35.4	135	246	25.7	<13.0	16.9	14.5
714	C2	Type 3	Mn-dol	08a25	23.8	1950	157	550	44.7	263	<15.3	<1.93	<20.5	<2.75	<11.2
714	C3	Type 3	Mn-dol	08a26.1	12.6	1870	224	1150	143	782	365	184	435	60.8	281
714	C3	Type 3	Mn-dol	08a26.2	14.3	1580	263	1260	197	1040	556	219	602	75.8	358
714	C3	Type 3	Mn-dol	08a27.1	19.2	1770	129	441	<0.952	<14.0	481	<3.94	21.4	24.6	<3.76
714	C3	Type 3	Mn-dol	08a27.2	19.1	1900	<1.11	<0.318	<0.269	<4.09	<1.77	<1.30	<5.36	<0.716	<1.06
714	C3	Type 3	Mn-dol	08a28	12.5	1710	71.5	176	7.62	138	97.7	25.0	95.5	5.65	25.7
714	C5	Type 3	qz	08a34	<11.1	1600	<3.42	<3.76	<1.16	<12.0	<14.2	<2.05	<13.8	<1.12	<4.58
714	Single	Type 3	qz	08a37	<10.2	813	<3.53	<1.51	<2.13	<15.3	<14.0	<4.39	<8.08	<2.40	<8.39
718	Single	Type 1	qz	08a38	<2.02	92.8	<0.544	<0.547	<0.386	<2.55	<3.02	<0.682	<3.29	<0.444	<1.52
718	C6	Type 1	qz	08a39	<22.3	<38.8	<2.53	<4.81	<4.04	<26.8	<14.1	<9.61	<40.7	<4.66	<15.9
718	C6	Type 1	qz	08a40	<8.96	<19.4	<2.70	<2.00	<1.68	<11.2	<11.1	<2.97	<12.8	<0.839	<10.6
718	C6	Type 1	qz	08a41	5.85	10.9	<1.58	<0.648	<0.938	<6.81	<6.18	<1.95	<5.97	<0.905	<3.70
718	Single	Type 1	qz	08a42	5.50	80.0	6.82	12.4	3.21	<3.26	<3.32	<0.889	<4.14	<0.627	<2.56
718	Single	Type 1	qz	08a44	7.92	1300	<0.0507	<0.0444	<0.0426	<0.207	<0.0867	<0.0232	0.124	<0.0494	<0.119
718	C7	Type 1	qz	08a45	4.65	535	<0.0266	0.0485	<0.00935	<0.229	<0.147	<0.0395	<0.142	<0.0268	<0.163
718	C7	Type 1	qz	08a46	23.5	1080	<0.186	<0.285	2.50	1.62	<1.03	0.329	<1.52	<0.209	<1.02
718	Single	Type 1	qz	08a47	7.71	2150	<0.0595	0.136	<0.156	<0.278	<0.734	<0.241	4.47	0.0755	<0.539
718	C7	Type 1	qz	08a48	4.74	468	<0.175	<0.141	<0.0510	2.48	<0.337	<0.296	<1.18	<0.195	<0.468
718	Single	Type 1	qz	08a50	90.5	963	10.3	<0.194	<0.415	<2.53	<2.43	<0.544	<1.96	0.540	<0.642
718	C8	Type 1	qz	08a54	<31.0	<29.1	<7.66	<3.61	<5.43	<30.2	<35.8	<11.3	<49.7	<2.89	<28.3
718	C9	Type 1	qz	08a55	<5.28	<12.2	<1.34	<1.15	<1.13	<6.29	<9.03	<1.98	<6.09	<1.08	<2.17
718	C9	Type 1	qz	08a56	<34.2	<69.4	<9.93	<5.26	<7.18	<51.3	<47.4	<7.73	<52.9	<6.88	<17.3
718	C9	Type 1	qz	08a57	<3.19	33.0	<1.01	1.16	<0.769	<4.74	<5.63	<1.35	<5.40	<0.634	<2.60
718	C10	Type 1	qz	08a58	1.59	6.13	<0.102	<0.0647	<0.0541	<0.429	0.165	<0.0396	<0.426	<0.0820	<0.212
718	C10	Type 1	qz	08a59	<10.1	<19.4	<1.72	<1.72	<0.665	<3.70	<9.51	<3.89	<12.7	<1.38	<5.66
718	C8	Type 1	qz	08a60	2.27	47.4	0.554	<0.0671	<0.143	<0.904	<0.945	<0.286	<0.907	<0.113	<0.703
718	C9	Type 1	qz	08a61	<10.9	14.4	<2.93	<1.35	<3.01	<6.27	<13.7	<1.98	<7.16	<2.64	<4.43
718	C11	Type 1	qz	08a62	<2.35	79.2	<0.556	<0.464	<0.466	<1.10	<1.31	<0.926	<2.46	<0.553	<2.27
718	C12	Type 2	qz	08a63.1	<95.0	<223	<24.7	<29.9	<10.4	<115	<153	<31.2	<132	<19.8	<40.9
718	C12	Type 2	qz	08a63.2	<9.98	376	<2.30	<2.87	<0.804	<10.7	<14.5	<2.82	<12.3	<1.85	<6.29
718	C12	Type 2	qz	08a64	<13.3	301	<3.95	<3.58	<1.54	<16.6	<17.0	<6.31	<9.77	<2.45	<11.7
718	C11	Type 1	qz	08a65	<2.21	12.0	<0.527	<0.214	<0.551	<2.03	<3.32	<0.777	<2.80	<0.349	<1.43
718	C11	Type 1	qz	08a67	<4.14	146	1.54	<0.534	<0.446	<5.99	<5.37	<1.43	<2.83	<0.920	<3.77
718	C12	Type 2	qz	08a68	13.1	565	<0.732	<0.273	<0.501	<3.89	<4.65	<0.881	<4.45	<0.587	<1.96
718	C11	Type 1	qz	08a69	2.27	118	<0.0488	0.0559	<0.0324	<0.180	<0.0764	<0.0935	<0.302	0.0863	<0.208
718	C13	Type 1	qz	08a73	<10.6	<30.2	<3.75	<1.90	<2.85	<15.9	<10.6	<5.96	<21.5	<2.39	<11.2
718	C13	Type 1	qz	08a75	<4.25	<9.08	<0.966	<0.961	<0.807	<5.85	<3.16	<0.839	<6.03	<0.776	<3.72
718	C13	Type 1	qz	08a76	<15.6	<28.0	<4.75	<1.76	<2.92	<19.6	<23.3	<7.00	<22.4	<2.81	<11.5
718	C15	Type 1	qz	08a79	<8.63	449	<2.08	<2.06	<1.98	<7.94	<9.46	1.72	<9.11	<1.37	<5.62
718	C15	Type 1	qz	08a80	<6.81	63.4	<1.86	<0.725	<1.38	<6.44	<7.67	<2.04	<8.82	<1.11	<2.42
822	C16	Type 3	Mn-dol	08a81	<19.3	921	<2.56	145	98.0	636	578	28.2	609	216	327
822	C17	Type 3	Fe-dol	08a85	14.1	606	4.03	17.7	6.46	40.0	45.0	<0.223	59.9	13.7	82.7
822	C18	Type 3	Fe-dol	08b01	<22.2	424	5.86	<1.77	<3.80	<21.3	<25.4	3.65	<35.3	3.00	<5.96
822	C18	Type 3	Fe-dol	08b02	<11.9	528	<2.92	<3.50	<1.18	<6.60	<19.7	<2.08	<19.0	<1.14	<11.7
822	C18	Type 3	Fe-dol	08b03	6.54	599	1.46	11.5	6.34	40.9	17.2	<0.868	<7.33	3.72	2.81
822	C18	Type 3	Fe-dol	08b04	11.0	558	7.91	32.3	14.1	41.1	30.4	2.97	21.2	7.20	4.97
822	C19	Type 3	Fe-dol	08b05	<16.6	296	13.9	60.4	25.5	120	86.3	3.78	89.5	25.7	102
822	C19	Type 3	Fe-dol	08b06	15.9	391	7.09	14.8	7.95	39.0	<5.16	<0.493	<4.98	2.02	47.4
822	C19	Type 3	Fe-dol	08b07	<13.9	896	5.41	15.8	4.10	14.9	11.6	<4.78	30.5	8.92	51.9
709	C20	Type 1	qz	09a30	5.61	1300	<0.291	<0.146	<0.122	<1.91	<0.815	<0.536	<1.58	<0.117	<0.483
709	C20	Type 1	qz	09a31	5.00	44.7	<0.650	<0.360	<0.740	<3.11	<3.69	<0.538	<1.92	<0.289	<2.19
709	C20	Type 1	qz	09a33	<16.0	<35.8	<4.33	<2.26	<1.90	<10.6	<21.1	<3.39	<20.2	<3.04	<7.49
709	C20	Type 1	qz	09a34	<129	<343	<22.1	<42.1	<18.8	<171	<125	<33.6	<120	<18.1	<74.3
709	C21	Type 1	qz	09a38	<2.55	5180	<0.539	<0.545	<0.243	<1.36	<1.61	<0.432	<2.93	<0.441	<1.81
709	C21	Type 1	qz	09a39	<30.8	682	<4.71	27.9	<6.55	<22.5	<26.6	<7.14	<25.6	<7.29	<15.8
714	C22	Type 2	qz	10a04	<20.4	<44.9	<3.42	<3.41	<4.64	<25.9	<19.0	<10.3	<29.6	<4.47	<18.2
714	C23	Type 1	qz	10a05	2.77	128	<0.382	1.27	25.3	<1.07	<2.74	<0.558	<2.04	<0.185	0.837
714	C23	Type 1	qz	10a06	<13.5	<27.0	<3.33	<1.91	<1.61	<8.97	<21.7	<5.72	<10.3	<1.55	<6.32
714	C22	Type 2	qz	10a07	<8.68	45.3	<2.00	<2.00	<2.27	<11.2	<11.1	<2.93	<10.7	<1.62	<7.92
714	C23	Type 1	qz	10a08	3.51	64.5	8.64	16.7	<0.159	5.53	<1.05	2.25	1.49	<0.428	<1.27
718	C26	Type 1	qz	10a15	<22.2	51.1	<5.28	6.73	<2.56	<14.3	<16.9	<7.76	<28.2	2.72	<10.0
718	C26	Type 1	qz	10a16	87.1	64.8	28.0	1.27	<0.811	10.4	<2.38	<1.19	<2.29	21.3	<3.59
718	C26	Type 1	qz	10a18	<2.37	50.8	<0.495	<0.234	<0.415	<1.10	<1.30	<0.888	<2.64	<0.189	<0.771
718	C26	Type 1	qz	10a19	<4.64	124	<0.460	31.8	12.2	<2.15	<2.55	<0.677	<4.78	<0.371	<2.95

Table 2.10 (continued): Chemical composition (ppm) of fluid inclusions from LA-ICP-MS analysis.

Sample	FIA	FI Type	Host	Spot ID	Ho	Er	Tm	Yb	Lu	W	Au	Pb	Bi	Th	U
714	C1	Type 3	Mn-dol	08a23	6.26	<4.98	<1.23	<6.22	<1.69	<2.72	<4.53	998	<4.85	<0.984	<0.797
714	C1	Type 3	Mn-dol	08a24.1	27.7	<6.92	<1.59	<7.17	<2.60	<7.48	<9.12	1450	<7.26	<1.43	<1.79
714	C1	Type 3	Mn-dol	08a24.2	16.6	<6.59	<1.49	<6.70	<2.23	<7.00	<7.85	1510	<5.84	<1.32	<1.48
714	C2	Type 3	Mn-dol	08a25	<1.10	<9.55	<1.05	<14.0	<1.09	<14.6	<11.4	1270	<9.30	<2.26	<1.44
714	C3	Type 3	Mn-dol	08a26.1	36.3	82.9	11.7	87.0	13.2	<3.39	<1.86	1390	<1.31	<0.359	<0.331
714	C3	Type 3	Mn-dol	08a26.2	53.0	94.5	19.4	136	12.8	<10.2	<5.75	1320	<3.87	<1.09	<1.01
714	C3	Type 3	Mn-dol	08a27.1	<2.54	<5.49	<1.78	<8.06	21.6	<8.41	<7.87	1230	<6.07	<1.74	<2.00
714	C3	Type 3	Mn-dol	08a27.2	<0.852	<1.78	<0.576	<2.61	<0.739	<2.72	<2.60	1610	<2.12	<0.594	<0.695
714	C3	Type 3	Mn-dol	08a28	<0.636	<2.81	<1.02	<2.74	2.49	<2.86	<4.45	1420	6.80	<0.641	<0.592
714	C5	Type 3	qz	08a34	<2.94	<6.38	<2.08	<12.5	<3.61	<11.8	<13.0	1270	<7.26	368	<2.33
714	Single	Type 3	qz	08a37	<2.80	<8.13	<2.04	<9.19	<2.12	<12.6	<7.66	427	55.8	<1.17	9.97
718	Single	Type 1	qz	08a38	<0.391	<1.14	<0.495	<2.44	<0.384	<2.10	<1.65	58.1	11.2	4.84	<0.333
718	C6	Type 1	qz	08a39	<2.17	<6.30	<2.05	<23.5	<5.41	<24.9	<21.4	<18.2	<12.3	<3.73	<3.07
718	C6	Type 1	qz	08a40	<1.70	<4.95	<2.39	<9.82	<1.67	<7.70	<9.66	<9.93	198	<1.11	<1.38
718	C6	Type 1	qz	08a41	<0.551	<2.76	<1.37	<5.30	<1.22	3.68	<4.80	33.5	1100	8.84	1.71
718	Single	Type 1	qz	08a42	<0.594	<1.72	<0.562	<1.31	<0.646	6.82	<2.34	238	4280	1650	2.48
718	Single	Type 1	qz	08a44	<0.0377	<0.110	<0.0357	<0.130	<0.0424	27.8	<0.210	96.9	26.7	81.9	<0.0315
718	C7	Type 1	qz	08a45	<0.0281	<0.0657	<0.00896	<0.0966	<0.0222	<0.0430	<0.0337	73.5	1.41	19.1	2.36
718	C7	Type 1	qz	08a46	<0.193	<0.458	<0.229	<0.935	<0.0727	1.02	<0.995	78.5	7.98	<0.141	0.204
718	Single	Type 1	qz	08a47	<0.112	<0.327	<0.106	<0.480	<0.136	<0.629	<0.622	136	18.1	<0.0744	<0.109
718	C7	Type 1	qz	08a48	<0.148	<0.430	<0.113	<0.220	<0.0506	0.805	<0.428	2650	4.49	<0.101	0.186
718	Single	Type 1	qz	08a50	<0.373	<1.22	<0.155	<1.33	<0.366	2.13	<1.33	351	35.8	540	<0.293
718	C8	Type 1	qz	08a54	<7.23	<21.0	<5.16	<33.7	<8.79	<29.6	<19.6	<24.1	<23.4	<4.82	<5.01
718	C9	Type 1	qz	08a55	<1.26	<2.80	<0.524	<4.85	<1.24	<5.20	<5.59	8.83	<3.72	<0.790	<0.744
718	C9	Type 1	qz	08a56	<7.22	<26.9	<8.75	<30.9	<8.21	<38.4	<35.9	<32.6	<21.5	<7.12	<5.40
718	C9	Type 1	qz	08a57	<0.405	<2.25	<0.809	<1.73	<0.907	<3.04	<4.25	<2.51	2.23	<0.613	<0.336
718	C10	Type 1	qz	08a58	<0.0935	<0.0657	<0.0213	<0.288	<0.0759	<0.308	<0.308	12.8	0.754	38.7	<0.0506
718	C10	Type 1	qz	08a59	<0.669	<4.21	<1.67	<7.56	<1.73	<6.61	<6.33	22.0	<5.91	<1.68	<1.30
718	C8	Type 1	qz	08a60	<0.163	<0.344	<0.111	<0.241	<0.116	<0.746	<0.585	42.0	<0.456	8.59	<0.0725
718	C9	Type 1	qz	08a61	<1.13	<7.19	<2.62	<4.85	<2.04	<14.8	<7.45	<9.00	<6.28	<1.95	<1.40
718	C11	Type 1	qz	08a62	<0.469	<1.69	<0.499	<2.26	<0.518	<1.78	<1.89	45.2	<1.35	95.0	<0.267
718	C12	Type 2	qz	08a63.1	<17.8	<67.4	<25.3	<99.0	<22.7	<81.1	<89.8	161	<46.6	<17.4	<13.5
718	C12	Type 2	qz	08a63.2	<1.61	<6.39	<2.45	<9.40	<2.15	<7.33	<9.30	2040	<4.65	<1.73	<1.31
718	C12	Type 2	qz	08a64	<1.55	<4.50	<2.83	<15.4	<3.53	<11.7	<11.9	990	<7.93	<1.94	<2.05
718	C11	Type 1	qz	08a65	<0.444	<1.47	<0.169	<1.90	<0.434	<2.02	<2.13	58.9	3.06	<0.297	<0.321
718	C11	Type 1	qz	08a67	<0.815	<1.31	<0.767	<3.48	<0.796	8.47	<4.22	179	37.2	<0.797	<0.778
718	C12	Type 2	qz	08a68	<0.617	<0.667	<0.216	<0.979	<0.492	<2.80	<2.20	628	<1.82	<0.483	0.552
718	C11	Type 1	qz	08a69	<0.0116	<0.0946	<0.0306	<0.0495	<0.0113	0.241	<0.116	806	52.7	323	0.0297
718	C13	Type 1	qz	08a73	<1.61	<4.68	<2.36	<6.88	<3.33	<14.3	<5.71	<9.30	78.9	<2.05	<1.70
718	C13	Type 1	qz	08a75	<0.480	<2.38	<0.999	<4.09	<0.933	<3.67	<4.08	22.7	<2.64	<0.570	<0.613
718	C13	Type 1	qz	08a76	<4.01	<8.59	<3.34	<17.2	<3.47	<15.9	<10.5	26.2	<10.2	<2.71	<2.19
718	C15	Type 1	qz	08a79	<0.668	<4.20	<1.66	<7.55	<1.41	<6.44	<8.50	387	<4.88	<0.359	<1.27
718	C15	Type 1	qz	08a80	<1.17	<3.41	<1.48	<5.98	<1.53	<8.24	<6.55	26.9	<4.17	<1.11	<0.851
822	C16	Type 3	Mn-dol	08a81	86.3	84.8	<11.8	190	22.3	<9.65	<27.3	2560	260	<1.16	<1.07
822	C17	Type 3	Fe-dol	08a85	16.3	33.5	5.28	35.2	4.73	1.89	<1.95	2280	2990	<0.230	0.791
822	C18	Type 3	Fe-dol	08b01	<4.82	5.65	<3.64	<16.6	<1.49	37.4	<13.8	2040	<25.4	<2.08	<0.755
822	C18	Type 3	Fe-dol	08b02	<1.19	<3.48	<1.12	22.6	<2.93	<5.29	<8.87	1190	<11.1	<2.03	<1.69
822	C18	Type 3	Fe-dol	08b03	<0.497	<1.45	<1.09	<2.14	<1.13	<7.27	<5.14	1030	<4.80	<0.268	<0.575
822	C18	Type 3	Fe-dol	08b04	<0.251	<2.02	<0.652	<1.08	<0.245	<1.12	<3.68	1860	<3.64	<0.549	<0.438
822	C19	Type 3	Fe-dol	08b05	21.3	47.3	5.94	67.6	4.95	<12.9	<12.9	651	1590	<1.91	<1.77
822	C19	Type 3	Fe-dol	08b06	1.39	4.02	0.800	10.2	4.35	<3.50	1.52	761	<3.47	<0.152	<0.142
822	C19	Type 3	Fe-dol	08b07	6.27	7.92	<3.49	13.8	2.93	<6.16	<10.0	2700	<11.1	<0.743	<1.87
709	C20	Type 1	qz	09a30	<0.302	<0.360	<0.285	<1.08	<0.299	<0.569	<1.46	875	<1.43	<0.0679	<0.162
709	C20	Type 1	qz	09a31	<0.303	<1.63	<1.01	<2.41	<0.300	<1.40	<2.68	8.69	60.3	<0.308	<0.299
709	C20	Type 1	qz	09a33	<3.18	<5.59	<3.00	<13.8	<1.88	<14.7	<17.2	<17.6	<13.4	<2.04	<1.02
709	C20	Type 1	qz	09a34	<18.9	<55.4	<17.9	<154	<35.1	<87.6	<153	<168	<112	<10.4	<19.0
709	C21	Type 1	qz	09a38	<0.244	<0.714	<0.230	<1.05	<0.455	<2.14	<1.68	325	<2.08	<0.253	<0.292
709	C21	Type 1	qz	09a39	<4.03	<22.4	<3.80	<17.4	<6.47	<18.7	<33.2	221	2620	106000	<3.47
714	C22	Type 2	qz	10a04	<2.87	<15.8	<5.10	<12.4	<5.30	<21.8	<19.8	<18.7	<18.0	<2.89	<3.01
714	C23	Type 1	qz	10a05	<0.193	<0.941	<0.183	<0.829	<0.368	<1.76	<1.53	18.4	342	2870	0.516
714	C23	Type 1	qz	10a06	<1.61	<4.72	<1.53	<6.93	<1.59	<15.5	<12.1	<15.7	32.0	<1.76	<1.41
714	C22	Type 2	qz	10a07	<0.870	<4.93	<1.59	<7.24	<2.24	<4.09	<6.22	<9.21	<5.73	<0.467	<1.02
714	C23	Type 1	qz	10a08	<0.489	<0.949	9.61	<0.683	6.51	<0.746	<1.45	11.3	88.0	<0.262	<0.164
718	C26	Type 1	qz	10a15	<5.21	<7.51	<2.43	<11.0	<2.52	<12.1	<16.5	79.2	454	<2.37	4.40
718	C26	Type 1	qz	10a16	<0.361	<1.06	2.78	<1.56	<0.898	19.0	<3.04	45.1	213	684	3.47
718	C26	Type 1	qz	10a18	<0.197	<0.577	<0.186	<0.849	<0.408	<0.928	<1.90	33.0	6.84	<0.271	<0.0990
718	C26	Type 1	qz	10a19	<0.386	<1.13	<0.366	<1.67	<0.739	<1.82	<3.83	8.53	<3.27	<0.547	<0.379

Table 2.10 (continued): Chemical composition (ppm) of fluid inclusions from LA-ICP-MS analysis.

Sample	FIA	FI Type	Host	Spot ID	Li	B	Na	Mg	Al	Si	Cl	K	Ca	Mn	Fe
718	A33	Type 2	qz	10a28	<263	<1630	82100	5580	<397	-	-	22300	75600	5800	10100
718	Single	Type 2	qz	10a30	<48.4	<298	94000	8520	23000	-	-	31200	51000	498	5240
718	Single	Type 2	qz	10a31	<155	<1010	118000	850	<221	-	-	1570	38000	391	3300
718	Single	Type 2	qz	10a32	4360	1320	53400	13700	179000	-	-	8410	132000	353	1390
718	A34	Type 2	qz	10a33	1500	1010	120000	2400	68100	-	-	11200	26600	124	1290
718	A35	Type 2	qz	10a34	2270	<1360	112000	981	48400	-	-	<1000	49400	1050	<2160
718	Single	Type 2	qz	10a35	512	<326	97400	4170	10100	-	-	2840	69700	1090	37700
718	A35	Type 2	qz	10a36	750	522	77700	3690	5290	-	-	4560	104000	1270	2430
718	A35	Type 2	qz	10a37.1	900	194	78400	2130	26400	-	-	10900	49000	4310	1810
718	A35	Type 2	qz	10a37.2	835	<41.5	111000	1660	4320	-	-	903	46800	275	<62.7
718	Single	Type 2	qz	10a38	<42.6	354	93100	1790	<60.6	-	-	6650	75600	2610	560
718	C31	Type 2	qz	10a39	870	<1840	86300	802	22400	-	-	4740	47600	3890	<2850
718	Single	Type 2	qz	10a40	<71.6	<414	29500	55600	<98.0	-	-	4700	121000	195	6730
709	A21	Type 2	qz	10a43	<187	<1120	78600	<529	<254	-	-	17000	69900	19500	2790
SFB240	A42	Type 3	Mn-dol	10a45	174	<336	102000	-	1370	<15100	-	11700	58900	-	-
SFB240	A36	Type 3	Mn-dol	10a47	147	<308	93700	-	<84.2	<13500	-	27800	58900	-	-
SFB240	A36	Type 3	Mn-dol	10a48	150	242	95300	-	186	<7840	-	25000	58900	-	-
SFB240	A36	Type 3	Mn-dol	10a49	166	402	93400	-	<71.1	<11000	-	25900	58900	-	-
SFB240	C35	Type 3	Mn-dol	10a50	153	<339	93300	-	155	14300	-	28400	58900	-	-
718	C36	Type 3	qz	12a03	837	498	94400	1920	36400	-	-	16100	63700	3640	11500
718	C36	Type 3	qz	12a04	<27.3	382	96900	7260	22300	-	-	20300	46200	4120	14000
718	Single	Type 3	qz	12a05	<30.6	342	79700	5190	30700	-	-	25200	81200	3190	13000
718	Single	Type 1	qz	12a06.1	<76.8	<449	62100	13100	5140	-	-	4600	42500	<88.2	1550
718	C37	Type 1	qz	12a06.2	<1010	<5860	92700	<2510	3380	-	-	10800	<54300	<1190	<12800
718	Single	Type 1	qz	12a07	3240	<1270	60100	7740	50800	-	-	15000	43300	469	10900
718	C38	Type 1	qz	12a09	2080	<2330	44400	3830	45300	-	-	7290	85800	<502	12800
718	C38	Type 1	qz	12a10	1620	<951	65900	3570	32600	-	-	11000	44400	396	<2190
718	Single	Type 1	qz	12a11	<85.4	<441	80700	4230	2320	-	-	7090	18900	220	3370
718	C39	Type 1	qz	12a15	<332	<1830	95100	<839	<468	-	-	5020	<18700	<399	<3990
718	C39	Type 1	qz	12a16	<35.2	<183	89000	270	<46.7	-	-	5160	10600	42.4	<398
718	C39	Type 1	qz	12a17	1670	<2170	92100	<849	19400	-	-	12000	46900	<442	11100
718	C39	Type 1	qz	12a18	456	<277	66000	11500	3050	-	-	4380	29500	1300	3740
718	C39	Type 1	qz	12a19	673	1860	67700	3600	9600	-	-	7510	24800	433	2330
718	Single	Type 1	qz	12a22	178	<156	73200	3250	3220	-	-	814	38300	66.2	<300
718	C40	Type 1	qz	12a23	42.5	<64.2	85800	1760	1420	-	-	402	17900	33.6	<129
718	Single	Type 1	qz	12a24	507	<278	53200	5350	<77.4	-	-	4580	67400	402	2640
718	Single	Type 1	qz	12a25	<30.8	<168	42600	22700	<41.9	-	-	11400	57100	<34.6	2610
718	Single	Type 1	qz	12a26	3010	<3660	53400	2000	49100	-	-	17800	61300	937	66900
718	Single	Type 1	qz	12a27	<131	<696	42500	1560	<175	-	-	7990	84000	5480	2320
718	Single	Type 1	qz	12a30	<1060	<5800	40100	2560	<1400	-	-	4730	89200	<1160	19600
848	C41	Type 3	Fe-dol	12a32	138	246	92600	-	347	<7590	-	20500	58900	-	-
848	C41	Type 3	Fe-dol	12a33	81.6	278	93900	-	1030	8120	-	17700	58900	-	-
848	C41	Type 3	Fe-dol	12a34	121	582	95500	-	4860	<11700	-	17500	58900	-	-
848	C42	Type 3	Fe-dol	12a35	156	<562	102000	-	<167	34500	-	26300	58900	-	-
848	C43	Type 3	Fe-dol	12a39	121	<353	88800	-	972	<17200	-	26700	58900	-	-
848	C43	Type 3	Fe-dol	12a40	<154	<824	98000	-	5990	<38700	-	14700	58900	-	-
848	C44	Type 3	Fe-dol	12a41	72.6	<316	95700	-	<88.3	<14700	-	13500	58900	-	-
848	C44	Type 3	Fe-dol	12a42	156	<750	88100	-	<201	<33600	-	34900	58900	-	-
714	C45	Type 3	Mn-dol	12a48	120	908	77600	-	<50.2	11100	-	23600	58900	-	-
714	C45	Type 3	Mn-dol	12a49	226	1360	81100	-	<82.6	<15800	-	30000	58900	-	-
714	C45	Type 3	Mn-dol	12a50	447	2330	114000	-	<533	<102000	-	23900	<20700	-	-
211	C47	Type 2	qz	12a53	<18.9	<100	54200	22000	29500	-	-	7170	35900	510	3030
211	C47	Type 2	qz	12a54	<18.6	<90.5	54900	27100	19600	-	-	8640	42000	603	5490
211	C47	Type 2	qz	12a56	1950	<1330	87300	15100	99700	-	-	16600	29400	<241	<1690
211	C48	Type 3	Fe-dol	12a57	127	394	81000	-	2930	<4680	-	19700	58900	-	-
211	C48	Type 3	Fe-dol	12a58	75.7	<210	82700	-	<60.3	<9330	-	18700	58900	-	-
211	C48	Type 3	Fe-dol	12a59	102	<205	83500	-	<59.7	<9230	-	18200	58900	-	-
211	C48	Type 3	Fe-dol	12a60	709	753	67200	-	3510	<24000	-	37200	58900	-	-
211	C48	Type 3	Fe-dol	12a61.1	101	446	80500	-	<32.9	<5040	-	20600	58900	-	-
211	C48	Type 3	Fe-dol	12a61.2	155	708	75500	-	<46.6	<7080	-	32200	58900	-	-

Table 2.10 (continued): Chemical composition (ppm) of fluid inclusions from LA-ICP-MS analysis.

Sample	FIA	FI Type	Host	Spot ID	Co	Ni	Cu	Zn	As	Br	Rb	Sr	Mo	Ag	Sb
718	A33	Type 2	qz	10a28	474	<900	<197	1760	<1360	-	149	1690	<35.2	<43.0	109
718	Single	Type 2	qz	10a30	562	665	122	572	1850	-	157	721	<12.0	<7.06	226
718	Single	Type 2	qz	10a31	1230	<579	380	799	7010	-	<27.2	565	<37.7	<25.8	<55.1
718	Single	Type 2	qz	10a32	324	13500	8560	1120	5600	-	1240	845	745	493	350
718	A34	Type 2	qz	10a33	126	1580	<14.6	183	193	-	19.9	957	1.57	10.5	137
718	A35	Type 2	qz	10a34	<20.2	<811	<133	1270	<1150	-	<37.0	1110	<55.9	<37.0	81.8
718	Single	Type 2	qz	10a35	300	241	117	721	741	-	20.5	844	55.7	<8.19	163
718	A35	Type 2	qz	10a36	1410	5430	298	2010	4800	-	58.4	1050	6.98	769	34.6
718	A35	Type 2	qz	10a37.1	137	281	401	1910	1070	-	72.4	1430	<2.52	10.6	76.2
718	A35	Type 2	qz	10a37.2	<0.619	106	<3.72	1260	<33.9	-	5.82	1610	<1.62	<1.06	16.6
718	Single	Type 2	qz	10a38	134	11300	127	1270	295	-	17.2	1930	<5.85	10.6	<16.2
718	C31	Type 2	qz	10a39	<32.2	<1180	<196	681	<1560	-	<57.5	2580	<28.8	<44.4	<97.7
718	Single	Type 2	qz	10a40	377	832	760	1400	2730	-	27.4	239	269	109	<20.4
709	A21	Type 2	qz	10a43	21.4	<857	<111	4040	<1040	-	180	4970	<22.1	<23.8	133
SFB240	A42	Type 3	Mn-dol	10a45	<7.84	<259	<35.7	954	<211	-	41.3	3230	32.0	<8.19	<17.0
SFB240	A36	Type 3	Mn-dol	10a47	<6.64	<224	<30.6	3340	<186	-	116	3330	<12.1	23.8	<17.0
SFB240	A36	Type 3	Mn-dol	10a48	9.27	<123	<16.9	2100	310	-	92.9	2060	<2.25	20.1	<8.30
SFB240	A36	Type 3	Mn-dol	10a49	<5.21	<174	53.5	5170	<151	-	114	1730	<9.13	16.2	29.8
SFB240	C35	Type 3	Mn-dol	10a50	634	849	57.2	3130	2990	-	111	2240	22.4	20.6	<15.7
718	C36	Type 3	qz	12a03	6.02	<161	<18.6	3650	<182	-	117	1890	<1.63	<7.93	69.2
718	C36	Type 3	qz	12a04	65.0	<88.2	153	3880	<132	-	162	2090	<1.25	31.6	60.6
718	Single	Type 3	qz	12a05	1350	1740	130	5350	9060	-	113	2450	<5.46	10.3	73.9
718	Single	Type 1	qz	12a06.1	76.8	<344	52.2	130	740	-	14.9	23.6	<27.0	<14.9	<45.3
718	C37	Type 1	qz	12a06.2	<80.5	<4320	<570	<1610	<4840	-	<189	1100	<303	<189	<593
718	Single	Type 1	qz	12a07	1960	6860	1790	2970	7300	-	1470	31.9	<36.4	97.9	<121
718	C38	Type 1	qz	12a09	1210	2400	306	1510	9190	-	72.0	709	<95.9	96.7	<219
718	C38	Type 1	qz	12a10	1230	3860	305	592	4950	-	<32.2	458	<40.3	<32.5	87.7
718	Single	Type 1	qz	12a11	211	<400	<47.7	222	551	-	<17.8	210	<18.0	129	<42.2
718	C39	Type 1	qz	12a15	<27.3	<1260	<140	<412	<1710	-	<57.7	472	<66.1	<52.4	<149
718	C39	Type 1	qz	12a16	<3.18	<129	<16.2	<40.9	<174	-	9.59	613	<3.14	<5.00	<15.6
718	C39	Type 1	qz	12a17	46.3	<1490	<289	<528	<1860	-	<69.4	1110	<127	<56.8	<159
718	C39	Type 1	qz	12a18	3330	1880	<27.0	413	4270	-	14.8	739	<5.30	7.15	<20.8
718	C39	Type 1	qz	12a19	386	<324	<45.4	239	1360	-	<14.7	650	120	<12.7	63.3
718	Single	Type 1	qz	12a22	21.1	401	<15.1	66.2	632	-	<4.66	478	<7.05	12.4	<13.7
718	C40	Type 1	qz	12a23	<1.27	<45.3	<6.83	<16.1	<57.9	-	<2.30	241	<2.54	<1.83	<5.49
718	Single	Type 1	qz	12a24	64.5	2460	<36.0	1730	<261	-	12.2	536	<9.36	7.90	<22.9
718	Single	Type 1	qz	12a25	980	1240	316	3610	6520	-	189	19.7	<5.42	9.06	30.4
718	Single	Type 1	qz	12a26	1590	12300	4980	2920	41400	-	<118	75.2	247	178	<292
718	Single	Type 1	qz	12a27	1220	1820	144	4250	6800	-	<23.4	564	<16.6	48.7	<59.9
718	Single	Type 1	qz	12a30	2300	96900	<732	9410	50300	-	<180	<76.7	<165	<146	706
848	C41	Type 3	Fe-dol	12a32	64.0	113	290	2640	300	-	78.6	2250	<5.21	22.6	<7.85
848	C41	Type 3	Fe-dol	12a33	61.6	93.0	1160	2420	282	-	75.3	2250	7.99	540	<6.55
848	C41	Type 3	Fe-dol	12a34	333	588	528	1360	1200	-	64.5	1620	32.8	111	<11.1
848	C42	Type 3	Fe-dol	12a35	<11.2	<419	<64.2	2160	1810	-	73.3	2260	24.9	697	<26.8
848	C43	Type 3	Fe-dol	12a39	<8.75	<254	<34.2	4830	<233	-	136	3020	<10.0	<7.13	<17.5
848	C43	Type 3	Fe-dol	12a40	935	1260	2390	2210	2930	-	59.2	3020	<20.0	237	<43.7
848	C44	Type 3	Fe-dol	12a41	144	<247	413	3210	242	-	83.8	3080	20.2	61.5	<14.6
848	C44	Type 3	Fe-dol	12a42	<16.3	<477	<84.1	2870	627	-	96.1	1390	<21.7	<15.5	<31.9
714	C45	Type 3	Mn-dol	12a48	153	<112	250	2170	1060	-	71.2	4120	15.6	52.2	<14.2
714	C45	Type 3	Mn-dol	12a49	190	<168	<25.1	4430	<279	-	95.2	<5.70	78.4	21.1	<22.1
714	C45	Type 3	Mn-dol	12a50	471	<1150	412	2800	<1790	-	<62.6	<19.1	425	<44.7	<136
211	C47	Type 2	qz	12a53	<1.95	<64.9	32.6	<14.9	<62.7	-	21.0	379	<2.01	<2.11	6.54
211	C47	Type 2	qz	12a54	9.12	<60.3	54.2	52.2	<60.4	-	20.6	468	<1.02	1.91	<4.17
211	C47	Type 2	qz	12a56	<26.6	<910	<166	<204	<895	-	<39.2	1040	<47.1	<25.8	72.6
211	C48	Type 3	Fe-dol	12a57	<2.38	<82.8	21.2	683	<66.6	-	70.4	4830	<1.51	<1.43	<5.47
211	C48	Type 3	Fe-dol	12a58	<4.68	<148	<26.0	1270	<137	-	73.7	2190	<2.76	4.50	<10.7
211	C48	Type 3	Fe-dol	12a59	<4.85	<155	<26.3	758	197	-	66.5	2340	<9.05	<3.36	<10.1
211	C48	Type 3	Fe-dol	12a60	<11.6	<382	<70.0	540	383	-	224	11700	<18.1	<11.3	<25.4
211	C48	Type 3	Fe-dol	12a61.1	22.3	<77.1	<13.2	777	<71.7	-	73.2	5290	<3.79	2.33	<5.25
211	C48	Type 3	Fe-dol	12a61.2	<3.59	<119	21.8	1130	<101	-	111	4710	<6.52	2530	<8.17

Table 2.10 (continued): Chemical composition (ppm) of fluid inclusions from LA-ICP-MS analysis.

Sample	FIA	FI Type	Host	Spot ID	Cs	Ba	La	Ce	Pr	Nd	Sm	Eu	Gd	Tb	Dy
718	A33	Type 2	qz	10a28	<32.6	2700	26.2	<8.44	<5.97	<18.4	<21.8	<5.81	<21.0	<3.17	61.5
718	Single	Type 2	qz	10a30	<5.41	126	<1.34	<0.513	<0.430	<5.12	<2.85	<0.757	<2.74	<0.413	<1.69
718	Single	Type 2	qz	10a31	<17.6	55.5	<5.00	<4.20	<1.91	<10.7	<23.3	<3.36	<12.2	<1.83	<7.49
718	Single	Type 2	qz	10a32	765	754	212	88.4	300	24.5	<6.55	17.8	11.6	92.7	48.6
718	A34	Type 2	qz	10a33	3.78	44.1	7.33	<0.118	<0.325	6.32	<3.25	7.52	<2.07	0.120	0.429
718	A35	Type 2	qz	10a34	<22.2	263	<5.11	<2.42	<5.20	<11.3	<13.4	<7.52	<12.9	<1.94	<16.7
718	Single	Type 2	qz	10a35	<6.04	263	<1.91	29.1	<0.492	<2.75	54.1	<0.866	<9.24	2.18	<1.93
718	A35	Type 2	qz	10a36	37.4	303	2.37	20.4	6.06	23.6	0.956	3.56	<1.52	21.4	<0.936
718	A35	Type 2	qz	10a37.1	7.78	858	<0.323	0.187	0.134	0.451	<0.482	<0.128	<0.464	<0.178	<0.915
718	A35	Type 2	qz	10a37.2	3.30	302	<0.205	<0.0674	<0.0564	<0.316	<0.374	<0.0994	<0.360	<0.117	<0.589
718	Single	Type 2	qz	10a38	9.31	659	<1.14	<1.74	<0.950	<3.04	<3.60	<1.67	<7.14	<0.908	<4.38
718	C31	Type 2	qz	10a39	37.0	1010	<6.64	<3.18	<5.55	<14.9	<17.7	<11.9	<17.0	<6.44	<21.7
718	Single	Type 2	qz	10a40	<7.92	9.22	75.4	152	43.9	92.2	79.0	<1.03	48.3	4.87	<4.85
709	A21	Type 2	qz	10a43	<19.7	1880	<4.96	<2.45	<4.14	<11.5	<27.5	<7.30	<26.5	<3.96	<8.03
SFB240	A42	Type 3	Mn-dol	10a45	<6.70	<3.73	3.42	33.3	12.7	91.1	15.5	30.5	30.2	<0.881	7.39
SFB240	A36	Type 3	Mn-dol	10a47	24.4	934	2.54	15.1	<0.932	67.7	78.9	<1.99	140	26.3	79.3
SFB240	A36	Type 3	Mn-dol	10a48	15.3	736	3.54	51.6	13.8	164	201	27.6	270	53.2	248
SFB240	A36	Type 3	Mn-dol	10a49	31.3	917	<1.02	<0.822	<0.294	9.65	47.2	7.09	53.0	6.88	32.4
SFB240	C35	Type 3	Mn-dol	10a50	18.3	807	<0.639	1.49	4.07	<7.05	83.1	24.0	79.3	21.5	156
718	C36	Type 3	qz	12a03	<3.73	632	<0.179	<0.177	<0.147	<0.812	<0.969	<0.256	<0.936	<0.140	0.636
718	C36	Type 3	qz	12a04	124	498	0.757	36.5	<0.112	7.57	<2.65	1.23	<2.56	0.832	<1.57
718	Single	Type 3	qz	12a05	7.14	614	0.870	2.59	0.477	1.58	<0.851	<0.225	<3.12	<0.123	<0.504
718	Single	Type 1	qz	12a06.1	<8.00	173	2.34	8.52	<1.74	<9.61	<16.0	<3.03	<11.1	<1.66	<6.78
718	C37	Type 1	qz	12a06.2	<102	<263	<21.8	<21.6	<17.9	<98.8	<179	<31.1	<114	<17.1	<69.7
718	Single	Type 1	qz	12a07	62.1	827	<6.61	14.5	<3.27	<18.0	<21.5	<5.68	<34.6	<3.12	<59.0
718	C38	Type 1	qz	12a09	48.9	147	<10.5	<4.99	<4.13	<22.8	<27.2	<7.17	<26.2	<3.94	<16.1
718	C38	Type 1	qz	12a10	<16.4	133	<2.28	<2.26	<1.87	<19.9	<23.7	<3.25	<11.9	<1.78	<7.27
718	Single	Type 1	qz	12a11	<8.80	89.0	22.6	249	12.2	25.7	<4.84	1.41	<10.2	<1.53	<2.86
718	C39	Type 1	qz	12a15	<35.2	<56.8	<7.17	<3.06	<2.53	<40.1	<16.6	<4.38	<37.3	<2.41	<9.80
718	C39	Type 1	qz	12a16	<3.54	7.77	<0.340	<0.337	<0.279	<1.54	<4.82	<1.60	<1.77	<0.265	<1.08
718	C39	Type 1	qz	12a17	<39.5	71.8	<4.91	<4.88	<4.03	<50.5	<26.4	<6.96	<48.4	<3.83	<15.6
718	C39	Type 1	qz	12a18	<5.42	45.4	<1.17	51.9	<0.960	<2.59	<6.29	<0.812	<2.98	3.15	4.02
718	C39	Type 1	qz	12a19	7.96	26.0	<0.690	<0.685	<0.566	5.76	<3.71	104	<8.62	<0.537	<5.26
718	Single	Type 1	qz	12a22	<3.01	79.6	1.07	<0.240	<0.198	<3.01	<3.57	<0.342	<3.94	<0.421	1.94
718	C40	Type 1	qz	12a23	<1.16	19.0	<0.273	<0.271	<0.115	<1.24	<0.754	<0.387	<0.728	<0.109	<0.444
718	Single	Type 1	qz	12a24	<5.27	229	<0.400	<0.397	2.29	<1.81	<2.15	<0.566	<5.23	<0.311	<1.27
718	Single	Type 1	qz	12a25	318	163	3.11	74.1	<0.477	<4.07	21.3	3.37	16.7	1.91	<1.84
718	Single	Type 1	qz	12a26	<72.7	1150	<16.4	<16.3	<7.18	<39.7	<47.1	<12.4	<45.5	<6.82	<27.7
718	Single	Type 1	qz	12a27	<14.4	189	<3.98	<1.77	<1.46	<8.08	<40.8	<2.52	<17.3	<1.39	<10.6
718	Single	Type 1	qz	12a30	<99.8	<140	<39.6	<28.4	<14.5	<80.3	<154	<25.1	<149	<22.3	<56.1
848	C41	Type 3	Fe-dol	12a32	8.14	535	10.2	134	35.9	195	103	6.73	174	41.6	260
848	C41	Type 3	Fe-dol	12a33	6.99	509	9.18	87.0	20.7	124	93.2	6.69	154	40.5	243
848	C41	Type 3	Fe-dol	12a34	7.72	433	165	1330	285	1570	790	60.7	1070	251	1530
848	C42	Type 3	Fe-dol	12a35	13.3	327	241	1790	388	2090	1110	33.8	1560	311	1890
848	C43	Type 3	Fe-dol	12a39	8.82	723	34.9	250	50.4	280	111	2.26	137	32.2	225
848	C43	Type 3	Fe-dol	12a40	<13.5	1900	28.2	50.6	<1.74	45.8	56.0	<3.02	<3.01	16.2	187
848	C44	Type 3	Fe-dol	12a41	<5.63	729	29.3	129	28.9	215	113	6.11	163	17.2	223
848	C44	Type 3	Fe-dol	12a42	<11.0	918	15.5	<2.29	<0.809	<10.5	<5.34	<4.04	<17.1	<0.770	<3.15
714	C45	Type 3	Mn-dol	12a48	24.3	1390	<0.701	<0.181	<0.454	<0.834	<0.988	<1.00	<4.81	<0.143	<1.76
714	C45	Type 3	Mn-dol	12a49	27.4	1880	<0.236	<0.234	<0.724	<4.02	<4.76	<0.337	<1.24	<0.898	<2.81
714	C45	Type 3	Mn-dol	12a50	<35.3	482	<5.68	<5.64	<6.12	<6.81	<30.8	<8.12	<7.80	<1.17	<18.2
211	C47	Type 2	qz	12a53	2.80	233	<0.521	<0.563	<0.382	<1.79	<2.12	<0.663	<1.12	<0.407	<1.48
211	C47	Type 2	qz	12a54	3.30	154	<0.337	<0.268	<0.222	<1.54	<1.82	<0.155	<1.42	<0.303	<0.862
211	C47	Type 2	qz	12a56	<21.0	<14.7	66.9	<1.83	<3.35	<8.47	<27.1	<2.64	<9.71	<3.90	<5.91
211	C48	Type 3	Fe-dol	12a57	4.14	551	136	545	69.7	351	124	27.2	188	22.9	227
211	C48	Type 3	Fe-dol	12a58	4.86	439	4.51	<0.288	<0.549	<1.33	<3.63	11.9	<4.33	<0.226	<0.927
211	C48	Type 3	Fe-dol	12a59	6.48	433	<0.956	<0.827	<0.258	<3.12	12.4	<1.19	<3.58	<0.741	<2.66
211	C48	Type 3	Fe-dol	12a60	<9.11	844	290	572	128	110	97.8	24.0	130	87.9	157
211	C48	Type 3	Fe-dol	12a61.1	4.80	507	294	941	40.0	605	91.1	24.3	293	68.0	119
211	C48	Type 3	Fe-dol	12a61.2	6.27	446	236	724	15.8	337	96.3	11.8	314	27.3	196

Table 2.10 (continued): Chemical composition (ppm) of fluid inclusions from LA-ICP-MS analysis.

Sample	FIA	FI Type	Host	Spot ID	Ho	Er	Tm	Yb	Lu	W	Au	Pb	Bi	Th	U
718	A33	Type 2	qz	10a28	<3.30	<20.8	<3.12	<14.2	<6.93	<15.6	<22.5	257	33.2	4.01	4.02
718	Single	Type 2	qz	10a30	<0.430	<1.26	0.687	<1.86	<0.897	<2.03	<5.28	87.2	619	1380	1.91
718	Single	Type 2	qz	10a31	<1.91	<5.60	<4.44	<15.2	<3.44	<8.98	<19.3	116	4210	<1.02	2.16
718	Single	Type 2	qz	10a32	10.3	<2.90	28.5	43.1	<0.967	83.4	<3.73	546	239	2.38	247
718	A34	Type 2	qz	10a33	0.437	<0.290	16.3	<0.426	0.488	95.8	<1.58	37.3	18.4	131	1.43
718	A35	Type 2	qz	10a34	<4.26	<5.94	<1.91	<8.74	<1.98	<9.53	<16.1	456	<21.0	<1.08	<2.16
718	Single	Type 2	qz	10a35	<0.491	<1.44	<0.464	<2.12	<0.480	6020	<4.80	283	50.8	6.34	34.4
718	A35	Type 2	qz	10a36	<0.0974	1.59	14.5	2.89	0.915	139	3.19	907	2240	936	37.9
718	A35	Type 2	qz	10a37.1	<0.233	<0.213	<0.220	<0.804	<0.0710	32.3	<1.02	391	473	<0.160	1.12
718	A35	Type 2	qz	10a37.2	<0.150	<0.165	<0.142	<0.529	<0.0551	1.47	<0.646	406	6.43	<0.101	<0.0761
718	Single	Type 2	qz	10a38	<0.946	<1.59	<0.511	<4.09	<0.529	<4.45	<3.58	263	23.4	<0.507	<0.481
718	C31	Type 2	qz	10a39	<2.65	<16.2	<5.23	<11.5	<2.60	<12.5	<28.9	631	<18.3	3730	<2.81
718	Single	Type 2	qz	10a40	<1.23	111	4.27	7.07	4.00	<2.74	<6.47	59.1	324	1.27	130
709	A21	Type 2	qz	10a43	<2.04	<6.00	<1.93	<17.8	<2.00	<9.59	<21.4	1030	82.2	<2.68	<2.10
SFB240	A42	Type 3	Mn-dol	10a45	14.7	<7.40	2.41	46.8	4.37	<5.35	<4.96	115	<3.71	<0.494	<1.01
SFB240	A36	Type 3	Mn-dol	10a47	35.8	32.1	1.23	48.4	13.4	<4.36	<5.35	1310	<3.63	<0.502	0.810
SFB240	A36	Type 3	Mn-dol	10a48	44.8	94.6	3.54	55.2	<0.606	<0.984	<2.69	1260	<2.05	<0.384	<0.524
SFB240	A36	Type 3	Mn-dol	10a49	<0.982	120	18.4	90.5	14.9	1.52	<3.25	1410	<2.77	<0.463	<0.150
SFB240	C35	Type 3	Mn-dol	10a50	20.2	64.3	<0.505	35.0	15.4	<6.61	<3.96	1200	796	<0.766	1.32
718	C36	Type 3	qz	12a03	<0.147	<0.431	<0.139	<0.628	<0.144	128	<3.53	849	60.2	20.9	<0.0711
718	C36	Type 3	qz	12a04	1.50	<0.329	<0.491	<0.479	1.04	10.4	<1.95	1220	447	1.61	68.5
718	Single	Type 3	qz	12a05	<0.129	<0.378	<0.122	<0.550	<0.126	5.64	<2.82	551	6540	0.175	2.53
718	Single	Type 1	qz	12a06.1	<1.74	<5.08	<1.64	<7.40	<2.37	<8.22	<11.7	11.7	15.0	<0.909	3.40
718	C37	Type 1	qz	12a06.2	<17.8	<52.2	<16.8	<76.1	<26.5	<84.5	<136	<119	<136	<9.34	<8.61
718	Single	Type 1	qz	12a07	123	<9.53	<3.07	<13.9	<3.18	<25.7	<23.7	212	253	28.3	416
718	C38	Type 1	qz	12a09	<4.11	<25.0	<3.87	<17.5	<4.01	<19.5	<39.1	428	2270	<4.46	51.6
718	C38	Type 1	qz	12a10	<3.59	<5.44	<1.75	<7.92	<1.81	<8.80	<7.01	170	1430	2230	9.37
718	Single	Type 1	qz	12a11	<1.60	<2.14	<0.688	<8.30	<0.713	<3.46	<8.40	186	370	0.693	2.07
718	C39	Type 1	qz	12a15	<5.84	<24.1	<5.48	<10.6	<2.44	<27.5	<22.1	<29.1	<37.6	<1.30	<5.10
718	C39	Type 1	qz	12a16	<0.276	<0.806	<0.559	<1.17	<0.268	<2.81	<4.02	6.88	<3.14	<0.309	<0.132
718	C39	Type 1	qz	12a17	28.1	<11.6	159	<16.9	<3.87	<18.8	<15.2	92.2	<32.7	857	<1.91
718	C39	Type 1	qz	12a18	<1.15	<1.36	5.84	<4.87	<0.451	<2.19	<4.38	96.5	1370	368	1.10
718	C39	Type 1	qz	12a19	2.48	<1.63	<0.525	<2.37	1.40	<2.64	<2.14	2090	203	311	<0.918
718	Single	Type 1	qz	12a22	<0.439	<1.57	<0.184	<0.828	<0.190	<2.54	<2.06	71.2	43.2	223	0.448
718	C40	Type 1	qz	12a23	<0.114	<0.331	<0.250	<0.936	<0.110	<0.536	<1.26	40.9	<1.16	390	<0.127
718	Single	Type 1	qz	12a24	<0.817	<2.38	<0.304	<1.37	<0.314	<1.53	1.33	776	101	2430	0.797
718	Single	Type 1	qz	12a25	3.19	<1.38	9.15	<2.00	2.42	<3.44	22.4	545	328	1280	37.5
718	Single	Type 1	qz	12a26	<7.10	<38.8	<12.5	<30.0	<6.88	<33.5	<60.8	579	3130	16.5	90.6
718	Single	Type 1	qz	12a27	<1.45	<4.21	<1.36	<6.11	<1.40	<12.8	<5.54	932	1410	392	21.7
718	Single	Type 1	qz	12a30	<14.4	<41.9	<21.8	<60.6	158	<127	<55.0	1330	5690	3130	108
848	C41	Type 3	Fe-dol	12a32	56.6	137	20.2	140	20.1	<2.14	<2.29	2350	110	<0.0539	<0.215
848	C41	Type 3	Fe-dol	12a33	60.6	143	21.0	162	27.8	<1.26	<1.75	1810	114	<0.178	<0.216
848	C41	Type 3	Fe-dol	12a34	315	784	110	856	124	<2.44	<3.40	1290	489	<0.457	<0.461
848	C42	Type 3	Fe-dol	12a35	351	968	137	1100	156	<8.43	<7.85	1390	<6.19	<1.06	<1.17
848	C43	Type 3	Fe-dol	12a39	44.0	117	15.4	96.8	15.9	<1.51	<1.22	2760	<3.44	<0.856	<0.516
848	C43	Type 3	Fe-dol	12a40	64.7	185	19.5	106	<2.19	<12.6	<8.68	2420	1730	<1.17	144
848	C44	Type 3	Fe-dol	12a41	41.7	137	29.0	115	35.4	<3.99	<3.23	2000	539	0.207	<0.562
848	C44	Type 3	Fe-dol	12a42	<1.87	<5.48	<2.17	<7.91	<1.82	<3.83	<7.22	1010	<7.62	<0.969	<1.51
714	C45	Type 3	Mn-dol	12a48	<0.149	<0.435	<0.425	<0.637	<0.559	<0.704	<1.76	2030	470	<0.234	1.23
714	C45	Type 3	Mn-dol	12a49	<0.193	<0.562	<0.182	<3.07	<0.187	<3.39	<0.752	2940	37.5	<0.100	2.76
714	C45	Type 3	Mn-dol	12a50	<4.64	<13.6	<1.15	<5.19	<4.51	<5.74	<18.1	2240	777	<2.42	0.725
211	C47	Type 2	qz	12a53	<0.318	<0.509	<0.164	<1.61	<0.309	<0.824	<1.65	14.0	1.29	503	<0.0834
211	C47	Type 2	qz	12a54	<0.0886	<1.12	<0.207	<1.17	<0.0860	<1.49	<1.37	22.0	2.84	585	<0.182
211	C47	Type 2	qz	12a56	<1.50	<4.40	<1.42	<6.41	<3.21	<15.7	<20.0	<15.0	<16.4	<1.71	<1.94
211	C48	Type 3	Fe-dol	12a57	13.4	57.5	5.84	3.74	5.92	<1.33	<1.10	935	<1.09	<0.243	<0.134
211	C48	Type 3	Fe-dol	12a58	1.95	40.5	<0.722	<1.00	<0.228	<2.57	<2.12	672	<2.33	<0.281	<0.404
211	C48	Type 3	Fe-dol	12a59	<0.254	<2.26	<0.726	<2.36	<0.536	<1.21	<2.64	561	<1.99	<0.568	<0.438
211	C48	Type 3	Fe-dol	12a60	76.4	<6.15	<1.74	36.1	<1.49	<8.79	<5.99	340	<4.91	<1.37	<1.26
211	C48	Type 3	Fe-dol	12a61.1	26.8	84.5	2.39	14.0	<0.153	<0.750	<1.89	658	3.18	<0.200	<0.229
211	C48	Type 3	Fe-dol	12a61.2	16.0	44.5	5.54	44.8	1.34	<1.56	<3.03	845	<1.98	<0.333	<0.367

Table 2.10 (continued): Chemical composition (ppm) of fluid inclusions from LA-ICP-MS analysis.

Sample	FIA	FI Type	Host	Spot ID	Li	B	Na	Mg	Al	Si	Cl	K	Ca	Mn	Fe
SFB240	B1	Type 3	Mn-dol	05a07	145	211	83400	-	-	1300	240000	17600	54100	-	-
SFB240	B1	Type 3	Mn-dol	05a08	178	316	83400	-	-	<4610	298000	27700	54100	-	-
SFB240	B1	Type 3	Mn-dol	05a09	173	363	83400	-	-	3000	245000	26900	54100	-	-
SFB240	Single	Type 3	Mn-dol	05a10	171	309	83400	-	-	<2560	284000	25100	54100	-	-
SFB240	B2	Type 3	Mn-dol	05a13	279	504	83400	-	-	3360	314000	37000	54100	-	-
SFB240	B2	Type 3	Mn-dol	05a15	184	298	83400	-	-	3760	250000	25600	54100	-	-
SFB240	B1	Type 3	Mn-dol	05a16	245	454	83400	-	-	2680	349000	41500	54100	-	-
SFB240	B1	Type 3	Mn-dol	05a17	170	353	83400	-	-	4650	265000	27100	54100	-	-
SFB240	B1	Type 3	Mn-dol	05a19	197	451	83400	-	-	3320	288000	34200	54100	-	-
SFB240	B3	Type 3	Mn-dol	05a22	121	88	83400	-	-	1460	268000	12600	54100	-	-
SFB240	B3	Type 3	Mn-dol	05a23	148	101	83400	-	-	<3490	264000	10800	54100	-	-
SFB240	B3	Type 3	Mn-dol	05a24	106	86	83400	-	-	<1030	249000	10100	54100	-	-
SFB240	B3	Type 3	Mn-dol	05a25	169	212	83400	-	-	<2970	284000	19000	54100	-	-
SFB240	B3	Type 3	Mn-dol	05a26	171	150	83400	-	-	<2970	281000	19100	54100	-	-
709	Single	Type 2	qz	04a75	<30.9	220	105000	1030	-	<9010	295000	6700	38100	4900	<365
709	B4	Type 2	qz	04a76	305	803	86100	1150	-	<2310	203000	24300	44900	15300	2400
709	B4	Type 2	qz	04a77	396	691	90900	260	-	<3680	251000	21400	42500	13100	5910
709	B4	Type 2	qz	04a78	978	268	93900	792	-	<4960	386000	7360	62900	490	198
709	B5	Type 2	qz	04a81	370	<36.5	105000	592	-	<6240	261000	2050	47500	67.0	<250
709	B5	Type 2	qz	04a82	410	197	95600	1710	-	<1480	229000	8340	54400	4410	336
709	B5	Type 2	qz	04a84	<111	<171	113000	389	-	<31900	380000	5700	30500	214	1420
709	B5	Type 2	qz	04a86	618	129	85700	2700	-	<4230	231000	10200	68000	6570	598
709	B6	Type 2	qz	04a88	395	130	108000	774	-	<7560	244000	11800	25700	7260	2140
709	B6	Type 2	qz	04a89	1780	288	67000	13300	-	<4530	251000	20700	70400	10200	3310
709	B7	Type 2	qz	04a90	1680	269	48900	4330	-	<7670	182000	16400	120000	10100	13200
709	B7	Type 2	qz	04a91	<2.87	89	112000	1480	-	<856	211000	5840	25500	4670	1040
709	B7	Type 2	qz	04a93	516	78	98000	93	-	<1400	262000	18600	40000	6530	1400
709	B8	Type 2	qz	04a94	1350	146	75500	<146	-	<10900	364000	8570	90800	3430	<443
709	B8	Type 2	qz	04a95	1930	141	79500	<41.9	-	<3640	272000	3850	84600	8190	<147
709	B9	Type 2	qz	04a96	756	150	72600	<74.1	-	<7230	310000	9750	88700	6780	<290
709	B9	Type 2	qz	04a97	588	220	109000	1700	-	<3600	223000	12300	24600	6490	2120
709	B9	Type 2	qz	04a99	813	248	93900	340	-	<5570	299000	20300	43500	8550	1780
718	B10	Type 1	qz	04a20	1410	128	40500	9010	-	<8840	172000	17200	68400	396	1820
718	B10	Type 1	qz	04a28	<3.08	241	68800	1930	-	<1080	189000	17400	25600	980	560
718	B10	Type 1	qz	04a32	489	347	34000	2440	-	<239	190000	9760	87000	1610	17800
718	B10	Type 1	qz	04a33	3600	390	63700	564	-	<737	147000	27500	22800	323	1600
718	B10	Type 1	qz	04a35	998	292	62100	4130	-	<530	151000	10300	38000	2450	1930
718	B10	Type 1	qz	04b12	457	159	46300	14100	-	<580	139000	20300	47400	2350	5360
718	B10	Type 1	qz	04b13	<1.62	85	66300	11800	-	<451	160000	7130	24100	1030	3300
718	B10	Type 1	qz	04b14	<15.3	344	63900	3770	-	<4200	182000	26800	26300	529	2930
718	B10	Type 1	qz	04b15	<0.819	182	52100	16800	-	<220	136000	15500	36800	1090	6950
718	B10	Type 1	qz	04b16	<3.04	362	41400	12300	-	<788	130000	44200	43000	2370	7670

Table 2.10 (continued): Chemical composition (ppm) of fluid inclusions from LA-ICP-MS analysis.

Sample	FIA	FI Type	Host	Spot ID	Co	Ni	Cu	Zn	As	Br	Rb	Sr	Mo	Ag	Sb
SFB240	B1	Type 3	Mn-dol	05a07	-	-	-	3160	-	3980	77.0	1920	-	-	-
SFB240	B1	Type 3	Mn-dol	05a08	-	-	-	5320	-	5530	137	2400	-	-	-
SFB240	B1	Type 3	Mn-dol	05a09	-	-	-	3820	-	4890	121	2640	-	-	-
SFB240	Single	Type 3	Mn-dol	05a10	-	-	-	4570	-	4630	136	1810	-	-	-
SFB240	B2	Type 3	Mn-dol	05a13	-	-	-	6650	-	6910	193	3440	-	-	-
SFB240	B2	Type 3	Mn-dol	05a15	-	-	-	5830	-	4430	119	2110	-	-	-
SFB240	B1	Type 3	Mn-dol	05a16	-	-	-	6590	-	7610	172	1510	-	-	-
SFB240	B1	Type 3	Mn-dol	05a17	-	-	-	4340	-	5100	125	1900	-	-	-
SFB240	B1	Type 3	Mn-dol	05a19	-	-	-	5870	-	5700	152	2130	-	-	-
SFB240	B3	Type 3	Mn-dol	05a22	-	-	-	1370	-	4710	38.0	5060	-	-	-
SFB240	B3	Type 3	Mn-dol	05a23	-	-	-	1580	-	4230	36.0	3420	-	-	-
SFB240	B3	Type 3	Mn-dol	05a24	-	-	-	983	-	3500	37.0	2590	-	-	-
SFB240	B3	Type 3	Mn-dol	05a25	-	-	-	4980	-	5160	89.0	2580	-	-	-
SFB240	B3	Type 3	Mn-dol	05a26	-	-	-	5380	-	5060	83.0	4130	-	-	-
709	Single	Type 2	qz	04a75	-	-	-	1880	-	3110	57.0	1870	-	-	-
709	B4	Type 2	qz	04a76	-	-	-	6200	-	2460	169	2800	-	-	-
709	B4	Type 2	qz	04a77	-	-	-	4800	-	905	161	3120	-	-	-
709	B4	Type 2	qz	04a78	-	-	-	300	-	6840	52.0	2210	-	-	-
709	B5	Type 2	qz	04a81	-	-	-	22.0	-	2030	16.0	971	-	-	-
709	B5	Type 2	qz	04a82	-	-	-	1060	-	2480	25.0	1390	-	-	-
709	B5	Type 2	qz	04a84	-	-	-	176	-	6670	<41.0	802	-	-	-
709	B5	Type 2	qz	04a86	-	-	-	796	-	2600	84.0	2240	-	-	-
709	B6	Type 2	qz	04a88	-	-	-	1520	-	1880	67.0	1870	-	-	-
709	B6	Type 2	qz	04a89	-	-	-	4350	-	3170	130	4610	-	-	-
709	B7	Type 2	qz	04a90	-	-	-	6020	-	5020	61.0	4430	-	-	-
709	B7	Type 2	qz	04a91	-	-	-	1190	-	1310	44.0	1230	-	-	-
709	B7	Type 2	qz	04a93	-	-	-	2850	-	3300	80.0	2480	-	-	-
709	B8	Type 2	qz	04a94	-	-	-	2930	-	3390	57.0	3880	-	-	-
709	B8	Type 2	qz	04a95	-	-	-	944	-	1780	40.0	3620	-	-	-
709	B9	Type 2	qz	04a96	-	-	-	4760	-	4460	92.0	5400	-	-	-
709	B9	Type 2	qz	04a97	-	-	-	1350	-	1360	82.0	1240	-	-	-
709	B9	Type 2	qz	04a99	-	-	-	2880	-	3350	139	2800	-	-	-
718	B10	Type 1	qz	04a20	-	-	-	388	-	2090	47.0	331	-	-	-
718	B10	Type 1	qz	04a28	-	-	-	621	-	2160	43.0	579	-	-	-
718	B10	Type 1	qz	04a32	-	-	-	6540	-	3200	33.0	1440	-	-	-
718	B10	Type 1	qz	04a33	-	-	-	1250	-	2330	103	588	-	-	-
718	B10	Type 1	qz	04a35	-	-	-	421	-	763	37.0	841	-	-	-
718	B10	Type 1	qz	04b12	-	-	-	1340	-	1740	44.0	739	-	-	-
718	B10	Type 1	qz	04b13	-	-	-	313	-	693	24.0	482	-	-	-
718	B10	Type 1	qz	04b14	-	-	-	405	-	1840	112	677	-	-	-
718	B10	Type 1	qz	04b15	-	-	-	535	-	3030	57.0	762	-	-	-
718	B10	Type 1	qz	04b16	-	-	-	855	-	3700	130	676	-	-	-

Table 2.10 (continued): Chemical composition (ppm) of fluid inclusions from LA-ICP-MS analysis.

Sample	FIA	FI Type	Host	Spot ID	Cs	Ba	La	Ce	Pr	Nd	Sm	Eu	Gd	Tb	Dy
SFB240	B1	Type 3	Mn-dol	05a07	14.0	532	-	-	-	-	-	-	-	-	-
SFB240	B1	Type 3	Mn-dol	05a08	19.0	922	-	-	-	-	-	-	-	-	-
SFB240	B1	Type 3	Mn-dol	05a09	23.0	885	-	-	-	-	-	-	-	-	-
SFB240	Single	Type 3	Mn-dol	05a10	22.0	881	-	-	-	-	-	-	-	-	-
SFB240	B2	Type 3	Mn-dol	05a13	34.0	1820	-	-	-	-	-	-	-	-	-
SFB240	B2	Type 3	Mn-dol	05a15	22.0	1110	-	-	-	-	-	-	-	-	-
SFB240	B1	Type 3	Mn-dol	05a16	36.0	1190	-	-	-	-	-	-	-	-	-
SFB240	B1	Type 3	Mn-dol	05a17	22.0	889	-	-	-	-	-	-	-	-	-
SFB240	B1	Type 3	Mn-dol	05a19	28.0	1050	-	-	-	-	-	-	-	-	-
SFB240	B3	Type 3	Mn-dol	05a22	4.00	81.0	-	-	-	-	-	-	-	-	-
SFB240	B3	Type 3	Mn-dol	05a23	4.00	292	-	-	-	-	-	-	-	-	-
SFB240	B3	Type 3	Mn-dol	05a24	4.00	74.0	-	-	-	-	-	-	-	-	-
SFB240	B3	Type 3	Mn-dol	05a25	12.0	662	-	-	-	-	-	-	-	-	-
SFB240	B3	Type 3	Mn-dol	05a26	14.0	716	-	-	-	-	-	-	-	-	-
709	Single	Type 2	qz	04a75	<7.11	644	-	-	-	-	-	-	-	-	-
709	B4	Type 2	qz	04a76	10.0	1970	-	-	-	-	-	-	-	-	-
709	B4	Type 2	qz	04a77	10.0	2240	-	-	-	-	-	-	-	-	-
709	B4	Type 2	qz	04a78	<4.04	950	-	-	-	-	-	-	-	-	-
709	B5	Type 2	qz	04a81	<5.12	70.0	-	-	-	-	-	-	-	-	-
709	B5	Type 2	qz	04a82	3.00	726	-	-	-	-	-	-	-	-	-
709	B5	Type 2	qz	04a84	<26.6	33.0	-	-	-	-	-	-	-	-	-
709	B5	Type 2	qz	04a86	<3.36	436	-	-	-	-	-	-	-	-	-
709	B6	Type 2	qz	04a88	<6.16	1190	-	-	-	-	-	-	-	-	-
709	B6	Type 2	qz	04a89	13.0	2650	-	-	-	-	-	-	-	-	-
709	B7	Type 2	qz	04a90	<6.07	1540	-	-	-	-	-	-	-	-	-
709	B7	Type 2	qz	04a91	4.00	613	-	-	-	-	-	-	-	-	-
709	B7	Type 2	qz	04a93	8.00	1510	-	-	-	-	-	-	-	-	-
709	B8	Type 2	qz	04a94	13.0	1880	-	-	-	-	-	-	-	-	-
709	B8	Type 2	qz	04a95	12.0	1640	-	-	-	-	-	-	-	-	-
709	B9	Type 2	qz	04a96	18.0	2590	-	-	-	-	-	-	-	-	-
709	B9	Type 2	qz	04a97	4.00	654	-	-	-	-	-	-	-	-	-
709	B9	Type 2	qz	04a99	8.00	1430	-	-	-	-	-	-	-	-	-
718	B10	Type 1	qz	04a20	<6.09	183	-	-	-	-	-	-	-	-	-
718	B10	Type 1	qz	04a28	2.00	97.0	-	-	-	-	-	-	-	-	-
718	B10	Type 1	qz	04a32	6.00	485	-	-	-	-	-	-	-	-	-
718	B10	Type 1	qz	04a33	2.00	53.0	-	-	-	-	-	-	-	-	-
718	B10	Type 1	qz	04a35	6.00	658	-	-	-	-	-	-	-	-	-
718	B10	Type 1	qz	04b12	4.00	506	-	-	-	-	-	-	-	-	-
718	B10	Type 1	qz	04b13	2.00	388	-	-	-	-	-	-	-	-	-
718	B10	Type 1	qz	04b14	<3.28	80.0	-	-	-	-	-	-	-	-	-
718	B10	Type 1	qz	04b15	4.00	677	-	-	-	-	-	-	-	-	-
718	B10	Type 1	qz	04b16	7.00	577	-	-	-	-	-	-	-	-	-

Table 2.10 (continued): Chemical composition (ppm) of fluid inclusions from LA-ICP-MS analysis.

Sample	FIA	FI Type	Host	Spot ID	Ho	Er	Tm	Yb	Lu	W	Au	Pb	Bi	Th	U
SFB240	B1	Type 3	Mn-dol	05a07	-	-	-	-	-	-	-	1450	-	-	-
SFB240	B1	Type 3	Mn-dol	05a08	-	-	-	-	-	-	-	2240	-	-	-
SFB240	B1	Type 3	Mn-dol	05a09	-	-	-	-	-	-	-	2100	-	-	-
SFB240	Single	Type 3	Mn-dol	05a10	-	-	-	-	-	-	-	1860	-	-	-
SFB240	B2	Type 3	Mn-dol	05a13	-	-	-	-	-	-	-	3170	-	-	-
SFB240	B2	Type 3	Mn-dol	05a15	-	-	-	-	-	-	-	1980	-	-	-
SFB240	B1	Type 3	Mn-dol	05a16	-	-	-	-	-	-	-	2910	-	-	-
SFB240	B1	Type 3	Mn-dol	05a17	-	-	-	-	-	-	-	2050	-	-	-
SFB240	B1	Type 3	Mn-dol	05a19	-	-	-	-	-	-	-	2500	-	-	-
SFB240	B3	Type 3	Mn-dol	05a22	-	-	-	-	-	-	-	362	-	-	-
SFB240	B3	Type 3	Mn-dol	05a23	-	-	-	-	-	-	-	386	-	-	-
SFB240	B3	Type 3	Mn-dol	05a24	-	-	-	-	-	-	-	323	-	-	-
SFB240	B3	Type 3	Mn-dol	05a25	-	-	-	-	-	-	-	1900	-	-	-
SFB240	B3	Type 3	Mn-dol	05a26	-	-	-	-	-	-	-	1970	-	-	-
709	Single	Type 2	qz	04a75	-	-	-	-	-	-	-	1230	-	-	-
709	B4	Type 2	qz	04a76	-	-	-	-	-	-	-	5280	-	-	-
709	B4	Type 2	qz	04a77	-	-	-	-	-	-	-	4050	-	-	-
709	B4	Type 2	qz	04a78	-	-	-	-	-	-	-	163	-	-	-
709	B5	Type 2	qz	04a81	-	-	-	-	-	-	-	52.0	-	-	-
709	B5	Type 2	qz	04a82	-	-	-	-	-	-	-	642	-	-	-
709	B5	Type 2	qz	04a84	-	-	-	-	-	-	-	36.0	-	-	-
709	B5	Type 2	qz	04a86	-	-	-	-	-	-	-	431	-	-	-
709	B6	Type 2	qz	04a88	-	-	-	-	-	-	-	2520	-	-	-
709	B6	Type 2	qz	04a89	-	-	-	-	-	-	-	3250	-	-	-
709	B7	Type 2	qz	04a90	-	-	-	-	-	-	-	1070	-	-	-
709	B7	Type 2	qz	04a91	-	-	-	-	-	-	-	1040	-	-	-
709	B7	Type 2	qz	04a93	-	-	-	-	-	-	-	2500	-	-	-
709	B8	Type 2	qz	04a94	-	-	-	-	-	-	-	404	-	-	-
709	B8	Type 2	qz	04a95	-	-	-	-	-	-	-	288	-	-	-
709	B9	Type 2	qz	04a96	-	-	-	-	-	-	-	2590	-	-	-
709	B9	Type 2	qz	04a97	-	-	-	-	-	-	-	1480	-	-	-
709	B9	Type 2	qz	04a99	-	-	-	-	-	-	-	3950	-	-	-
718	B10	Type 1	qz	04a20	-	-	-	-	-	-	-	176	-	-	-
718	B10	Type 1	qz	04a28	-	-	-	-	-	-	-	47.0	-	-	-
718	B10	Type 1	qz	04a32	-	-	-	-	-	-	-	2340	-	-	-
718	B10	Type 1	qz	04a33	-	-	-	-	-	-	-	152	-	-	-
718	B10	Type 1	qz	04a35	-	-	-	-	-	-	-	81.0	-	-	-
718	B10	Type 1	qz	04b12	-	-	-	-	-	-	-	474	-	-	-
718	B10	Type 1	qz	04b13	-	-	-	-	-	-	-	66.0	-	-	-
718	B10	Type 1	qz	04b14	-	-	-	-	-	-	-	42.0	-	-	-
718	B10	Type 1	qz	04b15	-	-	-	-	-	-	-	135	-	-	-
718	B10	Type 1	qz	04b16	-	-	-	-	-	-	-	158	-	-	-